STP as a Reaction Control System

Thesis report for the prototype design of a Solar Thermal Propulsion reaction control thruster for the Green SWaP project

Niklas Gebhardt

Delft University of Technology

TU Delft

STP as a Reaction Control System

Thesis report for the prototype design of a Solar Thermal Propulsion reaction control thruster for the Green SWaP project

by

Niklas Gebhardt

Student Name

Niklas Gebhardt

Supervisor :	A. Cervone
PhD Assistants Supervisors:	R. Cambertoni & L. Dall' Osto
Project Duration:	February, 2025 - November, 2025
Faculty:	Faculty of Aerospace Engineering, Delft

Cover: Canadarm 2 Robotic Arm Grapples SpaceX Dragon by NASA under CC BY-NC 2.0 (Modified)

Style: TU Delft Report Style, with modifications by Daan Zwaneveld

TU Delft

Preface

Before you lies the master's thesis; "STP as a reaction control system: Thesis report for the prototype design of a Solar Thermal Propulsion reaction control system for the Green SWaP project." It has been written for the completion of the Space Engineering master track at the Technological University of Delft in Delft, Netherlands. I was actively working on the thesis from February to October of 2025.

Throughout my previous studies, I have noticed that I have a love for propulsion technology and wanted to use this opportunity to explore this further, and develop my skills in this field. I have had the opportunity to extensively work with Ansys Mechanical, Ansys SPEOS and Ansys Fluent, three very powerful simulation tools. I have furthered my understanding of the thermodynamics and the fluid dynamics of a propulsion system. I have also learnt about the difficulties and discipline required in working from home and on my own schedule. This has taught me many things that will be invaluable both in my professional and personal life.

I would like to thank my supervisor, A. Cervone, for allowing me to design a propulsion system. Providing me with a challenge, I very much enjoyed working on. I am extremely grateful to you for all the support and patience you showed me throughout my thesis. I would also like to thank my two PhD Assistant Supervisors, R. Cambertoni & L. Dall'Osto, for all the excellent support and guidance provided; without them, I would have had a much more difficult time.

I would also like to thank my family and friends, who were very supportive throughout my thesis and were a great help.

Niklas Gebhardt
Delft, January 2026

Summary

This report aims to produce an efficient, accurate, and reliable STP thruster prototype to validate the use of an STP thruster in the Green SWaP RCS system. The Green SWaP mission goal is the development of an in-orbit capability in converting H_2O into H_2O_2 and H_2, which are used as propellants. The report first gathers the required information through a literature study, using this information to produce a series of concepts, and choosing one concept to be evaluated further. Implementing both ideal rocket theory and the thermodynamic heat equations to develop the prototype design. Verifying the prototype against the requirements set by the Green SWaP project, using numerical results to increase the certainty in the verifications made. Implementing both a steady state and transient thermal simulation with Ansys Mechanical, evaluating the system's thermal characteristics before the introduction of the propellant. An implementation of a ray-tracing simulation with Ansys Speos, evaluating the luminosity gradient seen across different cavity geometries. Evaluating the thermal and fluid properties of the system with propellant flow using Ansys Fluent, implementing a steady state simulation of the whole prototype, and a simplified 2D simulation of the nozzle, evaluating both the steady state and transient properties. The verified prototype has a nominal thrust value of 0.851827 [N], about a 14.8% reduction from the requirement due to the decrease in the effective throat and exit area caused by wall boundary conditions and a partial flow separation at the nozzle wall. Producing a specific impulse of 644.77 [s], significantly above the requirement of 500-600 [s], depending on the purity of the Hydrogen.

Contents

Nomenclature

Abbreviations

Abbreviation	Definition
AFRPL	Air Force Rocket Propulsion Laboratory
AR	Aspect Ratio
CAD	Computer Aided Design
CD	Convergent Divergent Nozzle
CFD	Computational Fluid Dynamics
CFESat	Cibola Fire Experiment Satellite
CTE	Coefficient of Thermal Expansion
DMC	Disaster Monitoring Constellation
DNS	Direct Numerical Simulation
C/E	Chamber to Exit Pressure Ratio
E-D	Expansion deflection Nozzle
FZP	Fresnel Zone Plate
GEO	Geosynchronous Earth Orbit
LEO	Low Earth Orbit
LH_2	Liquid Hydrogen
LO_2	Liquid Oxygen
LPF	Light Path Finder
MNG	Multi Nozzle Grid
PSF	Point Spread Function
RANS	Reynolds Averaged Navier-Stocks
RCS	Reaction Control System
RSS	Restricted Shock Separations
SST	Shear Stress Transport
STP	Solar Thermal Propulsion
TBC	To Be Confirmed
TIC	Truncated Ideal Contour
TOC	Thrust Optimised Parabolic

Symbols

Symbol	Definition	Unit
A	Area	$[m^2]$
C_f	Thrust Coefficient	$[-]$
$c*$	Characteristic Exhaust Velocity	$[m \cdot s^{-1}]$
F	Force or Thrust	$[N]$
g_0	Gravitational acceleration	$[m \cdot s^{-2}]$
h	Convective Heat Coefficient	$[W \cdot m^{-2} \cdot {}^\circ K^{-1}]$
I_{sp}	Specific Impulse	$[s]$
k	Thermal Conductivity	$[W \cdot m^{-1} \cdot {}^\circ K^{-1}]$
M	Mass	$[kg]$
$\mathcal{M}$	Mean Molar Mass	$[g \cdot mol^{-1}]$
m	mass flow rate	$[kg \cdot s^{-1}]$
Nu	Nusselt number	$[-]$

Symbol	Definition	Unit
T	Temperature	$[^\circ K]$
t	Time	$[s]$
R	Specific gas constant	$[J \cdot {}^\circ K^{-1} \cdot kg^{-1}]$
Re	Reynolds Number	$[-]$
P	Pressure	$[Pa]$
Pr	Prandtl Number	$[-]$
U, V, v, u	Velocity	$[m \cdot s^{-1}]$
α	Nozzle Half Angle	$[rad]$
Δv	Delta V	$[m \cdot s^{-1}]$
ρ	Density	$[kg/m^3]$
Γ	Vandenkerckhove Function	$[-]$
γ	Specific Heat Ratio	$[-]$
μ	Viscosity	$[Pa \cdot s]$

1

Introduction

Current space missions are not limited by the reliability and function of the system components but often by the available propellant on board. With multi-million dollar space missions being forced to end their mission prematurely before running out of propellant, to reduce the amount of space debris in orbit. This is an immense waste of resources; the capability of the spacecraft to produce its own propellant in orbit could drastically extend the lifetime and capabilities of these missions.

Furthering this goal, the Green Solar-to-Propellant Water Propulsion project (Green SWaP) was started, with the mission statement of the project being "to develop an in-orbit system capable of converting water into Hydrogen peroxide (H_2O_2) and Hydrogen (H_2) for use as propellants. The system will feature a $200\ [N]$ chemical thruster ($H_2O_2 + H_2$, with an $I_{sp} > 360\ [seconds]$) and $1\ [N]$ solar thermal thruster (providing an $I_{sp}$of$\sim 500\ [seconds]$)." The focus of this report is on the second part of the project, the initial design of a prototype solar thermal thruster to be used in the reaction control system. The specific aim is "the production of an efficient, accurate and reliable solar thermal propulsion thruster prototype, allowing for the validation of their use in a reaction control system"

To this extent, the report starts with a literature study, investigating the research questions posed, furthering the understanding of the topics related to the design of a solar thermal propulsion system. Concentrating on the design of the absorber/heat-exchanger and the thruster, generating a series of concepts through an idea tree, and choosing a single concept to pursue. Then, going on to do the initial sizing of the thruster and the heat-exchanger in their respective chapters. Presenting the prototype design to be evaluated and verifying the prototype against the requirements set by Green SWaP. Going on to reinforce the verification through the implementation of numerical analysis, providing the final verification of the prototype to the requirements. Finishing the report with a conclusion and suggestions for possible future work to be conducted.

2

Literature Study

2.1. literature Introduction

The Green Solar-to-Propellant Water Propulsion project (Green SWaP) aims to develop an in-orbit system capable of converting stored water into Hydrogen and Hydrogen peroxide. With a mission statement: ”To use solar energy to produce propellants onboard the spacecraft by converting water (H_2O) to propellants, H_2O_2 and H_2, developing innovative propulsion systems based on them.” Part of the system capability is to use the stored Hydrogen for reaction control through the use of a Solar Thermal Propulsion (STP) system.

This Literature study aims to investigate the literature surrounding the use of the STP system in space, to assist in the development of the Green SWaP reaction control system. To help investigate the literature, four separate research questions are proposed:

- **How are rocket propulsion characteristics and performance estimations calculated, with a focus on Hydrogen as a propellant?**
- **How have ground-based STP systems been designed, and have any mission plans been generated?**
- **What advances in nozzle design could improve system performance, including associated performance estimations?**
- **What is the most optimal design for the solar collector system, considering material choice and Hydrogen handling?**

Each of the research questions is answered in its respective section, first with the introduction to rocket propulsion theory, where the propulsion characteristics and performance are explained. Then, moving on to an investigation into the state of STP missions and what experimental literature exists on such systems. Continuing with the introduction of the nozzle theory, analysing redevelopment in nozzle geometries and performance estimations. Thereafter, a more in-depth review of the two major components of an STP system, as well as an investigation into the handling of Hydrogen. Finally, a conclusion on the literature study as a whole.

2.2. Rocket Propulsion Theory

This section aims to answer the research question: ”How are rocket propulsion characteristics and performance estimations calculated, with a focus on Hydrogen as a propellant?”. With that at hand, the section starts with a quick introduction to rocket history and the fundamentals of rocketry. Then, a more in-depth explanation of the ideal rocket theory will be provided, yielding a set of equations to evaluate rocket performance characteristics. Finally, explaining why Hydrogen is such a good propellant and why it currently has little use outside launch vehicles.

2.2.1. Rocket History and Fundamentals

The concept of propelling an object forward through the ejection of high-velocity exhaust has been around for more than 2000 years, with examples of heated steam being forced through a nozzle generating rotational force being observed in ancient Greece, [1]. With more concepts coming along through the ages, such as ancient Chinese rocket-propelled arrows, [2]. However, the idea of using rockets to explore the stars was first established in the science fiction book ”From Earth to the Moon” by Jules Verne, [3]. Later described scientifically by Tsiolkovsky in his famous 1903 paper ”The Exploration of the Cosmic Space by Means of Reaction Devices” [4], where he describes the use of a chemical reaction to propel a rocket into space, giving birth to modern rocketry.

Tsiolkovsky is mostly known for deriving the Tsiolkovsky equation, also known as the Rocket equation, which equates the change in velocity directly to the exhaust velocity and the loss of propellant. Providing the derivation of the Rocket equation, [5]. For a stable system at time t and at time $t + \Delta t$ where a small mass ($-\Delta M$) has been expelled at a relative velocity of $-w$

Starting from the Momentum equations at time t:

$$I_t = M \cdot v \tag{2.1}$$

and $t + \Delta t$:

$$I_{t+\Delta t} = (M + \Delta M) \cdot (v + \Delta v) - \Delta M \cdot (v - w) \tag{2.2}$$

Following that, the momentum must be the same; from Newton’s laws of conservation, the momentum balance becomes.

$$M \cdot v = (M + \Delta M) \cdot (v + \Delta v) - \Delta M \cdot (v - w) \tag{2.3}$$

Reducing and assuming an infinitesimal small velocity change, the equation becomes:

$$M \cdot dv = -dM \cdot w \tag{2.4}$$

Integrating both sides provides the rocket equation:

$$\Delta v = w \cdot ln\left(\frac{M_0}{M}\right) \tag{2.5}$$

Where Δv is the change in velocity, w is the exhaust velocity, M_0 is the initial mass, and M is the final mass of the space vehicle. The maximum Δv is the limiting factor in the destinations a space vehicle can reach.

2.2.2. Ideal Rocket Theory

Having understood the fundamentals of rocket theory, the performance characteristics can be analytically determined. Referring heavily to the thermal propulsion books by B.T.C Zandbergen and M.J.L Turner, [5] [6]. Rocket Theory can be a very complex subject; thus, providing a quick illustration of how a rocket motor functions, using the RS-25 Rocket motor as an example. Figure 2.1, provides a diagram of the combustion cycle for the RS-25 engine, the RS-25 runs a Fuel-rich dual-shaft staged combustion cycle. Most of the Hydrogen is pumped into the two preburners, with a little oxygen, in a fuel-rich configuration, powering the two turbopump assemblies. The Hydrogen-rich exhaust from the preburners is brought to the main combustion chamber, where it fully combusts with the rest of the oxygen and is expelled through the throat and out the nozzle, producing thrust. The use of combustion to generate hot gases is different from how an STP system would do so; however, the fundamental theories and equations hold for both systems. How an STP system functions will be described in more detail in section 2.3.

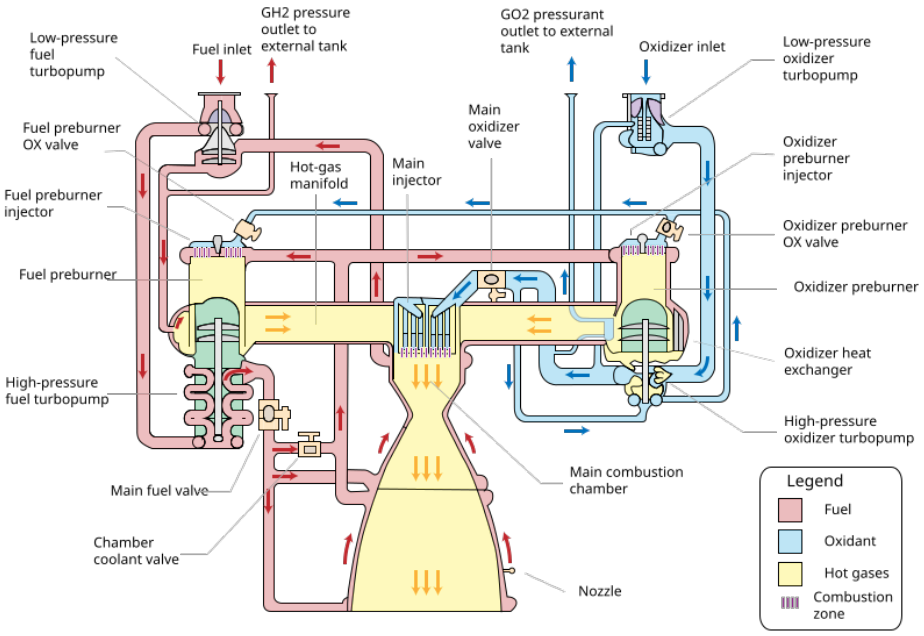

Figure 2.1: Diagram of the SR-25 Rocket engine cycle [7]

With rocketry being such a complex system, often an ideal system is used, making these assumptions: the exhaust gasses are homogeneous and have a constant composition, the gas or gas mixture expelled follows the ideal gas law, the heat capacity of the gas expelled is constant and the flow through the nozzle is one-dimensional, steady and isentropic, [5]. With these assumptions, the explanation of Ideal Rocket Theory can begin with the calculation for thrust. Deriving the thrust from a force equilibrium due to internal and external pressure forces, giving Equation 2.6. Assuming ideal expansion (exit and ambient pressures are equal), the thrust equation can be simplified to $F = m \cdot U_e$.

$$F = m \cdot U_e + (P_e - P_a) \cdot A_e \tag{2.6}$$

The velocity of the exhaust gases through the divergent part of the nozzle can be determined by Equation 2.7, Where M is the mean molar mass of the exhaust gases, R_A is the universal gas constant, γ is the ratio of the specific heat and T_c, P_c are the chamber temperature and pressure respectively. Of most interest is the velocity of the exhaust gases at the exit of the nozzle, referred to as the exhaust velocity, which can be calculated by implementing the exhaust pressure (P_e) into Equation 2.7

$$U = \sqrt{2 \cdot \frac{\gamma}{\gamma - 1} \cdot \frac{R_A}{\mathcal{M}} \cdot T_c \cdot \left[1 - \left(\frac{P}{P_c}\right)^{\left(\frac{\gamma-1}{\gamma}\right)}\right]} \tag{2.7}$$

The mass flow through the rocket engine can be determined, knowing that with the continuity equation, the mass flow rate must be constant throughout the engine. Equating the mass flow in the combustion chamber and that of the nozzle throat, Equation 2.8 can be derived with Γ being defined by the "Vendenkerckhove function", R referring to the specific gas constant and A_t being the throat area.

$$m = \frac{\Gamma \cdot P_c \cdot A_t}{\sqrt{R \cdot T_c}} \tag{2.8}$$

The nozzle area ratio between the throat and exit of the nozzle can be calculated using Equation 2.9. Providing a relationship between the pressure ratio P_e/P_c and nozzle expansion ratio A_e/A_t.

$$\frac{A_e}{A_t} = \frac{\Gamma}{\sqrt{\frac{2\gamma}{\gamma-1} \cdot \left(\frac{P_e}{P_c}\right)^{\left(\frac{2}{\gamma}\right)} \cdot \left[1 - \frac{P_e}{P_c}^{\left(\frac{\gamma-1}{\gamma}\right)}\right]}} \tag{2.9}$$

The thrust coefficient is a characterisation of how much the nozzle (and hence gas expansion) contributes to the total thrust produced, with the full equation for the characteristic thrust being defined by Equation 2.10. Providing a useful insight into the nozzle performance.

$$C_F = \Gamma \cdot \sqrt{\frac{2\gamma}{\gamma-1} \cdot \left[1 - \left(\frac{P_e}{P_c}\right)^{\left(\frac{\gamma-1}{\gamma}\right)}\right]} + \left(\frac{P_e}{P_c} - \frac{P_a}{P_c}\right) \cdot \frac{A_e}{A_t} \tag{2.10}$$

The characteristic velocity is a property that reflects the available energy of the propellant to propel the rocket forward and is defined by equations 2.11 and 2.12. Unlike the I_{sp}, the characteristic velocity is independent of the pressure ratio.

$$c^* = \frac{1}{\Gamma} \cdot \sqrt{R \cdot T_c} \tag{2.11}$$

$$c^* = \frac{P_c \cdot A_t}{m} \tag{2.12}$$

With both the characteristic velocity and thrust coefficient, the thrust and specific impulse can be rewritten in terms of C_F and c^* as seen in equations 2.13 and 2.14.

$$F = m \cdot C_F \cdot c^* \tag{2.13}$$

$$I_{sp} = \frac{U_e}{g_o} = \frac{C_F \cdot c^*}{g_0} \tag{2.14}$$

When using these equations, one must realise that these are idealised values and that the actual values will differ from the calculated ones. Several quality factors exist, comparing the ideal values to experimental values generated empirically. These allow for a better estimation of the performance of the rocket motor. However, for an initial design, the Ideal Rocket Equation provide a good base to work off.

2.2.3. Hydrogen Propellant Performance Analysis

Why use Hydrogen as a propellant and not other substances? A paper by J.M. Martinez discusses the performance of a cold/warm gas propulsion system with different propellants, [8]. Cold gas thrusters are a better analogy to STP systems, with none of the complex turbopump plumbing required to run a conventional chemical rocket, however, cold gas thrusters run at considerably lower temperatures.

The important aspect of understanding Hydrogen as a fuel is Hydrogen's molecular mass of 2.01588 g/mol, the lowest possible molecular mass, with Hydrogen being the lightest element on the periodic table. Looking at Equation 2.7 the exhaust velocity is proportional to $1/\sqrt{\mathcal{M}}$, meaning a decrease in molar mass will increase the exhaust velocity of the rocket motor and hence increase the specific impulse. J.M. Martinez provides an excellent illustrative graph, seen in Figure 2.2a, comparing the specific impulse of different propellants for a set reference rocket motor. Hydrogen is the best possible option in terms of pure efficiency, so why is it not widely used in the aerospace industry? This mostly comes down to Hydrogen's terrible volumetric energy density, clearly indicated in Figure 2.2b, where Hydrogen has the lowest volumetric impulse (defined as $I_{vol} = I_{sp} \cdot g_0 \cdot \rho_p$). This makes it much less desirable due to the high volume and thus mass cost required for the storage of Hydrogen and hence has historically been reserved for launch vehicles, where the Hydrogen is liquified at $-250\ [^\circ C]$ [9] to further increase its density, allowing for smaller tanks.

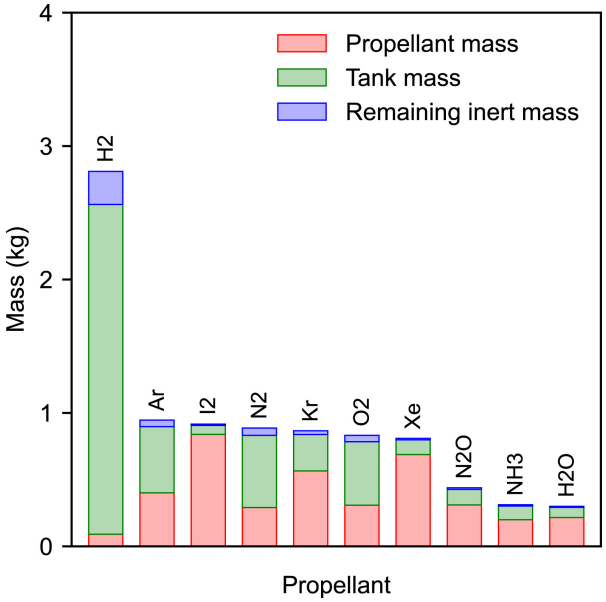

Figure 2.3: Comparison of spacecraft masses for different propellants

As far as this report could find, no satellite uses Hydrogen in its propellant, either in liquid or gaseous form (excluding launch vehicles). This fact can be best illustrated in Figure 2.3, where for Hydrogen, most of the mass goes towards containing the gas in a heavy, high-pressure tank. Thus, Hydrogen provides the best possible propellant choice for high efficiency, but Hydrogen's low density presents a problem with its high volumetric requirements on the launch vehicle. Of course, most of these concerns disappear if you can produce Hydrogen in orbit.

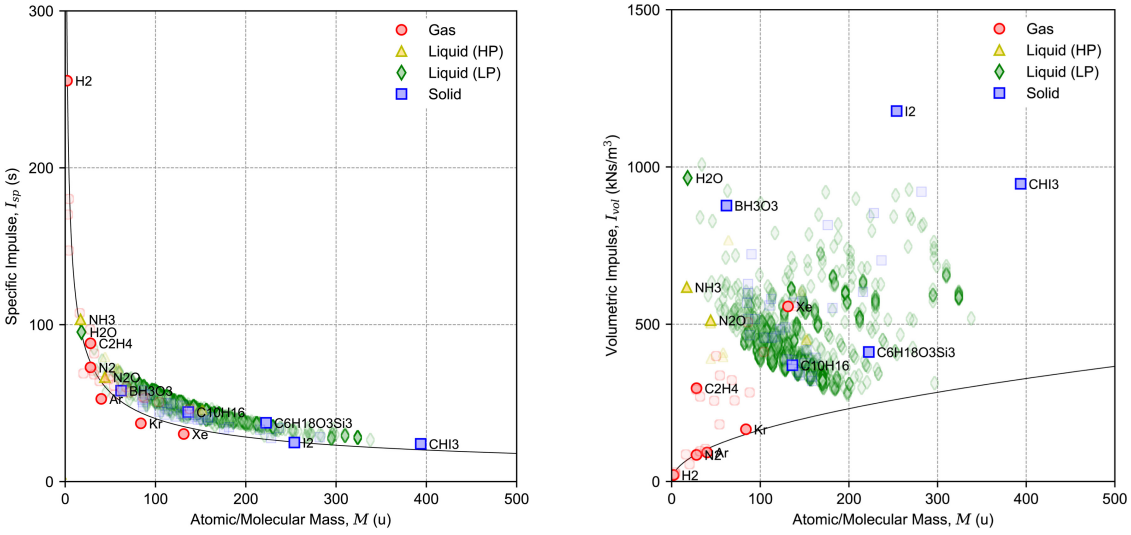

(a) Plot comparing the specific impulse of propellant to their molecular mass

(b) Plot comparing the volumetric impulse of propellant to their molecular mass

Figure 2.2: Figure comparing the Specific and volumetric impulses of a cold gas thruster for several different propellants [8]

2.3. Investigation into STP Systems

STP systems have been proposed for more than half a century. Thus, this section aims to answer the following research question: " How have ground-based STP systems been designed, and have any mission plans been generated?". First, providing a quick background on the history and functionality of an STP system. Then going on to provide several examples of proposed STP, designs and mission

profiles, as well as explaining some of the only ground testing done for an STP system.

2.3.1. STP Background

Solar Thermal Propulsion was first proposed and developed in 1956 by K. Ehricke [10]. Despite nearly 70 years of development, as of this report, no known STP system has flown. Early research focused on out-competing conventional cryogenic bi-propellant chemical rockets; however, for the STP system to compete with conventional rocketry, the large scale of the solar collector meant that STP was deemed a promising yet complicated design, [11]. The first system-level report was published in 1979 by F.G. Ethridge [12], defining a 28-ton solar thermal spacecraft, with the report acting as a basis for the next 10 years of research. STP was declared feasible in 1989 by the Air Force Rocket Propulsion Laboratory (AFRPL). Since then, multiple studies and reports have been published demonstrating the possibilities and capabilities of STP.

Providing a quick description of the functionality and difficulties involved in the development of an STP system, Figure 2.4 shows a simplified diagram of how an STP system functions. Solar energy is collected and focused through the **Solar Concentrator**, where the concentrated solar flux is absorbed by the **Absorber/Heat Exchanger**, converting the concentrated solar flux into heat, used to increase the temperature of the propellant. Once the Hot propellant exits the heat exchanger, it goes through a conventional convergent-divergent **Thruster**, expelling the hot propellant out the back of the spacecraft, producing thrust. Because of the high temperature and the capability of having Hydrogen as an exhaust gas (with conventional LH2/LO2 cryogenic chemical rockets, the exhaust gas is mostly water) allows an STP system to be much more efficient than conventional chemical rockets. Whilst the basic concept of an STP system is quite simple, designing a concentrator big and light enough to be effective is proving difficult, and the development of an efficient absorber/heat exchanger that is capable of working at $> 2000\ [°C]$ has also slowed STP development.

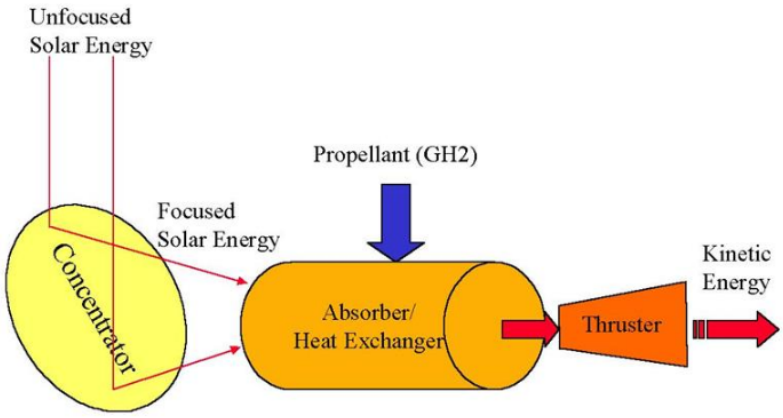

Figure 2.4: Functionality diagram of STP system, [10]

2.3.2. STP Design History

Having understood the basics of STP history and system functionality, several STP designs will be explained and discussed, going over the main system specifications and design choices and philosophies. Indicating where the proposed STP system excelled and where more work is needed. First, investigating some older examples to give a reference to where this technology began, going through time, discussing more and more advanced STP systems.

"Solar Thermal Propulsion for Orbit Transfer Vehicles" by C.R. Ford, [13]

Building on the 1979 report by F.G. Ethridge [12], C.R. Ford proposes using STP for an Orbital Transfer Vehicle, between low Earth orbit (LEO) and geosynchronous Earth orbit (GEO), with the Air Force Astronautics Laboratory realising the increased demand for geosynchronous satellites. The report starts with a statement that the increased cost of launches will necessitate the use of an orbital transfer

vehicle, with an effective concept being the use of a Solar Thermal Propulsion system, and continues by placing an STP's system efficiency between chemical rockets and ion propulsion. A comparison is made between the three different propulsion systems Table 2.1, with the report noting that STP provides a substantial increase in payload to GEO over chemical propulsion, whilst taking much less time than ion propulsion.

The report provides a preliminary Vehicle concept, with the use of two off-axis $30m$ diameter solar collectors that reflect and concentrate solar flux into an absorber. Estimating that each of these solar collectors will be able to concentrate $10\ [kW]$of solar power into the black body absorber. The paper describes the absorber as a "black body radiation absorption cavity made of coiled Rhenium tubes." The propellant flowing to the tubes reaches a temperature of $2800\ [^{\circ}K]$. The report goes on to estimate an I_{sp} of $900\ [s]$ can be achieved when using Hydrogen as a propellant.

Concluding that an STP orbital transfer vehicle will be a cost-effective solution for non-time-critical payloads. Cutting the propellant cost in half when compared to chemical rockets, providing a significant cost reduction in propellant alone over 10 years.

Table 2.1: Performance comparison for different propulsion systems[13]

	Low Thrust Cryo	Solar Rocket	Mercury Ion
Thrust (N)	2224	222	125E-3
I_{sp} (s)	460	900	2900
Propellant	LO_2/LH_2	LH_2	Mercury
Trip Time (Days)	2.75	30	180
Initial Mass (kg)	28120	28120	28120
Payload Mass (kg)	9070	15200	19960

"Solar-powered space flight" by M.H.D Kemp, [14]
Moving 25 years into the development of STP, the paper by M.H.D Kemp illustrates a similar mission analysis to C.R. Ford, where Kemp's paper discusses the use of an STP system for orbital insertion, orbital transfer and post-orbital flight. Going into much more detail about the power and mass requirements of the system.

The paper first goes into the power requirements to reach orbit for an STP system, ignoring the effects of atmospheric drag. The paper imagines a scenario where the spacecraft accelerates horizontally from the surface of the Earth until reaching orbital velocity, deriving a series of equations from the conservation of energy and momentum. Deriving the optimal exhaust velocity (limited to $10,000[m\cdot s^{-1}]$) and the optimal angle. Implementing several power levels given in $E/m(0)\ [kW\cdot kg^{-1}]$ where E is the solar power and $m(0)$ is the launch mass of the vehicle. The performance characteristics of which are given in Table 2.2. The velocity profile over time is given by Figure 2.5, for an $E/m(0)$ of $10\ [kW\cdot kg^{-1}]$. The paper then introduces the effects of atmospheric drag, noting that for such large and lightweight structures, even drag at higher altitudes becomes an issue. The paper proposes a maximum allowable drag force of $0.1\ [g\cdot N]$ for a collector mass of $5\ [g\cdot m^{-2}]$. Using high-altitude atmospheric density models to calculate the maximum allowable velocity at several altitudes. This resulted in the paper stating that at an altitude of $500\ [km]$ the maximum allowable velocity is $46.5\ [km\cdot s^{-1}]$, which is much higher than the required orbital velocity and hence can be ignored past this altitude. Going on to suggest the use of chemical rockets to bring the system to $500\ [km]$ where the STP second stage will complete the orbital insertion and any orbital transfers required.

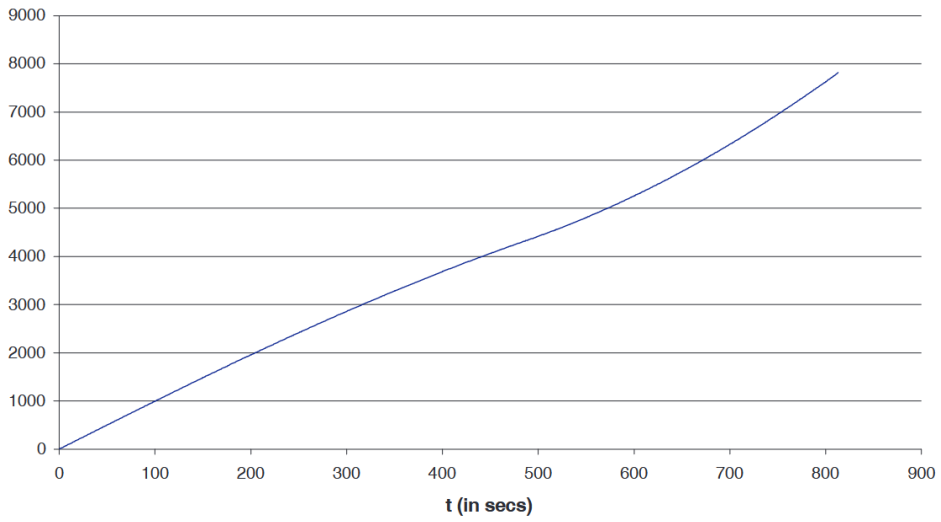

Figure 2.5: Plot of the velocity profile over time, when the propellant is exhausted at the optimal speed and angle[14]

Table 2.2: Performance characteristics to reach orbital velocity for a range of $E/m(0)$ when the vehicle accelerates horizontally and ejects propellant at optimal velocity and angle [14]

$E/m(0)$ $[kW \cdot kg^{-1}]$	Ratio of Propellant to empty mass	E (kW per kg of empty mass)	Flight time to reach v_0 (s)	Maximum accelerations $[m \cdot s^{-1}]$
100	1.3	227	280	45
50	1.6	131	540	26
30	2.3	100	669	20
15	4.2	79	774	16
10	6.2	72	813	14
8	7.7	69	829	14
6	10.1	67	845	13

The paper estimates that for an orbital insertion/transfer vehicle to be effective, it would need a $E/m(0)$ of about $20 - 100\ [kW \cdot kg^{-1}]$, equating to a collector area of about $15 - 73\ [m^2]$ per kilogram of empty mass. The paper states that a collector mass of $5\ [g \cdot m^{-2}]$ results in a mass of $0.08 - 0.37\ [kg]$ for an empty mass of $1\ [kg]$. Continuing to describe the ideal characteristics of the concentrator to be: concentrating solar flux as much as possible, reducing the mass of the absorber/heat-exchanger, minimising as far as possible the surface area of the collector, ensuring that the collector is perpendicular to the sun and having the collector being dragged behind the vehicle to enhance vehicle stability during flight.

The paper decides that using a rotationally symmetric aplanatic two-stage mirror arrangement fits the criteria best, using the sine criterion to determine the shape of the mirrors whilst still producing a sharp focus. This provided 14 possible overall layouts of the collector design, the characteristics of which can be summarised as the effective aperture area factor, the mirror surface area factor and the aberration factor. From these criteria, an optimal design was chosen, seen in Figure 2.6. Having provided an optimal shape for the solar collector, the paper moves on to the design of the solar absorber/heat-exchanger, however, the design is very simple, imagining it as a hollow plate with a throat and nozzle on one side and having the solar flux impinging on the other. Stating that the maximum allowable temperature that can be reached is about $5,900\ [°K]$ due to the second law of thermodynamics implying that one can not concentrate solar radiation to a higher temperature than the source, however, the required exhaust speed of $10,000\ [m \cdot s^{-2}]$ can be achieved at temperatures of $3700\ [°K]$. A theoretical efficacy of about 73% is calculated using an exhaust temperature of $1000\ [°K]$ however, an estimation

is made that the net conversion efficiency of solar energy into thrust would not exceed 40%, due to additional losses in the system. This would cause the overall mass of the solar collector to increase about threefold, still within a feasible range when looking at low $E/m(0)$ values.

Identifying that maintaining the shape of the main collector is crucial for optical stability and, hence, the functionality of the STP system. With the proposed collector design being akin to a solar sail, there is no inherent rigidity in the sail material requiring a sub-structure to hold the mirror shape. Thus stabilising the primary mirror through the use of tension cables and centrifugal forces exerted by a spinning spacecraft.

Comparing the two papers, it is clear that there has been a lot of work on the use of STP, however, the paper by M.H.D Kemp is still not a full system design, only really investigating the energy requirements and the design of the collector. With M.H.D. Kemp calling for more work to be done on the use of an STP system.

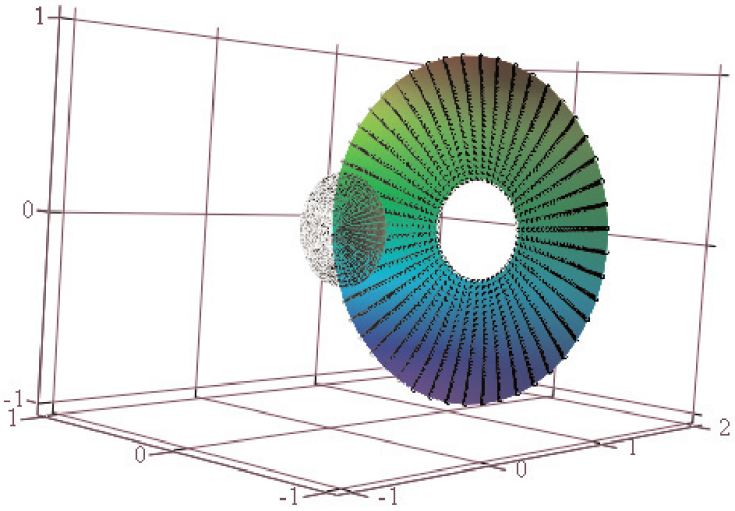

Figure 2.6: 3D render of the collector mirrors, with a mirror layout of $q_1 = 1, q_2 = -0.3 \; and \; sgn(h) = -1$

"Preparing for flight: The Surrey Space Center's Microscale Solar Thermal Propulsion Experiment" by F.G Kennedy et al. [15]
The paper by F.G Kennedy et al. is a very interesting case study for this report, with this paper, as of the writing of this report and to the best knowledge of the author, being the only example of a high-temperature test (ground test) of an STP system. Discussing two separate mission cases, the first being the minimum-impact experiment on the next Disaster Monitoring Constellation (DMC) satellite and the second being the drag makeup and life extension of the Cibola Flight Experiment satellite (CFESat). Suggesting the use of STP as a high-efficiency alternative to other propulsion systems.

Discussing first the minimal impact experiment of the DMC, the paper suggests the use of an STP system to perform an end-of-life deorbit manoeuvre. DMC satellites orbit at an altitude of $686 \; [km]$ and have a high ballistic coefficient, meaning that without an end-of-life manoeuvre, the spacecraft could have an on-orbit lifespan of up to a century. This is unacceptable and greatly increases the risk of an in-orbit collision. The paper suggests the lowering of the perigee from 686 to $300 \; [km]$ with a delta-v expenditure of $112 \; [m \cdot s^{-1}]$, significantly reducing the time required to deorbit. The paper does discuss the use of a numerical simulation to provide the system performance from several configurations, choosing one to test, this being the use of four $14 \; [cm]$ diameter aluminium monolith concentrator mirrors producing $74 \; [W]$ of input power, a $95 \; [g]$ ceramic heat exchanger couples to each of the mirrors with a low

attenuation fibre optic cable, insulated with a carbon foam jacket and a fed through a vapour-pressure ammonia propellant feed tank. After a 15 minute heat-up time and a one-minute hold time, the system is fired for $40.4\ s$ leading to a thrust of $1.31\ [N]$ and an average I_{sp} of $151\ [s]$. The heating and firing profiles can be seen in Figure 2.7. Unfortunately, with the current design of the DMC satellites, there is not enough surface area to place four separate concentration mirrors, requiring the use of a folding mirror system. There are also not enough proper storage opportunities on the DMC satellite, only having a 2.5-litre tank, with ammonia, this would correspond to $43\ [m \cdot s^{-1}]$ or a reduction of $150\ [km]$ in the perigee.

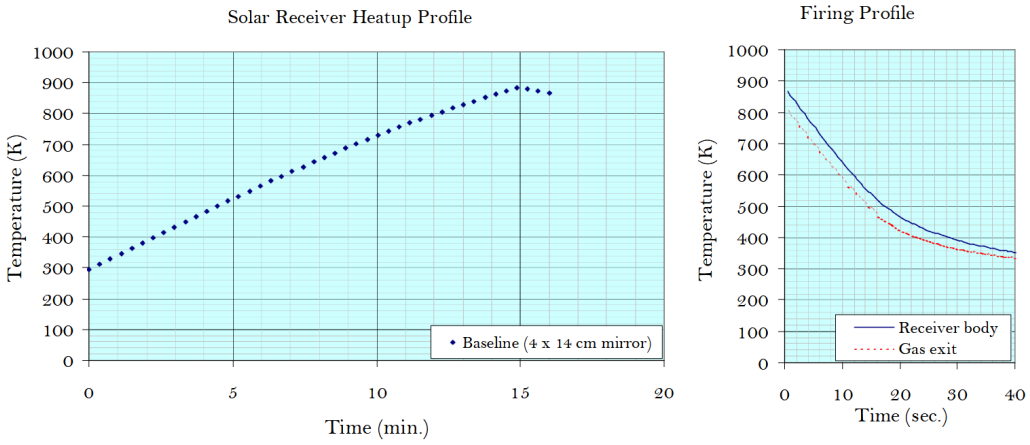

Figure 2.7: Performance of STP System, solar receiver heat up (left) and rocket firing profile (right)[15]

Unlike the DMC, CFESat has the opposite problem and requires orbit-keeping, with an orbital altitude of $560\ [km]$ and worst-case scenarios, the spacecraft could de-orbit in as little as 4.5 years. This results in the use of several smaller burn spaces a few months apart to keep the spacecraft in the correct orbit. With each burn requiring about $\sim 5.8[m \cdot s^{-1}]$, of delta-v. The paper thus alters the experimental methodology appropriately, reducing the burn time for each test to $2.5\ [s]$ and only using a single monolithic mirror, but altering the size of the mirror. The receiver was given a 15-minute heat-up where the temperature reached $1200\ [°K]$, dropping to $1115\ [°K]$ after a one-minute hold before firing. The paper completed a total of 366 test fires using ammonia as a fuel, with the results being shown in Table 2.3. The paper concludes that for the CFESat, other than what may be expected, a larger mirror does not lead to an increase in payload mass, rather concluding that the $14\ [cm]$ is the optimal design providing the most payload mass.

Table 2.3: Performance of STP systems for several mirror diameters[15], *7cm mirror did not reach the desired baseline temperature, of $600\ [°K]$ and only $350\ [°K]$

Concentrator Diamiter	**14 cm**	**7cm**	**20 cm**	**30 cm**
Input Power $[W]$	19	5	38	71
Elapsed orbit time $[hrs.]$	583	429	409	311
Manoeuvres	366	270	257	196
$\Delta V\ [m \cdot s^{-1}]$	5.8	5.8	5.8	5.8
Propellant used $[g]$	410	680	390	380
Engine "on-time" $[min.]$	15.2	14.6	14.2	13.7
Average $I_{sp}\ [s]$	246	150*	259	264
Mirror Mass $[kg]$	0.3	0.07	0.61	1.36
System Mass $[kg]$	0.33	0.11	0.64	1.39
Final Payload Mass $[kg]$	164.26	164.21	163.97	163.23

"On a New Type of Combined Solar–Thermal/Cold Gas Propulsion System Used for LEO Satellite's Attitude Control" by C. Sandu et al. [16]
The paper by C. Sandu et al. introduces some experimental results and describes the use and testing of a combined solar thermal/cold gas propulsion system for attitude control. Where the cold gas is first heated by solar radiation in a heating chamber before being expelled, increasing the efficiency of a cold gas propulsion system. Allowing for an increased orbital service duration of 2.5 times when compared to conventional cold gas propulsion systems.

Illustrating the experimental setup, seen in Figure 2.8, with the sun being replaced by infrared lamps (1), radiating onto the parabolic mirror (2), which concentrates and focuses the light onto the propellant tank (3). The nitrogen feed came from the main tank (4) at $200\ bar$ and fed the gas through a pressure regulator (5), regulating the pressure to $20\ bar$, feeding the propellant tank. When testing, the solenoid (6) was briefly opened ($0.1 - 0.4\ s$), expelling the gas through the Laval nozzle (7) to generate thrust. The thrust was recorded using a force transducer (8). Temperatures were measured using five thermal couples; the first was mounted to the propellant tank (9a), three others were used to measure heat dissipation and were placed at different distances from the IR source and the mirror (9b) and the last was used to measure room temperature (9c). A pyrometer (10) was placed in the line of sight of the IR source to measure the irradiation onto the mirrors. A pressure transducer was mounted on the propellant tank. All the pressures and temperatures were recorded on a data acquisition system (11). The experiment does use the pyrometer and potentiometer to control the output of the IR-source to $1360\ Wm^{-2}$. However, the system is not in a thermal vacuum chamber, meaning that convective heat transfer will be a factor in the experimentation. The system also has no way of measuring exhaust speed, meaning that an I_{sp} of the system can not be measured.

With the experimental procedure calling for filling the tank with $20\ bar$ of Nitrogen gas, turning on the IR source and letting the system reach the operating temperature ($60 - 125\ °C$), opening the solenoid value for a set time ($0.1 - 0.4\ s$) on a ten-second interval until the pressure in the propellant tank reaches ambient. A comparison between the thrust produced with and without heating can be seen in Figure 2.9, The paper states that the increase in temperature provides an increase in the total impulse of the system, extrapolating to the theoretical temperature limit of the system ($450°C$) could provide a total impulse increase of 1.5 to 2.5 depending on the extrapolation used, linear and polynomial respectively. Concluding that the actual result may lie somewhere in between, considering temperature and pressure are linearly dependent in the ideal gas law, however, radiation is proportional to temperature to the fourth power. Giving a final closing note that a spacecraft's service duration may be increased by 2.73 times, for a mass increase of $1150\ g$ compared to a similar capable cold gas system.

The paper presents an excellent approach to the initial testing of STP systems, with future recommendations being the testing under more accurate LEO conditions. However, the lack of the calculation of the I_{sp} makes the rocket performance hard to compare to other STP systems. The low testing temperature of the systems also makes it difficult to compare, with material and propellant properties changing drastically at $> 2000\ °C$.

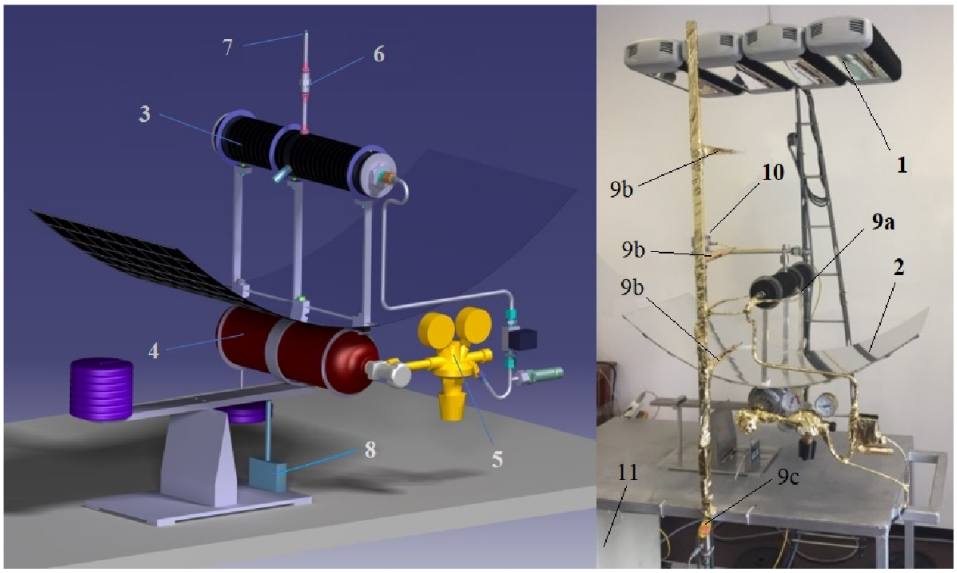

Figure 2.8: Design concept (left) and photo (right) of experimental equipment[16]

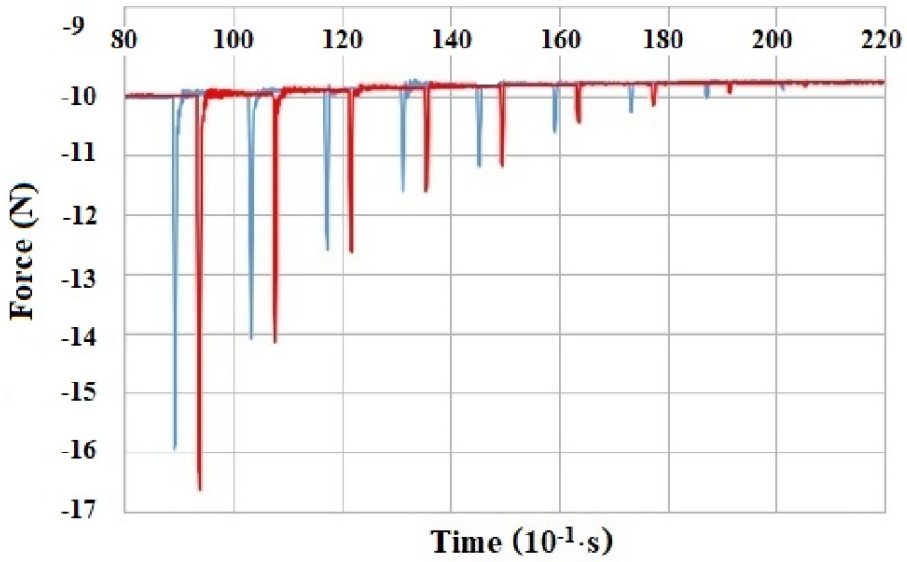

Figure 2.9: Comparison of Thrust impulse force for cold gas in blue ($26°C$) and hot gas in red($80°C$), for a valve opening time of $0.3\ s$ [16]

"Design and characterisation of a bi-modal solar thermal propulsion and power system for small satellites" by F. Leverone et al. [17]
F. Leverone suggests the bi-modal use of an STP system, allowing for the system to generate power when propelling the spacecraft. This is of obvious advantage, allowing for the reduction or elimination of solar arrays, reducing overall spacecraft mass. Leverone suggests the use of a micro-organic Rankine Cycle, where an organic fluid is heated, passed through a turbine and condensed to be reused. The use of an organic working fluid allowed for operation at much lower temperatures. There are some mission constraints when it comes to propulsion, essentially, the system must choose between generating power or propelling the spacecraft.

"A Solar Thermal Steam Propulsion System Using Disassociated Steam for Interplanetary Exploration" by L. Vance et al. [18]
L. Vance et al. investigate an interesting approach with the use of an STP system, proposing heating water to a maximum of $\sim 4000\ ^\circ C$. At these temperatures, water dissociates into mostly Hydrogen and oxygen ions, theoretically leading to a lower molecular average for the exhaust gases and thus increasing exhaust velocity.

2.4. Advances in Nozzle Design

Nozzles are one of the most vital parts of the propulsion system, contributing a large part of the performance. The basic concept of the nozzle is the expansion of the exhaust gases, ideally to ambient conditions, allowing for an increase in the exhaust velocity. This section aims to answer: "What advances in nozzle design could improve system performance, including associated performance estimations?". When it comes to designing rocket nozzles, it can become quite complicated with many different variables contributing to the design and geometry. Thus, in conventional nozzle design, there are two main aspects: the first being the analytical approach to define a simple geometry to optimise the design, and the second being the implementation into computational fluid dynamics. Thus, in this section, first, an explanation of the Analytical nozzle design is given, then going into how CFD is used to determine and estimate the performance of the nozzle.

2.4.1. Analytical Nozzle Design

There are several types of rocket nozzles, each having its own advantages and disadvantages. There is an ideal nozzle shape allowing for the optimal expansion of the exhaust gases, which is characterised as Equation 2.9 or equivalent written as Equation 2.15 [19]. Whilst this is ideal for the expansion of the exhaust gases, it is not ideal in other characteristics, the main being that the ideal rocket nozzle is very long and hence heavy. Because of this, there are several different variations of the nozzle shapes, each having its strengths.

$$\frac{A_e}{A_t} = \left(\frac{\gamma-1}{2}\right)^{\frac{1}{2}} \cdot \left(\frac{2}{\gamma+1}\right)^{\frac{(\gamma+1)}{2(\gamma-1)}} \cdot \left(\frac{P_a}{P_c}\right)^{-\frac{1}{\gamma}} \cdot \left[1-\left(\frac{P_a}{P_c}\right)^{\frac{\gamma-1}{\gamma}}\right]^{-\frac{1}{2}} \tag{2.15}$$

Conical Nozzles
Conical nozzles were often used in the early stages of rocket design, with the main appeal of the nozzle being the ease of manufacturing and easy adaptability to different area/pressure ratios. The conventional design for a conical nozzle is seen in Figure 2.10. At lower divergence angles (α), the conical nozzle is very similar in performance to the ideal nozzle shape, where at 15° there is only a 1.7% [20] difference in the thrust coefficient between the conical nozzle and the ideal rocket nozzle. Another promising aspect of a conical nozzle is that the length of the nozzle can be easily reduced by increasing the divergence angle. However, with an increasing divergence angle, the flow exiting the nozzle will move further and further from the axial direction of the rocket, leading to a reduction of thrust of the propulsion system. With the correction factor being calculated by Equation 2.16. With the all-important thrust coefficient being given by Equation 2.17, for a conical nozzle in vacuum conditions.

$$\lambda = \frac{1+cos(\alpha)}{2} \tag{2.16}$$

$$C_{fvc} = \frac{P_e}{P_c} \cdot \frac{A_e}{A_t} + \left(\frac{1+cos(\alpha)}{2}\right) \cdot \frac{\rho_e V_e^2 A_e}{P_c A_t} \tag{2.17}$$

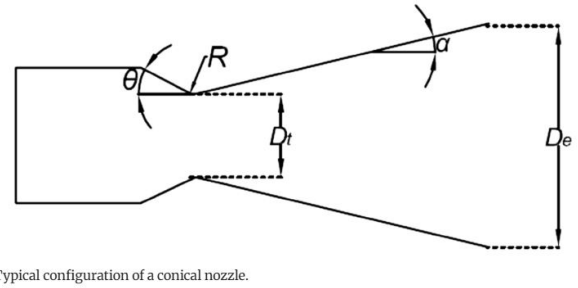

Figure 2.10: Diagram of a Conventional Conical Rocket Nozzle [19]

Bell/Contour Nozzles

Bell nozzles are the most commonly used rocket nozzle geometry in the aerospace industry today, with the bell nozzle providing good performance and size characteristics when compared to the conical nozzle geometry. Often being described as a percentage length of a $15°$ angle conical nozzle, for example, a 80% bell nozzle's length is equivalent to 80% the length of a conical nozzle, with both nozzles having the same expansion ratios. The defining feature of the bell nozzle is the large initial divergent angles being of the order of $20° - 50°$, then following a parabolic curve to a much reduced divergence angle at the exit of the nozzle, ideally below $10°$. An example of the bell nozzle geometry can be seen in Figure 2.11. With the values θ_n and θ_e being given by the Figure 2.12, depending on the percentage length and expansion ratio expected.

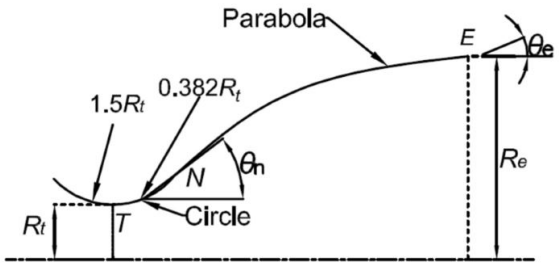

Figure 2.11: Diagram of the geometry of a bell nozzle

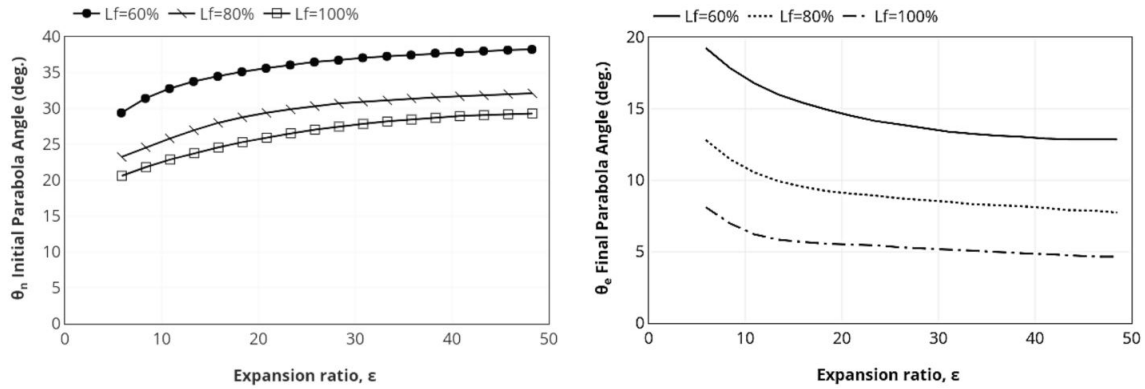

(a) Initial parabolic angle after throat

(b) Final parabolic angle at nozzle exit

Figure 2.12: Initial and final parabolic angle for a bell nozzle [21]

However, the nozzle contour can be improved, minimising the loss of thrust, leading to contoured nozzles, which can provide a performance improvement compared to a bell nozzle. There are several methods in the literature on how the nozzle can be contoured, with methods consisting of both semi-empirical and analytical methods. Unlike conical nozzles, there is no simple way to determine the

thrust coefficient of a contoured nozzle as it depends not only on the exit geometry of the nozzle but rather the full geometry; hence, the thrust coefficient for a contoured nozzle is given by Equation 2.18. One of the first and quite reliable methods for determining an optimal contour is described by Guderley and Hantsch [22], deriving Equation 2.19, where the equation is iterated along the length of the nozzle to determine the optimal divergent angle at each section. Allowing for similar performance as a 15° conical nozzle at only $\sim 80\%$ of the length.

$$C_{fc} = \int_{A_e} \frac{P}{P_c A_t} 2\pi r dr + \int_{A_e} \frac{\rho V^2 cos(\theta)}{P_c A_t} 2\pi r dr \tag{2.18}$$

$$\frac{P - P_a}{(1/2)\rho V^2} \sqrt{M^2 - 1} = sin(2\theta) \tag{2.19}$$

Another method mentioned for the contouring of the nozzles described by Allman and Hoffman [23], where, after an initial circular arc expansion contour, a second degree polynomial is used, where the coefficients of the polynomial are determined by the attachment angle, the exit radius and requiring the polynomial to be tangential to the initial circular arc. Comparing this to the previous methods only results in a 0.2% deviation for zero ambient pressure, justifying the use of this methodology.

So far, there have been two main design contours: these being the Truncated Ideal Contour (TIC) and the Thrust Optimised Parabolic (TOP). Frey et al [24] described a new methodology merging the designs of TIC and TOP nozzle contours, aiming to achieve the best of both methodologies. The design does not induce restricted shock separations (RSS) as with the TIC nozzle contour, as well as increasing the pressure at the exit of the nozzle reduces the chance of separation at the nozzle exit. The new nozzle contour is generated by first using the ideal nozzle contour until a transition point, where a parabolic contour is now followed; an illustration of the geometry can be seen in Figure 2.13. This leads to a nozzle contour with similar performance to the TOP nozzle contour, whilst not having the high sideloads seen in TIC nozzle contours.

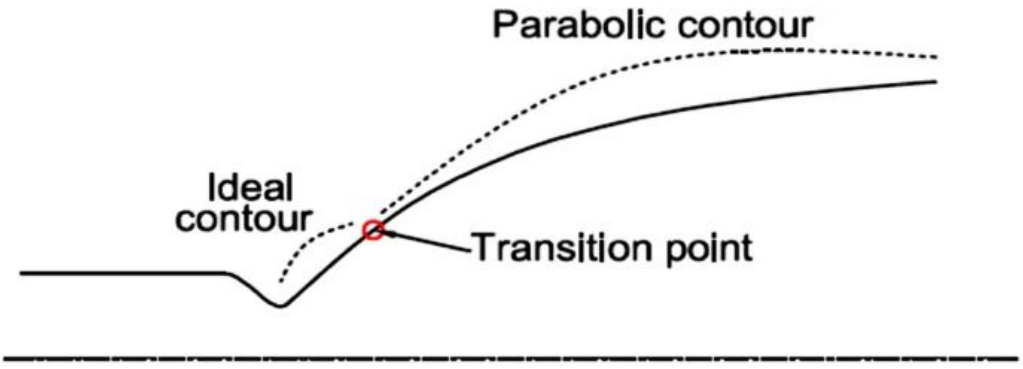

Figure 2.13: Diagram of a TICTOP nozzle contour [24]

Plug Nozzles

Plug nozzles are one of the most advanced nozzles, made up of a more conventional throat and a heavily truncated nozzle, where a plug is then used to help with the expansion of the exhaust gases. This allows for a nozzle less susceptible to flow separation. These benefits arise from the generation of an expansion fan at the primary nozzle lip that interacts with pressure behaviours along the plug wall. An illustration of a plug nozzle can be seen in Figure 2.14. The main benefit of plug nozzles is that the nozzle will always adapt to the ambient pressure conditions, whereas a conventional CD nozzle is only optimised to one ambient pressure. This makes plug nozzles a great choice for launch vehicles where the rocket goes through a large variation in external pressure, with plug nozzles having a much better performance at lower pressure ratios, between chamber and ambient pressures. However, plug nozzles are comparable to conventional CD nozzles in vacuum conditions, leading to plug nozzles not being considered in vacuum conditions due to the increased complexity in designing a plug nozzle.

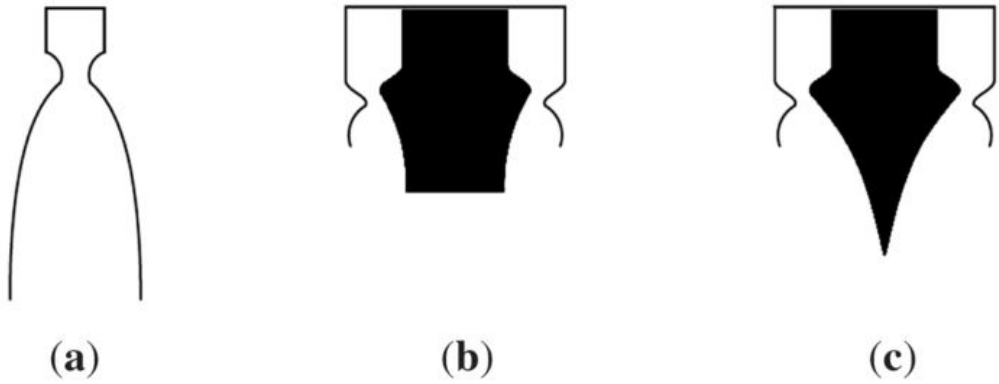

Figure 2.14: Diagram of several nozzles, Conventional CD nozzle (a), Truncated plug nozzle (b), and Plug nozzles (c)

Expansion-Deflection nozzles

Expansion-deflection (E-D) nozzles are another example of an altitude-compensating rocket nozzle. Where E-D nozzles are similar to bell nozzles with the addition of a 'pintle' or 'centre body' just after the throat of the nozzle, diverting the flow to the walls of the nozzle. One benefit of this design is that the flow is moved more outwards, allowing for a shorter nozzle when compared to conventional nozzles, at similar expansion ratios. The E-D nozzle works in two modes, these being the open and closed wake modes. In the closed wake mode, all of the nozzle is filled with the exhaust gas, in this mode, the nozzle acts very similarly to how a conventional bell nozzle would work. The transition pressure at which the nozzle goes from open to closed mode is known as the design pressure. When running in the open mode, not all of the nozzle is filled with exhaust gases; rather, the centre of the nozzle is filled with ambient air, which leads to a similar phenomenon as used in the plug nozzle. This allows the E-D nozzle to have altitude correction in its design. Whilst for a vacuum rocket nozzle, the altitude correction feature of the E-D nozzles is not exactly used, the shortening of the nozzle is very much of interest when designing a space system where mass is often a driving requirement.

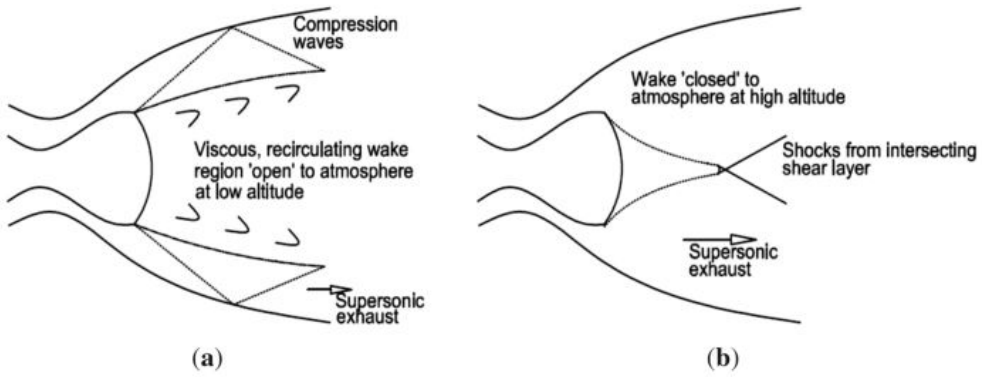

Figure 2.15: Diagram of the Expansion-deflection nozzle, with the open mode in (a) and the closed mode in (b)

Duel Bell Nozzle

The dual bell nozzle, as the name suggests, is a nozzle that combines the two bell nozzles of different expansion ratios, where, after the throat, there is a low expansion ratio contour until a certain point where the contour changes into that of a larger, higher expansion ratio. This allows the dual bell nozzle to be adapted to two separate ambient pressures. At sea level, there is an oblique shock that causes the second contour to be effectively ignored and giving the nozzle an effectively lower expansion ratio. As the altitude increases, the nozzle will use more and more of the second contour, allowing for a larger expansion ratio, leading to increased efficiency in the propulsion system. This can be seen in Figure 2.16. This allows for a higher average efficiency over the entire flight, especially for launch

vehicles. Another aspect of this design is nozzle extension, where a nozzle extension was mechanically moved into place to increase the expansion ratio of the nozzle in the middle of flight.

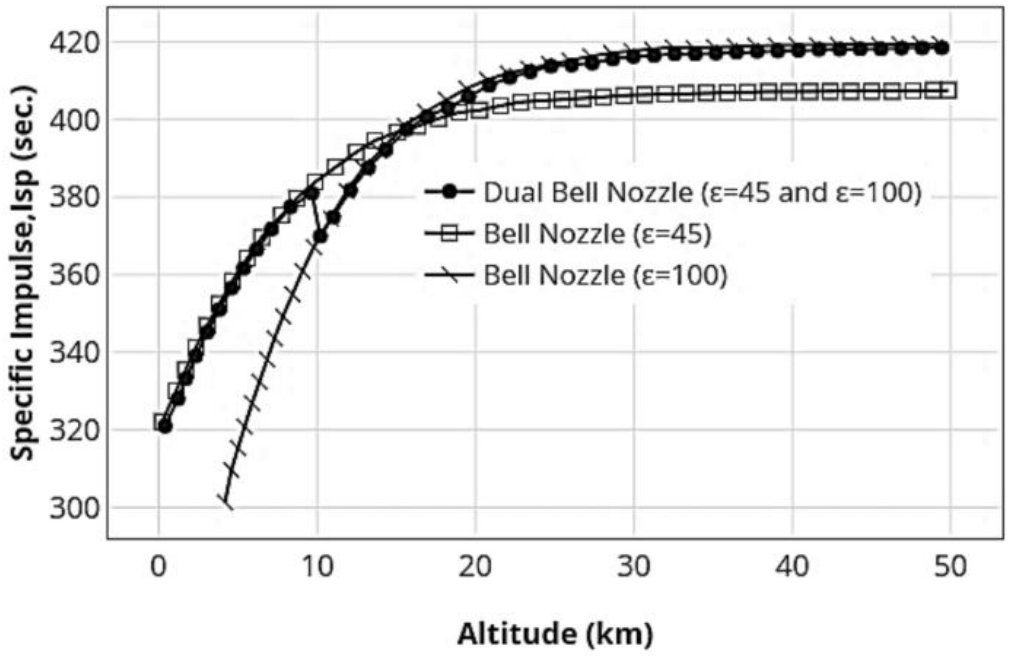

Figure 2.16: Plot showing the Specific impulse of a couple bell nozzles at different expansion ratios, as well as that of a dual bell nozzle

Multi nozzle grid

Multi-nozzle grids (MNG) are a series of smaller nozzles that are placed next to each other, reducing the overall length of the nozzle, whilst still having the same expansion ratio. This allows for a small, compact system that has the potential to be as efficient as a single conventional nozzle. When compared to an equivalent nozzle, there is a reduction of about 3% due to the increase in viscous losses in the nozzles. But when compared to a full conventional nozzle, the system is capable of achieving 11% better performance because of the reduction in mass and length.

Nozzle Summary

There are several nozzle designs as seen above; each of these designs has its benefits and downsides, with the main characteristics of each of the nozzle designs being provided in Table 2.4.

Table 2.4: Table showing the characteristics of the major nozzle design of rocket motors [19]

Types of nozzle	Characteristics
Ideal	Give maximum thrust performance
	Long and heavy
Conical	Easier manufacturing
	Easier optimization
	Flow at exit is not completely axial
	Requires a trade-off between divergence angle and nozzle length
	Pressure thrust is not optimum at all altitudes
Bell	Lesser length as compared to conical nozzle
	Performance is higher as compared to conical nozzle
	Manufacturing is difficult
	Pressure thrust is not optimum at all altitudes
	Optimization is difficult
Plug	Flow separation can be avoided
	Allow near optimum expansion at all altitudes
	Less noisy
	Lesser size as compared to conventional nozzle
	Cooling of central plug is difficult
E-D	Allow near optimum expansion at all altitudes
	Size is lesser as compared to conventional nozzle
	Easier cooling
	Combustion chamber is compact
	Performance is low as compared to plug nozzle
	Higher throat heat fluxes relative to a conventional bell nozzle with an equal throat area
Dual bell	Can carry more payload as compared to conventional nozzles
	Controlled flow separation
	Easier cooling
	Higher performance and reliability
	Difficult to optimize the wall contour
	Lesser side loads
	Lower weight
	Difficult to manufacture
MNG	Better performance as compared to other types of nozzles
	Lesser length

2.4.2. Computational Fluid dynamics

With nozzle designs having so many different factors that determine the efficiency and performance of the propulsion system, computational fluid dynamics is often used to fully evaluate the performance of the nozzle. With CFD allowing for relatively rapid and cheap iteration of nozzle geometry. Thus, in this section, two main parts will be discussed first: a comparison between the different turbulence models used in CFD and how well they estimate the nozzle flow conditions. The second is a few examples of how CFD is done for rocket nozzles, investigating the boundary conditions and flow setup.

Turbulence model comparison

The paper by A. Balabel et al, [25], compares the different turbulence models available for CFD at different pressure ratios. Validating the results with experimental data. The governing equation for fluid

flow is the Navier-Stokes equation. However, there is no analytical solution to the Navier-Stokes equations, leading to the use of a numerical solution. Unfortunately, to accurately calculate the numerical solution, the required cell size is so small that the computational power needed is so large that even the largest supercomputers in the world would struggle; this is known as a Direct Numerical Solution (DNS) in CFD, [26].

Because of the large computing power required to solve a DNS, a Reynolds Averaged Navier-Stokes (RANS) model is introduced, including an additional RANS equation, which aims to simulate the effects of the smallest scales of turbulence without needing the required mesh size to accurately determine the flow. The inclusion of the continuity and energy conservation equations allows for the determination of the compressible fluid field.

Continuity equation:

$$\frac{\partial}{\partial x_i}(\rho u_i) = 0 \tag{2.20}$$

RANS equations:

$$\frac{\partial}{\partial x_i}(\rho u_i u_j) = -\frac{\partial p}{\partial x_i} + \frac{\partial}{\partial x_j}\left[\mu\left(\frac{\partial u_i}{\partial x_j} + \frac{\partial u_j}{\partial x_i} - \frac{2}{3}\delta_{ij}\frac{\partial u_l}{\partial x_l}\right)\right] + \frac{\partial}{\partial x_j}(-\rho\overline{u_i' u_j'}) \tag{2.21}$$

Energy equations:

$$\frac{\partial}{\partial t}(\rho E) + \frac{\partial}{\partial x_i}[u_i(\rho E + p)] = \frac{\partial}{\partial x_j}\left(\left(k + \frac{C_p \mu_t}{0.85}\right)\frac{\partial T}{\partial x_j} + u_i(-\rho\overline{u_i' u_j'})\right) \tag{2.22}$$

With the addition of the $\rho\overline{u_i' u_j'}$, known as the Reynolds stress tensor. This is an unknown variable that is solved by the introduction of the different turbulence models. A. Balabel et al describe the use of 6 different turbulence models, 5 of which are known as eddy viscosity turbulence models and one Reynolds stress model. These being the standard $k-\epsilon$ model (STD), the extended k-ϵ model (ETD), the k-ϵ-v^2-f(v^2-f-1) model, the realizable k-ϵ-v^2-f(v^2-f-2) model, shear-stess transport (SST) k-ω model and the Reynolds stess model (RSM). Each of these models has several equations to determine the transport of turbulence down the turbulence cascade.

Eddy viscosity models

Eddy viscosity models assume that the apparent turbulent shearing stress can be related to the rate of mean strain through an apparent scalar turbulent or ”eddy” viscosity. Boussinesq assumption for the general Reynolds stress tensors gives;

$$-\rho\overline{u_i' u_j'} = \mu_t\left(\frac{\partial u_i}{\partial x_i} + \frac{\partial u_j}{\partial x_i}\right) - \frac{2}{3}\left(\rho k + \mu_t\frac{\partial u_k}{\partial x_k}\right)\delta_{ij}, \tag{2.23}$$

where δ_{ij} is the the Kronecker delta function, k is the turbulent kinetic energy and μ_t is the turbulent viscosity. Other transport equations are needed to evaluate the turbulent viscosity, here, the eddy viscosity models differ from each other. Presenting the transport equations for the different models.

The k-equation:

$$\frac{\partial}{\partial x_j}(\rho u_j k) = \frac{\partial}{\partial x_j}\left[\left(\mu + \frac{\mu_t}{\sigma_k}\right)\frac{\partial k}{\partial x_j}\right] + \rho(P_k^* - \beta_1\epsilon - \beta_2 k\omega) \tag{2.24}$$

The ϵ-equation:

$$\frac{\partial}{\partial x_j}(\rho u_j \epsilon) = \frac{\partial}{\partial x_j}\left[\left(\mu + \frac{\mu_t}{\sigma_\epsilon}\right)\frac{\partial \epsilon}{\partial x_j}\right] + \frac{\rho}{T}\left(C_{1\epsilon}P_k - C_{2\epsilon}\epsilon + C_{3\epsilon}\frac{P_k^2}{\epsilon}\right) \tag{2.25}$$

The v^2-equation:

$$\frac{\partial}{\partial x_j}(\rho u_j v^2) = \frac{\partial}{\partial x_j}\left[\left(\mu + \frac{\mu_t}{\sigma_k}\right)\frac{\partial v^2}{\partial x_j}\right] + \rho\left(kf - v^2\frac{k}{\epsilon}\right) \tag{2.26}$$

The f-equation:

$$L^2 \frac{\partial^2 f}{\partial^2 x_j} - f = \frac{1}{T}\left[(-4.6)\frac{v^2}{k} - \frac{0.8}{3}\right] - 0..3\frac{P_k}{k} \tag{2.27}$$

The ω-equations:

$$\frac{\partial}{\partial x_j}(\rho u_j \omega) = \frac{\partial}{\partial x_j}\left[\left(\mu + \frac{\mu_t}{\sigma_\omega}\right)\frac{\partial \omega}{\partial x_j}\right] + \rho^2 \frac{\gamma_1}{\mu_t} P_k - \rho\beta_3\omega^2 + F_{SST} \tag{2.28}$$

The difference between the two v^2-f models lies in their time scales T, with the v^2-f-1 models time scale being:

$$T = max\left[\frac{k}{\epsilon}, 6\sqrt{\frac{v}{\epsilon}}\right] \tag{2.29}$$

The v^2-f-1 model is known to have difficulties in converging, with Sveningsson and Davidson [27] suggesting the implementation of a realizability constraint to increase the model's convergence. With the time scale for v^2-f-2 being given by:

$$T = min\left[max\left[\frac{k}{\epsilon}, 6\sqrt{\frac{v}{\epsilon}}\right], \frac{0.6}{\sqrt{3}}\frac{k}{v^2 C_\mu \sqrt{2S_{ij}S_{ij}}}\right] \tag{2.30}$$

Reynolds Stress model (RSM)

In the Reynolds stress model, rather than computing the μ_t and calculating the Reynolds stress tensor using Equation 2.23, the Reynolds stress tensor is calculated directly; this is much more complex than an eddy viscosity model, generally increasing the computational requirement, with the equations being given in [28].

Model Comparison

A. Balabel et al. go on to compare the different models under several different pressure ratios. For a nozzle, the paper uses a conventional convergent-divergent nozzle with a mesh size of 260 × 100 inside the nozzle, with a total of 118,592 cells both inside and outside the nozzle. The boundary conditions and input variables for the different models can be seen in [25]. Giving the final comparison for three different pressure ratios, as well as the experimental results in Figure 2.17. The paper goes on to conclude that the best models are the SST k-ω and the realisable v^2-f models when compared to experimental values. The paper does go on to explain that the v^2-f model does have two additional equations when compared to the SST k-ω model, leading to an increase in the computational power required, whilst not providing much additional accuracy in the simulation.

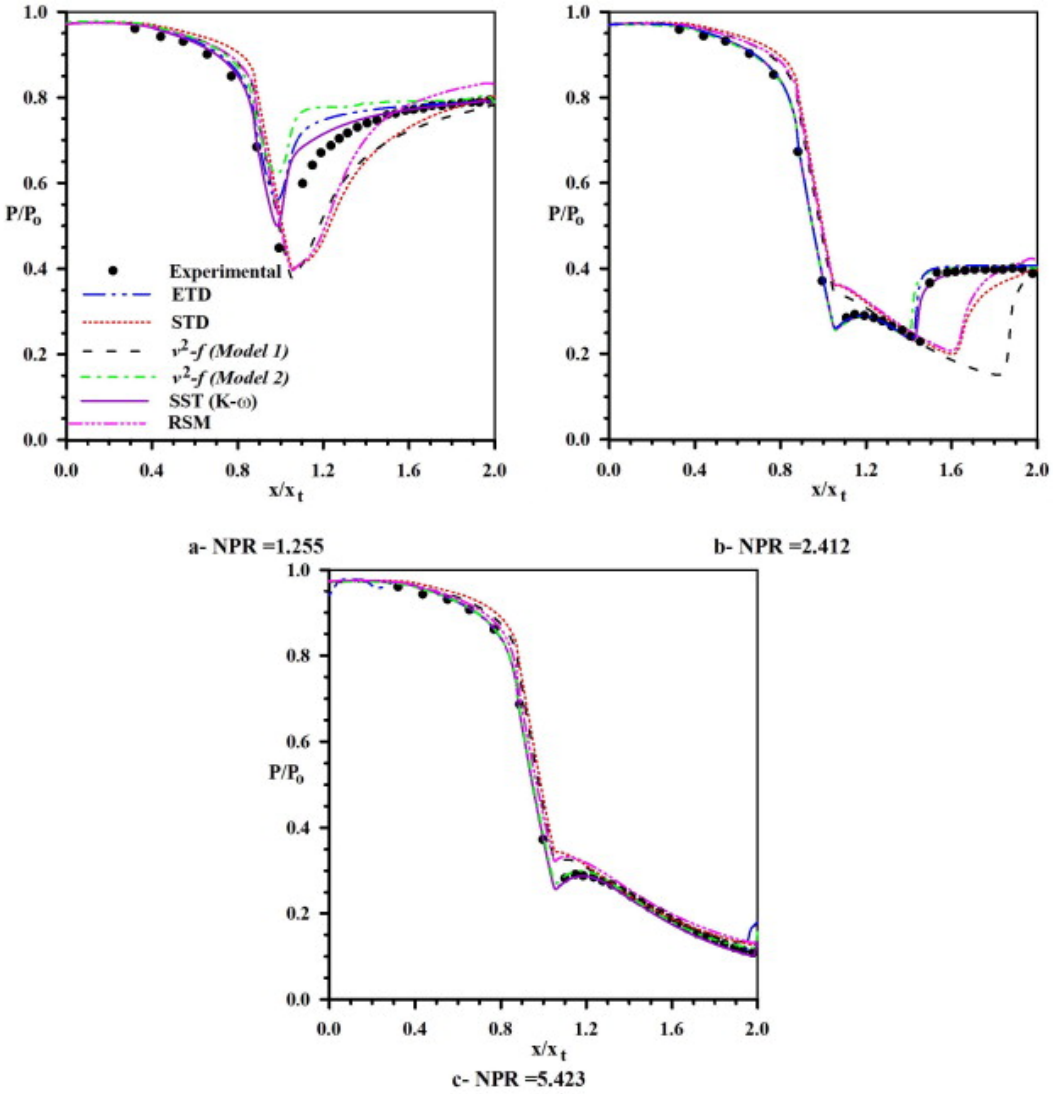

Figure 2.17: Graph showing the Pressure ratio throughout the nozzle for several pressure ratios

2.5. STP Component Design

As explained in the section 2.3, there are two main components in an STP system, these being the solar collector and the receiver/heat-exchanger. Thus, this section aims to answer ”What is the most optimal design for the solar collector system, considering material choices and Hydrogen handling?” by first explaining the available literature on Solar collectors. Then, going onto the design concepts proposed for the receiver/heat-exchanger and the struggles with using Hydrogen as a propellant.

2.5.1. Solar Collector

With the Sun being one of the largest sources of energy in space, and considering it is freely available, there are a variety of ways to collect this solar energy to do work. One of the first concepts envisioned is the use of an inflatable mirror that can unfold and inflate once in orbit, providing a very large collection surface, [12]. Inflatable concentrators are capable of providing a very lightweight and small launch volume when compared to more conventional polished metal mirror arrays, whilst still providing similar optical quality. Figure 2.18 shows the solar collector concept for an interplanetary transfer vehicle. G. Grossman et al. [29] propose the use of an inflatable solar collector to shuttle satellites from LEO to GEO orbit. The paper describes how the concentrator would be designed, being made of several flat sheets of reflective membrane, which are then welded together, forming the required shape once

pressurised. The paper also spends a lot of time discussing the optical properties of the concentration, aiming to only have a deviation of $1\ millirad$, indicating that the seams may cause large distortions both due to stress non-uniformities in the membrane as well as the effects of the seams themselves. Another aspect of using such a large and thin concentrator is the effects of micro meteorites and the potential to puncture the pressurised structure.

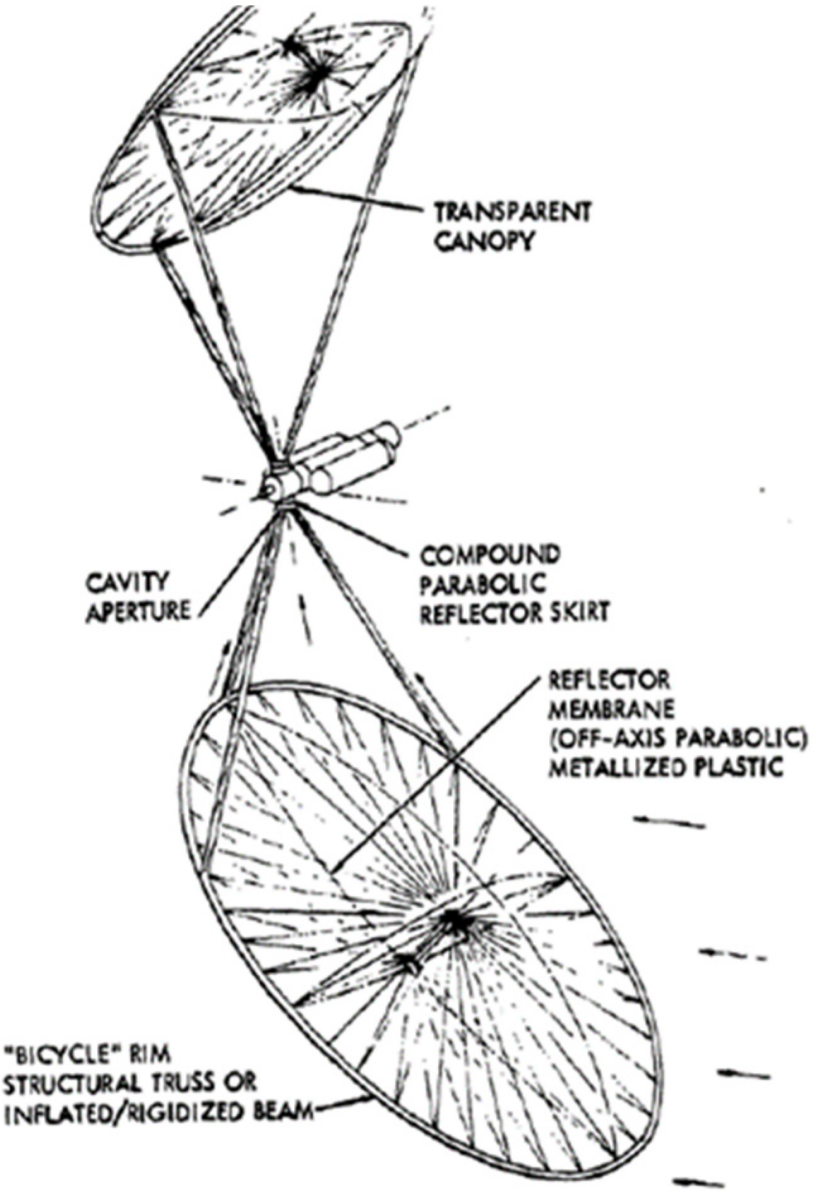

Figure 2.18: Non-Ridged, inflatable, off-axis solar concentrator design [12]

M. J. O'Niell [30] proposes another concept for a solar concentrator, using a set of linear Fresnel lenses, which is made of a planar sheet of material that can focus incoming light onto a single line. O'Niell proposes the use of these lenses to concentrate solar energy onto a line of solar cells, producing similar amounts of power for a much reduced cost when compared to a conventional solar array. The Fresnel array allowed for an $8x$ concentration of sunlight. Another promising aspect of the Fresnel lens is its error tolerance, where conventional mirrors are highly sensitive to shape errors, with even marginal changes to the mirror's shape distorting the reflected image. One aspect where the Fresnel lenses are lacking, and the main reason that these lenses have not been used in optical telescopes,

is the dispersion of light, leading to a non-uniform distribution of solar flux at the focal point of the lens. O'Niell has two patents for such a lens, the first being an inflatable version of the lens, [31], and a spring-loaded stretched lens [32]. An example of the stretched lens can be seen in Figure 2.19.

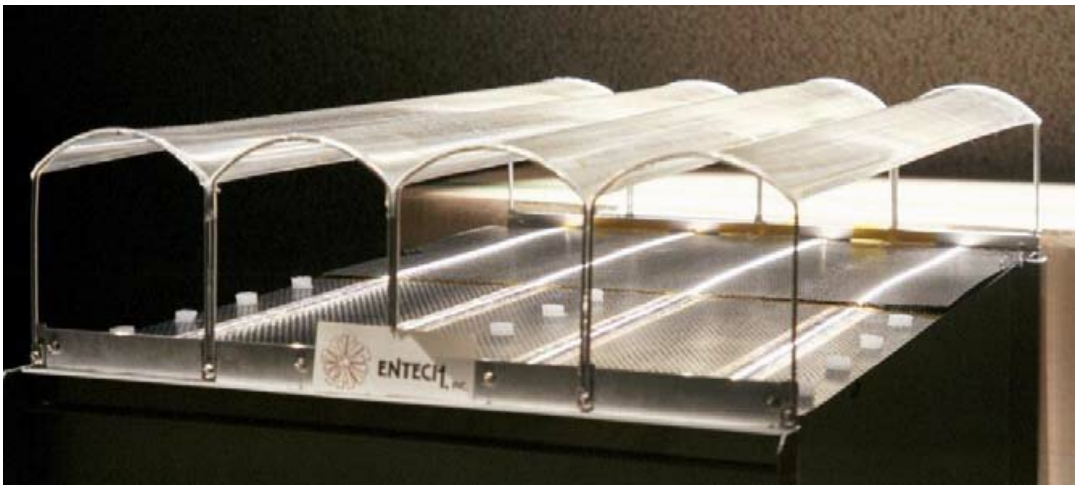

Figure 2.19: Image of the Stretched Fresnel lens solar array

Another form of the Fresnel lens is that of the Fresnel zone plate (FZP), where the light is not refracted by the 3D geometry of the lens but rather by the Diffraction of light as it passes through small gaps in the plate. FZP are generally composed of a series of opaque rings and gaps that diffract the light onto a singular focal point. Linear FZP also exist that focuses the light onto a singular line similar to O'Niell's design. Because of the high adaptability of the lens to different electromagnetic waves, FZP has been proposed for both telecommunication antennas [33] as well as for x-ray telescopes [34]. One aspect of the FZP that makes it less suitable for large scales is how to keep the rings aligned. One solution is the use of a Photon Sieve, [35], where the concentric rings are replaced with a series of holes. This allows for the photon sieve to be made of a single continuous sheet, allowing the system to be scaled to much larger proportions. This does not change the largest issue surrounding the use of FZP in the manufacturing of the rings, with the gap/hole size being determined by the wavelength of light; for solar radiation, these holes can become very small, with the smallest holes being of the scale of $76.5\ \mu m$, [35]. Another aspect of the Photon sieve compared to an FZP is the reduction in the intensity of the Point-Spread Function (PSF), where for a photon sieve, there is about 50% reduction in the intensity when compared to FZP.

2.5.2. Receiver/Heat-Exchanger

The solar receiver/heat-exchanger is a vital part of the STP system. However, arguably, this is also the most underdeveloped subsystem, with very little literature focusing on the design of a high-efficiency solar receiver. Considering that generally for an STP system, the higher the propellant temperature, the more efficient the propulsion system will be, leading to very high demand on the optical and mechanical properties of the material and design choices.

The paper by C. C. Selph [36] provides several conceptual designs for the solar receiver, the first and most simple being a hollow cavity with no window where the solar radiation is trapped and absorbed by the receiver. Propellant is then fed through the walls of the absorber, heating up before entering a combustion chamber and exiting through the nozzle. Another, more complex solution is to place a window into the side of the combustion chamber, allowing the concentrated solar radiation to directly enter the combustion chamber, shining onto a transportation-cooled liner where the propellant is injected into the combustion chamber. However, both of these have little ability to store thermal energy, thus, Selph proposed the use of refractory particles with the final design involving a rotating porous drum where the Hydrogen is pumped through, interacting with the heated refractory particles inside the drum. An illustration of the design can be seen in Figure 2.20. R. A. Alexander et al. [37], proposed a similar receiver to some of the first designs of Selph's, being composed of a hollow tube with the propellant

feed lines being twisted around the tube, ending in a conventional convergent-divergent nozzle.

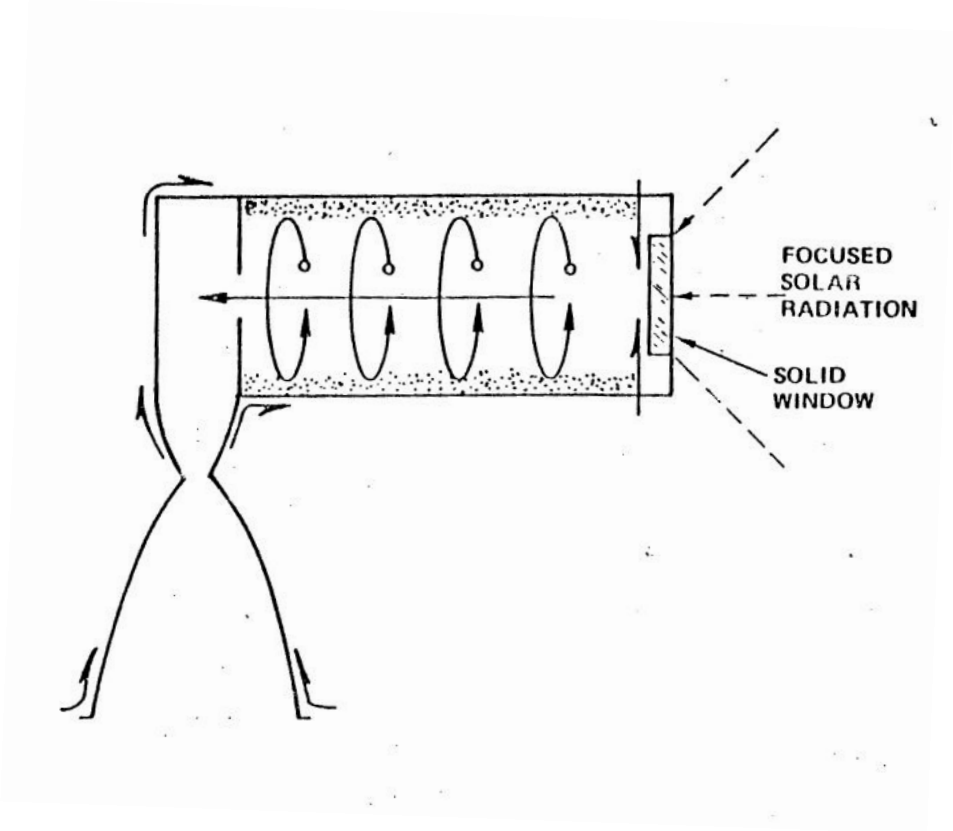

Figure 2.20: Diagram of Solar Receiver [36]

One of the most detailed explanations of the design for the solar receiver is by F.G. Kennedy et al. [38]. The basic concept of the design is an absorption cavity where the incoming solar radiation is trapped and absorbed by a Boron Carbide (B_4C) particle bed, held in place by a boron nitride (BN) cage enclosing the system. The propellant is then fed through a series of Molybdenum tubes passing through the B_4C particle bed, heating up to $2000\ K$ and pushed through a conventional nozzle; a cut-away of the receiver can be seen in Figure 2.21. Keller thoroughly discusses the material choices and bonding types, with the receiver design expecting to reach $2000\ K$, there are several difficulties present. One of the main issues is the bonding of the different elements of the BN cage. BN being an inert ceramic, there are few possibilities for bonding, with the main two being metallic brazing and hot-pressing of components; however, there is some recent literature on the bonding of BN [39]. Another aspect of high-purity BN ceramics is that it is a porous material, leading to potential fuel leakage during firing. The use of ceramics also provides difficulties in the manufacturability of the material, with the design by Keller requiring the use of relatively thin ceramic parts.

One of the main aspects of material choice is the high temperature, which poses two problems. The first being the capability of the material to hold its structure and mechanical properties at such high temperatures, for example, steel has a melting point of $\sim 1500\ °C$ but its strength significantly reduces at a temperature of just $\sim\ 600\ °C$ [40]. The second is the coefficient of thermal expansion (CTE), where a material will increase in volume with increasing temperature, which can become problematic for high-tolerance interfaces. For this reason, Keller chose to use ceramics for the main body of the receiver, which has a lower CTE, as well as the use of Molybdenum instead of tungsten because of its still relatively high melting point, whilst having much better machinability than tungsten.

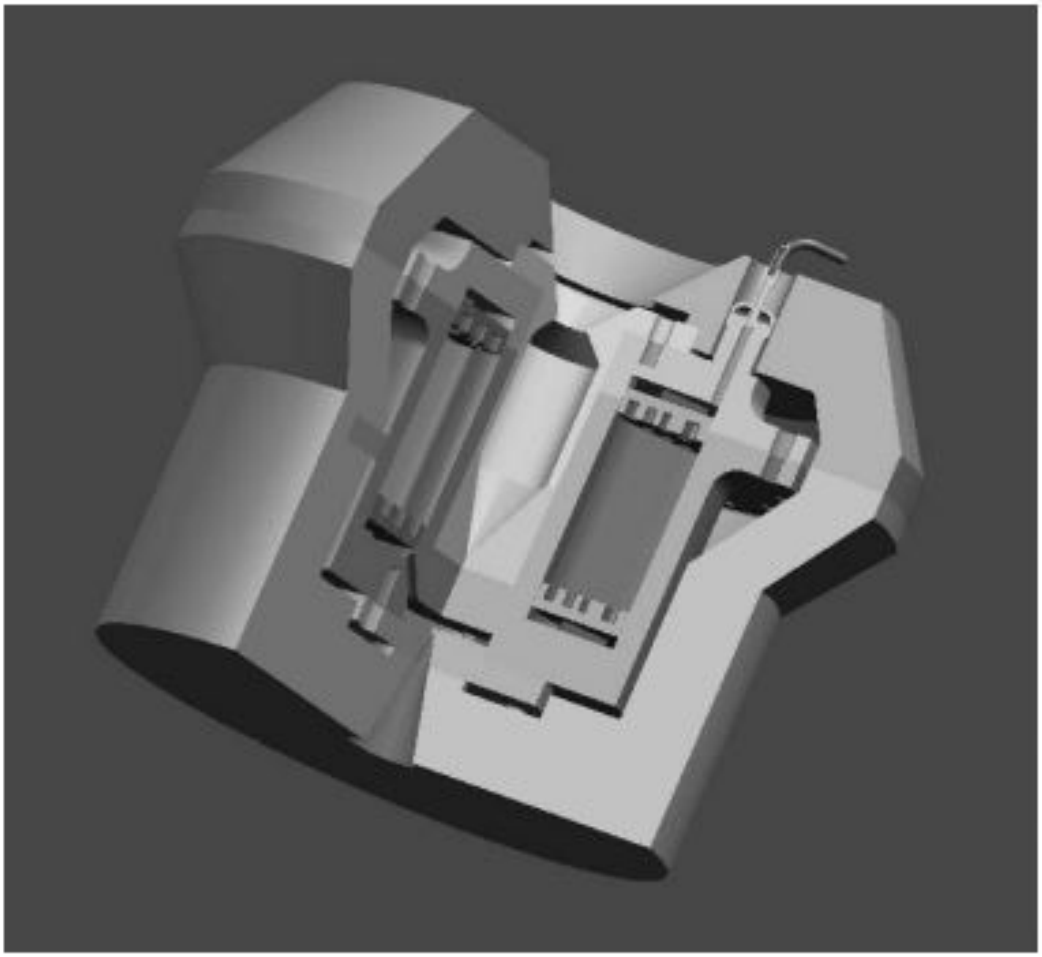

Figure 2.21: Cutaway view of the Receiver [38]

One novel approach is the use of a liquid heat exchanger, as suggested by this article [41], where the writer suggests the use of a rotating drum of liquid Rhenium heated to the maximum solar temperature of $5700\ K$, where Hydrogen is bubbled through the liquid Rhenium, heating up and being expelled through a nozzle. With the liquid Hydrogen acting as a cooling loop before being bubbled through, allowing for the use of existing material such as Tantalum-Hafnium Carbide, a ceramic type material able to withstand temperatures of $4000\ K$. However, the writer did design this around a very large rocket motor having thrust in the range of kN to MN, thus, it is somewhat unknown how well this system would be scaled down. Though the use of phase-changing materials as a form of thermal storage has often been stated in literature to allow for longer duration burns with no solar input [42].

2.5.3. Hydrogen Handling

When handling or using Hydrogen, three main aspects need to be considered these being the reaction with materials used in the STP system, the potential for explosions and leakage. First is the potential for explosions, as Hydrogen is a highly explosive substance only requiring a Hydrogen percentage of 4% to 75% with air at $25\ °C$ to form an explosive mixture. Luckily, Hydrogen has a quite high auto ignition temperature of $250\ °C$ to $550\ °C$ [43] depending on the pressure. However, with the use of an STP system, there is only one propellant being used, meaning that there is little risk of explosion as there is no oxidising agent. One other aspect to remember is that at a temperature of $3000\ K$ and pressures of at least 50 bar, Hydrogen is much more reactive than at standard temperatures.

The second aspect is the reactivity of Hydrogen. Hydrogen is known to invade metals, reducing the toughness and ductility of the material, which is known as Hydrogen embrittlement [44, 45, 46]. With most of the elements that cause this problem being the group one and two metals, as well as the

transition elements [47], steel is also a metal that struggles with Hydrogen embrittlement due to the carbon content, with Hydrogen happily bonding with carbon, nitrogen, oxygen and the halide elements. Hydrogen embrittlement is also accelerated by high pressures and temperatures. Hydrogen also reacts with ceramics at high temperatures and pressures [48], with Al_2O_3 (alumina) providing the highest stability, being stable up to a temperature of $1200 - 1300\ ^\circ C$ in pure Hydrogen and up to $> 1800\ ^\circ C$ at 10% moisture content, with other ceramics such as Mullite ($3Al_2O_32SiO_2$) and magnesia (MgO) preforming poorly. One issue is that there is very little literature on the reactivity of Hydrogen at these high temperatures and pressures. There is, of course, the theoretical side where one can calculate the likely reactions to take place concerning reaction enthalpy.

Hydrogen leakage is another large aspect of Hydrogen handling. With Hydrogen being the smallest element, it is much more likely to pass through materials and find gaps in seals. A. Mafliano et al.[49] provides a comprehensive overview of the leakage issue of Hydrogen, stating that there is a large safety concern with the risk of fire and explosions, as well as the efficiency losses in the system. J. Ishimoto [50] provides a comprehensive computational model for reactive Hydrogen leakage in high-pressure tanks.

2.6. Conclusion

Having now completed an investigation into the literature surrounding Solar Thermal propulsion (STP) systems, a conclusion can be drawn for each research question. Starting with ”How are rocket propulsion characteristics and performance estimations calculated, with a focus on Hydrogen as a propellant?”. The report describes the use of ideal rocket theory to estimate the propulsion characteristics and performance, providing the accompanying equations. Hydrogen is also investigated as a propellant, concluding that it provides the highest exhaust velocity but requires a large storage volume, reducing its current use to launch vehicles.

Investigating ”How have ground-based STP systems been designed, and have any mission plans been generated?”. Several STP missions and designs were investigated, providing their stated mission goals and profiles as well as any designs for such a system, with most of the literature focusing on the estimated capabilities of an STP system, with only in recent years more detailed designs of their components being proposed. Two examples of ground-based testing of an STP system were also investigated, concluding that the system can provide a substantial efficiency boost to the propulsion system.

”What advances in nozzle design could improve system performance, including associated performance estimations?”. Investigating several different nozzle geometries, providing their advantages and disadvantages, and concluding that a conical nozzle would be most reasonable for the early prototyping phase of the design, with its high adaptability to changes in ambient conditions and its ease of manufacturing and design. Understanding that, for a final nozzle implementation, the use of a bell/contour nozzle would provide a better performance of the system. With multi-nozzle grids being of interest due to their mass reduction. A thorough investigation into the performance estimation of rocket nozzles concludes that a Computational Fluid Dynamics (CFD) model is capable of accurately estimating the performance of a nozzle.

Finally, investigating ”What is the most optimal design for the solar collector system, considering material choices and Hydrogen handling?”. There is little consensus on the design of a solar collector, with older designs favouring the use of a thin membrane inflatable parabolic mirror, while others focus on the use of Fresnel lenses or, more recently, Fresnel zone plates. There have been many concepts proposed for the design of the receiver/heat-exchanger, mostly focusing on the use of ceramics to withstand the high temperatures and high-temperature metals to feed the fuel through the system. Hydrogen handling was also investigated, noting the potential dangers of Hydrogen embrittlement, weakening the materials used in the propulsion system, and also noting the potential dangers of Hydrogen leaks.

3

Thesis Introduction

The Green SWaP project aims to develop an in-orbit system capable of converting water into Hydrogen peroxide and Hydrogen gas to be used in the system's propulsion systems. Green SWaP has tasked this thesis with the development and analysis of a prototype for the Hydrogen-based solar thermal propulsion thruster to be used in the validation of the use of solar thermal propulsion in a reaction control system. Taking the Green SWaP mission goal and requirements into account, the objective of this thesis can be stated as: **"The development of a solar thermal propulsion prototype for the use of the reaction control system for the Green SWaP project, using gaseous Hydrogen as a propellant, requiring a thrust of $1\ [N]$ and a specific impulse of $\sim 500\ [s]$. Delivering a complete system CAD model that has been verified by both analytical and numerical means"**

Understanding the findings of the literature study and the thesis objective, four research questions can be developed to be answered in this thesis. Following what was learned from the investigation into the estimation of rocket characteristics and performance, and the insight into nozzle design, the research question can be posed, **"What thruster/nozzle design is best suited for an STP reaction control system, considering the requirements set by Green SWaP?"**

Investigating the literature on past STP concepts, there is a variety in heat-exchanger designs, leading to the proposed research question: **"What design choices affect heat-exchanger design, with respect to the material choices, Hydrogen handling and high temperature requirements?"**

Taking what has been learned from both he investigation into Hydrogen as a propellant and past STP absorber concepts, a research question can be posed: **"How can different absorber designs be verified, using the best representation of the expected solar flux, to evaluate the most suited to the Green SWaP goals?**

Regarding what was learned from the evaluation of numerical analysis in nozzle design, and the need to verify the system, it can be posed: **"How can the complete STP prototype be numerically analysed to allow for development of a physical testing methodology and the verification and validation of the prototype to the physical results?"**

With the objectives in mind, the thesis begins with the concept generation, where initial concepts are evaluated with one being chosen to be taken forward, leading into the thruster design, from which the best-suited thruster and nozzle are calculated, answering the first research question. From this follows the heat-exchanger design, developing the best-suited heat-exchanger and evaluating the absorber with respect to the expected solar flux. Answering the second and third research questions. Going on to present the initial prototype, discussing the design choices made and providing an initial verification against the requirements set. Furthering the verification and answering the final research question through a numerical simulation analysis of the prototype design, providing the required information to conduct a more thorough verification of the prototype. Finally, providing a conclusion of the prototype design and a suggestion of possible future work to improve the prototype further.

4

Concept Generation

The start of any design project is the generation of a design concept, evaluating the concepts with respect to the requirements set by Green SWaP. Thus, in this Chapter, a concept will be generated and evaluated against the requirements, which will then be further investigated. First, providing a functional diagram of an STP system as a whole, then going on to provide the requirements and project aim set by Green SWaP. Then, concentrating on the thruster and heat-exchanger, discussing the different design concepts and ideas. Finally, evaluating and comparing the concepts, choosing which to take forward.

4.1. Function Diagram

Before proceeding with the design of the prototype thruster, it is advisable to gain a deeper understanding of the overall functionality of an STP system. Through the use of a function diagram, a useful tool that allows for the separation of a complex system into its base functions. The function diagram for the STP system can be seen in Figure 4.1. Similar functions can be grouped into subsystems. For the STP system, these are: The Concentrator, the Optical Guide, the Absorber/Heat-exchanger, the thruster and the support equipment, with each of these being discussed in their respective subsections.

Concentrator

The concentrator is responsible for the collection and concentration of the Solar flux and ideally outputting a collimated beam. Depending on whether the flux source is produced by a Solar* radiation source, initiating the flux environment in LEO requires the use of a concentrator and collimator to produce a collimated beam. Or if the source is a laser source, which, by the nature of lasers, is a collimated beam, not requiring the use of a concentrator or collimator. There are safety concerns with the generation of the collimated beam, requiring a function to safely discard any unwanted flux.

Optical Guide

The main function of the optical guide is to, as the name suggests, guide the collimated beam from the concentrator to the absorber subsystems.

Absorber/Heat-Exchanger

The Absorber/Heat-Exchanger converts the collimated solar beam into hot propellant. Having the function of receiving the incoming collimated beam and converting the beam into what is required by the Absorber. This in itself is responsible for absorbing the solar flux and converting it into thermal energy. Thermal storage is provided by a thermal battery, storing thermal energy for the heat exchanger, which transfers the thermal energy into the propellant.

Thruster

The Thruster sub-system is responsible for converting the high-temperature propellant into thrust, as well as providing a way to remove the exhaust gases produced by the thruster safely.

*Solar refers to a radiation source mimicking the Sun's radiation spectrum, not necessarily flux from the Sun itself.

Support Equipment

The support equipment is there to provide the rest of the sub-systems with what they need. Providing water for cooling purposes, if required, as well as regulating the propellant for the STP system through the use of a regulator and pressure gauge.

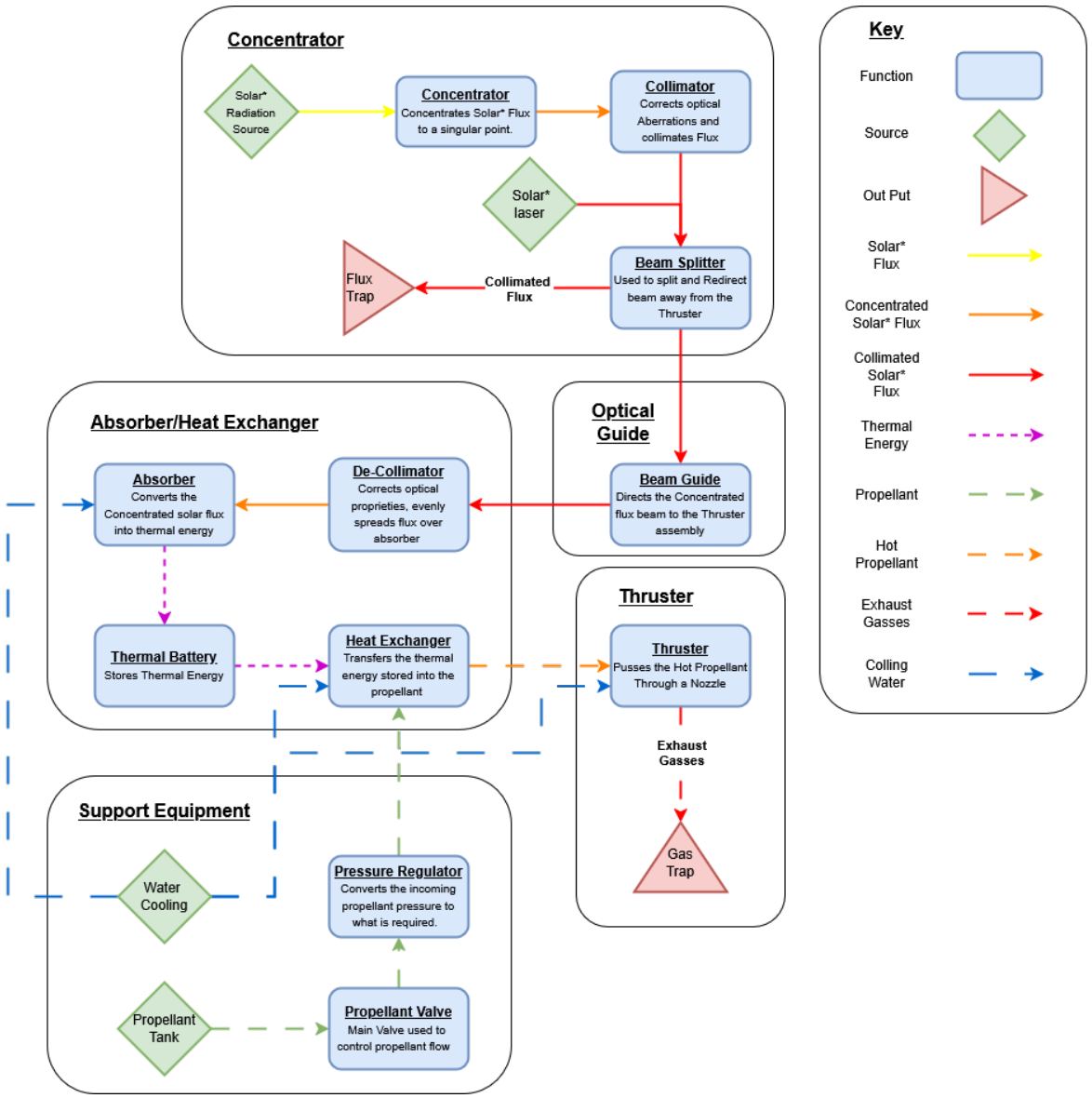

Figure 4.1: Function Diagram for an STP system, highlighting the main functions of the STP, from Solar* flux collection to thrust generation.

4.2. Requirements and Project Aim

This section will introduce the requirements set by Green SWaP. Requirements are the driving factor behind whether or not a system does useful work. If a system works, but it operates far outside the requirements, it may as well not have been developed in the first place. Thus, the requirements set by Green SWaP are seen in Table 4.1, with each requirement being given a tag, which will be used throughout the report when referring back to the requirements.

The Overall Aim set out by Green SWaP is the development of an in-orbit system capable of converting water into Hydrogen peroxide and Hydrogen for the use of thrust. Both for a main chemical thruster burning the Hydrogen and Hydrogen peroxide, and a solar thermal RCS using gaseous Hydrogen as a

propellant. This report aims to develop a functional prototype for the Solar Thermal RCS, designing the system for the use of Hydrogen, understanding that the system may be scaled to use other propellants for validation purposes when testing. The Report will be focused on designing the Absorber/Heat-Exchanger and the thruster. This was decided because of the limited time, as well as the report's aim being the design of a prototype system for lab testing. Meaning that a concentrator, as would be seen in a space application, would become impractical and unnecessary for lab testing, several more practical solutions for generating concentrated heat flux are already in existence.

Evaluating how the requirements influence the design, for each of the requirements as follows;

RCS-Sub-010
The thrust requirement provides the main sizing of the system, with this being a relatively low thrust rocket motor requiring the production of at least $1\ [N]$ of thrust in vacuum.

RCS-Sub-020
The Specific impulse of the system determines the efficiency of the system, with $500\ [s]$ being above most chemical rockets in use today, and well above the cold gas thrusters generally used for an RCS. Though when looking at the I_{sp} values generated by other proposed STP systems, this should be achievable.

RCS-Sub-030
Total Propellant Throughput determines the expected total burn time or lifetime of the system, with the system being able to produce its own fuel; the burn time is not limited by propellant availability but by the reliability of the rocket motor. Depending on the mass flow rate through the system, this could be quite large.

RCS-Sub-040
Response Time indicates how fast a system can react to a request, a crucial aspect to consider for an RCS, with its high pulse rate and high burn accuracy requirements. Though the limit has been set quite generously at $5\ [s]$ with a cold gas thruster having a response time of $5\ [ms]$, [51].

RCS-Sub-050
Reignition time is the time required to bring a system from a cold state to one at operating temperature, with no set value having been given at this time. This is highly dependent on the design and the external environment.

RCS-Sub-060
Minimum Impulse Bit is the minimum impulses the system has to be able to provide in one thrust pulse, in this case being set at $100\ [mN \cdot s]$. very high when considering a response time of $100\ [ms]$ is needed at $1\ [N]$ of thrust.

RCS-Sub-070
Thrust Accuracy is the allowable range of thrust values from one burn to the next, again, important for an RCS. With an allowable total uncertainty of less than 10% (3 sigma) from the determined nominal thrust.

RCS-Sub-080
Power Consumption is simply the electrical power required by the system; with no electrical components or heating, this would be zero.

RCS-Sub-090
Propellant Compatibility: All RCS components must be compatible with the propellant, with Hydrogen being somewhat of a hazardous propellant, this has to be considered. Also, the use of other propellants should be taken into account for later testing.

One aspect that is not mentioned is the maximum mass and cost of the system. Whilst there is no constraint placed on the system through the requirements, it is logical that for an RCS, the mass and cost of each thruster should be minimised to reduce the overall mass and cost of the RCS. This leads to

an extra constraint to limit mass and cost where possible and appropriate for the design of the system, providing requirements INT-Mass-010 and INT-Cost-010 respectively.

Table 4.1: Requirements for the Reaction control system of the Green SWaP project

Tag	Name	Description
RCS-Sub-010	Thrust Level - RCS	The RCS shall provide a vacuum thrust level of more than 1 N
RCS-Sub-020	Specific Impulse - RCS	The RCS shall achieve a vacuum specific impulse of more than 500 seconds to ensure efficient propellant utilisation.
RCS-Sub-030	Total Propellant Throughput - RCS	The main thruster shall be able to achieve a total propellant throughput of 3 kg [TBC].
RCS-Sub-040	Response Time - RCS	The thruster shall be capable of achieving full thrust within <5 s [TBC] after actuation.
RCS-Sub-050	Reignition Time - RCS	The RCS shall be able to reignite after a minimum of [TBD] seconds.
RCS-Sub-060	Minimum Impulse Bit - RCS	The RCS shall be able to provide a minimum impulse bit of 100 mNs [TBC].
RCS-Sub-070	Thrust Accuracy – RCS	Each RCS thruster shall deliver a thrust level with a total uncertainty less than 10% (TBC) (3 sigma) with respect to the selected nominal thrust value.
RCS-Sub-080	Power Consumption - RCS	The RCS shall not exceed [TBD] W of electrical power peak.
RCS-Sub-090	Propellant Compatibility - RCS	All RCS components shall be compatible to the propellants used by the system.
INT-Mass-010	Mass Budget - Internal	The mass of the components shall be reduced where deemed possible and appropriate.
INT-Cost-010	Cost Budget - internal	The cost of the components shall be reduced where deemed possible and appropriate.

4.3. Design Concepts

As noted in section 4.2, this design process will focus on the Absorber/Heat-Exchanger and the thruster creation. Thus, in this section, the initial design process and concept generation will be discussed. Separating the two subsystems, starting with the conceptual design process for the Absorber/Heat-Exchanger. First, developing an Idea-tree, then eliminating infeasible and/or impractical ideas, justifying each with the requirements set by Green SWaP, and providing initial conceptual designs to be taken to the next steps of designing and evaluation. The same process can be followed for the Thruster design, in its respective section.

4.3.1. Absorber/Heat-Exchanger

The Absorber/Heat-Exchanger, as mentioned before, is responsible for converting the concentrated solar flux into thermal energy and then imparting that energy onto the propellant, increasing the propellant temperature. The idea tree seen in Figure 4.2, is made up of all the possible solutions for completing the functions required of an Absorber/Heat-Exchanger. Each of the ideas has been labelled with a small coloured tag: Red, which indicates a failure to meet one or more requirements; Orange, there is doubt or uncertainty if the requirement can be met, and Green, the requirements can clearly be met. Indicating the feasibility of the idea for its respective function, relating to the requirements and observations made throughout the literature study. The reasoning behind each evaluation has been notated below.

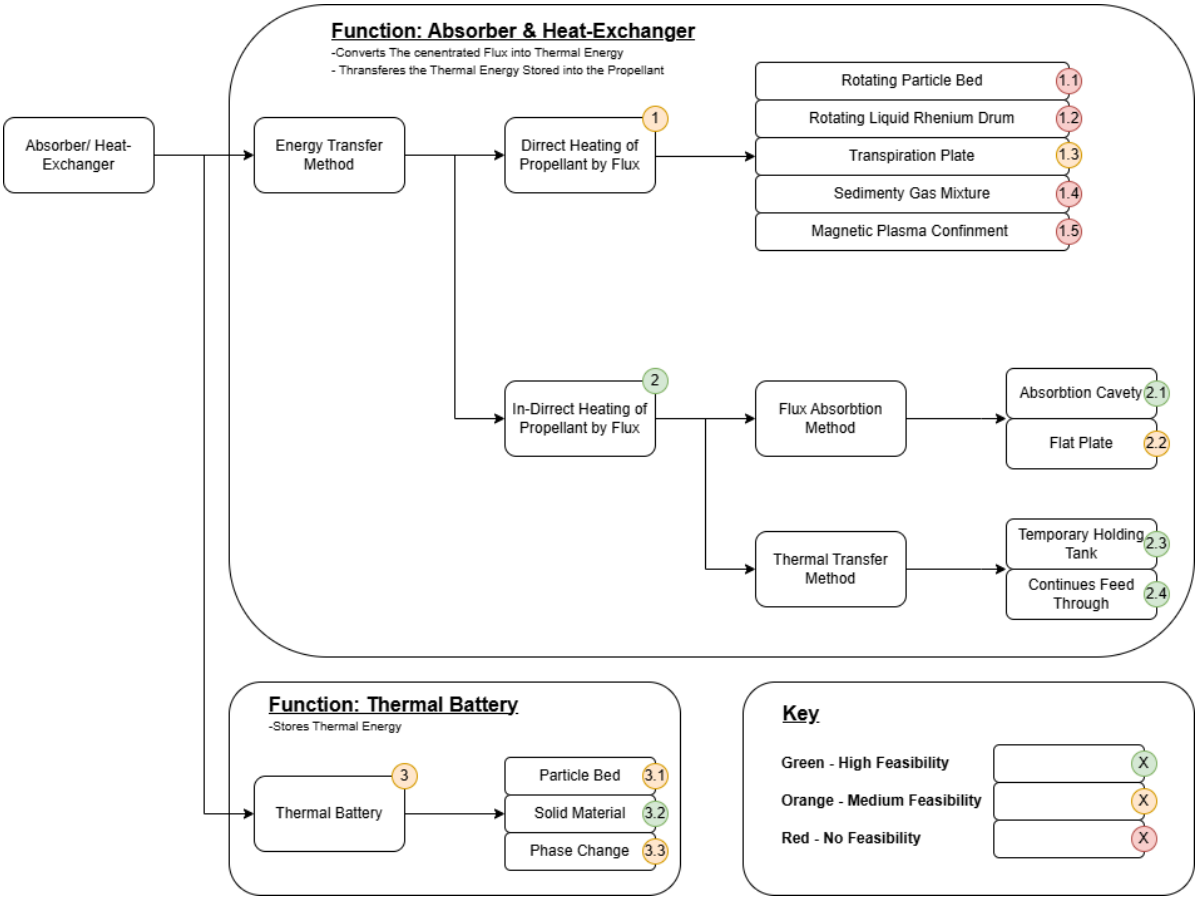

Figure 4.2: Idea Tree for the Absorber/Heat-Exchanger

1-(Orange) **[Direct Heating of Propellant by flux]** Whilst this may seem to reduce complexity, from literature, often a medium (particles, liquid Rhenium) is required to increase the energy transfer rate, leading to more uncertainty in thrusting accuracy and a reduced reliability.

1.1-(Red) **[Rotating Particle Bed]** For a small thruster, this adds a large amount of complexity and moving parts, breaking the power requirements. RCS-Sub-080 would also require constant rotation to stop the medium from escaping, reducing reliability.

1.2-(Red) **[Rotating Liquid Rhenium Drum]** similar issue to 1.1 with the power requirement, but with added wait time for the Rhenium to liquefy before the engine can be used, requirement RCS-Sub-050.

1.3-(Orange) **[Transpiration Plate]** Does not have the complexity of rotating components or liquid Rhenium, but there is some unknown if the transportation distance is enough to allow time for the propellant to heat up to the required temperature, potentially not meeting RCS-Sub-020.

1.4-(Red) **[Sedimentary Gas Mixture]** This is not possible due to this design breaking the mission objectives of Green SWaP, producing all required propellant for the craft from water. Could impact RCS-Sub-010 and RCS-Sub-060, due to an increase in molecular weight of exhaust products, increasing thrust but decreasing specific impulse.

1.5-(Red) **[Magnetic plasma confinement]** Requires extremely high temperature ($> 5500\ [°C]$) and high power for the magnetic containment fields required, breaking the power requirement. The TLDR for plasma thrusters is very low, with plasma thrusters just starting to be developed. [52]

2-(Green) **[Indirect heating of propellant by Flux]** This removes some of the complexity from the design as well as allowing for the separation of variables, being able to test the absorption system and heat-exchanger separately. It requires no power and can be sized to meet any required performance values.

2.1-(Green) **[Absorption Cavity]** Depending on geometry, Solar flux can be absorbed efficiently. Allows for

the separate analysis of different materials and coatings on the absorption efficiency. It requires no power and can be sized to meet any required performance values.

2.2-(Orange) **[Flat Plate]** The flat plate has the same advantages of separating variables as 2.1 and may be more intuitive to understand, but because of the lack of absorption from secondary reflection, the efficiency is massively reduced, potential not meeting the requirement RCS-Sub-020 or RCS-Sub-050.

2.3-(Green) **[Temporary Holding Tank]** While this is a very non-complex design, as was seen in [16], with a small enough volume and a high enough thermal transfer rate, this could meet the requirement RCS-Sub-050.

2.4-(Green) **[Continues Feed Through]** This would require a lot more thermal power to sustain the propellant temperature and maintain thrust, or require a reduction in thrust as the burn continues, stopping before the requirement RCS-Sub-070 is broken. But the system could theoretically have a response time of less than a second.

3-(Orange) **[Thermal Battery]** At these extreme temperatures, the materials available become drastically reduced, making the design of a thermal battery quite difficult, but not infeasible. With the thermal battery helping to achieve requirements RCS-Sub-050 and RCS-Sub-070.

3.1-(Orange) **[Particle Bed]** Particle beds can be a very good thermal battery, but it is uncertain how stable the ceramics conventionally used are at ($> 2500\ [^{\circ}C]$) with the use of Hydrogen, drawing uncertainty to requirement RCS-Sub-090, with most STP design from literature avoiding direct contact between Hydrogen and ceramic parts.

3.2-(Green) **[Solid Material]** Generally, the walls and material used in the heat-exchanger allow for easy integration, but reduced thermal capacity depending on the material used (high temperature metals). Care has to be taken to choose compatible materials.

3.3-(Orange) **[Phase Change]** Phase changing materials have often been used to increase the thermal capacity of a thermal battery, but conventional materials used are gases at the required temperature, reducing thermal conductivity. The use also increases the reignition time of the system, RCS-Sub-050.

4.3.2. Absorber/Heat-Exchanger Concepts

Having gone through the idea tree for the absorber/heat-exchanger and discarded any ideas that directly break any of the requirements, marked in red, the concept generation can start. Three separate concepts can be taken from the idea tree, these being explained below.

Absorber/Heat-exchanger Concept A

The use of a Transpiration Plate, with the use of a solid material for thermal storage. This provides an interesting concept with the inclusion of a transpiration plate. With the potential to provide a very compact design and 3D printing has enabled the production of select porous objects. It is unclear how well these objects behave at high temperatures or with the use of Hydrogen.

Absorber/Heat-exchanger Concept B

The second is the use of an absorption cavity with a temporary holding tank similar to what was tested by [16], with a solid material thermal battery. This provides a simple and as demonstrated experimentally tested system. Though the system will have a large reignition time, considering the time required to heat a larger bulk volume of fluid, it is unclear how far the thrust level will drop with each successive firing of the thruster.

Absorber/Heat-exchanger Concept C

Finally, a concept using an absorption cavity with the implementation of a continuous feed-through system, with a solid material. Providing a predictable and constant thrust for the system, however, requires a higher input solar* power load and greater care when considering thermal strain.

4.3.3. Thruster

The Thruster is responsible for converting the pressure and thermal energy of the hot propellant into usable thrust through the expulsion and expansion of the gas. Thus, the initial ideas for the thruster

will be shown through an idea tree, then going through and indicating the feasibility as done for the heat-exchanger. Again, the reasoning behind the choices made can be seen below.

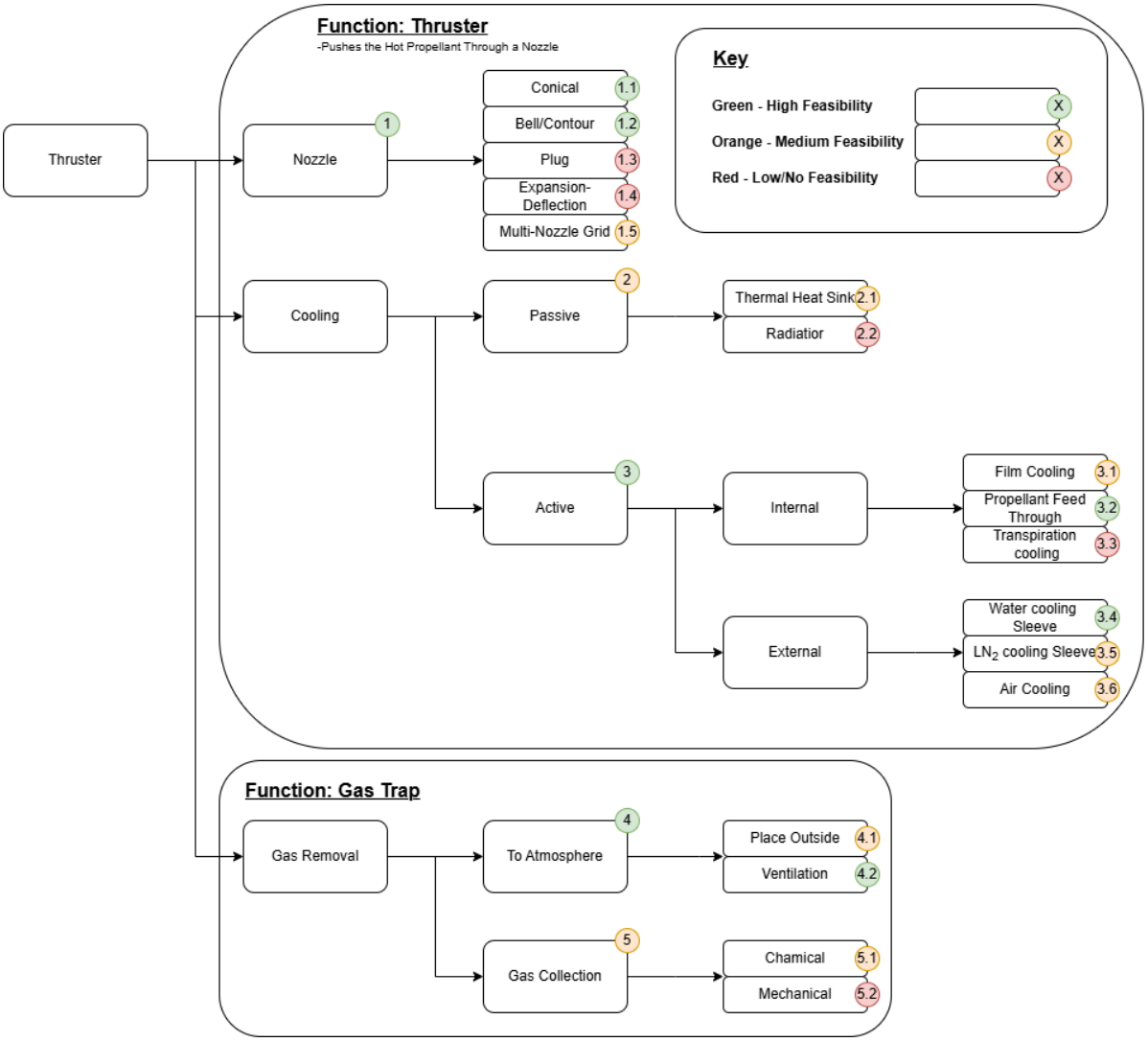

Figure 4.3: Idea tree for the Thruster

1-(Green) **[Nozzle]** The geometry of the nozzle is vital to achieve requirements RCS-Sub-010 and RCS-Sub-020.

1.1-(Green) **[Conical]** The conical nozzle geometry is a reliable and easy design that has predictable performance characteristics.

1.2-(Green) **[Bell/Contour]** Similar to the conical nozzle, Bell/contour nozzles can perform very well, they are slightly more complex to produce, but can reduce overall length for little downside.

1.3-(Red) **[Plug]** The plug nozzle uses a plug allowing for atmospheric adaptation, with the design being vacuum only, this added complexity is not needed.

1.4-(Red) **[Expansion-Deflection]** Similarly to the plug, this is also an adaptive nozzle, again not needed for a vacuum system, adding unnecessary complexity.

1.5-(Orange) **[Multi-Nozzle Grid]** Potentially interesting with the use of thrust vectoring for an RCS, but highly complex at this scale and temperatures, not compatible with STP designs.

2-(Orange) **[Passive Cooling]** With the very high power input into the system, in the kW range, passive cooling may not be sufficient.

2.1-(Orange) **[Thermal heat sink]** Would increase the mass of the system greatly whilst still limiting the maximum continuous burn time of the system, potentially interfering with RCS-Sub-050.

2.2-(Red) **[Radiators]** The overall size and mass that is required for a passive radiator to dissipate kW of power makes it impracticable, on a similar scale to the collimator.

3-(Green) **[Active Cooling]** Active cooling has a much higher cooling density, allowing for a much smaller system, though it would require an external chiller.

3.1-(Orange) **[Film Cooling]** Film cooling is an effect and often used method for cooling large rocket thrusters, but it wastes propellant that could have been used to generate thrust.

3.2-(Green) **[Propellant feed through]** Propellant feed through allows for the cooling and preheating of the propellant, providing both cooling and an efficiency gain.

3.3-(Red) **[Transpiration cooling]** Similar issues to film cooling with a more complex delivery system

3.4-(Green) **[Water cooling sleeve]** A very effective and potentially continuous method of cooling the thruster, if an external water chiller is used.

3.5-(orange) **[LN_2 cooling sleeve]** Higher cooling capability than water, but has to take into account the 2-phase flow of the cooling fluid.

3.6-(Orange) **[Air cooling]** Is very simple but could have difficulties if it needs to be done under vacuum, as well as the reduced cooling potential when compared to the other options.

4-(Green) **[Gas removal to atmosphere]** Allows for an easy and non-toxic (dependent on propellant) removal of the hot exhaust gases.

4.1-(Orange) **[Place outside]** This is the easiest but would not allow for the use of vacuum conditions, as well as the catastrophic reaction of high-temperature Rhenium with Oxygen.

4.2-(Green) **[Ventilation]** Ventilating to the outside allowed for a controlled environment whilst still removing exhaust gases, which could be complex if used in a vacuum chamber

5-(Orange) **[Gas removal through gas collection]**. A direct removal and collection of the gas may be more viable when used under vacuum.

5.1-(Orange) **[Chemical]** The removal of the exhaust gas through the use of a solid absorption material may be of use when operating in a vacuum, though any liquid would not be suitable.

5.2-(Red) **[Mechanical]** At the point where the gas is collected, there is no point in capturing the gas when it can be ventilated to the atmosphere (if the exhaust gases are non-toxic)

4.3.4. Thruster Concepts

For the thruster design, four main concepts meet the requirements of the project. These are the combination of either the Conical or Bell/Contour nozzle and the use of a propellant feed through or water cooling sleeve for cooling the nozzle.

Thruster Concept A

The use of a Bell/Contour nozzle and a propellant feed through system to cool the nozzle. Providing a very efficient system, with the implementation of the bell/contour nozzle and preheating of the propellant. Though there is an increased design process for creating the bell/contour, the nozzle is not easily adaptable to other ambient environments. Providing a complex but high-efficiency system.

Thruster Concept B

The use of a Bell/Contour nozzle and a water cooling sleeve to cool the nozzle. With similar effects due to the bell/contour nozzle, the water cooling sleeve is a very efficient method of removing heat, and is easily possible in a lab setting, though this is massively decreased when considering the use in space.

Thruster Concept C

The use of a Conical nozzle and a propellant feed through system to cool the nozzle. A conical nozzle has a theoretically worse value when compared to a bell/contour nozzle, though it is simple to design and adaptable to other ambient environments.

Thruster Concept D
The use of a Conical nozzle and a water cooling sleeve to cool the nozzle. Providing an easily adaptable and robust system.

4.4. Concept Evaluation & Trade-Off Process

A set of concepts has been generated for both the Absorber/heat-exchanger and thruster design of the system. An evaluation can be made on the concepts to determine which will be taken forward and developed further. First, an explanation of the trade-off process and criteria generation, then inspecting the concepts generated for the Absorber/heat-exchanger, and going on to evaluate the Thruster concepts to be used.

4.4.1. Trade-off Process

A trade-off table is a proven technique to evaluate the different designs. For both the trade-off process of the Absorber and Thruster concepts, the same criteria will be used. These are derived from the requirements set by Green SWaP, with the criteria and the expiration behind them being given below. The generation of the weights for the criteria and an explanation behind the reasoning can be seen in Appendix A.

- **Reliability** - The reliability criteria describe the reliability of the hardware and components of the concept. The requirements specifically states an expected life span of the concept and compatibility with the propellant.
- **Performance** - This criterion describes the performance capabilities of the concept. There are several requirements set by Green SWaP dictating the minimum thrust and specific impulse values, as well as the overall systems mass and cost performance.
- **Accuracy** - This criterion refers to the accuracy of the concept, both in terms of thrust and minimum impulse bit. The requirements are very clear on the required accuracy of the system.
- **Responsivity** - The Responsivity refers to how quickly the concept can respond. Referring both to the system's start-up time from an inactive state, and the time between the opening of propellant valves and the generation of full thrust.

4.4.2. Absorber/Heat-Exchanger Concept Evaluation

Taking the three concepts for the Absorber/heat-exchanger, and evaluating them against both the requirements and the aim of the Green SWaP project. Whilst at this stage of the design generation, the trade-off process can be seen as somewhat subjective, though care has been taken to refer back to chapter 2 whenever possible. Because of this reason, it was chosen not to directly apply numerical evaluations to the trade-off process. Rather, providing a symbolic evaluation where $-$, \ and $+$ correspond to "not sufficient", "sufficient" and "good" respectively.

First, discussing Concept A, the use of a transpiration plate or thrusting cavity, this is a concept that may have great promise. However, it adds a lot of complexity to this project, with the unknown of whether the concept will be able to survive the heat fluxes needed in an STP system. Thus, it was provided with a "not sufficient" evaluation for the reliability of the concept. The concept can provide an exceptional performance and accuracy, both in terms of thrust and specific impulse, as well as the possibility for a reduced mass. Providing the design with a "good" evaluation for the accuracy and performance criteria. Because of uncertainties in the restriction of the flow through a transpiration plate, the concept was given a "sufficient" for the Responsivity criteria.

For the second concept, the use of an absorption cavity with a temporary holding tank, while this is a proven concept for a temperature of $120\ [^{\circ}C]$, providing it with an evaluation of "good" for the reliability criteria. Both because this is one of the only concepts that has been tested, and the simplicity of the design. However, this concept calls into doubt whether it will be able to fully meet the accuracy and performance criteria. With the inherent thrust characteristics of a blow-down propellant feed system, there is a small range of allowable pressures that will produce the required nominal thrust before it falls outside the 10% uncertainty limit. Providing it with a "not sufficient" evaluation for the accuracy and performance criteria. There is also uncertainty in the system's capability to meet the requirement RCS-Sub-050 for the reignition time, with the heating of a relatively large amount of bulk fluid, resulting in a

”not sufficient” evaluation for the responsivity criteria. While this may be an achievable concept, there are too many uncertainties about whether the concept will meet the requirements. Generally requiring a long start-up time and having a variable trust value over time, raising doubt to meet requirements RCS-Sub-050 and RCS-Sub-070.

The third concept is the use of an absorption cavity with a continuous propellant feed through, which leads to a constant thrust value, unlike the use of a temporary holding tank; thus, the confidence in meeting the thrust accuracy requirement increases for a continuous system when compared to a pulsed or blow-down system. Resulting in a ”good” evaluation for the accuracy criteria. However, this may require the highest temperatures of all concepts to allow the propellant to heat up at a fast enough rate to achieve the required chamber temperatures before entering the thrust chamber. Leading to a ”sufficient” evaluation for the performance criteria for this concept. This concept is similar to the design presented by [38], and with the reduced risk of channel clogging when compared to the use of a transpiration plate, this concept is given a ”sufficient” rating for the reliability criteria.

Table 4.2: Trade-off table for the concept evaluation for the Absorber

Absorber Trade-off	Reliability	Performance	Accuracy	Responsivity	Normalised Total
Weights	0.18	0.36	0.18	0.27	
Concept A	-	+	+	\	0.96
Concept B	+	\	-	-	0.7
Concept C	\	\	+	+	1

With the evaluation of the concepts and the implementation of the trade-off process being completed, Concept C was chosen, the use of an absorption cavity with a continuous propellant feed through system. Though concept A also seems to provide a compelling choice with its use of a transpiration plate. However, whilst this is a point of interest for further investigation for the future generations of prototypes of the thruster. It was chosen not to implement a transpiration plate to reduce the complexity, allowing for an easier validation of the prototype. Concept B is lagging considerably behind in the trade-off process, mainly due to its inconsistent performance characteristics. Determining that Concept C has the highest certainty in meeting the requirements set by Green SWaP, whilst still allowing for a prototype design that is easily adaptable to different propellant and environmental conditions, allowing for the validation of the concept in a laboratory setting.

4.4.3. Thruster Concept Evaluation

For the four-thruster concepts, again, the same trade-off process is conducted using the same symbolic evaluation method as for the absorber concept evaluation.

Evaluating the nozzle geometry and cooling system separately for all the concepts, first going over the nozzle options, both bell/contour and Conical nozzle geometries are capable of meeting the requirements set. Whilst the bell/contour nozzle would have a slightly better performance for a set length, when compared to the conical nozzle, resulting in the bell/contour nozzle being provided a ”good” evaluation and the conical nozzle is given ”sufficient” as an evaluation. The design of a bell/contour nozzle is also complex, and there is uncertainty in the capability to produce the nozzle at the required scale when using bell/contour nozzle geometries. For both the accuracy and responsivity criteria, the conical and bell/contour nozzles perform similarly, both being given a ”sufficient” evaluation.

For the cooling of the nozzle, whilst the use of a water cooling sleeve would be a very capable cooling system, it does introduce the need for an external system to chill the water. Resulting in a ”not sufficient” for the reliability criteria, do to the multiple introduced points of failure, with an added water cooling system. With the introduction of a water cooling loop, there is an increase in the mass and cost of the system, whilst not directly set by Green SWaP, this does reduce the performance criteria evaluation to ”not sufficient” when considering the increased mass and cost. One advantage of separating the propellant input and the system’s temperature control is that, theoretically, the concept is

more responsive as the propellant has a reduced path length as it is not required to flow through cooling channels, resulting in a ”good” evaluation for the responsivity criterion.

Table 4.3: Trade-off table for the concept evaluation for the Thruster

Thruster Trade-off	Reliability	Performance	Accuracy	Responsivity	Normalised Total
Weights	0.18	0.36	0.18	0.27	
Concept A	+	+	\	\	1
Concept B	\	-	\	+	0.75
Concept C	+	\	\	\	0.86
Concept D	\	-	\	+	0.75

From the concept evaluation and the trade-off process, concept A has proven to be the option with the highest certainty in meeting the requirements. Though the trade-off process fails to consider one aspect of this thesis, and that is the production of a testing prototype to be used in the validation of an STP system from the Green SWaP reaction control system. Whilst the use of a bell/contour nozzle would result in a slightly higher performing prototype, it heavily sacrifices the prototype’s versatility to external environments. Where the bell/contour nozzle geometry is hard to adapt to different ambient pressures, whereas the conical nozzle can simply be shortened to meet the required pressure ratio. The use of a water cooling sleeve to control the nozzle temperature is a worse choice than the implementation of a propellant feed-through system to cool the nozzle. Thus, concept C becomes the preferred choice to be taken further, with the recommendation to implement an optimised bell/contour nozzle once the final version is generated, to benefit from the increased performance provided.

5

Thruster Design

The design of the thruster is the first thing to be considered, with the values calculated being used to size the heat exchanger. Thus, for this chapter, the first section will focus on the design and thought process behind the thruster sizing, illustrating the use of ideal rocket theory. The next section will discuss the results gathered from the investigation into the thruster sizing, illustrating several sizing parameters for a variety of different input variables. Finally, an evaluation of the results and a discussion on what the sizing properties of the thruster are to be carried forward into the heat-exchanger design.

5.1. Thruster Sizing

The section describes the thought process behind the thruster sizing, first providing an overview of the sizing processes, going over the theories used and assumptions made. Then, going on to describe the use of a Python script to calculate the sizing data for a variety of input variables, explaining the functionality and underlying mathematics used.

5.1.1. Sizing Thought Process

Determining the sizing data for the thruster, in this case, the values being: the thrust, mass flow, chamber pressure and temperature, the nozzle throat and exit dimensions, the specific impulse and the power required to heat the propellant. With these values, the initial sizing of both the heat-exchanger and nozzle geometry can be conducted. A powerful tool in the initial estimation of the thruster is the use of ideal rocket theory, a set of calculations that allows for the basic determination of the sizing data.

The use of ideal rocket theory does come with drawbacks, and there are assumptions being made that have to be considered. First is the use of the ideal gas law for the fluid flow, relating the gas's density, pressure, temperature and volume to the number of moles of the gas. Another assumption is that gas properties are homogeneous with a non-changing chemical composition, over the full range of expected pressures and temperatures. Other aspects to consider are that the effects of the boundary layer at the nozzle wall are not considered, as well as the loss of thermal energy to the environment. Because of this, there are many correction values available when using ideal rocket theory, using empirical values to provide a more accurate estimation of thruster performance.

Distributing the variables associated with ideal rocket theory, it was determined to choose the chamber pressure, chamber temperature and the chamber to nozzle-exit pressure ratio as the independent variables of this investigation, choosing these variables as they are the easiest to control in an experimental setting, allowing for easy verification. Because of the requirement set by RCS-Sub-010 and RCS-Sub-020, seen in section 4.2, it was chosen to use a constant thrust value of $1\ [N]$ and implement a vacuum condition, setting the ambient pressure to $0\ [Pa]$. This leaves the mass flow rate, the specific impulse, the nozzle throat and exit dimensions and the power required to heat the propellant as the dependent variables to be evaluated.

5.1.2. Thruster Sizing Code

To allow for the determination of the sizing data over a large range of the independent variables with enough detail to accurately analyse the results, a large number of data points is required. To allow for this, a Python script was written to automate and plot the implementation of ideal rocket theory. This code can be seen in section D.1.

Concerning the calculations made, the main function, which is looped, works as such, taking in the independent variables of $P_c, T_c, P_e/P_c$. Then, importing the thermodynamic properties of the propellant at the input pressure and temperature from a Python library (Cantera), going on to calculate the exhaust velocity U_e, the nozzle throat-exit area ratio A_e/A_t and the thrust coefficient C_f, using Equation 5.1,5.2,5.3. From that, the throat area can be calculated using Equation 5.4, which then allows for the calculation of nozzle exit area A_e, the specific impulse I_{sp}, the mass flow m, the exit and throat diameter D_e, D_t and the estimated power required, which is calculated as the energy needed to heat the propellant from $273[K]$ to the desired chamber temperature.

The material and thermodynamic properties of the propellant are calculated using Cantera [53], an open source materials library. The library is a powerful tool for calculating thermodynamic and transport properties of different materials, used to calculate the density and specific heat of the propellant at a set temperature and pressure. Using a data set named 'gri30_highT.yaml', which is generally a data set used for high temperature combustion, but does still include Hydrogen, as well as other elements associated with hydrocarbon-based combustion. Cantera is also able to calculate the dissociation of Hydrogen from H_2 to H^+, however, at a temperature of $3000\ [^\circ K]$, the dissociation is negligible $(< 10\%)$, graphs of which can be seen in Appendix C.

This main function is looped over the three independent variables, with chamber temperature being given a range of $1000 - 3000\ [^\circ K]$, with this range being chosen as, on the low end, this is below the minimum temperature required to meet the specific impulse requirement (RCS-Sub-020). On the high end, this is close to the operational limit of high-temperature metals and ceramics. The exit-chamber pressure ratio was given a range of $1000 - 10,000$. Theoretically, the higher the pressure ratio, the higher the specific impulse; however, there are physical constraints with large pressure ratios leading to longer and heavier nozzles. Thus, capping the pressure ratio at $10,000$, which already leads the exit to throat area ratio to be much larger than similarly powerful chemical rocket motors, [54]. The pressure range was given the full possible range from $1 - 50\ [bar]$, which is the maximum propellant supply pressure.

$$U_e = \sqrt{2 \cdot \frac{\gamma}{\gamma - 1} \cdot \frac{R_A}{M} \cdot T_c \cdot \left[1 - \left(\frac{P_e}{P_c}\right)^{\left(\frac{\gamma-1}{\gamma}\right)}\right]} \tag{5.1}$$

$$\frac{A_e}{A_t} = \frac{\Gamma}{\sqrt{\frac{2\gamma}{\gamma-1} \cdot \left(\frac{P_e}{P_c}\right)^{\left(\frac{2}{\gamma}\right)} \cdot \left[1 - \frac{P_e}{P_c}^{\left(\frac{\gamma-1}{\gamma}\right)}\right]}} \tag{5.2}$$

$$C_F = \Gamma \cdot \sqrt{\frac{2\gamma}{\gamma - 1} \cdot \left[1 - \left(\frac{P_e}{P_c}\right)^{\left(\frac{\gamma-1}{\gamma}\right)}\right]} + \left(\frac{P_e}{P_c} - \frac{P_a}{P_c}\right) \cdot \frac{A_e}{A_t} \tag{5.3}$$

$$A_t = \frac{F}{C_f \cdot P_c} \tag{5.4}$$

5.2. Thruster Sizing Results

Having calculated the sizing data, the results can be analysed. Thus, in this section, first, the results will be laid out and described. Then, going on to discuss the model's sensitivity to changes in input parameters, continuing to evaluate the effects on the Nozzle and heat-exchanger design.

5.2.1. Results

First, investigating the specific impulse, seen in Figure 5.1, it's clear that the specific impulse increases with an increase in either chamber temperature or chamber-exit (C/E) pressure ratio. The rate of increase in specific impulse is much greater for an increase in chamber temperature than for an increase in C/E pressure ratio. It can also be seen that chamber pressure does not affect the specific impulse, which is expected considering Equation 5.1 is not dependent on chamber temperature.

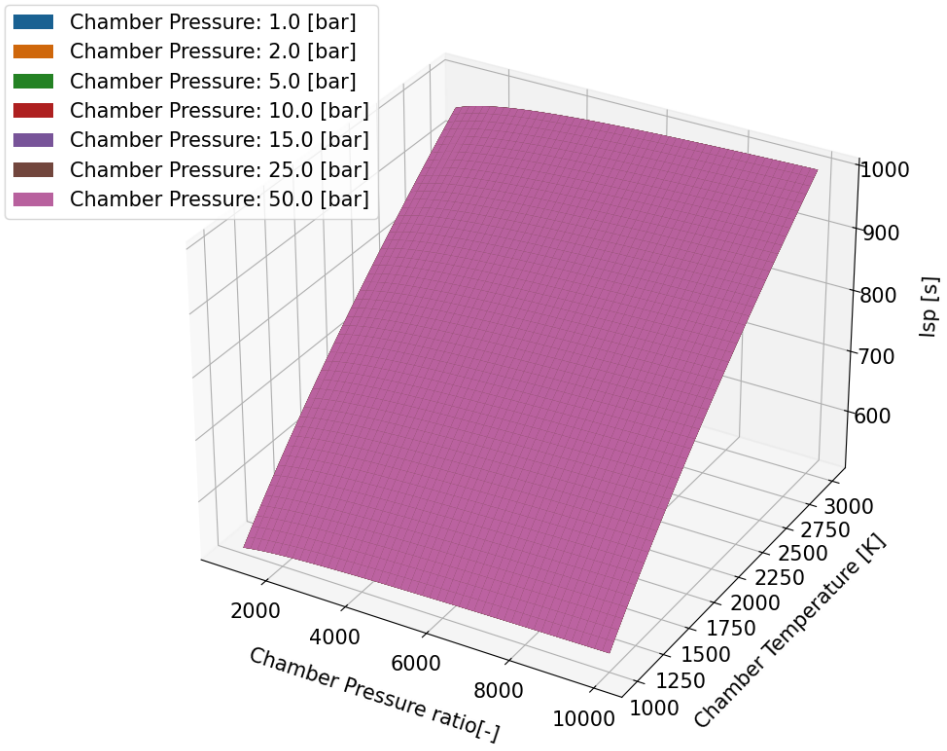

Figure 5.1: 3D surface plot showing Specific impulse (I_{sp}) over Chamber Temperature (T_c) and Chamber-Exit pressure ratio (P_c/P_e). For $1\ [N]$ of thruster at zero ambient pressure, using H_2 as propellant.

Analysing the mass flow, seen in Figure 5.2a, it can be seen that the mass flow decreases with increasing chamber temperature. The same is true for C/E pressure ratio, but to a much smaller extent. One peculiarity is that the mass flow is independent of chamber pressure. Even with chamber pressure, being in the equation for mass flow, this is explained by the fact that the thrust was held constant at $1\ [N]$. Taking a look at the power required, seen in Figure 5.2b, there is an increase in the power required with increasing chamber temperature. However, the opposite is true for C/E pressure ratio, with there being a slight decrease in power with increasing C/E pressure ratio. Again, chamber pressure is independent of power.

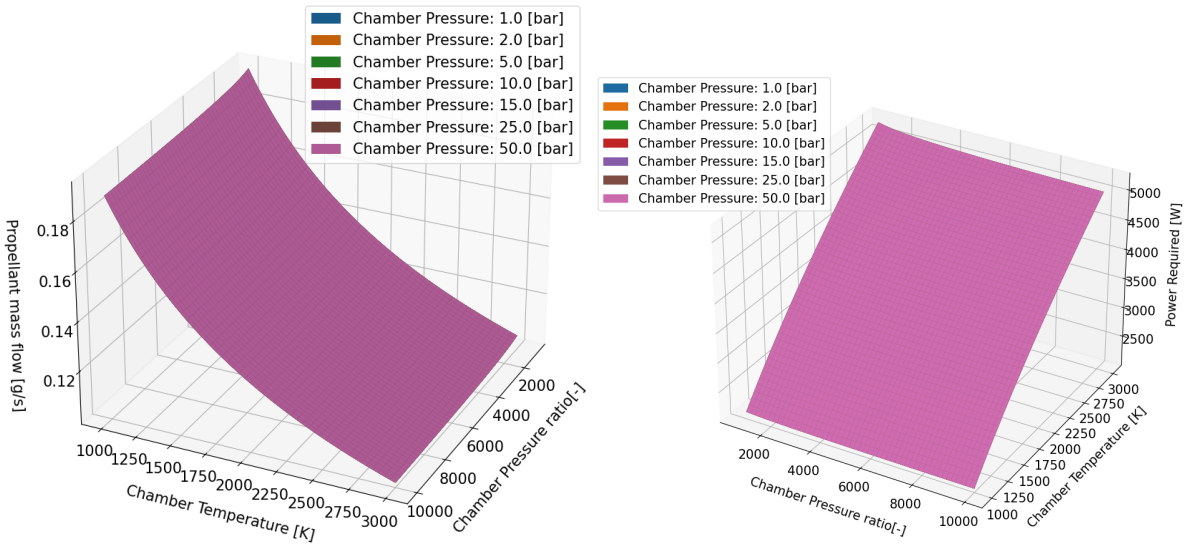

(a) 3D surface plot showing mass flow (m)

(b) 3D surface plot showing Power

Figure 5.2: Mass flow and Power plots over Chamber Temperature (T_c) and Chamber-Exit pressure ratio (P_c/P_e). For 1 $[N]$ of thruster at zero ambient pressure, using H_2 as propellant

Discussing the nozzle geometry, first with the area ratio seen in Figure 5.3, again, the chamber pressure is independent of the area ratio. At high C/E pressure ratios, there is a notable increase in the nozzle area ratio with increasing chamber temperature. This effect is much less prominent at low C/E pressure ratios. There is also a general increase in area ratio with increasing pressure ratio, which makes logical sense considering a longer and larger nozzle exit is required to expand the gas to the required C/E pressure ratio.

For the throat and exit diameters of the nozzle, seen in Figure 5.4, it stands out that they are both dependent on the chamber pressure. Taking a better look at the throat diameter, seen in Figure 5.4a, it's clear that there is little effect on the throat diameter from either chamber temperature or C/E pressure ratio, which is expected considering Equation 5.4. The exit diameter is much more sensitive to both a change in C/E pressure ratio and chamber temperature, especially at lower chamber pressures.

Concerning the dissociation of Hydrogen and the use of other propellants, the ones considered being Argon, Nitrogen and Helium, the data for which can be seen in Appendix C. There is a general decrease in specific impulse as expected with increasing molar mass of the exhaust gas, generally having a higher mass flow rate, and a lower power required than the use of Hydrogen. For the dissociation of the propellant, all other investigated propellants other than Hydrogen have a mass fraction of $< 1\%$ for the ionic form of the propellant, with Hydrogen having a mass fraction of about $< 10\%$, which causes the chamber pressure to no longer be independent of most variables, though this only occurs at the upper end of the chamber temperatures investigated.

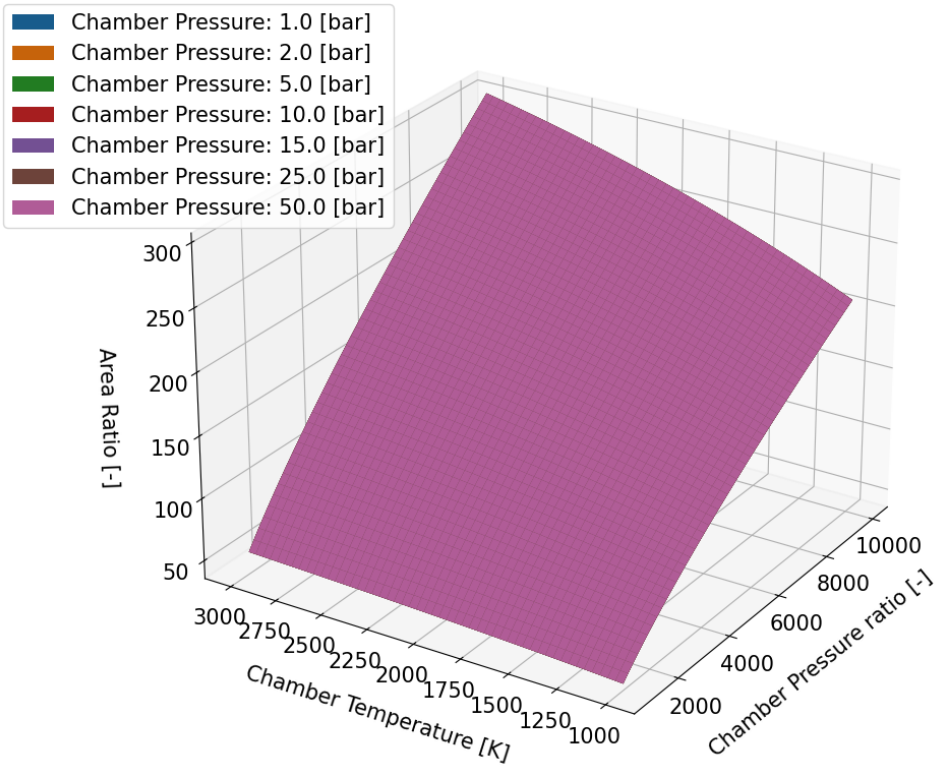

Figure 5.3: 3D surface plot showing nozzle Exit-Throat area ratio, over Chamber Temperature (T_c) and Chamber-Exit pressure ratio (P_c/P_e). For $1\ [N]$ of thruster at zero ambient pressure, using H_2 as propellant.

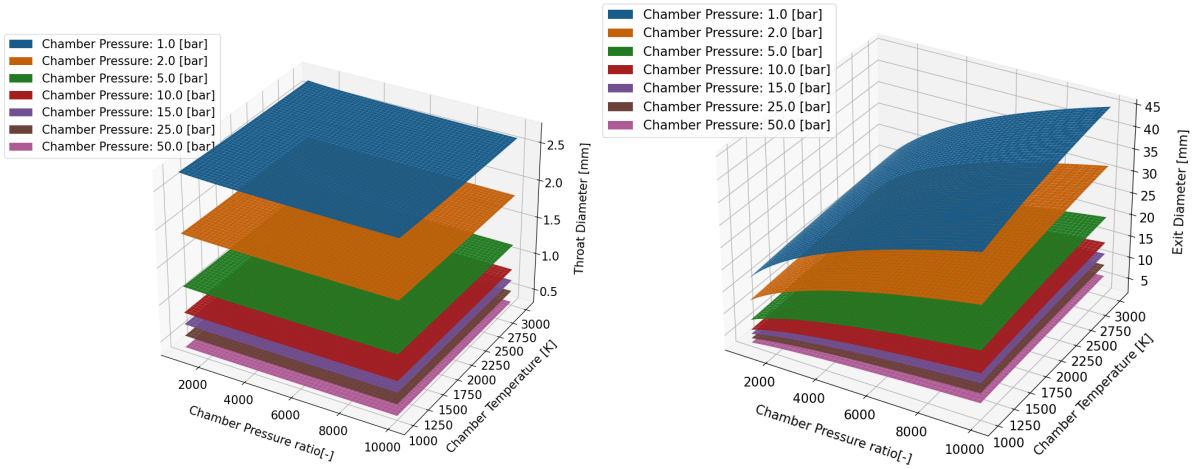

(a) 3D surface plot showing Throat Diameter (D_t)

(b) 3D surface plot showing Exit Diameter (D_e)

Figure 5.4: Throat and Exit Diameter plots over Chamber Temperature (T_c) and Chamber-Exit pressure ratio (P_c/P_e). For $1\ [N]$ of thruster at zero ambient pressure, using H_2 as propellant

5.2.2. Model Sensitivity Analysis

Before determining the sizing of the thruster, it would be wise to investigate the uncertainties present in the thruster sizing model. The model holds the thrust constant for the calculations, which provides an uncertainty in the sensitivity of the thrust to a change in the input parameters. Therefore, evaluating the thrust uncertainty of this thruster sizing model, changing the chamber temperature and pressure, and the chamber-exit pressure ratio, by $\pm 20\%$, the evaluation can be seen in Figure 5.5. It can be noted that the thrust is very sensitive to the pressure and much less sensitive to a change in both the chamber

temperature and the chamber-exit pressure ratio. With an increase in any of the input variables, the thrust of the system increases. Clearly, for the system to perform as expected, the chamber pressure has to be carefully controlled.

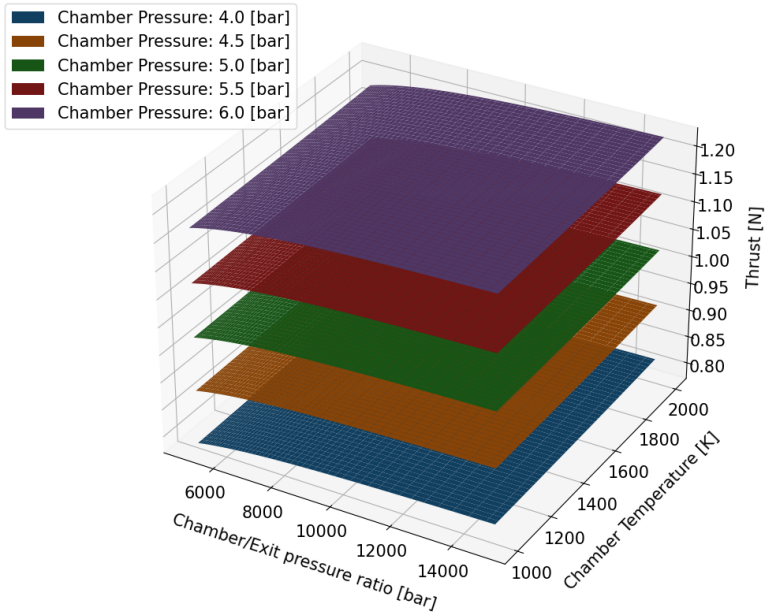

Figure 5.5: Thrust uncertainty analysis for the chosen thruster sizing

To better understand the uncertainties present in the models' implementation of ideal rocket theory, it would be helpful to evaluate the effects of each of the input parameters on the output of the model. This can be done with the implementation of a first-order sensitivity analysis, which statistically ranks the importance of each of the input parameters for the model outputs. Implementing the Python library SALib [55] to calculate the first-order sensitivities for each of the model outputs, the results of which can be seen in Figure 5.6. As dissociation was not implemented, the mass fraction is constant and thus is independent of the input parameters; this is not the case when considering dissociation, which can be seen in Appendix C. The first observation that can be made is that the specific impulse, the mass flow and the thermal power required are all close to solely dependent on the chamber temperature. This indicates that any uncertainty in the temperature of the incoming propellant will have a large effect on the efficiency of the system. The throat diameter is only dependent on the chamber pressure, or more accurately, the effects due to changes in chamber pressure are several orders of magnitude more influential than the other input parameters. The area ratio is highly dependent on the pressure ratio, as expected, with a small contribution from chamber temperature. The exit diameter is the only output parameter that is not highly dependent on just a single input, with the leading dependence being the chamber pressure, followed by the pressure ratio. Finally, it can be seen that the thrust is highly dependent on the chamber pressure.

It can be determined that uncertainties in the temperature of the incoming propellant could lead to large changes in the efficiency of the system. Where uncertainties in the incoming propellant pressure lead to greater uncertainties in the thrust produced by the thruster. Uncertainties in the pressure ratio of the thruster results in large changes to the area ratio and can somewhat affect the nozzle exit diameter.

Whilst difficult to evaluate, there have been several assumptions made using ideal rocket theory, the main being the simplification of the flow parameters. In a physical system, the flow will experience boundary layer effects and thermal loss to the environment, which will negatively impact the performance of the thruster both in terms of thrust and efficiency. Both the sensitivity of the model to uncertainties in the input parameters, as well as the effects caused by the assumption made, should be taken into account when deciding on the final sizing for the thruster.

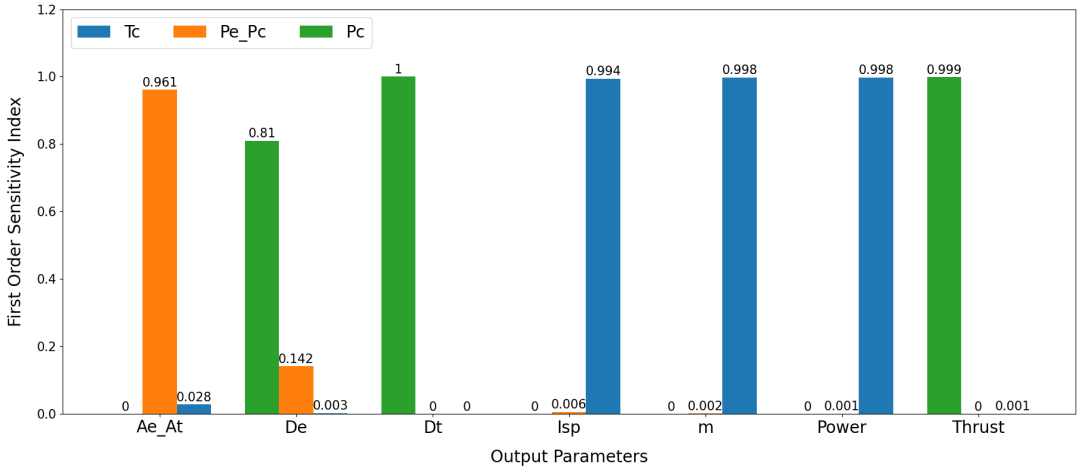

Figure 5.6: First Order sensitivity Analysis for the Thruster Sizing model

5.2.3. Thruster Sizing Discussion

Having calculated the results and knowing the requirements set by Green SPaW, the sizing can be chosen from the result set. Because of how the code was written, with thrust being constant at $1\ [N]$, any choice made for chamber pressure, chamber temperature or C/E pressure ratio will comply with requirement RCS-Sub-010. Requirement RCS-Sub-020 states that the system shall have a specific impulse of more than $500\ [s]$. When looking at Figure 5.1, a value of $1500\ [°K]$ provides a specific impulse range of $644.9\ [s]$ to $673.6\ [s]$. The Hydrogen provided may not be pure and may include water vapour; thus, it has been recommended to increase the requirement RCS-Sub-020 to $600\ [s]$ when considering the use of pure Hydrogen. Thus, the choice of $1500\ [°K]$ provides a safety margin to account for the increased molecular mass of the mixture and hence a reduction in exhaust velocity.

A value of $10,000$ was chosen for the /EC pressure ratio, with the I_{sp} range provided by choosing $1500\ [K]$ as the chamber temperature; the choice in pressure ratio was much more relaxed. Choosing $10,000$ allows for a buffer to the I_{sp} requirement, taking into account the inaccuracies and assumptions made when using ideal rocket theory to estimate thruster performance. This choice does provide a rather large value for the nozzle throat to exit area ratio, but still provides reasonable throat and exit dimensions.

For the choice in chamber pressure, $5\ [bar]$ was chosen, with no dissociation of the propellant; the chamber pressure is independent of most variables other than the nozzle throat and exit dimensions. $5\ [bar]$ provides a good size for the throat diameter at just above $1[mm]$ in size, as well as leading to a reasonable exit diameter of under $20\ [mm]$. Providing a good middle ground between manufacturability and total nozzle length. Choosing a reduced pressure is also preferable when considering the large changes in material properties with the chamber temperature being $1500\ [K]$. The full list of results for the chosen variables can be seen in Table 5.1.

Table 5.1: Table showing the results of the Ideal Rocket Theory analysis

Chamber Pressure		**Chamber Temperature**		**Chamber/Exit Pressure ratio**	
5 [bar]		1500 [K]		10,000 [-]	
Exit/Throat Area Ratio	**Nozzle Exit Diameter**	**Nozzle Throat Diameter**	**Specific Impulse**	**Mass Flow**	**Power Required**
$238.55[-]$	$18.28[mm]$	$1.18[mm]$	$673.60[s]$	$0.149[g \cdot s^{-1}]$	$2942.31[W]$

6

Heat Exchanger design

This chapter will discuss the initial sizing of the Heat Exchanger, developing the required sizing characteristics to heat the propellant to the target chamber temperature of $1500\ [K]$. First, it will go through the initial simulation used to calculate the possible configurations. Then, using the characteristics to develop the initial CAD model to be used in CFD simulation.

6.1. Initial Heat-Exchanger sizing

This section focuses on the design and sizing simulation for the heat exchanger, determining the effects on the propellant final temperature with changing heat-exchanger characteristics. First, explaining the reasoning behind the decisions made in the design of the code. Then, going on to explain the code and providing the results. Finally, extrapolating the required characteristics to develop a CAD prototype model to be used for CFD.

6.1.1. Heat Exchanger Sizing

The values of interest for the heat-exchanger sizing, needed to reach the required temperatures for the thruster, are as follows: the overall length of the heat-exchanger, the size and geometry of the propellant channels through the system, the number of channels and the pressure drop across the system. When inspecting the requirements for the Green SWaP project, the aim for the sizing of the heat-exchanger can be inferred to produce a highly efficient, accurate and reliable system, with the addition of reducing mass where possible, whilst still providing the target exit temperature and pressure, determined in the thruster sizing.

For the determination of the convective connection between the heat-exchanger wall and the fluid, a constant value was used for laminar flow, and the method suggested by J. R. McCarthy for turbulent flows, the determination of turbulent wall friction was given by A.R. Vatankhah. It was also chosen to numerically discretise the thermodynamic equation for heat transfer.

This adds to the set of assumptions made for the heat-exchanger sizing. The first being the use of a bulk fluid temperature and constant thermodynamic fluid properties over the fluid volume, care has to be taken to ensure that the channel diameter is small enough to adhere to this assumption. The second is the discretisation error introduced by the use of the numerical method; a small enough discretisation has to be used to minimise the error introduced. Another aspect is that only Convective heat transfer is considered between the wall and the bulk fluid; no radiative heat transfer is assumed. In practice, the contribution due to radiation is small. Finally, the wall temperature is held constant, which is the largest difference from reality, but was chosen to allow for a quicker determination of the heat-exchanger sizing.

6.1.2. Code Explanation

The code for the Heat-Exchanger sizing can be seen in section D.2. The code's main loop begins with the importation of the geometry profile for the channel, which can be either a straight channel or a helical channel. Whilst the straight channel is somewhat self-explanatory, the helix is defined through

its pitch, helix diameter and length of the helix. The helix is discretised into several smaller sections to allow for the calculation of the propellant temperature, a diagram of which can be seen in Figure 6.1.

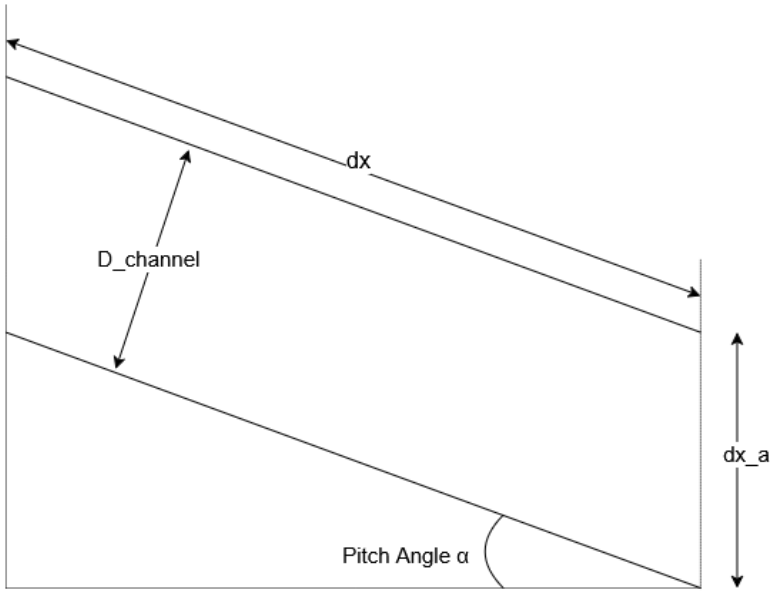

Figure 6.1: Diagram of the discretisation of the helical channels

From that, the initial values for fluid velocity, pressure and temperature can be input, as well as the initial thermodynamic properties of the propellant, needed for the calculation of the Reynolds and Prandtl dimensionless numbers. Again, the Cantera Python library was used for the determination of the thermodynamic properties of the propellant.

With the initial values, the discretisation can be conducted. Inside a loop, first, the Nusselt number is calculated, depending on the turbulence of the flow, described as a Reynolds number lower than 2300. For laminar flow, the Nusselt number is set to 3.66 and for turbulent flow Equation 6.1, a Nusselt equation design for the flow of Hydrogen through a pipe, [56]. Re and Pr are the Reynolds number and Prandtl number, respectively, with l being the total length of the helix, D is the diameter of the channel, T_w and T_b are the Wall and fluid bulk temperature, respectively. From the Nusselt number, the coefficient of convection can be calculated using Equation 6.2, where K_f is the thermal conductance of the propellant. The change in temperature over one discretisation can now be calculated using Equation 6.3. The final temperature of the propellant is then fed to the next iteration of the discretisation loop.

$$Nu = 0.045 \cdot Re^{0.8} \cdot Pr^{0.4} \cdot \left(\frac{l}{D}\right)^{-0.15} \cdot \left(\frac{T_w}{T_b}\right)^{-0.55} \tag{6.1}$$

$$h = \frac{k_f \cdot Nu}{D} \tag{6.2}$$

$$dT = \frac{h \cdot \pi \cdot D \cdot (T_w - T_b)}{m \cdot Cp} \cdot \frac{dx_a}{sin(\alpha)} \tag{6.3}$$

For the calculation of the drop in pressure due to friction, again done for each discretisation, the Darcy-Weisbach equation was used, Equation 6.4, where f_d is the friction coefficient. For the determination of the friction coefficient, the Vatankhah 2014 friction function was used, given in Equation 6.5 [57], providing an accurate and large range friction function for the turbulent Hydrogen flow through a pipe. The updated pressure is then given to the next discretisation iteration. Another aspect is the change in velocity, knowing the temperature and pressure, the change in velocity can be calculated using the equation for the conservation of mass flow $m = A \cdot \rho \cdot v$.

$$dP = f_d \cdot \frac{dx_a}{sin(\alpha) \cdot D} \cdot \frac{v^2 \cdot \rho}{2} \tag{6.4}$$

$$\begin{aligned} \delta &= \frac{6.0173}{Re \cdot (0.07(\epsilon/D) + Re^{-0.885})^{0.109}} + \frac{\epsilon/D}{3.71} \\ f_d &= \left(\frac{2.51/Re + 1.1513 \cdot \delta}{\delta - (\epsilon/D)/3.71 - 2.3026 \cdot \delta \cdot log(\delta)} \right)^2 \end{aligned} \tag{6.5}$$

With this simulation being a discretisation of the helix, it is important to determine the effect of the discretisation size on the results of the simulation. Figure 6.2 is a plot showing the final temperature of the heat-exchanger for different discretisation step sizes. Looking at the graph, it's clear that any discretisation step larger than $0.01\ [m]$ is not sufficient to determine the final temperature accurately. Choosing a discretisation value of $1 \cdot 10^{-4}\ [m]$, provided results within $\sim 0.2\ [°K]$ of the final temperature when compared to a step size of $1 \cdot 10^{-7}\ [m]$, whilst completing the simulation in much less time.

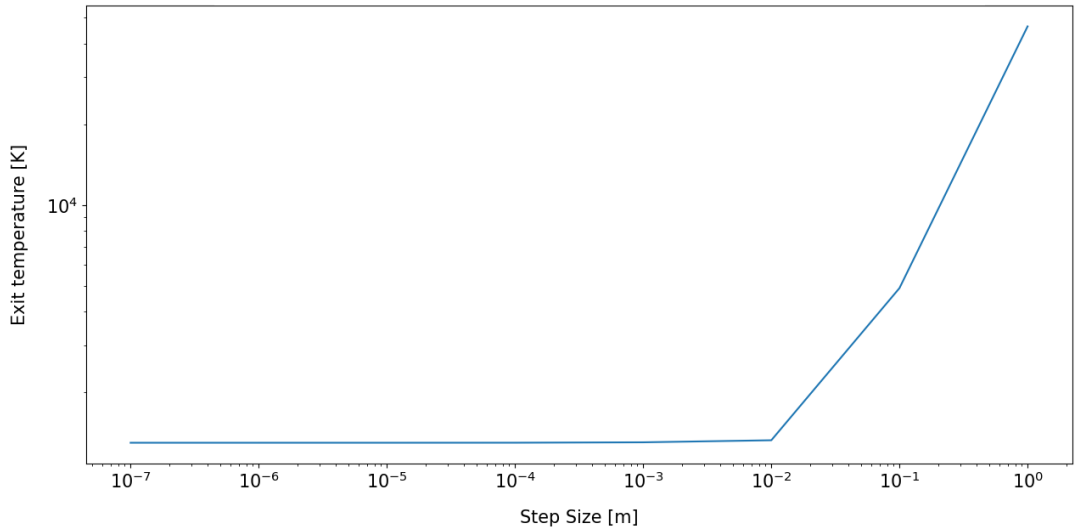

Figure 6.2: Sensitivity analysis for the Heat-Exchanger sizing Python simulation

6.1.3. Results

Having gathered the required data, the results can be analysed to allow for the determination of the most appropriate choice in Pitch, Helix Diameter, channel Diameter and the Number of individual channels. To avoid repetition, for all the graphs shown, the Input pressure and temperature are set at $5\ [bar]$ and $293\ [°K]$ respectively, as well as, where appropriate, the wall temperature, the helix diameter, helix pitch, number of channels and channel diameter where set to; $1700\ [°K]$, $15.5\ [mm]$, $8\ [mm]$, $3\ [-]$ and $1\ [mm]$ respectively. These may not be the best variables, but they allow for a valid result and the comparison between different graphs. For each of the graphs, the final exit temperature of the fluid is given, for a heat exchanger length of $20[mm]$ where appropriate.

First, investigating the Pitch, it makes logical sense that the smaller the pitch, the higher the final temperature of the propellant when leaving the heat exchanger, because of the increased path length the fluid is required to travel. This can also be seen in Figure 6.3. Another aspect to consider is the spacing between channels; if the pitch is too small, there may not be enough material to allow for the conduction of heat around the entire channel circumference, leading to a large reduction in the thermal energy transfer rate to the propellant.

Then, going on to investigate the effects due to a change in wall temperature, seen in Figure 6.4, it can be seen that there is a linear relationship between the wall temperature and the final fluid exit temperature. This makes logical sense when looking at Equation 6.3.

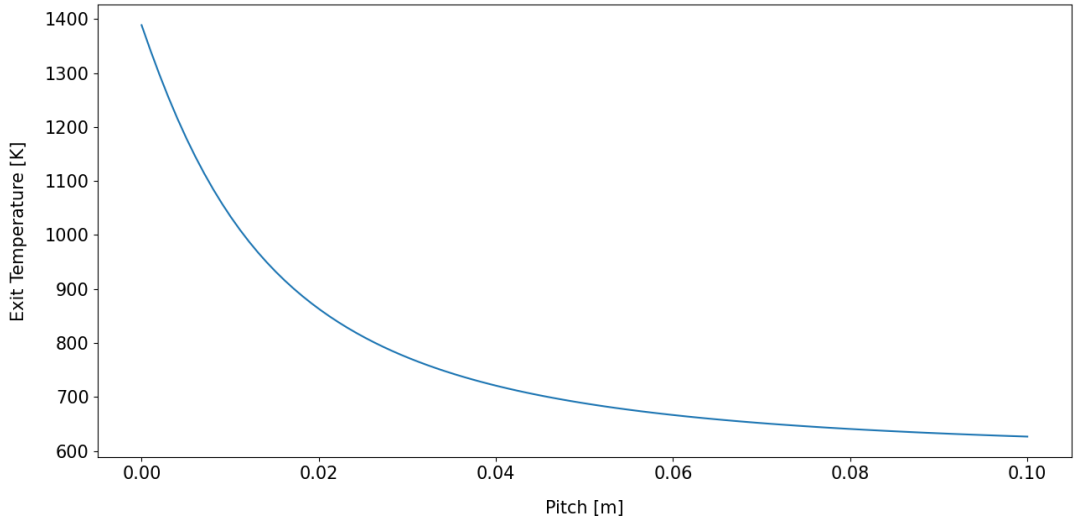

Figure 6.3: Heat Exchanger Sizing, sensitivity analysis on Pitch

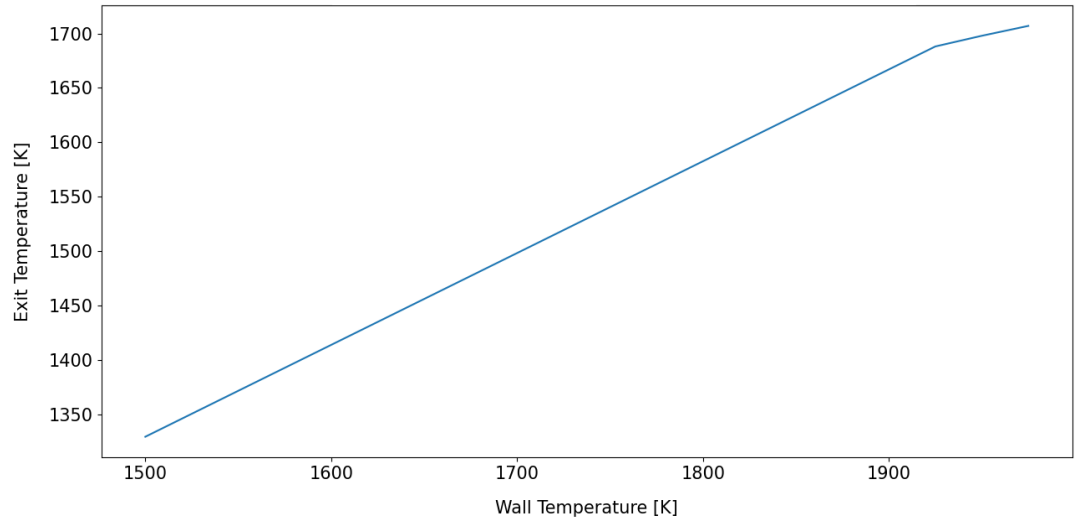

Figure 6.4: Heat Exchanger Sizing, sensitivity analysis on wall temperature

Investigating the effects of the number of channels on the final temperature, seen in Figure 6.5. These results were for a pitch of $8\ [mm]$. Generally, it's clear to see that an increasing number of channels would result in a higher exit temperature for the propellant. However, there is an increase in the exit temperature for a low number of channels. This is likely explained by the fact that at lower channel numbers, the flow is turbulent, leading to an increased rate of heat transfer between the heat-exchanger wall and the fluid. With a clear maximum at three channels. The fluid returns to laminar flow once the channel number exceeds $4-5\ [-]$, reducing the heat transfer rate and hence the exit temperature of the heat-exchanger. It is to be noted that this is a factor of both the velocity of the flow and the channel diameter; hence, the channel number at which the flow becomes laminar will change with channel diameter.

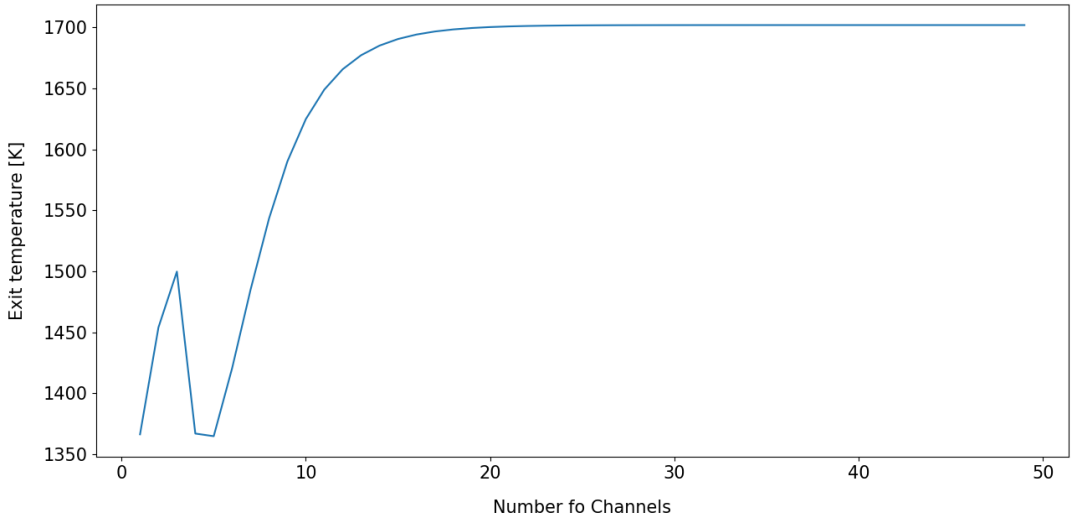

Figure 6.5: Heat Exchanger Sizing, sensitivity analysis on number of channels

Combining the pitch and channel number investigation into a contour gives Figure 6.6. Implementing a minimum distance between neighbouring channel walls to $1\ [mm]$, allowing for the conductive transfer of thermal energy around the channel circumference. The required temperature ($1500\ [°K]$) set by the Thruster sizing can be seen along the dashed line. Again, the increased exit temperature due to a turbulent flow can be seen at low channel numbers, and as described before, a reduction in the pitch leads to an increase in the exit temperature. It can also be seen that a helical geometry allows for a reduction in the heat-exchanger length, with the straighter channels, a pitch of $100\ [mm]$, more than 40 channels are required to reach the same performance.

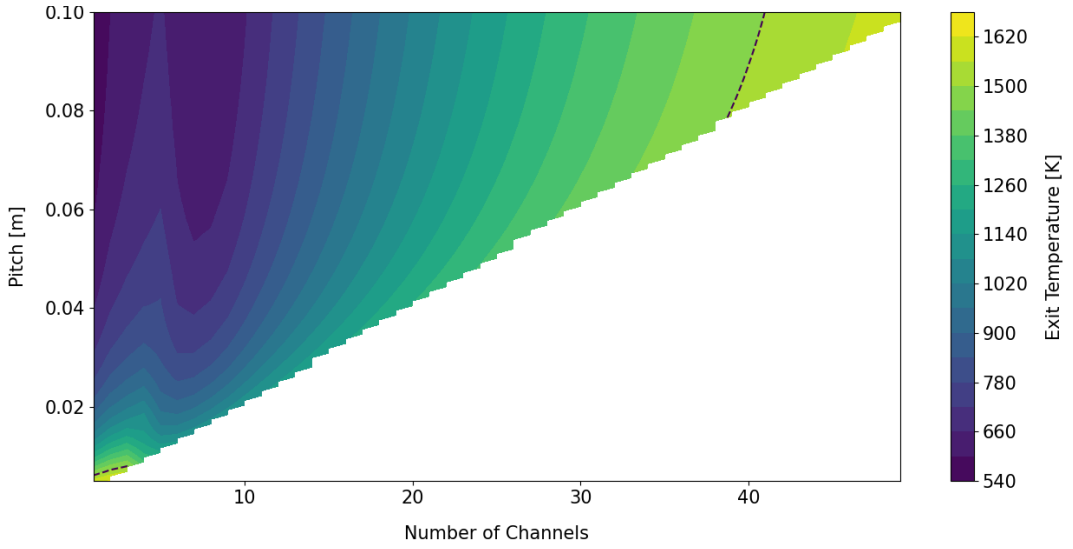

Figure 6.6: Heat Exchanger Sizing, Contour Plot evaluating pitch and number of channels

As expected, when looking at Figure 6.7 and Figure 6.8, an increase in the helix diameter or overall length of the heat-exchanger will result in a higher end temperature of the propellant. This is logical as both increase the overall length of the path taken by the propellant, whilst not affecting the Reynolds number, leading to flow changes.

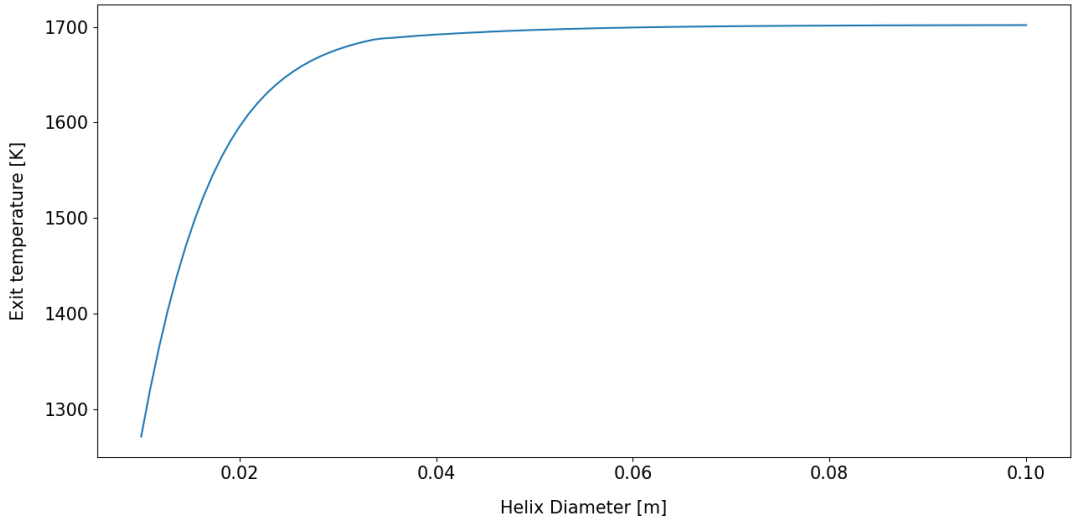

Figure 6.7: Heat Exchanger Sizing, sensitivity analysis on the helix diameter

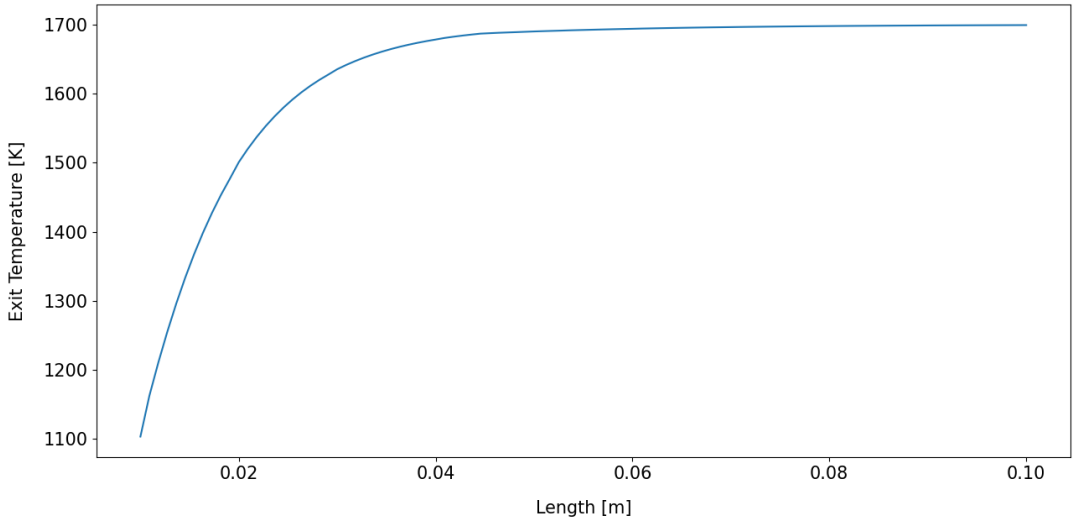

Figure 6.8: Heat Exchanger Sizing, sensitivity analysis on the heat exchanger length

Investigating the effects due to the channel diameter, looking at Figure 6.9 and Figure 6.11, it's clear that the channel diameter has an impact on the flow, with a general decrease in channel diameter leading to an increase in the exit temperature of the propellant. Figure 6.9 gives another good representation of the effects of turbulent flow, with the system having a linear decrease in exit temperature with increasing channel diameter until a channel diameter of $1.1\ [mm]$, where the flow changes from being turbulent to laminar. Leading to an increase in the rate of reduction in the exit temperature with increasing channel diameter, continuing on a nonlinear path, slowly levelling off.

With the reduction in the channel diameter, there is an increased risk of choked flow. For an ideal gas, this point is reached when the velocity of the gas exceeds the local speed of sound, producing a shock and hence a pressure reduction, fixing in place the mass flow rate. To determine if the flow is choked, Figure 6.10 shows the Mach number of the flow as it leaves the heat-exchanger. It can clearly be seen that at a diameter less than $0.535\ [mm]$ the flow is choked. However, this is far below the point at which the flow becomes turbulent, providing a lower bound for the channel diameter. With the match number being 0.265 with a channel diameter of $1\ [mm]$.

Figure 6.11 allowed for the verification of the channel diameter and pitch. When looking at Figure 6.11b, the target temperature is reached at a channel diameter of $0.995\ [mm]$ for a 3 channel system, with

Figure 6.11a providing a pitch of $8\ [mm]$ for that set channel diameter at the target exit temperature of the fluid.

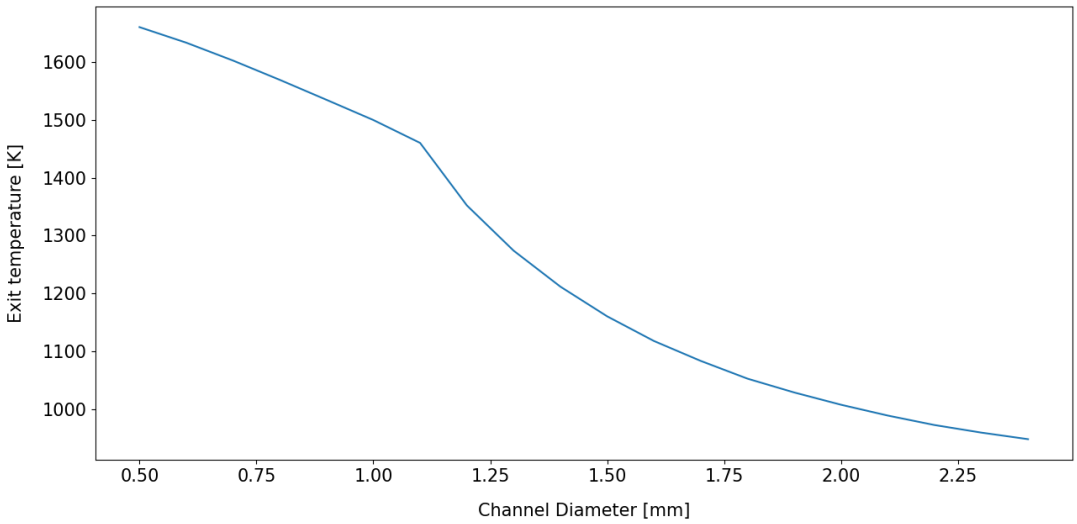

Figure 6.9: Heat Exchanger Sizing, analysis on the channel diameter

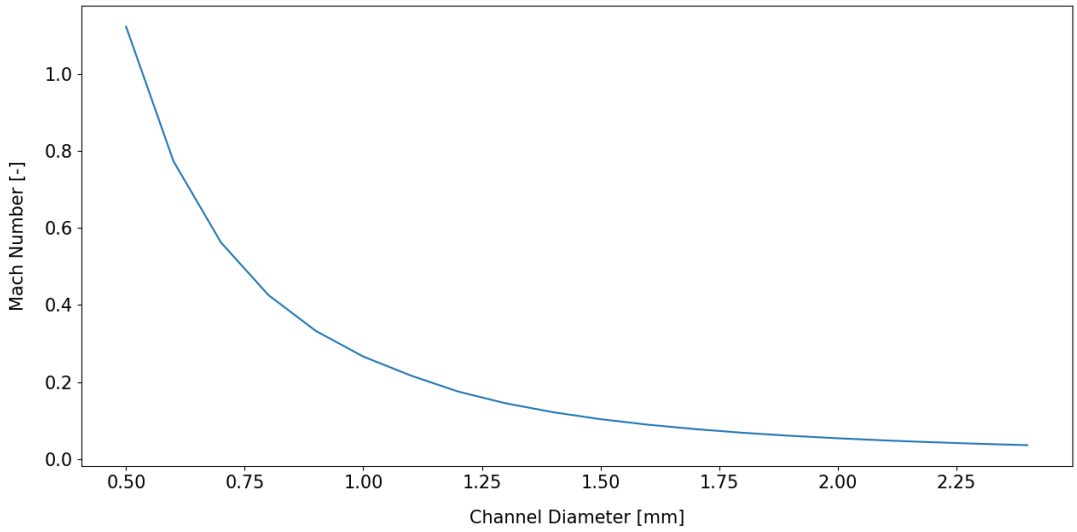

Figure 6.10: Heat Exchanger Sizing, analysis of choked flow for changing channel diameter

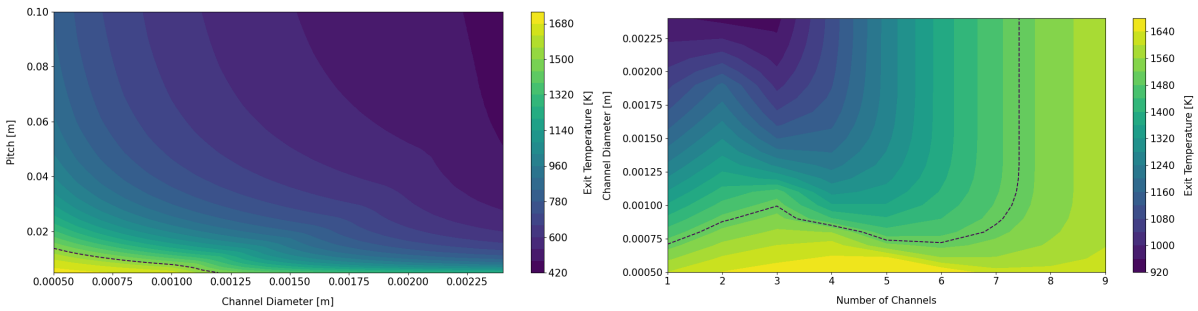

(a) Heat Exchanger Sizing, Contour plot evaluating Pitch and Channel diameter

(b) Heat Exchanger Sizing, Contour plot evaluating the number of channels and Channel diameter

Figure 6.11: Contour plots for the evaluation of the effects of a change in channel diameter

6.1.4. Heat-Exchanger Sizing Discussion

Having gone through the results of the heat-exchanger sizing investigation, some conclusions can be made about the sizing selection to be carried forward to the CAD designing phase; the chosen values can be seen in Table 6.1. Referring back to the aim of the sizing investigation, which is the creation of an efficient, accurate, reliable and low mass system, whilst still providing the required propellant exit temperature and pressure. When looking at the results, for both an efficient system and a low mass, the system size should be minimised, reducing the conductive path between the cavity and the propellant channels, and the overall volume of the system. Leading to a minimisation in the overall length and diameter of the heat-exchanger. Another aspect to consider is that the smaller the channel diameter, the faster the flow becomes, further decreasing the response time of the system. It is also clear from a minimisation perspective that the increase in convective transfer rate due to turbulent flow should be harnessed by limiting the number of channels and channel diameter, thus increasing the Reynolds number.

Figure 6.5 showed a clear indication of the number of channels that provide the maximal turbulence in the flow, in this case being $3\ [-]$ channels. This is confirmed by the Figure 6.6, from which the pitch of the helix can also be determined, with the lowest pitch possible being determined to yield the highest exit temperature. The pitch for the helix was set at $8\ [mm]$. For the sizing of the channel diameter, Figure 6.9 provides a clear upper limit of the channel diameter of $1.1\ [mm]$, thus choosing a channel diameter of $1\ [mm]$ as this is about the physical limit for cutting a channel with conventional machining methods. The height and width of the heat-exchanger were chosen to minimise the mass of the system whilst considering the dimensions of the cavity and the Thruster geometry, being set at $20\ [mm]$ and $15.5\ [mm]$ respectively. The wall temperature was set such that the target exit temperature is reached by the system. When looking at Figure 6.4, it's clear that for a $1500\ [^\circ K]$ exit temperature, a wall temperature of $1702\ [^\circ K]$ is required. Implementing these into a 3D rendition of the propellant temperature over the length of the heat-exchanger, seen in Figure 6.12, provides an exit temperature of $1498.7\ [^\circ K]$ for the heat-exchanger. Regarding the choice of these parameters, it must be noted that there are likely other combinations of sizing values that could provide similar results. When considering a change in the length and diameter of the system, ensuring the same thermal exchange area. For example, the extension of the length would require a reduction in the channel diameter to maintain the same exchange area, which leads to an increase in the Reynolds number, which in turn results in a higher convective transfer rate. The Reynolds number is inversely proportional to the channel diameter for a constant mass flow, which can be observed when looking at Figure 6.9.

Table 6.1: Table showing the chosen heat-exchanger sizing values

Value	Heat-Exchanger Sizing Parameters						
	Length $[mm]$	**Helix Diameter** $[mm]$	**Helix Pitch** $[mm]$	**Number of Channels** $[-]$	**Channel Diameter** $[mm]$	**Channel Wall Temperature** $[^\circ K]$	**Fluid Exit Temperature** $[^\circ K]$
	20	15.5	8	3	1.0	1702	1498.7

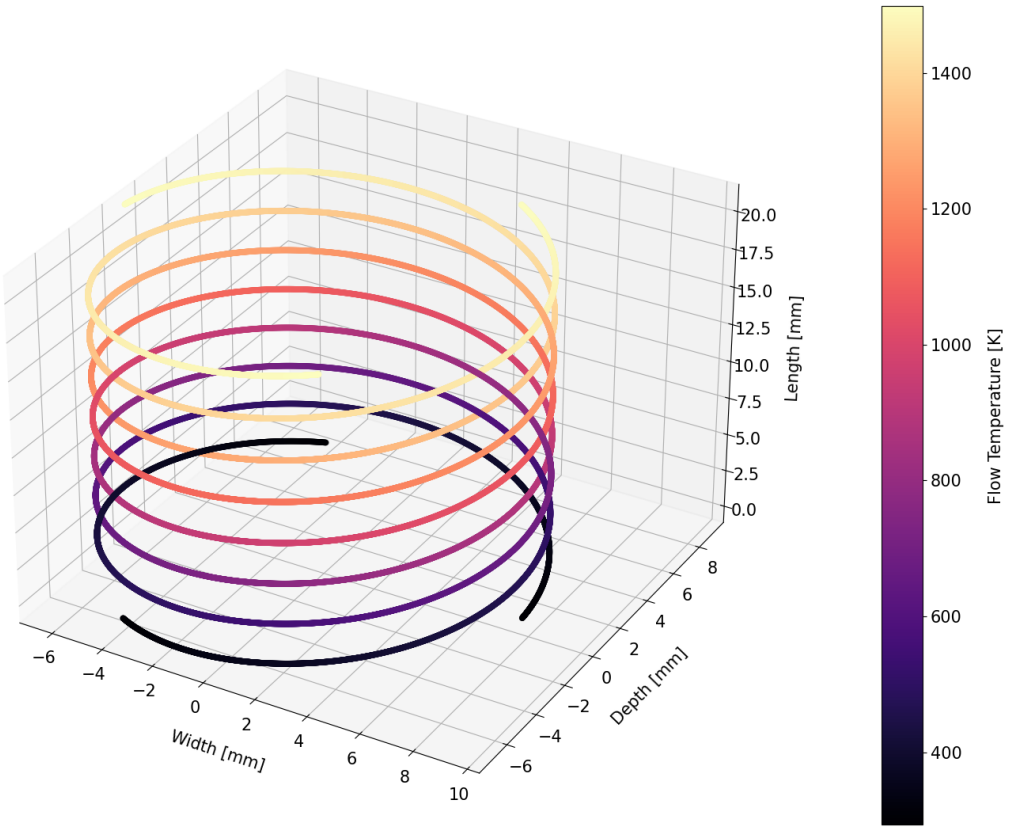

Figure 6.12: 3D illustration of the propellant temperature through the heat-exchanger for a three-channel system

6.2. Determination of the Cavity Design

The cavity is responsible for absorbing the incoming solar radiation, producing thermal energy to drive the thruster. Thus, care must be taken when designing the cavity to reduce the energy lost from the system. In this section, several cavity geometries will be evaluated, first presenting the different designs. Then, a ray-tracing analysis will be conducted to evaluate the luminosity distribution over the cavity surface, allowing for the evaluation of different cavity geometries. Then, providing a quick closing remark on the design of the cavity.

6.2.1. Cavity Design Testing

For the design of the Cavity, there must be a smooth and even heating along the cavity's length to reduce the chances of hotspots, which could melt or negatively affect the thruster materials. Preventing cold spots is also important for the performance of the heat-exchanger, as any spot colder than the surrounding fluid would extract heat from the flow rather than transferring heat to the flow. The other aspect is to reduce the amount of backscattering, rays that reflect back through the input optical guide, reducing the total energy absorbed by the system, and potentially impacting the functionality of the optical system.

Therefore, two aspects were considered to be investigated, these being the aspect ratio of the cavity, length vs. cavity diameter, and the internal geometry. The aim is to determine which geometry provides the most even luminance over the cavity surface, whilst allowing the least amount of rays to escape back through the optical guide. All the designs share some common features, these being a $5\ [mm]$ entrance hole for the optical guide, as well as the maximum diameter of the cavity being set $25\ [mm]$, with a minimal diameter being set at $1\ [mm]$. This was done to remove the points which lead to a reduction in simulation speed and increased error. The minimum diameter was reduced as much as possible without causing serious simulation error.

To evaluate the effects of the aspect ratio on the luminance of the cavity, a simple cylinder was chosen for the analysis, which allows for better isolation of the effects due to the aspect ratio chosen. As stated, each cylinder has a diameter of $25\ [mm]$, with three different aspect ratios being chosen, these being $1:5.9,\ 1:2.8,\ 1:1.3$ regarding the cavity diameter vs. length. A cross-section of the cylinders can be seen in Figure 6.13.

Four more designs are evaluated to determine the effects of the profile on the gradient of the luminance across the surface of the cavity. The first of which is the spherically capped cylinder, placing a half sphere at the end of the cavity to reduce the amount of reflected rays escaping through the optical guide, potentially leading to more internal reflections. The next design is a Cone, with its continuously sloped sides. The desired effect is to stop any ray from moving back towards the optical guide, however, this could potentially lead to a hot spot at the spike of the cone. The third design is a diverging-converging cone, aiming to have similar retention properties as the cone, whilst producing less of a hot spot at the end of the cavity. The final design is a combination of the diverging-converging cone and the cylinder, placing a cylinder between the end of the diverging section and the start of the converging section, potentially providing the best of both worlds with good, even luminance across the surface with minimal backscattering.

For the ray-tracing simulation, Ansys Speos was used, a complex optical simulation tool capable of determining the properties of a light ray through a variety of scenarios. For this simulation, it was chosen to do a direct simulation from source to sensor, to evaluate the luminance over the different geometries. For the optical properties of the bodies, it was chosen to use an emissivity of 0.425 [58], which is the observed emissivity of Rhenium at $2115\ [°C]$ for a wavelength of $500\ [nm]$, close to the wavelength of peak solar radiance. To simulate the properties of the Sun, the source was set to a blackbody with a surface temperature of $5800\ [°K]$, outputting a power of $3000\ [W]$ and $1000\ [W]$. A symmetric Gaussian distribution was chosen to simulate the expected distribution from an optical guide; the first standard deviation is set at $30°$ with a maximum angle of $180°$. An irradiance sensor was placed along the internal surface of each cavity, with another irradiance sensing plane placed $50[mm]$ from the optical guide opening to capture any backscattering.

The mesh for the calculations was generated by Speos following the recommended best practice by Ansys [59], with a proportional to face meshing sag value of 5000, a step size of 1000 and a meshing angle of $12°$. The simulation simulated a total of $1 \cdot 10^9$ rays, with an LPF max path length of $1 \cdot 10^6$. With the combined meshing and simulation of the system taking about one hour, with a simulation error rate of 0.078%.

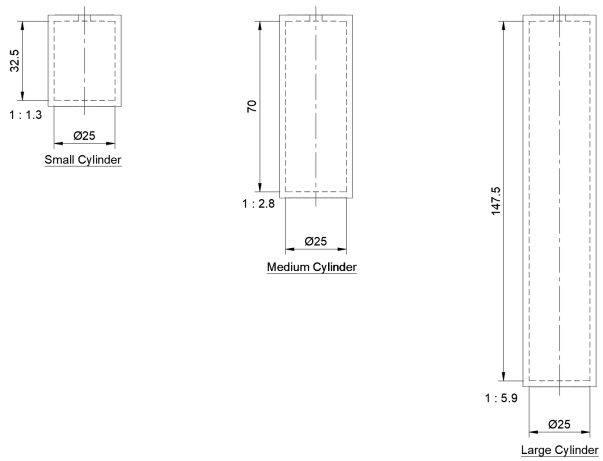

Figure 6.13: Diagram showing the cross-sections of the three cylindrical cavities, left to right being the Small, Medium and Large Cylinder. All measurements are given in $[mm]$

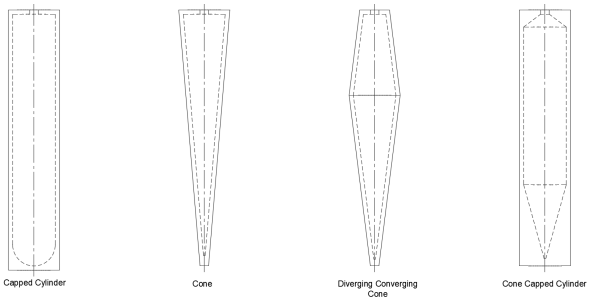

Figure 6.14: Diagram showing the cross-sections of the four different geometries, left to right being the Spherically Capped Cylinder, Cone, Converging Diverging Cone and Cone Capped Cylinder. All measurements are given in $[mm]$

6.2.2. Ray-Tracing Results

Analysing the results by evaluating the irradiance over the internal surface of the different cavities, as well as evaluating the backscattering captured by the sensing plane placed behind the source. Because of some of the geometry, there is a very large gradient in the luminosity, with large spikes directly across the optical guide input. The decision has been made to reduce the maximum luminosity shown in some of the figures to better illustrate the luminosity across the length of the cavity. Any value above the cut-off point is coloured white, with the value clearly being shown in the caption; the raw data can be seen in Appendix C.

Before continuing to the analysis of the results, it may be wise to better define what is meant by a smooth luminosity gradient and backscattering. For the smoothness of the luminosity gradient, it can be subjectively interpreted when looking at the luminosity across the cavity surface. However, to quantify what is meant, ideally, a constant luminosity is observed over the entire cavity surface, resulting in a luminosity gradient of zero. This is not possible when considering a single point source and a non-spherical cavity, meaning that a luminosity gradient will be present. To better illustrate the point, take a linear reduction in luminosity along the cavity surface, which would result in a constant luminosity gradient along the cavity surface, where the best-performing cavity would have the lowest gradient, indicating a smooth transition between points of high and low luminosity. Whilst a linear reduction in luminosity is not expected, resulting in a non-constant luminosity gradient, the cavity with the smallest difference between the highest and lowest gradients or the smoothest luminosity gradient would be considered best. The backscattering can be defined as the amount of rays that reflect off the cavity surface and return through the optical guide, being lost to the environment and not contributing to the heating of the cavity surface. Quantifying the backscattering can be done by either measuring the total power that leaves the cavity through the optical guide or as a proportion of the total input power supplied through the optical guide. Whilst the luminosity can be transferred into a heat flux, this is highly dependent on both the wavelength of the incoming rays and the emissivity of the material, which in turn is dependent on material type, surface finish and temperature. Because of this, the luminosity was not converted to heat flux.

Analysing the effects due to a change in the aspect ratio of the cavity, the three flat-ended cylinders can be seen in Figure 6.15. Comparing the three, it's clear that a change in the aspect ratio affects the distribution of luminosity over the cavity, with the small cylinder having the largest gradient in luminosity over the cavity length, with the largest seeming to have the smoothest. The maximum luminosity can be found at the centre of the end plate for each cylinder, with the values being provided in Table 6.2. The medium cylinder has the largest illuminance of the three; this is probably because the length of the medium cylinder favours the distribution of the incoming solar rays, leading to more reflection towards the centre point of the end plate. Where the small cylinder does not allow enough distance for the reflections to fully develop before impacting the end plate, the longer cylinder allows for more reflections to happen, reducing the intensity of the ray as they travel down the cavity. A glimpse into the backscattering can be seen from Figure 6.15 as well, with the Figure 6.15c having a clear reduction in illumination near the entrance to the cavity. This can be further motivated when investigating Figure 6.20, where it can be seen that the small cylinder has the highest amount of backscattering, with the medium and large cylinders having reduced backscattering. It can also clearly be seen that the simple geometry of a flat-faced cylinder massively increases the backscattering when compared to even just the large

cylinder with the addition of a spherical end cap (the Capped Cylinder).

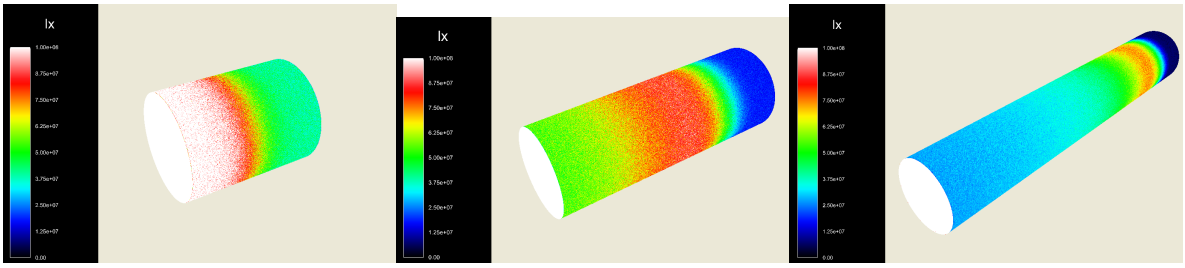

(a) Small Cylinder AR $1:1.3$ **(b)** Medium Cylinder AR $1:2.8$ **(c)** Large Cylinder AR $1:5.9$

Figure 6.15: Irradiance [lx] map over three cylinders of different aspect ratios, maximum luminosity capped to $1 \cdot 10^8$ $[lx]$.

For the effects do to the differing geometries, continuing with the analysis of the backscattering, it's clear that the change to the geometry radically reduces backscattering, when compared to a flat end cap, with the longer cone geometry having the smallest amount of backscattering, as expected, with the diverging-converging cone having slightly more backscattering. This is likely due to the closing taper trapping the incoming rays, directing the reflections towards the point of the cone, and reducing the chance of rays coming back through the optical guide. The Spherically Capped Cylinder and the Cone-Capped cylinder both performed well, still a significant reduction when compared to the flat end plate, but having a notable increase when compared to the Cone and the diverging-converging cone.

Table 6.2: Table showing the maximum illumination of the different cavity designs

Maximum Illuminance $[lx]$						
Small Cylinder	**Medium Cylinder**	**Large Cylinder**	**Capped Cylinder**	**Cone**	**Diverging-Converging Cone**	**Cone Capped Cylinder**
$5.28 \cdot 10^9$	$7.76 \cdot 10^9$	$1.41 \cdot 10^9$	$6.59 \cdot 10^9$	$1.58 \cdot 10^{10}$	$3.37 \cdot 10^{10}$	$3.07 \cdot 10^{10}$

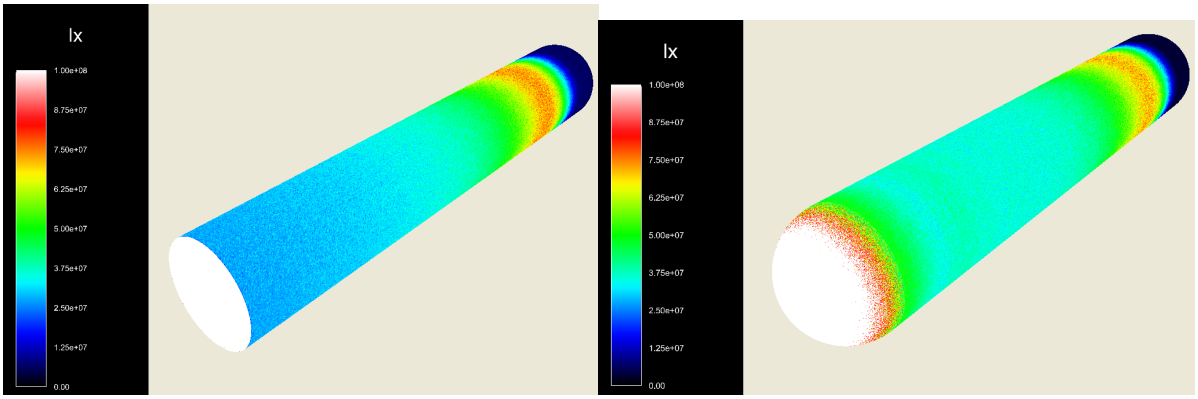

(a) Large Cylinder AR $1:5.9$ **(b)** Capped Cylinder

Figure 6.16: Irradiance [lx] map over the large cylinder and the capped cylinder, maximum luminosity capped to $1 \cdot 10^8$ $[lx]$.

Comparing the illuminance over the different cavity geometries, first comparing the large cylinder with the capped cylinder Figure 6.16, it's clear that the inclusion of the spherical end cap has caused the luminance over the length of the cavity to be more uniformly spread. This is likely due to the spherical end cap increasing the distribution of possible incident angles, leading to a greater spread of reflected rays, concentrating more reflections towards the end of the cavity. When analysing the other geometries, seen in Figure 6.17, the effect of the taper angle of the cone can clearly be seen, with the reduction

in the taper angle leading to an increase in the illumination over the cone. The implementation of the cone seems to have to opposite effect to a spherical end cap, leading to the concentration of rays rather than a more even distribution of reflected rays. However, when looking at the maximum illumination of the cavity, again seen at the end of the cavity for all geometries, there is an increase in the maximum illumination of the cavity for the more complex geometries. This makes logical sense of the cone-shaped geometries, showing that this geometry does, in fact, concentrate the rays towards the point. The spherical-capped cylinder also has a notable increase when compared to the large cylinder, indicating that whilst the spherical end cap does also cause a focusing of the rays to the centre of the end cap. This is further reinforced when looking at the size of the hot spot in the raw data.

The illuminance over the length of the cone-capped cylinder is comparable to the Large cylinder, with the cone end cap having a similar effect of not reflecting rays onto the cylindrical side wall as observed with the spherical-capped cylinder, leading to a reduction in the overall even illuminance of the cavity. For the Cone and the Diverging Converging cone, the reduction cap was increased to $1{\cdot}10^9$ to better understand the distribution over the cone. The cone has a much more even distribution over the cone length, but has a more concentrated hot spot at the point of the cone, than that of the Diverging-Converging cone.

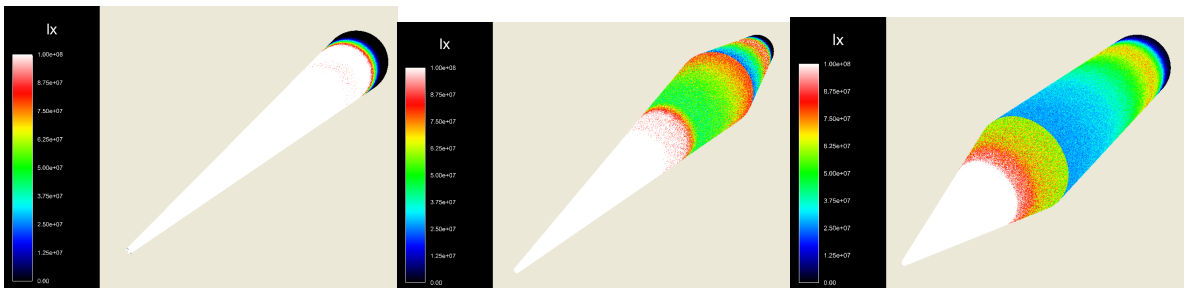

(a) Cone **(b)** Diverging-Converging Cone **(c)** Cone Capped Cylinder

Figure 6.17: Irradiance [lx] map over the Cone, the Diverging-Converging Cone and the Cone Capped Cylinder, maximum luminosity capped to $1 \cdot 10^8$ $[lx]$.

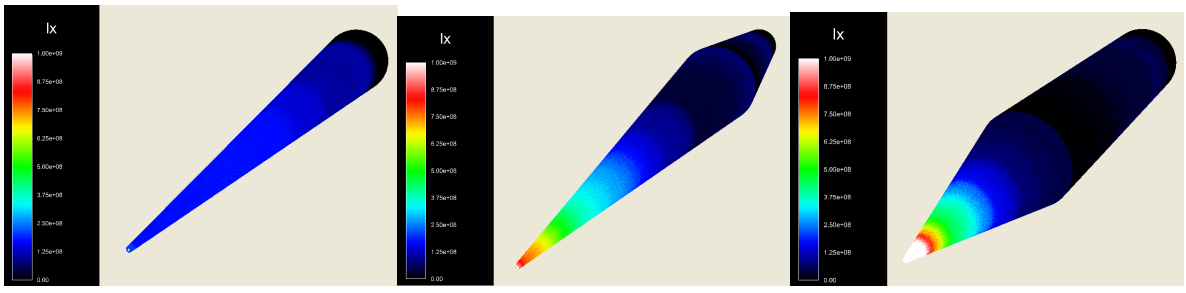

(a) Cone **(b)** Diverging-Converging Cone **(c)** Cone Capped Cylinder

Figure 6.18: Irradiance [lx] map over the Cone, the Diverging-Converging Cone and the Cone Capped Cylinder, maximum luminosity capped to $1 \cdot 10^9$ $[lx]$.

To provide a more quantified view of luminosity over the length of the different cavities, it was chosen to sample the luminosity along the cavity length, the results of which can be seen in Figure 6.19a. Using a spline to extrapolate between the samples allows for the calculation of the gradient, seen in Figure 6.19b. The use of a spline to extrapolate between the samples does introduce error into the measurements; however, a spline is a relatively good approximation, with a low implementation complexity. As explained previously, ideally, the luminosity across the length of the cavity is constant, resulting in a gradient of zero. As observed in the irradiance maps for the small, medium and large cylinders, they are relatively smooth, with the smoothness increasing with increasing cavity length, which is clear by the reduction in the difference between the maximum and minimum luminosity values. When looking at the gradient of the luminosity for the three cylinders, once again, the large cylinder performs best with the gradient being close to zero throughout the cavity length, with the others deviating further from

the ideal gradient. Investigating the more complex cavity geometries, it's clear that because of the cone shape, the Cone, Divergent-Convergent Cone and Cone Capped Cylinder all have very large differences between the maximum and minimum luminosity values along the cavity length. This results in very large gradients and deviations from the ideal, for the Divergent-Convergent Cone and Cone Capped Cylinder. However, luminosity increases over the length of the cone seems to be linear, resulting in a quite constant gradient value for the cone, though not at zero. The Spherically Capped cylinder performs well, arguably better than the large cylinder, where the luminosity is relatively constant over the length of the cavity. and the gradient again deviates little from the ideal gradient over the length of the cavity. When considering the backscattering observed with the use of the large cylinder, the use of a spherical capped cylinder provides the best cavity geometry. Though it should be noted that the values taken were along the sides of the cavity, meaning that the extreme luminosity values noted at the end faces of the cavity were excluded.

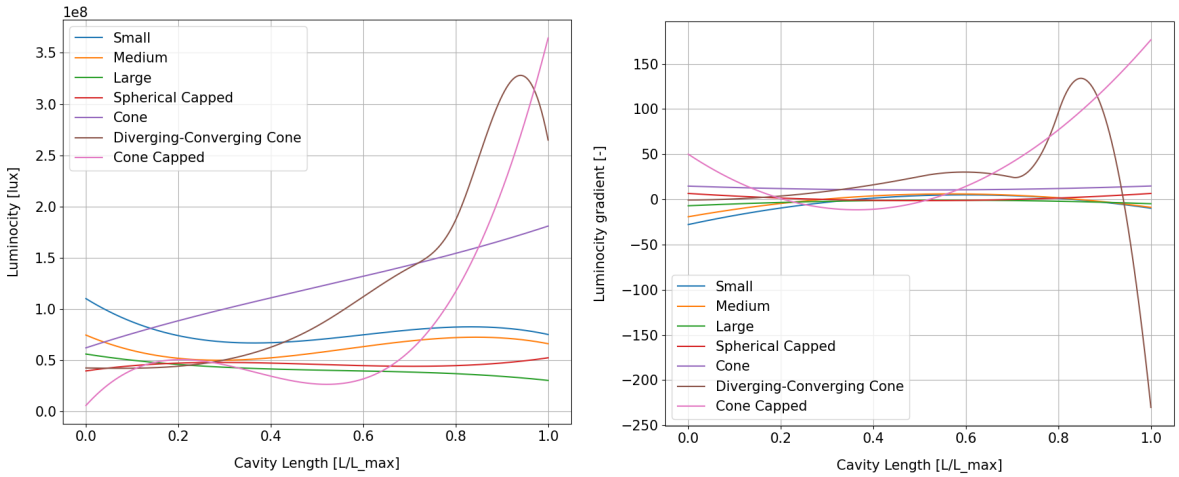

(a) Graph showing the luminosity over the length of the cavity

(b) Graph showing the luminosity gradient over the length of the cavity

Figure 6.19: Graph showing the values of the luminosity and gradient over the length of the cavity

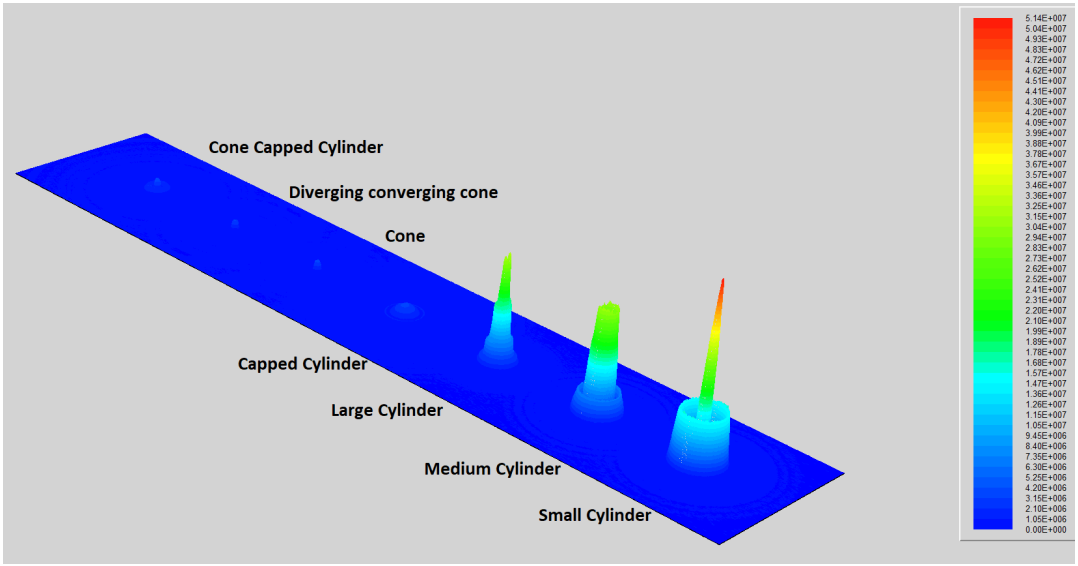

Figure 6.20: 3D illuminance graph of the backscattering measured in [lx]

6.2.3. Cavity Closing Remarks

For the cavity design choice going forward, the spherical capped cylinder was chosen, with it having the most even illumination over the length of the cavity, as well as having one of the lowest maximum

illuminance. Regarding the backscattering, the spherical capped cylinder performed well, with only a small percentage of rays returning to the source. Depending on how sensitive the inputting optical system is to backscattering, this may be acceptable. With this cavity choice, providing the most even thermal loading on the propellant moving through the heat exchanger, leading to a reliable and effective thruster design.

Other aspects to consider, whilst the material selected for the cavity wall was Rhenium, which is excellent at withstanding high temperature and the penetrating effects of Hydrogen, it does have a relatively low emissivity. Further investigation into the use of a different material with a higher emissivity across the solar spectrum could be investigated. The cavity could also be designed such that it does not directly interact with the propellant and instead can be removed and replaced to allow for the testing of a variety of materials or coatings. One Aspect this simulation does not take into account is the conductive path from the cavity's inner surface to the propellant flowing through the heat exchanger. It is possible that for the cone, because of the increased distance to the propellant channels as the cone moves towards its point (if they do not follow the contour of the cavity), the temperature at the propellant channels may be more evenly spread than the illumination simulation may suggest. This would have to be further investigated using steady-state and transient thermal simulations, incorporating the luminosity data generated.

6.3. Material Choice

For the design of an STP System, the material choice is an important decision to make, with the extreme temperatures needed and the reactivity of the Hydrogen propellant. With that being said, this section will focus on the material selection for the different material properties required of the system. First, going through what materials to consider for use in the central heat-exchanger and thruster, then discussing potential materials/coatings for the cavity walls.

6.3.1. Thruster & Heat-Exchanger Material Selection

For the thruster and heat-exchanger, the material choice becomes quite limited with very high requirements set by the basic functions of an STP design. With the material required to withstand extreme temperatures in excess of $2000\ [^{\circ}K]$, and the penetration and reactivity of the high-pressure high-temperature Hydrogen gas, whilst still performing the required functions of a thruster. Thus, the desired material properties for the Thruster and heat-exchanger are: a High-temperature tolerance with ideally a melting point above $2500\ [^{\circ}K]$ to reduce the likelihood of the thruster material weakening or melting during use. A high thermal conductivity means the system can operate at a lower temperature difference between the cavity and propellant channel walls, thereby reducing the maximum required operating temperature, as well as a high chemical resistance to Hydrogen or any other propellant used, and resistance to Hydrogen from penetrating the material. Other material properties to consider are a relatively high specific heat capacity, whilst this will increase the start-up time to reach operating temperature, it will allow for a longer firing and a relatively low coefficient of thermal expansion to reduce the changing geometry in the small channels inside the heat-exchanger and the throat, though this can be mitigated with knowledge of operating temperatures. One final aspect to consider is as with all space systems, the mass of the system should be taken into consideration.

With the high temperature requirements, there are not many materials that could withstand these temperatures, mostly leaving high temperature ceramics and metals. For the use of ceramics, referring back to subsection 2.5.2, the use of ceramics can be done as explained by F.G. Kennedy [38], but there are many limitations to their use, mostly concerning their direct contact with Hydrogen, which was also avoided by F.G. Kennedy, because of their inability to stop Hydrogen from penetrating the material lattice, when compared to metals, which tend to have a less porous structure. Another aspect is the difficulty in bonding ceramic parts together that are capable of withstanding high temperatures without failure. With the current techniques being either metallic brazing or hot pressing of the ceramics, with hot pressing being the only realistic option, as the brazed metal will simply melt away. There have been some advances in the bonding of ceramics, which may resolve the bonding issue surrounding ceramics. Concerning the relatively low thermal conductivity and high specific heat of ceramics, compared to the high-temperature metals. This causes the system to require more time to reach an operating temperature and increases the temperature difference across the system. This reduces the system's

maximum input power capabilities, as the melting temperature of the ceramic may be reached before the target channel temperature is achieved. This goes against the aim of the project to provide an accurate and quickly responding system. For these reasons, and the concerns around the manufacturing and durability of ceramic parts on this scale, it was chosen not to use ceramics in the design of this system. This leaves the high-temperature metals; a summary of the relevant material properties can be seen in Table 6.3.

When analysing the table, some metals stick out, the first being Hafnium [Hf], which performs terribly when compared to the others, having the lowest melting point and thermal conductivity, with its only redeeming factor being a relatively low coefficient of thermal expansion. Tungsten [W] is an obvious consideration, with it having the highest melting point of any metal, whilst also having a compatible, favourable thermal conductivity and coefficient of thermal expansion; however, it is also extremely dense, and one of the hardest metals, making it difficult to machine. Because of this, Rhenium [Re] is often considered instead for a high-temperature STP system, with it having the second-highest melting point and being about half the hardness of Tungsten, making it much easier to machine, though Rhenium does fall behind in most other aspects. Rhenium does have one catastrophic failure point where the metal oxidises in air at $700\ [^{\circ}C]$ to Re_2O_7, which has a melting point of $360\ [^{\circ}C]$, requiring an oxygen-free environment. Iridium [Ir] is one of the best contenders for an STP system that runs at lower temperatures, with it having some of the most promising properties other than its density. However, Iridium is also one of the most expensive metals, currently valued more than gold, making the manufacture of the engine exorbitantly expensive in material costs alone. The most suitable metal from the table below would be Molybdenum [Mo], with it having a relatively high thermal conductivity on par with Tungsten and Iridium (Ruthenium was measured at $20\ [^{\circ}C]$, so would be reduced at high temperatures), whilst having half the density. Molybdenum has a very good coefficient of thermal conduction, the second highest specific heat capacity and a more than sufficient Young's modulus; however, similar to Rhenium, Molybdenum also oxidises, though at a lower rate and higher temperature (still below the chamber temperature).

Table 6.3: Table containing the relevant material properties for the high temperature resistance metals

Element	Material Properties						
	Melting Point $[^{\circ}K]$ **[60]**	**Density** $[g \cdot cm^{-3}]$ **[60]**	**Thermal Conductivity** $[W \cdot m^{-1} \cdot {}^{\circ}K^{-1}]$ **[61]**	**Coefficient of Thermal Expansion** $[10^{-6} \cdot mm^{-1} \cdot {}^{\circ}K^{-1}]$ **[62]**	**Specific heat capacity** $[J \cdot kg^{-1} \cdot {}^{\circ}K^{-1}]$ **[60]**	**Young's Modulus** $[GPa]$ **[60]**	**Material Cost** $[USD \cdot kg^{-1}]$
Nb	2750	8.57	$67.5_{T=1200^{\circ}K}$	7	265	104.9	$\sim 83.45_{03/12/25}$ [63]
Mo	2895	10.2	$105_{T=1200^{\circ}K}$	5	251	330* [64]	$64.416_{02/12/25}$ [65]
Ru	2606	12.1	$116_{T=293^{\circ}K}$ [66]	9.1	238	414 [66]	$29,257.18_{31/10/25}$[65]
Hf	2506	13.3	$20.9_{T=1200^{\circ}K}$	5.9	144	138 [66]	$5,768.40_{03/12/25}$ [67]
Ta	3290	16.4	$61_{T=1200^{\circ}K}$	6.5	140	185.7	$\sim 381.00_{03/12/25}$ [63]
W	3687	19.3	$115_{T=1200^{\circ}K}$	4.5	132	411.0	$101.81_{03/12/25}$ [68]
Re	3458	20.8	$45.7_{T=1200^{\circ}K}$	6.7	137	469 [66]	$3,803.75_{03/12/25}$ [68]
Os	3306	22.5872	$61_{T=293^{\circ}K}$	$5\ -\ 6$	130	560 **[66]**	$\sim 345,850.00_{03/12/25}$ [69]
Ir	2719	22.5622	$120_{T=1200^{\circ}K}$	6.4	131	524 [66]	$144,678.36_{31/10/25}$[65]

To allow for a more quantitative evaluation of the material choice, a trade-off process can be conducted. For the trade-off criteria, the material properties can be used, providing seven trade-off criteria. Weighing each of the criteria against the requirements, using a decision matrix, which can be seen in Appendix A, along with the explanation of the choices made. Implementing each of the criteria weighting into the trade-off table seen in Table 6.4, the trade-off process can be started. For each of the criteria, the metals were given a score from 1 to 9 where 9 is the best performing in that criterion. Note that for certain criteria, such as density, a lower value is desired. providing the final normalised values for the trade-off table. As expected, Molybdenum is best suited, and Hafnium is the least suited for the design. Whilst for the lower melting point metals ($< 3000\ [^{\circ}K]$), Molybdenum is the obvious choice, Ruthenium would be a good choice if Molybdenum is unavailable for one reason or another. Tungsten performs second best in the trade-off process, with the highest melting point and a relatively high thermal conductivity. If higher temperatures are required, then Tungsten would be an ideal option; however, as mentioned before, Tungsten is extremely difficult to machine, with Rhenium being used instead. Whilst Rhenium performed worse than Tantalum in the trade-off process, Tantalum is highly

reactive with Hydrogen and should not be considered when using Hydrogen as a propellant. Iridium, alongside Osmium, are extraordinarily expensive metal, meaning a single thruster would be on the order of hundreds of thousands of dollars in material cost alone, far too expensive to consider as an appropriate material.

Concluding on the evaluation of the trade-off process, the clear winner is Molybdenum, which scored the highest in the trade-off process. When higher temperatures are desired or required, past the melting point of Molybdenum, Tungsten would be the obvious choice, with it being the second-highest-scoring metal in the trade-off process. Though due to the great difficulty in machining Tungsten, Rhenium is often substituted, though having considerably worse performance in the trade-off process. The use of a tungsten-based alloy retaining the thermodynamic properties of tungsten whilst increasing the alloy's machinability is a great point of interest for high-temperature STP thrusters. As the required operating temperature of the system allows for the use of Molybdenum, it is the clear choice for the material to be used in the thruster.

Table 6.4: Trade-off table of the material choice for the thruster. The weighting explanation is given in Appendix A.

	Melting Point	**Density**	**Thermal Conductivity**	**Coefficient of Thermal Expansion**	**Specific heat Capacity**	**Young's Modulus**	**Material Cost**	**Normalized Total**
Weight	0.14	0.07	0.29	0.07	0.21	0.14	0.07	
Nb	4	9	5	2	9	1	8	**0.84**
Mo	5	8	6	8	8	4	9	**1**
Ru	2	7	8	1	7	6	3	**0.88**
Hf	1	6	1	6	6	2	4	**0.48**
Ta	6	5	4	4	5	3	6	**0.70**
W	9	4	7	9	3	5	7	**0.93**
Re	8	3	2	3	4	7	5	**0.67**
Os	7	1	4	7	1	9	1	**0.66**
Ir	3	2	9	5	2	8	2	**0.80**

6.3.2. Cavity Material

For the cavity material, the surface properties are of more importance than the volumetric properties, with the aim of the cavity to absorb as much of the incoming light as possible, leading to a material that requires a high absorptivity or applying kirkoff's law, the emissivity for a given wavelength. Because volumetric parameters such as density and thermal conductivity are still factors, coatings are often used to get the required surface properties without sacrificing the volumetric properties, allowing for the combination of two sets of materials. Though there is some difficulty in finding a coating that could withstand extreme temperature cycles without cracking or flaking off the base material. Because of the complexity in the design of such material/coatings, with an abundant number of variables affecting the optical properties of a surface, it was chosen not to implement such a coating and instead rely on the base material, in this case, the same material as the thruster and heat-exchanger.

7

Prototype Design

Having completed the initial sizing estimation for both the Thruster and the heat-exchanger, a prototype design can be generated from these estimations. Thus, in this chapter, the design process for the prototype STP system evaluated throughout this report will be explained. First, going into the design choices made for the thruster and heat-exchanger, respectively. Then, going on to showcase the final prototype design, featuring how the design choices have been implemented. Finally, a verification is made on how different aspects of the system relate to both the system sizing dimensions calculated and the requirements set by Green SWaP.

7.1. Prototype Design Choices

The choices made in the design process have a large impact on the performance and reliability of the system; therefore, it is important to clearly state what drives the design choices. Thus, for this section, a quick review of the design requirements set by Green SWaP is made. Then, a discussion of the general design choices seen across the entire system. Going on to describe the specific choices made for both the thruster and heat-exchanger designs in their own subsection, respectively.

For the prototype design and verification process of this project, the design is being sized for the environmental conditions expected during operations, these being a space environment and the use of Hydrogen as a propellant, allowing for the verification of the system to the requirements set by Green SWaP. Understanding that the initial tests of this prototype design are likely not to use Hydrogen as a propellant or be operated under vacuum. Thus, there are some design considerations that have been taken, allowing the easier adaptation of the prototype to other environmental conditions and propellants.

7.1.1. Review of Design Requirements

Referring back to the design requirements set, again seen in Table 4.1, the requirements RCS-Sub-010 to RCS-sub-030 are directly related to the design of the thruster and nozzle, with the main contribution to meeting the required values set by the geometry and input variables of the thrusting chamber and nozzle. Where the rest of the requirements are related to the system as a whole rather than any one single element. An example of this is requirement RCS-Sub-060, the minimum impulse bit, where the limiting factor is likely to depend on how fast the propellant valve can open and close, rather than the geometry of the system.

7.1.2. General Design Choices

One general design choice that has been made is the material used throughout the heat exchanger. Firstly, it was decided to only use a single material for the entire system. This was done to minimise the effects due to thermal expansion. To avoid the situation where one material may change in size more than the other, presenting a gap between the parts, requiring the use of a flexible thermal interconnection. One potential solution to this is the use of a molten metal. Copper is suitable with a melting point of $1358\ [^{\circ}K]$, as well as providing an increase in energy retention due to the phase change of the

metal, though some care has to be taken with copper boiling at $2,835\ [^{\circ}K]$, a point of potential future investigation. Because of this, and from the data gathered throughout section 6.3, it was chosen to use Molybdenum throughout the system, providing high performance across the range of different properties for high-temperature metals, if the melting point of Molybdenum is considered to be too low for the safety factor considered with the design, Rhenium also provides an excellent choice for the system.

Considering the manufacturing process that could potentially be used, Conventional reductive machining is the process that will be considered when designing parts. Whilst additive machining would allow for much more complex designs, currently, additive manufacturing using high-temperature metals is still in the research phase [70], with limited commercial providers [71]. The process of additive manufacturing also induces a more porous structure, reducing the thermal conductivity of the material and the resistance to Hydrogen penetration. Thus, whilst additive manufacturing could hold many advantages and is something to be investigated further, with the first iteration of the design, it was chosen to use reductive machining to eliminate these risks from the prototype.

Another aspect to consider is the thermal management of the components surrounding the cavity with certain elements, such as the nozzle and exterior wall of the heat exchanger. Because of this reasoning, it was decided to flow the incoming propellant through a cavity surrounding the main thruster and heat-exchanger. The cavity is separated into three distinct volumes, one for each of the channels in the heat-exchanger. The cold propellant will enter at the end of the nozzle before moving towards the inlet of the heat-exchanger, past the nozzle throat and the outside of the heat-exchanger before entering the system. The three cavities have a channel height of $2\ [mm]$, and an individual volume of $3426.7\ [mm^3]$. The cavity follows the contour of the nozzle, resulting in a notable reduction of the cross-sectional area at the throat, though not enough to choke the flow. These channels act as a regenerative cooling system, preheating the flow before entering the heat-exchanger increases the efficiency of the system. Because of the gaseous nature of the propellant, it also acts as an insulating layer between the high-temperature core of the heat-exchanger and the outside wall facing the surrounding environment, reducing energy loss to the surroundings.

For all the pressure-dependent walls of the thruster, a thickness of $1.5\ [mm]$ was chosen, with the limiting factor not being the hoop stress of the system, with a calculated thickness value of $0.0132\ [mm]$, with the lowest tensile strength of $380\ [MPa]$ for Molybdenum. But rather, this was chosen to provide a sufficient thickness for practical machining and to minimise other external forces, such as bending and twisting during manufacture or transport.

To reduce the complexity of the design and to reduce the travel time of the heated propellant from the heat exchanger to the thrusting chamber, it was decided to combine the thruster and heat-exchanger geometry into a single part. Completely removing the need for specialised high-temperature piping, with the heat-exchange propellant output going straight into the thrusting chamber of the thruster. Splitting the system into three parts, these being the System Core, which defines the geometry of the heat-exchanger propellant channels, the thrust chamber and the nozzle. The Cavity Insert provides the geometry of the cavity, as well as sealing the propellant channels in the System Core. The final part is the Outer Housing, which seals the system from the outside environment and creates the regenerative cooling channels around the system.

7.1.3. Design Choices Made for the Thruster

For the thruster design, having calculated the required dimensions for the nozzle throat and exit diameters Table 5.1, there are some other aspects to consider in designing a thruster. First is the geometry of the nozzle; whilst there is a theoretical ideal nozzle geometry, there are several considerations to be made, with the ideal nozzle geometry providing an efficient but very long and heavy nozzle, as well as not being easily adaptable to other ambient conditions. Thus, because this is the first iteration of the design and is likely to be tested, a conical nozzle was chosen. There is a lot of empirical data on the performance of conical nozzles, and they are easily adaptable to ambient conditions by simply reducing the overall length of the conical nozzle. To allow for better comparison to other conical nozzles, the standard divergent angle of 15° was used. Keeping with tradition, a convergent angle of 50° is used for the nozzle; this is a common angle used in thruster design. With the implementation of a thrusting chamber to allow the flow to mix and become more homogenous before entering the throat, with an internal diameter of $20\ [mm]$ with a length of $\sim 9[mm]$.

7.1.4. Design Choices Made for the Heat-Exchanger

Whilst most of the dimensions of the heat-exchanger have been set by the heat-exchanger sizing, Table 6.1, other design choices still have to be factored in. The first to be considered is the cross-sectional geometry of the propellant channels, whilst the heat-exchanger sizing code assumed a circular cross-section, there is no current reductive machining technique that would allow for the bore of a helical channel through a metal at this scale. Because of this, it was chosen to use a square cross-section, allowing for the cutting of a groove, with the opening being closed by the Cavity Insert. Whilst this may affect the performance of the system, but it does increase the overall surface area of each channel, theoretically leading to a higher convective heat transfer rate.

The heat exchanger's helical geometry does induce a rotation in the flow that is carried over to the thrusting chamber; however, it is assumed that the thrusting chamber is large enough to allow for the flow's rotation rate to decrease before entering the throat. Thus, no additional geometry was added to straighten the flow.

For the sealing of the gaps between the three parts in the system, for the interface between the system core and the cavity insert, a friction fit is assumed to be used, where the Cavity Insert can be cooled before being placed into the system core. This provides a strong bond between the parts that increases in strength as the system heats up. If the cavity insert does not weld itself to the system core, it could be removed and replaced. The outer housing forms the main seal between the high-pressure propellant and the external environmental conditions. Unlike the cavity insert, a friction fit is not possible, and instead, the outer housing is welded to both the cavity insert and the system core. This provides an airtight seal, and because of the low stress, due to a similar material choice and relatively low pressure difference, the weld is not required to be structurally supporting, allowing for the use of a weaker welding method, enabling the system to be taken apart more easily. If this fails to properly seal the system, there are metal seals used for vacuum testing, whereas a softer metal ring is crushed between two continuous interlocking grooves, leading to a vacuum-tight seal. Though if this method is used, Molybdenum may not be suitable as the base material, with it having the lowest hardness out of the metals considered in Table 6.3.

To reduce the chance of cavity collapse between the System core and the outer housing, three flanges were created to help support the outer housing during transport and use. Whilst it does provide a direct conductive path from the cavity to the outside environment, the thickness was minimised to reduce the amount of energy lost to the surroundings.

7.2. Prototype Design Presentation

Presenting the prototype CAD design in Figure 7.1 and Figure 7.2. Where Figure 7.2 provides a detailed drawing of the final design, with dimensions given for the three parts. For a better visualisation of the design, a cross-sectional render can be seen in Figure 7.1. With Figure 7.1a providing a clear indication of the three separate parts through the use of several colours, the Outer Housing is blue, the System Core is green, and the Insert cavity is Red. Figure 7.1b provides a more realistic interpretation of the system, with Molybdenum having a shiny silvery complexion. A separate drawing of each part can be seen in Appendix B.

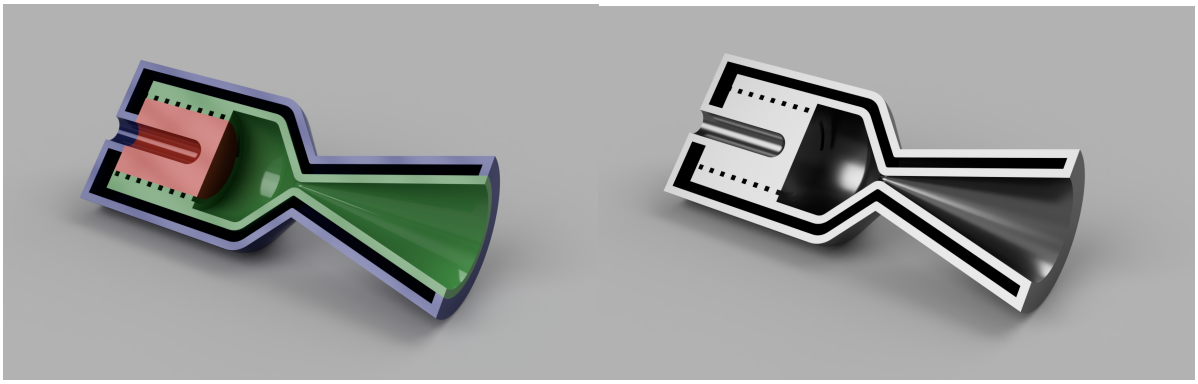

(a) Render with each part illustrated by colour, Outer Housing is blue, the System Core is green, and the Insert Cavity is Red

(b) Render with each part illustrated by the expected colour for Molybdenum

Figure 7.1: Render of two cross-sectional views of the prototype design

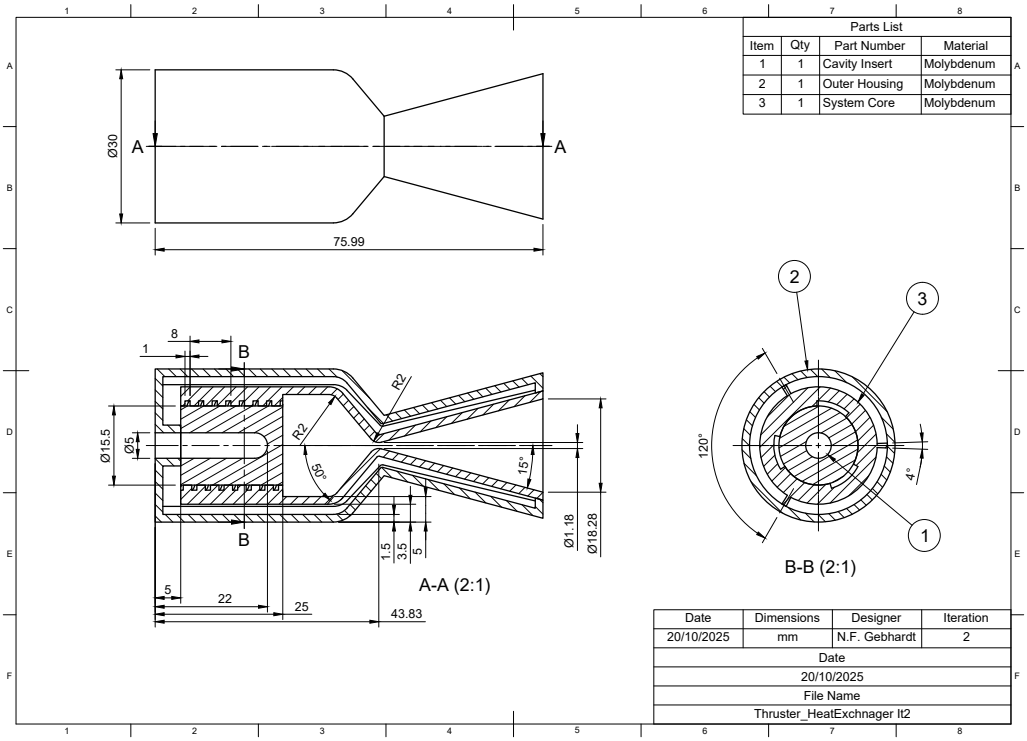

Figure 7.2: Technical Drawing of the proposed prototype design

7.3. Prototype Review

Having completed the design of the prototype CAD model, it is important to reflect on the results of the sizing investigations and requirements to verify that they have been met. Thus, this section will first go through the verification of the sizing data implementation. Then, going on to do a verification on how well the prototype meets the design requirements, and evaluating what may need further investigation.

7.3.1. Sizing Verification

Before continuing with further testing and verification, it is important to verify that the chosen sizing dimensions have been implemented into the CAD model. By first verifying the dimensions set by the thruster sizing investigation, setting the nozzle throat and exit diameter at $1.18\ [mm]$ and $18.28\ [mm]$. Figure 7.2, showed that these are, in fact, the dimensions implemented into the CAD model, in addition

to the prescribed convergent and divergent angles of the nozzle.

Moving on to the verification of the implementation of the sizing data gathered through the heat exchanger sizing investigation. Again, looking at Figure 7.2 it can be seen that the heat-exchanger does in fact have a length of $20\ [mm]$, a helical diameter of $15.5\ [mm]$ and a pitch of $8[mm]$. It can also be noted that there are three separate channels, with a channel diameter of $1.0\ [mm]$.

Regarding the cavity design, it can be seen that the spherically capped cylindrical geometry was implemented, with a total aspect ratio of $1:4.4$. This is in line with the decisions made during the choice of the cavity geometry. The material selected can also be seen as Molybdenum when looking at Figure 7.2.

7.3.2. Requirement Verification

For the verification of the requirements, each of the set requirements seen in Table 4.1, will be evaluated to determine if the requirement is met or if more data is required for the verification process.

RCS-Sub-010 - Thrust Level - RCS
The RCS shall provide a vacuum thrust level of more than $1[N]$. - Whilst the implementation of the Thruster sizing had a constant Thrust Value of $1\ [N]$, assumptions are being made about the flow, whilst these may only have a minimal effect on the flow, this is an unknown, leading to Ideal rocket theory not being enough to fully allow for the verification of the thrust value. To fully verify the thrust, either real-world testing or a validated numerical method should be implemented. Allowing for the comparison and evaluation of the effects due to the assumptions being made.

RCS-Sub-020 - Specific Impulse - RCS
The RCS shall achieve a vacuum specific impulse of more than 500 seconds to ensure efficient propellant utilisation. - With ideal rocket theory, a theoretical vacuum specific impulse of $673.6\ [s]$, this is still well above the requirement set, even when considering the non-pure Hydrogen flow, leading to a vacuum specific impulse requirement increase to $600\ [s]$. Though this could be evaluated and compared to the results gathered using a numerical method.

RCS-Sub-030 - Total Propellant Throughput - RCS
The main thruster shall be able to achieve a total propellant throughput of $3\ [kg]$ [TBC]. - With a propellant mass flow rate of $0.149\ [g \cdot s^{-1}]$, and a total propellant throughput leading to a total burn time of $\sim 5.6\ [hours]$, whilst this is a long burn time when comparing to the main engine on a boost stage, the system is not expected to utilise all the propellant in a single burn. Though with the material choice and design decision made, it is expected to survive the full duration of its expected lifetime, though this is difficult to verify without the direct physical testing of the system.

RCS-Sub-040 - Response Time - RCS
The thruster shall be capable of achieving full thrust within $< 5\ [s]$ [TBC] after actuation. - If the required time to heat the system to operating temperature is excluded from the requirement, the system shall easily be able to achieve full thrust within $5\ [s]$ with the flow passing through the heat exchanger in under $5 \cdot 10^{-5}\ [s]$. It is also assumed that without the need for combustion to generate the required chamber pressures, the start-up time is much reduced and more dependent on the flow speed.

RCS-Sub-050 - Reignition Time - RCS
The RCS shall be able to reignite after a minimum of [TBD] seconds. - Whilst no value for the requirement has been set at this time, a rough calculation can be made on the worst-case scenario. That being a cold start form $100\ [^{\circ}K]$, shaded space to its operating temperature of $1702\ [^{\circ}K]$, with the required input power and specific heat capacity, an estimation can be made on the time to reach operating temperature. For Molybdenum with a total mass of $219.247\ [g]$, the system requires $29.96\ [s]$, and with Rhenium with a total mass of $450.939\ [g]$ the system requires $33.60\ [s]$. Transient and steady state thermal simulation of the system can provide a more accurate understanding of the thermal distribution and startup time of the system.

RCS-Sub-060 - Minimum Impulse Bit - RCS
The RCS shall be able to provide a minimum impulse bit of $100\ [mN \cdot s]$ [TBC]. - To allow for a minimum impulse bit of $100\ [mN \cdot s]$, the thruster could either reduce thrust by reducing chamber pressure or

temperature and burn for a set duration, or the system can perform as normal, performing a $100\ [ms]$ burn to produce the required impulse bit. This is well within the closing and opening times of a solenoid valve, the limiting factor in the start-up procedure, with the thruster start-up likely being very quick on the order of $\sim 0.1\ [ms]$ as stated before.

RCS-Sub-070 - Thrust Accuracy – RCS
Each RCS thruster shall deliver a thrust level with a total uncertainty less than 10% (TBC) (3 sigma) with respect to the selected nominal thrust value. - With ideal rocket theory providing a fixed thrust level, there is some uncertainty in how accurately the thrust value of the system will be. Whilst some indication could be made from a series of numerical results, a real-world test would be best suited to establish the accuracy of the system under different conditions.

RCS-Sub-080 - Power Consumption - RCS
The RCS shall not exceed [TBD] W of electrical power peak. - With the current system requiring zero electrical power, this requirement is met; however, it must be taken into account that there are other aspects to consider in a full STP system, with components such as the collector or optical interconnect that may require power.

RCS-Sub-090 - Propellant Compatibility - RCS
All RCS components shall be compatible with the propellants used by the system. - The choice in material and design has been such that the system will be compatible with all widely used gaseous propellants, the ones that were taken into account being Hydrogen, Argon, Helium and Nitrogen.

Having now completed the verification of the implementation of the calculated sizing for both the thruster and the heat-exchanger, as well as the verification that the system still meets the requirements set by Green SWaP. Some requirements, RCS-Sub-010, RCS-Sub-020, RCS-Sub-040, RCS-Sub-050 and RCS-Sub-070 have been determined to require a more in-depth investigation into whether or not the system meets them. For this, it was chosen to complete both a thermal and a computational fluid dynamics (CFD) simulation to provide a better and more detailed understanding of the system, allowing for the verification of the requirements. Using the numerical simulation provided by Ansys, these include Ansys Mechanical and Ansys Fluent for their respective domains.

8

Numerical Simulation Analysis

Having developed the prototype design for the STP RCS thruster and analysed how the design relates to the requirements set by Green SWaP, it has been determined that more data is required to fully verify if the prototype complies with the requirements. This chapter will focus on the development of numerical models to provide the data to verify the requirements. Thus, the first section of the chapter will focus on the thermal analysis of the system, determining the maximum temperatures and time to reach operating conditions, evaluating RCS-Sub-050 and RCS-Sub-090. Then continuing in the next section with a Computational Fluid Dynamics (CFD) simulation, for the evaluation of the thermals of the system with propellant flow, as well as the propulsion characteristics of the thruster. This will allow for the verification of RCS-Sub-010 to RCS-Sub-050. Finally, going through the results and evaluating that the requirements have been met.

8.1. Simulation Parameters and Meshing

For any numerical simulation, it is vital to properly illustrate the boundary conditions, simulation parameters and the generated mesh. Thus, in this section, for each of the three main simulations, a discussion will be had on the boundary conditions, the meshing and the simulation parameters for the modelling of the flow will be given.

8.1.1. Thermal Simulation

For both the steady state and transient thermal simulations, the same boundary conditions and mesh were used. The boundary conditions can be seen in Figure 8.1, where the green heat-flow boundary is the simulated thermal heat load on the cavity surface, and the red radiation boundary is the radiative coupling of the outside surface to the environment. The heat-flow is set to a constant power of $2942.31\ [W]$, corresponding to the required power load calculated from the thruster sizing. This produces an evenly spread heat load across the cavity surface. The radiative boundary is the approximation of the radiative losses from all the external surfaces to the environment. Ansys Mechanical calculates the radiative losses, using the temperature of the exterior surface, the external environment temperature and the emissivity of the material. Implementing an environmental temperature of $295.15\ [^{\circ}K]$, room temperature, whilst temperature in orbit can fluctuate widely, the chosen environmental temperature provides a good middle ground. The emissivity was set at 0.425 for both metals [72, 58], whilst the emissivity of both Molybdenum and Rhenium varies greatly with temperature and surface finish, this value of emissivity was chosen as an appropriate value for the expected temperatures across the external surfaces. All the internal connections between bodies are simulated as bonded parts with a shared mesh for the contacting surface pairs.

For the material properties, the Ansys Granta library was used, implementing 'Molybdenum, Alloy 363, TZM' and 'Rhenium, commercial purity, hard'. Providing a comprehensive non-linear evaluation of the material properties, though some parameters have only been evaluated up to $2000\ [^{\circ}K]$. The material properties can be seen in Table 8.1. If a temperature is associated with a value, it indicates that the value has a non-constant value with temperature changes, corresponding to the temperature at which

the value was taken.

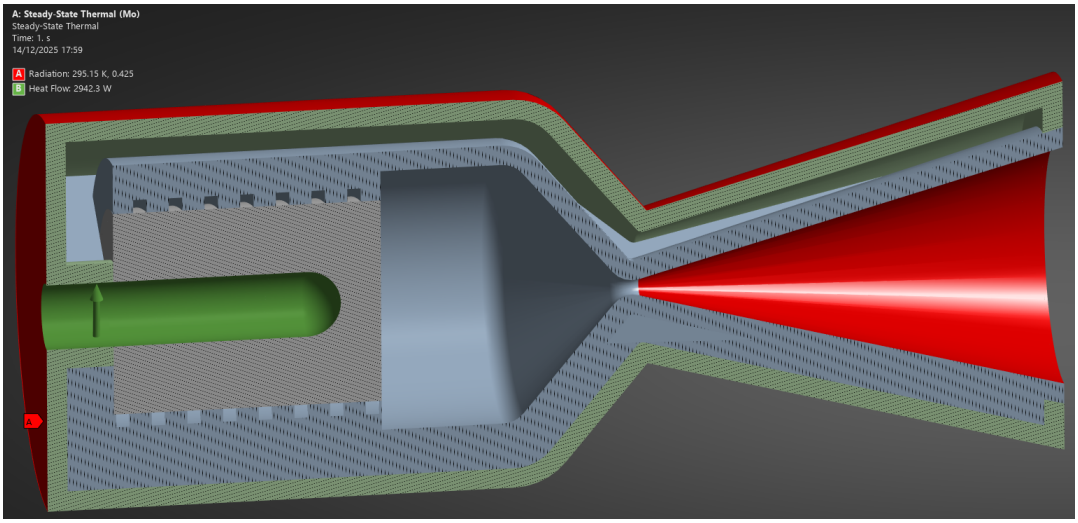

Figure 8.1: Boundary Conditions of the Thermal Simulation, No Propellant flow

Table 8.1: Table containing the relevant material properties for Molybdenum and Rhenium from the Ansys Granta materials library

Material	**Material Properties**				
	Density $[g \cdot cm^{-3}]$	**Thermal Conductivity** $[W \cdot m^{-1} \cdot {}^{\circ}K^{-1}]$	**Coefficient of Thermal Expansion** $[10^{-6} \cdot mm^{-1} \cdot {}^{\circ}K^{-1}]$	**Specific heat capacity** $[J \cdot kg^{-1} \cdot {}^{\circ}K^{-1}]$	**Young's Modulus** $[GPa]$
Molybdenum	10.15	137.7	5.084	264.8	314.8
Rhenium	21.01	$45.84_{T=1223.1^{\circ}K}$	$6.621_{T=1106.4^{\circ}K}$	$136.4_{T=1237.5^{\circ}K}$	$365.9_{T=1173.1^{\circ}K}$

For the meshing of the prototype for the thermal simulation, it is clear that the mesh should be designed such that it can properly capture the internal heat fluxes throughout the system. Resulting in a mesh that is refined, where the highest heat fluxes are expected, mainly being the internal flanges, the inside surface of the propellant channels and some of the internal edges. This provides a mesh with an overall body sizing of 0.5 $[mm]$, refining the mesh once along the propellant channels, and twice along the flanges and some internal edges. This results in a mesh with an overall element number of 4.19 million. Whilst a structured mesh was investigated, it proved too complex to implement a fully structured mesh with comparable mesh quality. Thus, an automated tetrahedral element generation was implemented.

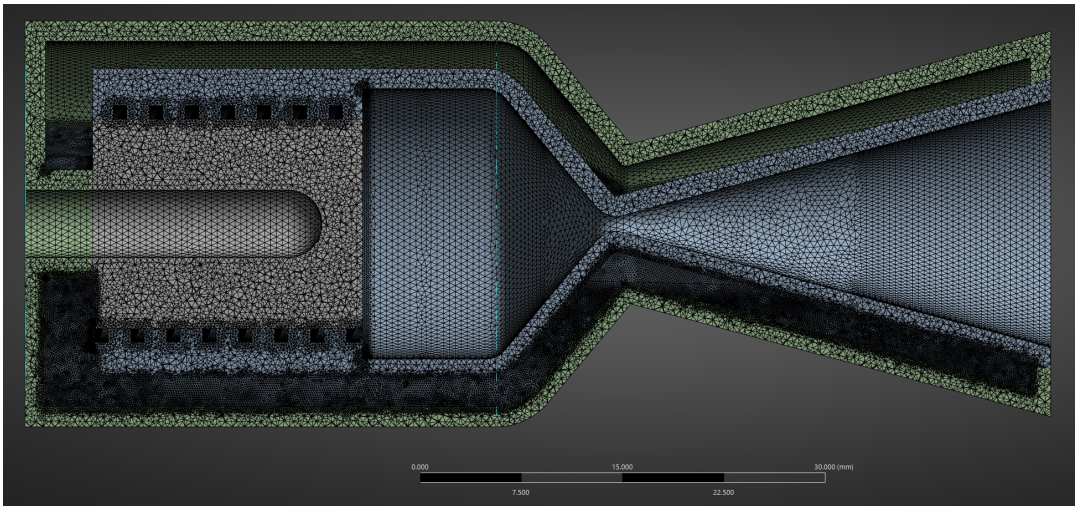

Figure 8.2: Mesh of the Thermal Simulation, No Propellant flow

8.1.2. Fluid Simulation, 3D

With the introduction of Fluid Flow, both the boundary conditions and the meshing become more complex. Requiring the implementation of thermal conditions as well as fluid conditions, again, all the boundary conditions can be seen in Figure 8.3. For the thermal boundary conditions, they are the same as those for the thermal analysis without propellant flow, with the only difference being that the heat load on the cavity surface is described as a flux rather than a single power. Where the heat-load on the cavity is denoted in red, and the external radiative coupling is denoted in green. For the two fluid boundaries, being the Inlet and outlet pressure boundaries, illustrated in blue and off-white, respectively. For the inlet pressure, a total gauge pressure of $6\ [bar]$ was implemented, knowing that there is an expected pressure drop across the heat-exchanger. Implementing an initial fluid temperature of $293\ [^{\circ}K]$, with a zero initial velocity and a turbulence intensity of 5%. The outlet total pressure was calculated as $1072.482[Pa]$, using the isotropic expansion equations. Whilst the use of other fluid inlet and outlet types where considered, mainly velocity and mass flow, they generally caused the system to not converge or have a lower convergence rate. The use of a pressure boundary condition is also a better analogue to real-world tests, though the mass flow rate does have to be checked and correspond with the expected value. Considering the simulation is conducted under vacuum conditions, the operating pressure of the system is set $0\ [Pa]$. For the internal boundaries, all the solid-to-solid connections are once again considered bonded, and the solid-to-fluid boundaries are modelled as a coupled thermal system, with a no-slip fluid boundary condition.

With the introduction of Hydrogen as a propellant, a new material has to be defined, which is taken from the Ansys Fluent material database, the properties of which can be seen in Table 8.2. Considering a compressible gas, the density is determined using the ideal gas law and the viscosity is calculated using the Sutherland model, a good model for the determination of viscosity in the nozzles. The specific heat is determined by a piecewise polynomial and is dependent on fluid temperature. For all the solid bodies, the Molybdenum alloy was used again.

Table 8.2: Table containing the relevant material properties for Hydrogen from the Ansys Fluent materials library

Material	**Material Properties**				
	Density $[g \cdot cm^{-3}]$	**Molecular Weight** $[kg \cdot kmol^{-1}]$	**Thermal Conductivity** $[W \cdot m^{-1} \cdot {}^{\circ}K^{-1}]$	**Specific heat capacity** $[J \cdot kg^{-1} \cdot {}^{\circ}K^{-1}]$	**Viscosity** $[kg \cdot m^{-1} \cdot s^{-1}]$
Hydrogen	Ideal-Gas	2.01594	0.1672	$\sim 16000_{T=1200^{\circ}K}$	Sutherland model

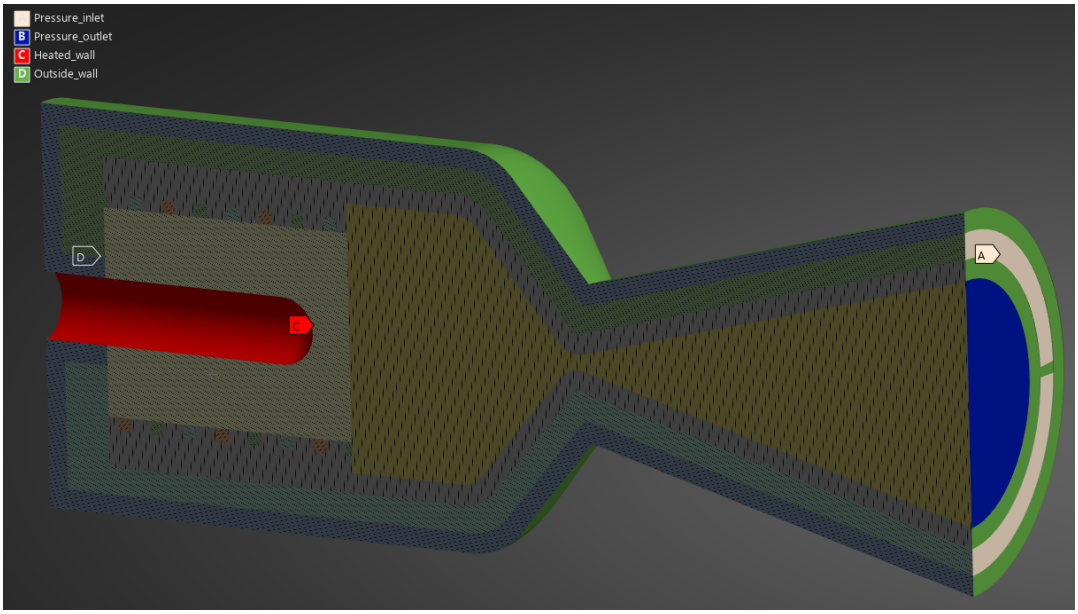

Figure 8.3: Boundary Conditions of the Thermal Simulation, With Propellant flow

For the meshing of the thermal simulation with fluid flow, the mesh can be seen in Figure 8.4. The first point of difference from the previous mesh is the implementation of the fluid bodies, which are required by Ansys Fluent to define the fluid domain. Again, to help in the reduction of the overall number of elements, the mesh is refined where needed. For fluid simulation, this corresponds to areas of high fluid velocity near a wall, mainly the heat-exchanger propellant channels and the nozzle walls and throat. This results in a mesh with an overall mesh size of $4.3518\ [mm]$ with a face sizing of $0.2\ [mm]$ along the propellant channels, thrust chamber and nozzle walls and a face sizing of $0.1[mm]$ over the walls around the nozzle throat. Resulting in a total of 15.2 million elements, it should be noted that the mesh should be refined further; however, it is already pushing the limits of the available computing power. Again, the use of a structured mesh was investigated; similarly, it was deemed too complex to produce a comparable mesh, so an automatic tetrahedral method was used instead.

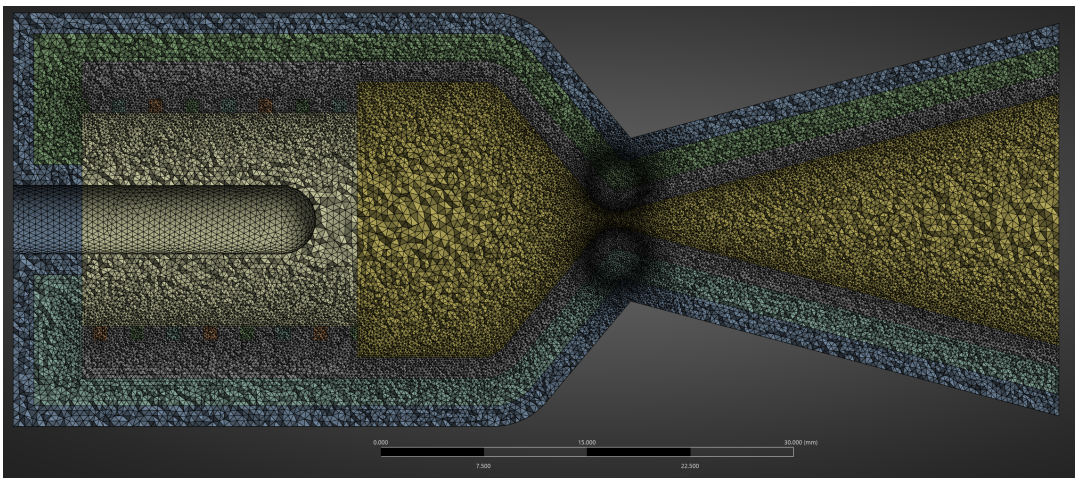

Figure 8.4: Mesh of the Thermal Simulation, With Propellant flow

For the setup of the Ansys Fluent solver, generally, the model is a 3D, density-based, steady-state fluid simulation, implementing the use of the energy conservation equation, with the viscous calculation handled by an SST k-ω turbulence model. The SST k-ω model is a 2-equation model, implementing the default model constants for an SST k-ω model [73]. Implementing an implicit second-order upwind

discretisation method for the fluid flow, turbulent kinetic energy and specific dissipation rate. Initialising the simulation from the pressure inlet, using the standard initialisation process with absolute values.

8.1.3. Fluid Simulation, 2D Nozzle

The simplification of the nozzle geometry into a 2D domain allows for a more accurate simulation of the fluid flow through the nozzle. The boundary conditions for the 2D simulation can be seen in Figure 8.5, with the farfield wall and thruster wall boundaries being two no-slip wall boundary conditions illustrated in blue and off-white, respectively. The system has an axis of symmetry illustrated by the red boundary condition. The pressure inlet, seen in green, is set to a total pressure of $5\ [bar]$, a fluid temperature of $1500\ [°K]$ and an initial velocity of zero with a turbulence intensity of 5%. The pressure outlet is set to have a backflow pressure of $50\ [Pa]$ with a fluid temperature of $293\ [°K]$. There are no solid bodies in this simplification of the nozzle, meaning the only material in use is Hydrogen.

Figure 8.5: Boundary Conditions of the 2D nozzle simulation

The simplification into the 2D domain allows for the use of a structured mesh, generally allowing for a higher quality mesh. Splitting the mesh into two parts, the bounding box and the thruster geometry, the bounding box is there to capture the immediate environmental effects and allow the flow to fully develop. The full mesh can be seen in Figure 8.6, the mesh was refined such that there is an increasing number of elements along the expected flow path of the thruster exhaust, ensuring that the mesh is kept smooth and orthogonal. The largest elements in the bounding box have a size of $1\ [mm]$. Zooming into the more refined mesh for the thruster geometry, seen in Figure 8.7, emphasis was taken to ensure that the mesh is refined enough at the wall to properly capture the fluid boundary conditions. This leads to a minimum element size of $\sim 0.5 \cdot 10^{-3}\ [mm]$ and a maximum of $\sim 0.25\ [mm]$, resulting in a total of 67450 elements for the mesh as a whole. To produce a smooth transition between different element sizes, a growth bias is applied to the edge sizing. This bias is kept between 1 and 15 except for the throat, where it is set to 80.

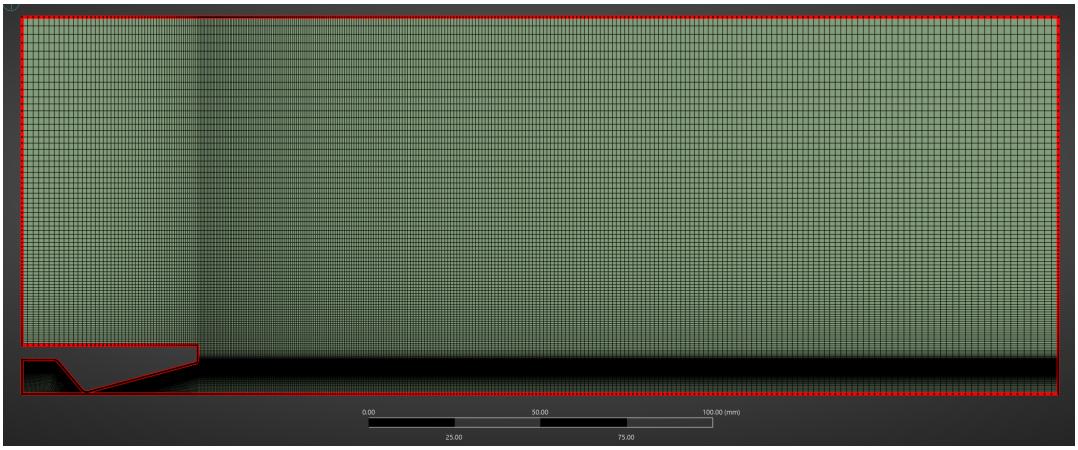

Figure 8.6: Mesh of the 2D nozzle simulation

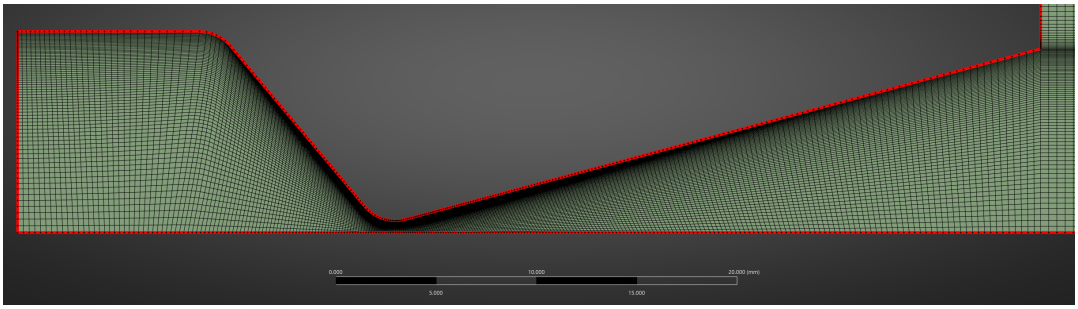

Figure 8.7: Zoomed in view of the mesh for the 2D nozzle simulation

Similarly to the previous fluid simulation, it can generally be described as a 2D, density-based steady-state or transient fluid simulation, implementing the use of the energy conservation equation. The simplification also allows for the use of a more complex turbulence model, in this case a Transition SST k-ω model, a 4-equation model implementing the default model parameters set by Ansys Fluent [74]. The simulation implements a radiation symmetry around the bottom axis, simulating the flow around the full thruster. For the differentiation of the steady-state simulation again an implicit second-order upwind method is used for the fluid flow, turbulent kinetic energy and the specific dissipation rate, and because of the more complex turbulence model, the flow intermittency and momentum thickness Re follow the same discretisation method. For the transient simulation, a second-order implicit discretisation was used in time. To increase the convergence rate and reduce the overall time required, high-speed numerics were implemented for both steady-state and transient simulations, setting the flow type as supersonic, the higher-order blending to 100% and a starting Courant number of 2. No notable effect on the results where noticed from the implementation of high-speed numerics.

8.2. Thermal Analysis, No Propellant Flow

To better understand the thermodynamics of the system before the propellant is introduced, an indication of the startup and reignition time of the system is required. Determining the maximal and minimal temperatures. A Thermal analysis is needed; thus, in this section, first, a steady state thermal simulation will be explored, then, continuing on to a discussion on a transient thermal simulation.

8.2.1. Steady State Simulation

For the determination of the maximal and minimal temperature of the system, it was decided to implement a steady state thermal simulation, both for the use of Molybdenum and Rhenium as a material choice. First, inspecting the Steady state simulation results for the system using Molybdenum as a base material, the section view of the thermal distribution can be seen in Figure 8.8. As expected, the

maximum and minimum temperatures of the system can be seen on the cavity surface and the end of the nozzle, respectively. It can also be seen that the maximum temperature ($3194.2\ [°K]$) exceeds the melting point of Molybdenum, indicating that the system cannot be allowed to reach thermal equilibrium, and the temperature must be carefully monitored so that the system does not melt. Regarding the thermal loss due to radiation, first, it can be seen that the outer housing does in fact reach relatively high temperature with a range over 1700 to $2200\ [°K]$, depending on location and proximity to a flange. Indicating that there is a large thermal flux through the flanges, this is reinforced when looking at Figure 8.9, where the total heat flux is seen through the system, with the flange having a value of $\sim 35\ [W \cdot mm^{-2}]$. The non-symmetry noted in both the temperature and heat flux cross sections is due to the presence of a flange in the lower portion of the cross section. This was done to illustrate the temperature and heat fluxes both for parts close to and far from the flange. The maximum total heat flux is seen along the edges of the Outer Housing. Whilst there is expected to be a high heat flux in this location, there is also a larger error concentration, leading to some doubt concerning these values, seen in Figure 8.10. Though the error across the system, as a whole, is very small, only concentrated along the vertices of the flange, leading to a higher confidence in the results around the heat-exchanger channels.

Whilst generally not considered throughout this report, the large temperature gradient seen in the simulation would result in the expansion of the material and hence cause a stress load across the system. Whilst the deformations to the nozzle throat can be counted for by over-sizing the throat, so that once the system reaches the operating temperature, the correct throat sizing is reached. The stresses produced are still considerable, especially considering the reduced material strength as the metals heat up to operating temperatures. As the location of any stress concentration is highly dependent on how the system is constrained, in 3D space, it is hard to determine the exact extent to which these stresses would affect the prototype. Because of this, it is recommended to complete a full stress analysis on the prototype to better define the stress distribution across the system. Whilst pinpointing the exact locations is difficult, there are some general considerations about possible high-stress locations. Mainly, the stress concentrations in the three flanges connecting the system core to the outer housing, and the connection point between the outer housing and the cavity insert, as both are expected to reach very high temperatures. The flanges are expected to be under compression and bending forces caused by the expansion of the cavity insert pushing the flanges into the outer housing, though this would depend on the constraining method. For the nozzle, whilst there is expected to be an expansion of the material, if the nozzle is not constrained in its expansion, there is enough space to allow the nozzle to expand without causing large stress concentrations throughout.

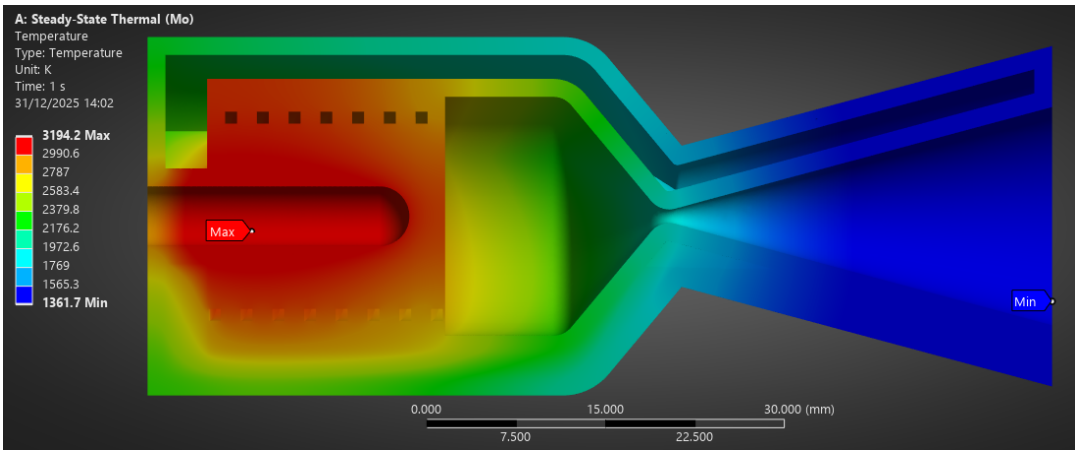

Figure 8.8: Section view of the Temperature distribution over the System, Molybdenum as base material.

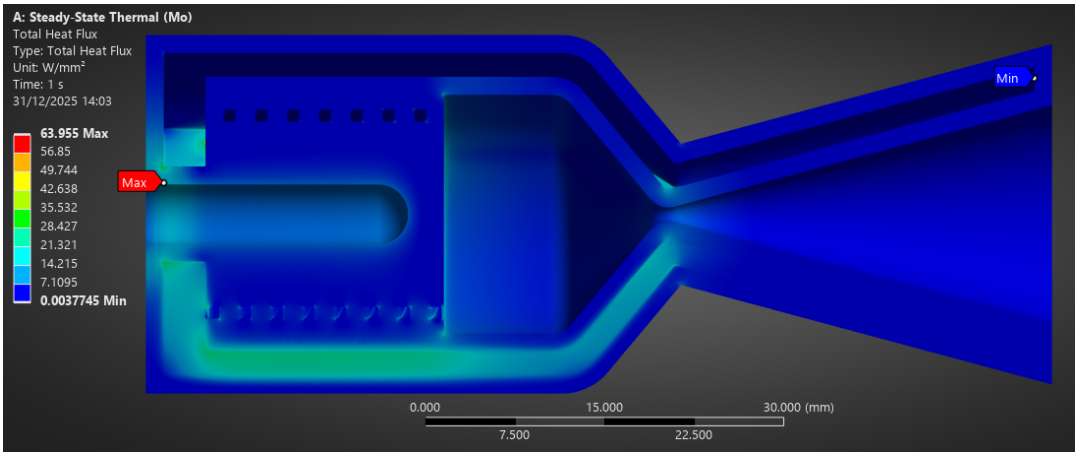

Figure 8.9: Section view of the total heat Flux over the System, Molybdenum as base material.

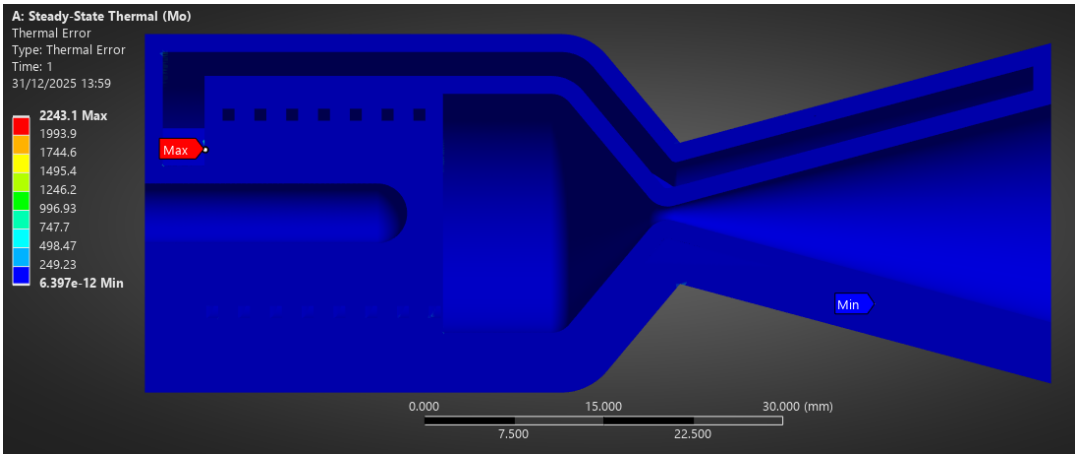

Figure 8.10: Section view of the Thermal Error over the System, Molybdenum as base material

When looking into the steady state thermal results for the system using Rhenium as a base material, it can be seen that the maximum temperature has increased and the minimum temperature has decreased. This is logical when considering that the thermal conductivity of Rhenium is quite a bit lower than that of Molybdenum, leading to a large temperature difference across the design. The maximum temperature ($4508.9\ [°K]$) is again over the melting point of Rhenium, requiring special care when in use. Similar to Molybdenum, the location of the maximum and minimum temperatures has not changed, except for the maximum temperature moving more towards the centre of the cavity. Regarding the thermal loss, it's clear that there is a larger temperature gradient to the environment, leading to a similar temperature of the outer housing, even with the increased cavity temperature. Again, there is a large total heat flux load through the flange with a value of $30\ [Wmm^{-2}]$.

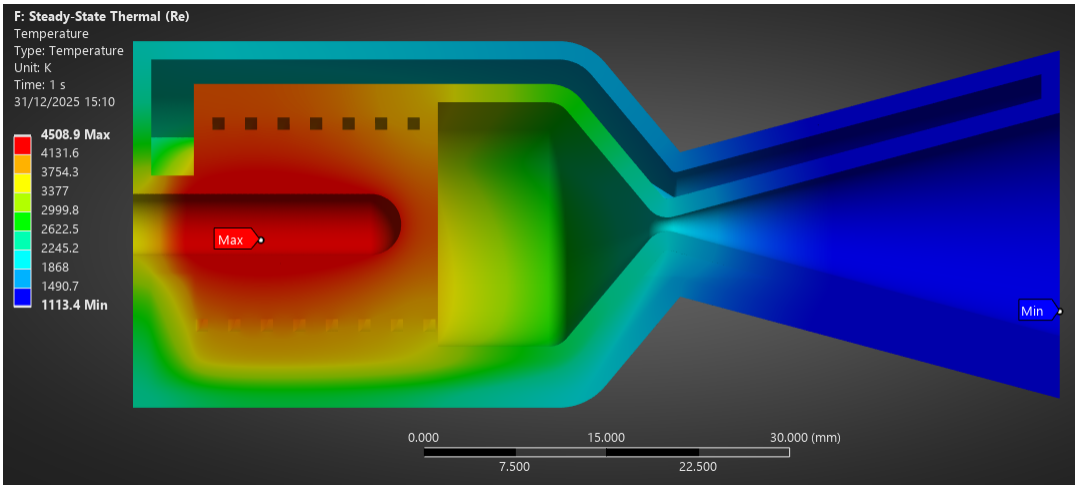

Figure 8.11: Section view of the Temperature distribution over the System, Rhenium as base material.

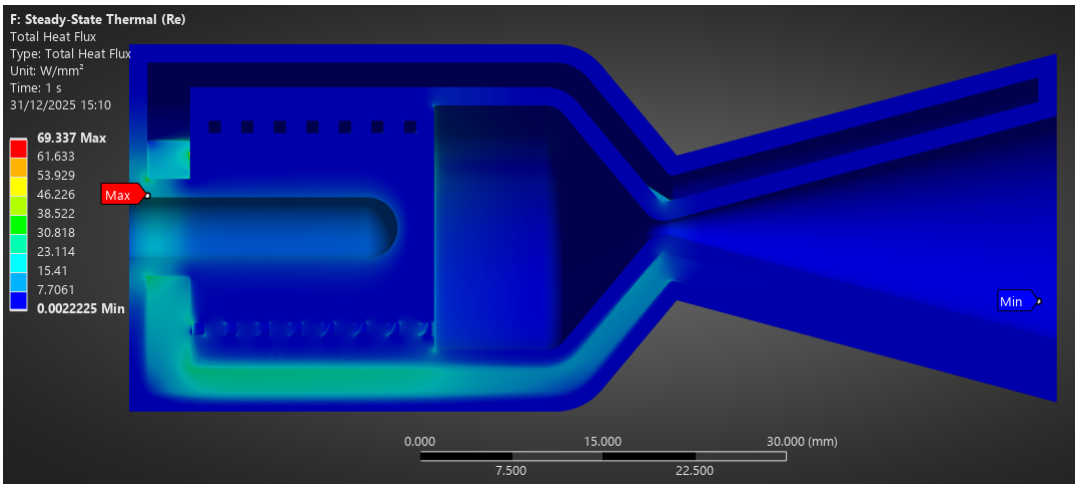

Figure 8.12: Section view of the total heat Flux over the System, Rhenium as base material.

8.2.2. Transient Simulation

To determine the initial start-up and reignition time of the system, a transient thermal model of the system was conducted. Again, investigating the use of both Molybdenum and Rhenium. The mesh and initial conditions for the simulation were kept the same as the steady state simulation, running the transient model for a total of $100\ [s]$ with an automated step size between 1 and $10\ [s]$, enough time to allow the system to reach equilibrium.

First investigating the system with Molybdenum as a base material, when looking at Figure 8.13 the system average temperature reaches $1500\ [°K]$ at $26\ [s]$, the heat-exchanger channels have a temperature ranging from 1850 to $2050\ [°K]$, all above the required $1702\ [°K]$ wall temperature calculated from the heat-exchanger sizing. Another promising aspect is that at this point the maximum temperature ($2251\ [°K]$) has not yet passed the melting point of Molybdenum, confirming that Molybdenum is a suitable material to be used. When looking at Figure 8.14, the temperature values of the system over time, it's clear to see that the nozzle is somewhat thermally isolated from the heat-exchanger with a notable lag in the temperature increase between the maximum and minimum temperatures of the system.

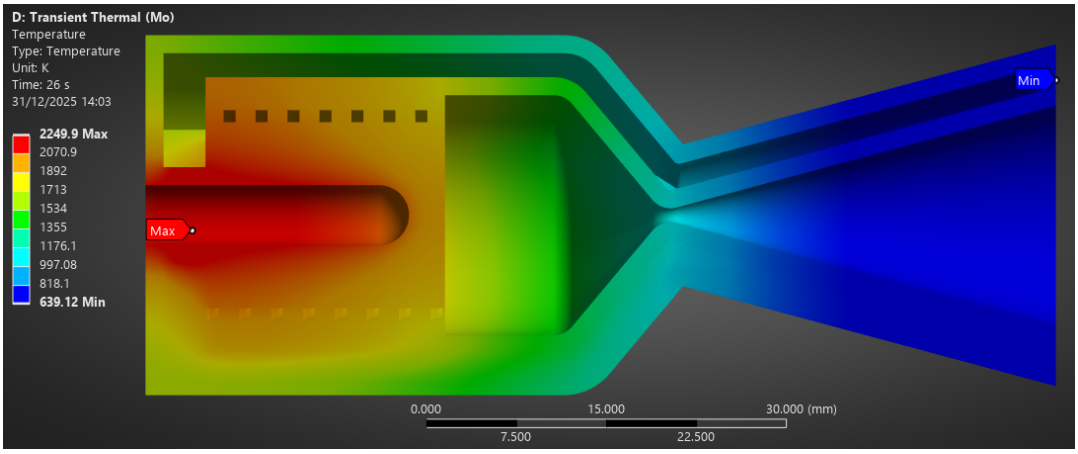

Figure 8.13: Section view of the temperature distribution over the System at a time of $26\ [s]$, Molybdenum as base material.

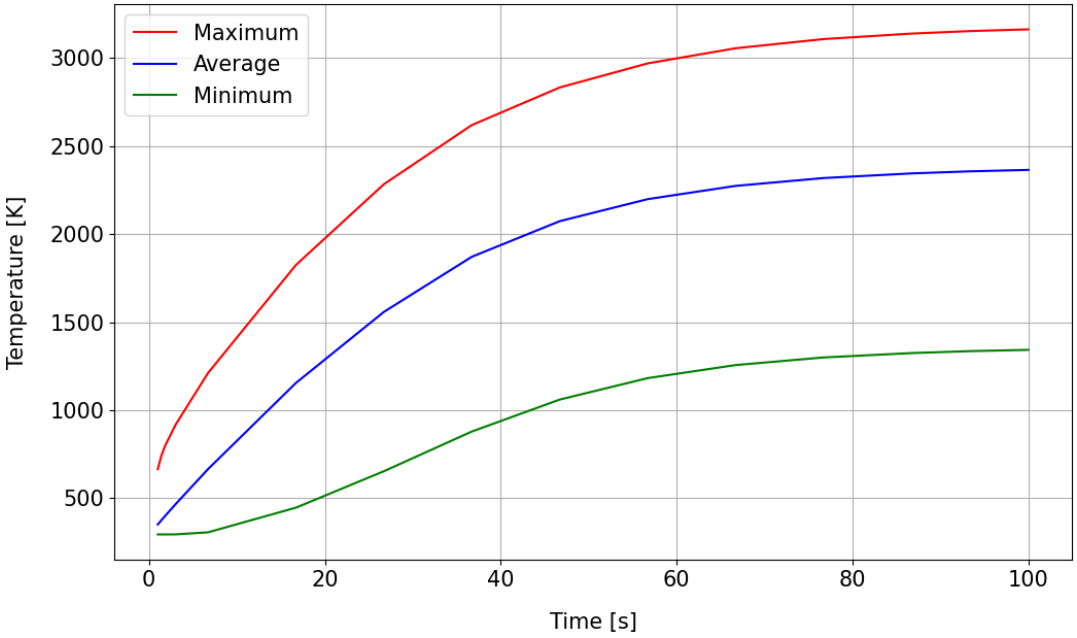

Figure 8.14: Graph of the Temperature over time for the system, Molybdenum as base material.

When investigating the use of Rhenium as a base material, first looking into the temperature profile, when the average temperature reaches $1500\ [°K]$, for Rhenium occurring at $31.2\ [s]$. Firstly, the maximum temperature reached by the system at this time is much higher at $2954.4\ [°K]$, than for the Molybdenum system. This makes sense when considering that the specific heat for Molybdenum is much higher than that of Rhenium. The maximum temperature of the system is also below the melting point of Rhenium, resulting in Rhenium being an appropriate material for the thruster, though producing a higher thermal gradient over the system as a whole. The temperature over the heat-exchanger channels is relatively similar for both the Rhenium and Molybdenum, with Rhenium having a slightly larger thermal gradient. Looking into the temperature of the system over time, seen in Figure 8.16, it's again visible how the material properties of the two metals differ; the lag time between the maximum and minimum temperature is much longer for Rhenium than for Molybdenum. With clever design, it is possible to take advantage of the lower thermal conductivity, isolating the system core from the external environment.

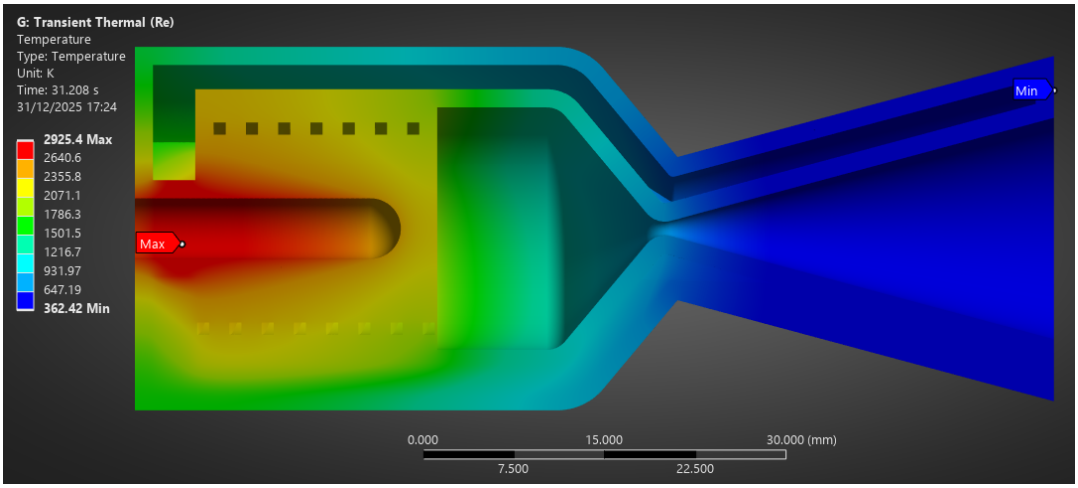

Figure 8.15: Section view of the temperature distribution over the System at a time of $31.2\ [s]$, Rhenium as base material.

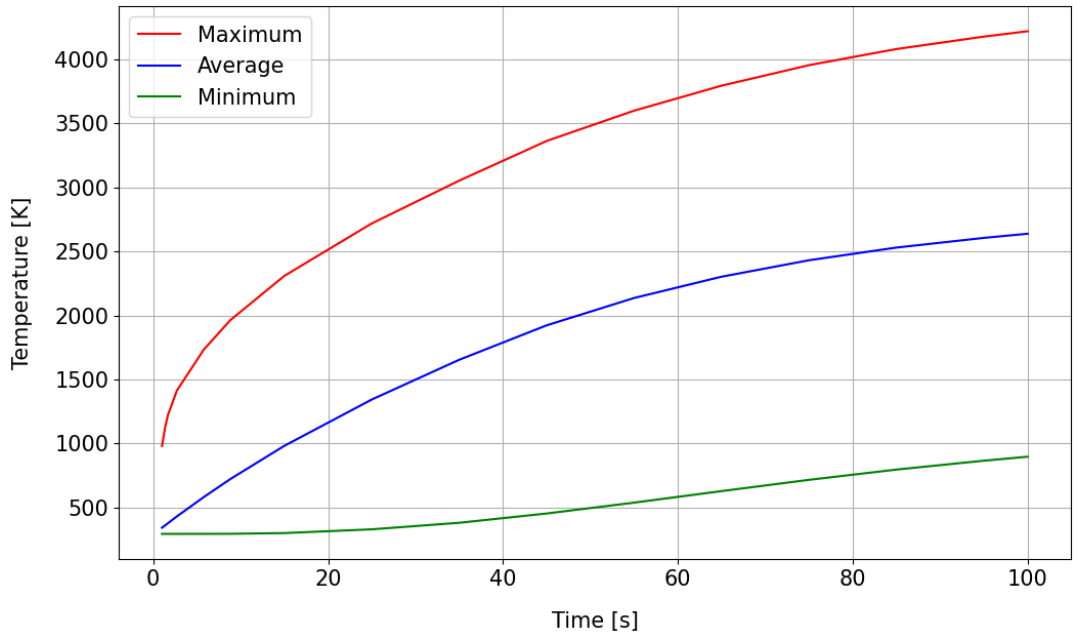

Figure 8.16: Graph of the Temperature over time for the system, Rhenium as base material.

8.3. Thermal Analysis, With Propellant Flow

Having now done a more in-depth investigation into the thermal properties of the prototype before the introduction of the propellant, an investigation into the thermal characteristics with propellant flow is required. Thus, for this section, more numerical studies are conducted to investigate the propellant flow properties through the prototype, first going through a steady state analysis of the system with the use of a CFD simulation to calculate the flow properties of the propellant as it moves through the heat-exchanger. To more accurately determine the thrusting characteristics of the system, a 2D CFD steady-state and transient simulation was done on the nozzle geometry.

8.3.1. Steady State CFD Analysis of Heat-Exchanger

To ensure that the requirements RCS-Sub-010 and RCS-Sub-020 are met, the target chamber temperature and pressure are required. Thus, to better evaluate the drop in pressure and the final temperature of the propellant leaving the heat-exchanger, a steady-state CFD simulation was done.

For the high-speed section of the fluid flow, these being the heat-exchanger and the nozzle, the mesh was refined to better capture the wall boundary layer. However, when calculating the Y+=1 wall distance for Hydrogen at the expected velocities, it's clear that the required mesh detail is $0.026\ [mm]$ and $0.005\ [mm]$ for the heat-exchanger and nozzle, respectively, meaning that the mesh is not refined enough to accurately evaluate the wall boundary layer. While the mesh size for the heat-exchanger is close enough to estimate the temperature of the propellant through the heat-exchanger, the same can not be said for the nozzle geometry. For this reason, it was determined to evaluate the nozzle geometry separately.

Having completed the simulation, an analysis can be made on the result gathered, first evaluating the simulation residuals, the graph of which can be seen in Figure 8.17. It should be noted that the prototype has been rotated $90°$ to better illustrate the propellant flow. The energy continuity and velocities converge to a residual below $1 \cdot 10^{-6}$ and the k-ω model residuals converge at $1 \cdot 10^{-3}$, producing a total mass flux of $-1.28 \cdot 10^{-8}\ [kg \cdot s^{-1}]$ and a heat loss of $38.29\ [W]$. Ideally, these values are as low as possible, with the mass flux being adequate, with the heat loss being rather high, though still only 1.28% of the heat added to the system.

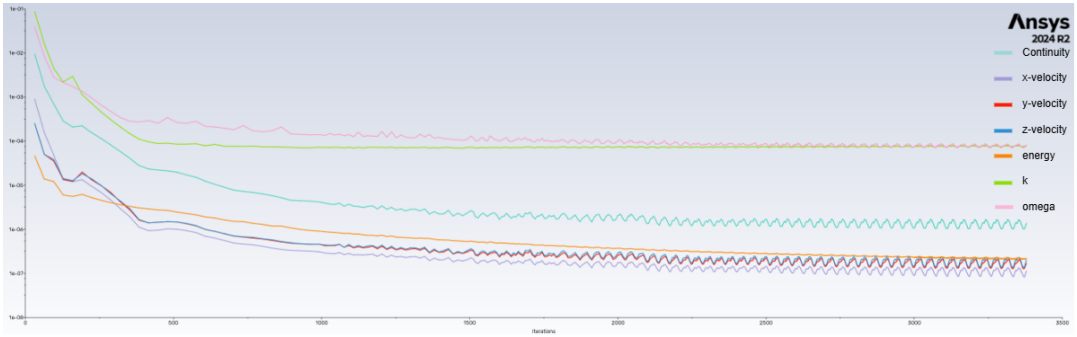

Figure 8.17: Residual for the Steady state CFD simulation

Looking into the temperature of the system, seen in Figure 8.18, with the temperature streamlines seen in Figure 8.19. As expected, the introduction of the propellant flow has reduced the temperature of the system overall, with the maximum temperature of the system being $2024\ [°K]$. It can also be seen that the heat-exchanger propellant channels do in fact reach the required temperature of $1702\ [°K]$, being around $\sim 1750\ [°K]$. It can also be seen that the temperature of the propellant before entering the heat-exchanger has already reached above $1000\ [°K]$, with the propellant matching the heat-exchanger wall temperature near the end of the heat-exchanger. This does differ from the expected end temperature of the propellant calculated during the heat-exchanger sizing; this is likely due to the increased starting temperature of the propellant entering the heat exchanger. Adapting the inlet temperature of the heat-exchanger sizing code leads to a calculated exit temperature of $1646\ [°K]$. However, it can also be seen that because of the expansion of the flow from the heat-exchanger channel to the thrust chamber, the temperature of the propellant drops down to a chamber temperature of $\sim 1500\ [°K]$, the target chamber temperature of the system.

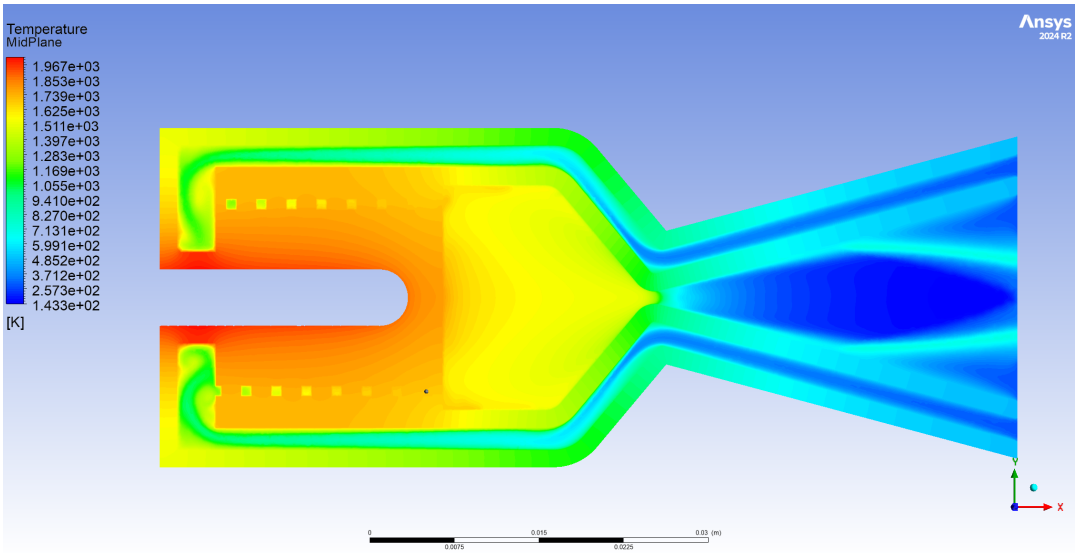

Figure 8.18: Steady state temperature profile for the heat exchanger

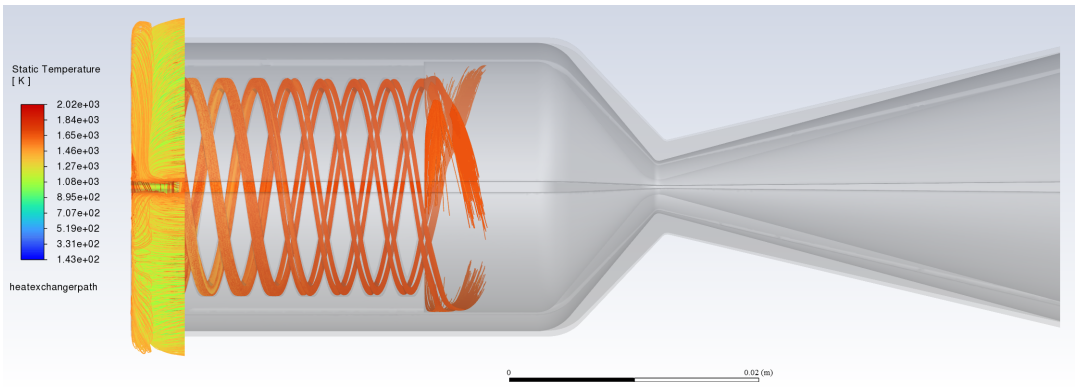

Figure 8.19: Steady state streamlines for the fluid temperature through the heat-exchanger

Regarding the pressure of the system, the mid-plane static pressure of the system can be seen in Figure 8.21. There is, as expected, a pressure drop across the heat-exchanger channel, with the pressure drop being $\sim 1.2\ [bar]$ leading to a chamber pressure of $4.8\ [bar]$, slightly lower than the chosen chamber pressure calculated using ideal rocket theory. Continuing to the evaluation of the velocity streamlines through the heat-exchanger, seen in Figure 8.20, it can be noted that the flow accelerates through the heat-exchanger channels, reaching a speed of $\sim 1000\ [m \cdot s^{-1}]$. This is far below the speed of sound for Hydrogen at these temperatures and pressures, meaning the flow is not choked when going through the heat-exchanger propellant channels. This is confirmed as no choked flow is observed throughout the heat-exchanger channels in Figure 8.21.

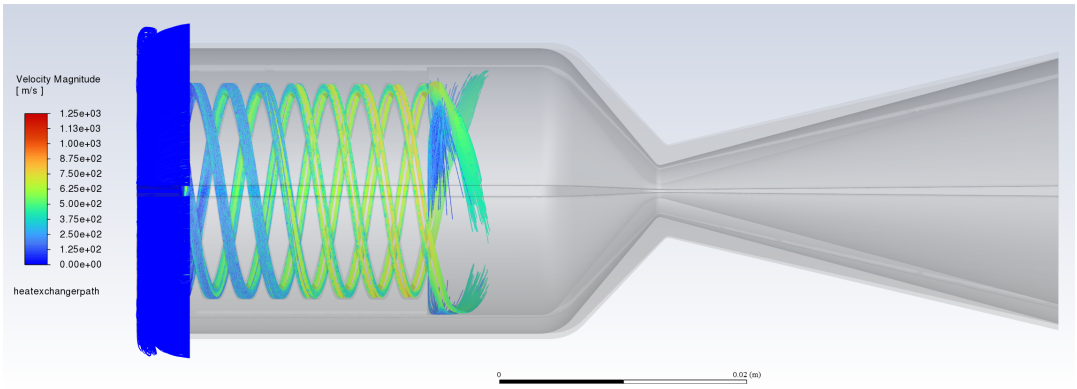

Figure 8.20: Streamlines for the fluid velocity through the heat-exchanger

Whilst the accuracy of the fluid flow through the nozzle can be called into doubt, the values can still be evaluated. Firstly, there is a shock at the throat location when looking at the static pressure, seen in Figure 8.21. From the velocity profile in Figure 8.22, the exit velocity of the system is $6.47\ [km \cdot s^{-1}]$. It can also be seen that the flow is over-expanded, and the flow separates from the nozzle wall. This leads the system to have a mass flow rate of $0.138\ [g/s]$ and a thrust of $0.772\ [N]$, which are both lower than what was calculated. This is likely due to the lower chamber pressure seen and the uncertainty of the boundary layer of the system. As well as the flow separation from the nozzle wall. To better evaluate the effect, a 2D simulation for the nozzle was conducted.

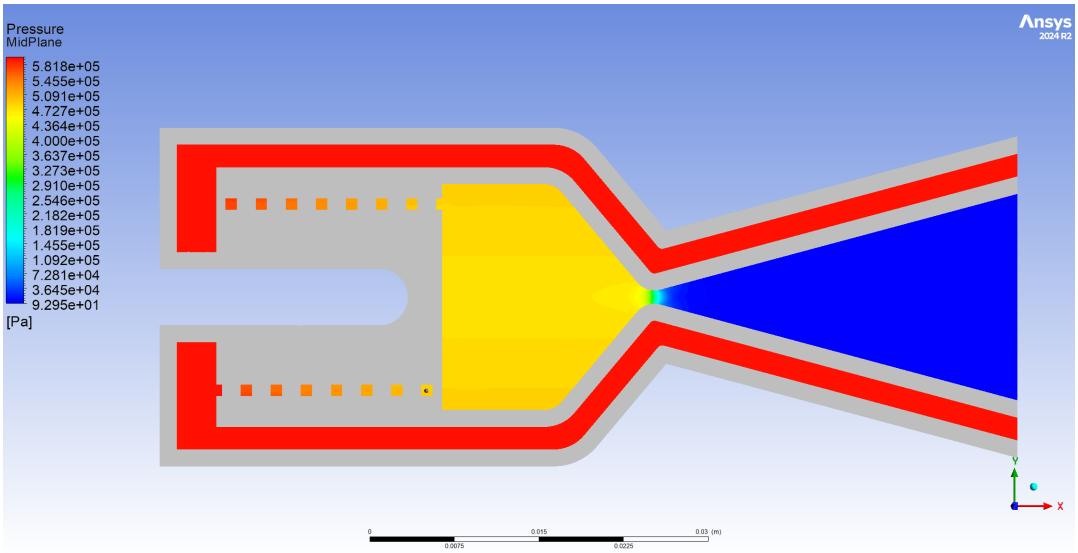

Figure 8.21: Steady State Static Pressure profile for the Heat-exchanger

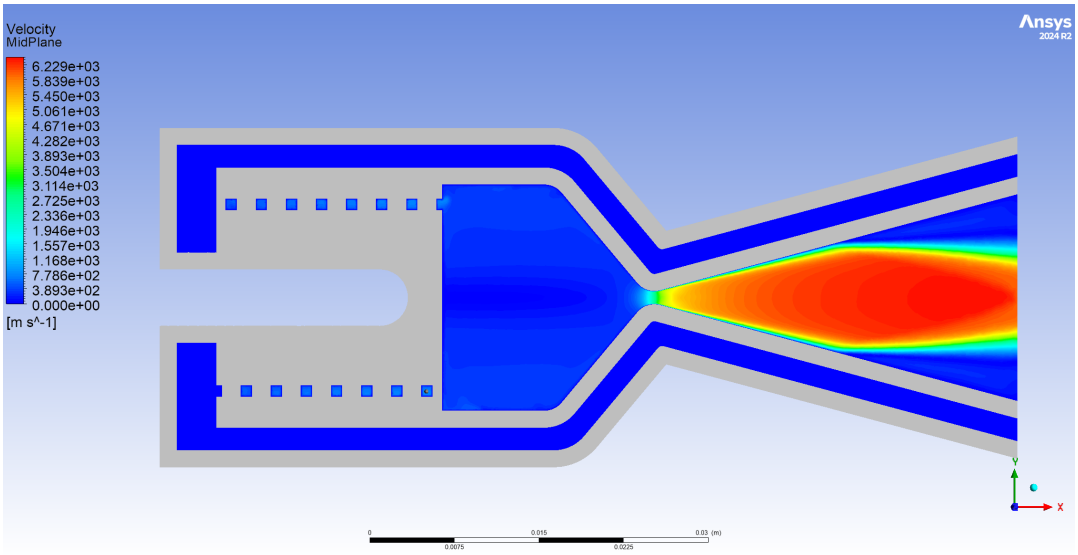

Figure 8.22: Steady State Velocity profile for the Heat-exchanger

8.4. Steady State CFD Analysis of Nozzle

To better determine the performance of the nozzle, it is important to fully capture the boundary layer. Thus, as the mesh generated for the Heat-exchanger steady-state CFD analysis is not refined enough around the nozzle geometry, a simplification of the nozzle was done. Implementing a 2D cross-section of the nozzle with symmetry through the centre.

The simplification also allows for the use of a more accurate model, this being a 4-equation k-ω Transition SST model. The simulation was run for 10000 iterations to allow the residuals to converge, reaching a convergence of $1.0 \cdot 10^{-10}$ to $5.9 \cdot 10^{-13}$, which can be seen in Figure 8.23. Producing a total mass flux of $-1.178 \cdot 10^{-10}$ $[kg \cdot s^{-1}]$ and a total heat transfer rate of $15.21[W]$, these are fluxes over the full domain of the system, though power is technically not a flux but is derived from the heat flux. Ideally, according to conservation equations, the total flux across any closed surface should be zero, as any flux going in must come out. Whilst the total mass flux of the system is very close to zero, the same can not be said for the total power, though the value is still orders of magnitude lower than the power input into the system.

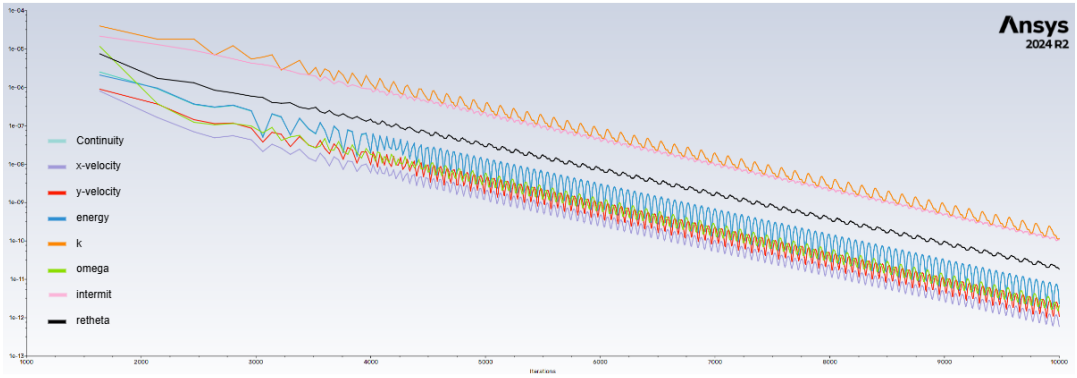

Figure 8.23: Graph Showing the residual convergence for the steady state nozzle CFD analysis.

First, investigating the static pressure across the nozzle, seen in Figure 8.25, the shock across the throat is in the correct location, indicated by the sudden pressure drop. The static pressure at the end of the nozzle is 169.054 $[Pa]$, which is above the ambient pressure, indicating that the exhaust has not been fully expanded. The under-expansion of the flow can be more clearly seen in the velocity

profile seen in Figure 8.24, the exhaust velocity can also be noted at $6.323\ [km \cdot s^{-1}]$. This is below the calculated exhaust velocity from ideal rocket theory ($6.605\ [km \cdot s^{-1}]$). This is logical when considering that the flow is not fully expanded, leading to an underutilisation of potential energy in the flow, reducing the final exhaust velocity.

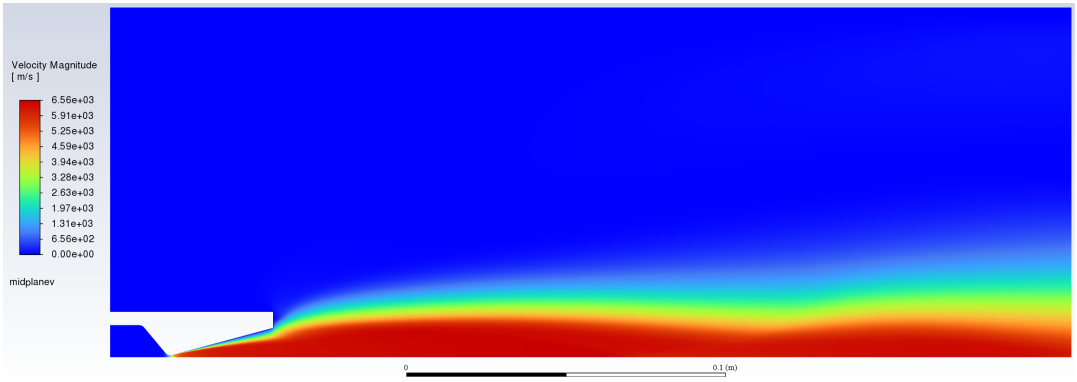

Figure 8.24: Velocity profile for the Steady State Nozzle analysis

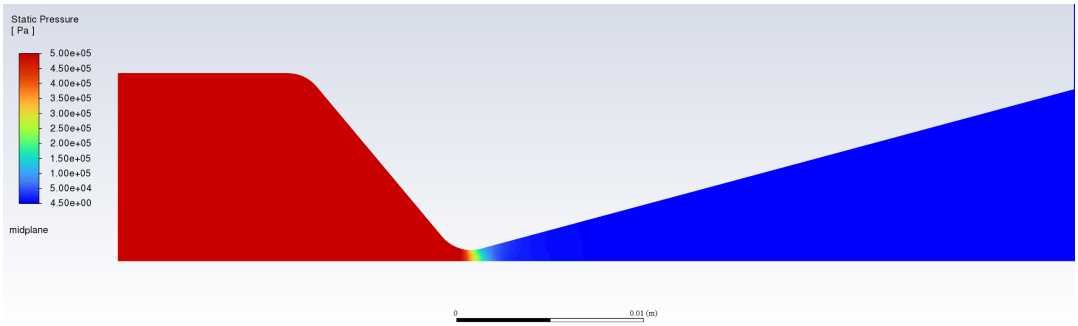

Figure 8.25: Static Pressure profile for the Steady State Nozzle analysis

Regarding the potential separation of the flow when looking at the velocity along the centre line of the nozzle, seen in Figure 8.26. Whilst the velocity does in fact increase going through the throat, reaching Mach one at the throat (placed at $x = 0\ [mm]$) and continues to increase past the throat, at a distance of $\sim 2\ [mm]$ the velocity flattens out, indicating a separation of the flow. Whilst the flow does seem to reattach to the nozzle geometry, with the flow continuing to accelerate after about 1 to $2\ [mm]$. This does seem to be the greatest factor in the under-expansion of the flow, leading to a reduction in thrust. The use of a $15°$ divergent angle for the nozzle may have been too large for a nozzle of this geometry. This is somewhat expected when considering that with an area ratio of 238.55, there is a higher chance of separation of the flow from the nozzle wall. However, the separation did not have a catastrophic effect on the performance of the system, only differing in thrust by 14.8% from the nominal value.

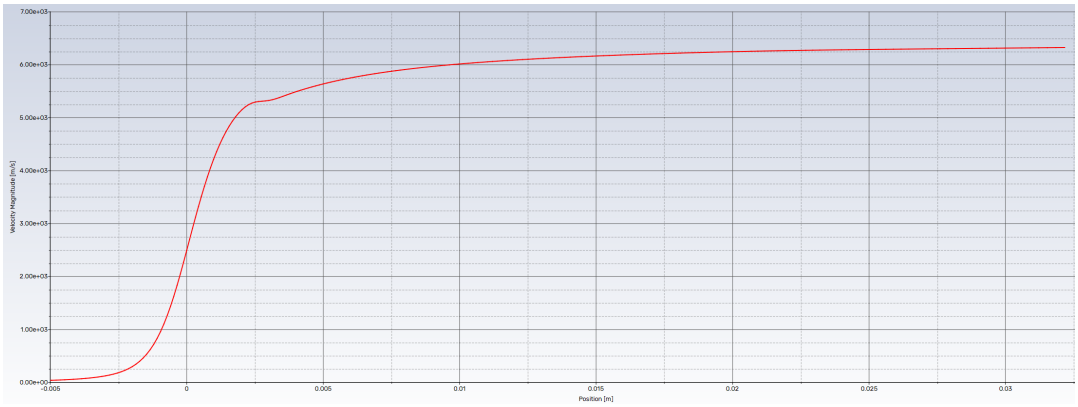

Figure 8.26: Graph showing the exhaust velocity as it travels through the convergent-divergent geometry.

Determining the characteristics of the nozzle, first, the mass flow can be calculated to be $0.143392\ [g \cdot s^{-1}]$, which is very close to the calculated value from the thruster sizing, differing by only 4%. This leads to a total thrust of $0.851827\ [N]$. This is lower than the thrust expected; this is due to an effective reduction in both the nozzle throat and exit areas, reducing the mass flow rate, and the expansion of the exhaust. There is some uncertainty in how much this effect is caused by the separation of the flow or by the inclusion of boundary layer effects.

Evaluating the effects of a vacuum environment, the exit pressure was set to $0\ [Pa]$, whilst this does cause the simulation to pin some of the pressure values to $1\ [Pa]$, leading to the residuals converging to a lesser extent. Having convergence values between $1 \cdot 10^{-6}$ to $1 \cdot 10^{-8}$, with a total mass flux of $-2.815 \cdot 10^{-5}$ and a total heat transfer of $-557.27[W]$, leading to an arguably less accurate model. However, still below the generally accepted minimum convergence of $1 \cdot 10^{-6}$, [75], whilst this is highly dependent on the problem, a value of $1 \cdot 10^{-6}$ is generally considered accurate enough for high-speed compressible flow with energy considerations.

The velocity profile can be seen in Figure 8.27, and a graph of the velocity through the nozzle can be seen in Figure 8.28. From this, it can be noted that the exhaust velocity is $6.326\ [km \cdot s^{-1}]$, a small increase to the exhaust velocity calculated previously. The exit pressure can also be determined at $169.056\ [Pa]$. Resulting in a small increase to the thrust, with the thrust produced being $0.852161[N]$. This indicates that the loss of thrust from the calculated value is indicative of errors in the design of the nozzle contour and not the ambient pressure. This is further reinforced when observing the velocity through the nozzle, where the same levelling off can be seen, correlating to a separation of the flow from the nozzle wall.

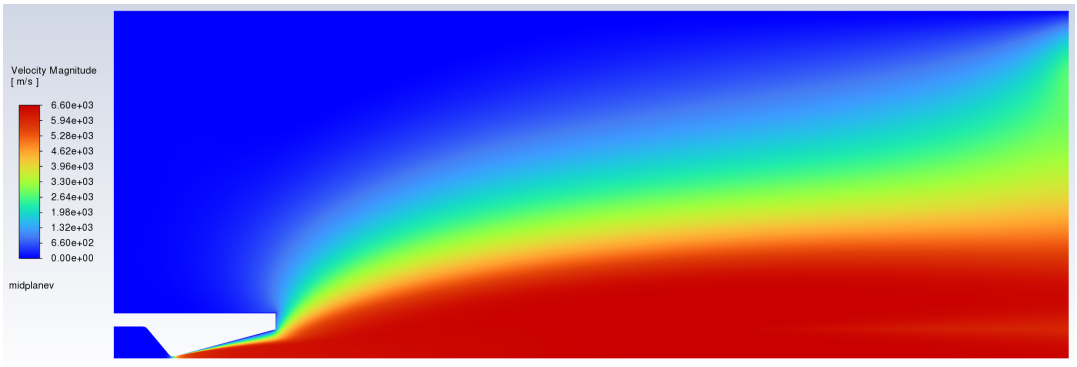

Figure 8.27: Velocity profile for the Steady State Nozzle analysis in vacuum conditions

To investigate the effects of the nozzle, the decision was made to change the nozzle divergence angle to $9°$ and $12°$ whilst adjusting the nozzle length to keep the same throat to exit area ratio. Implementing an ambient pressure of $50\ [Pa]$. Running each simulation for a total of 15000 iterations, with the simulation

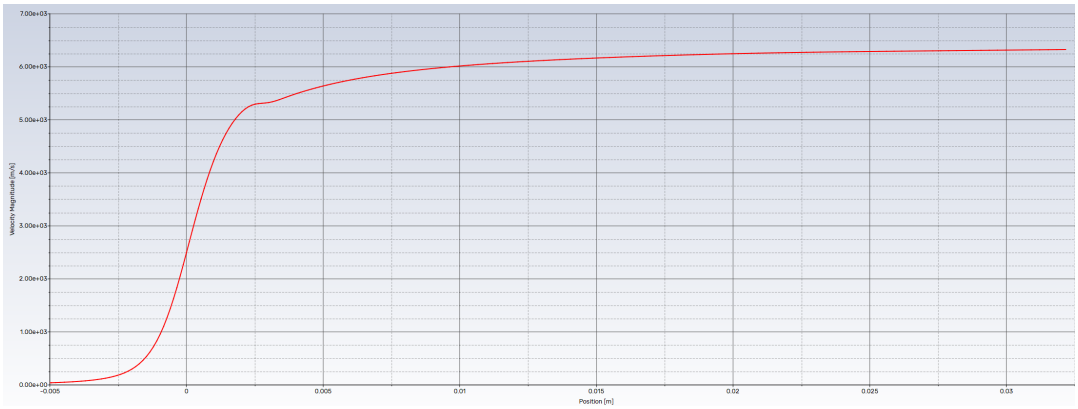

Figure 8.28: Graph showing the exhaust velocity as it travels through the convergent-divergent geometry, in vacuum

residuals converging to a value of $1 \cdot 10^{-8}$ to $1 \cdot 10^{-11}$. The velocity through the centre of the nozzle can be seen in Figure 8.29 and Figure 8.30 for the $9°$ and $12°$ divergence angle nozzles, respectively.

First, investigating the use of a $12°$ divergence angle for the conical nozzle, measuring a total mass flow of $0.143442\ [g \cdot s^{-1}]$, a thrust of $0.851469\ [N]$. This is slightly lower than the value for the nozzle with a $15°$ divergence angle, indicating that a change of $3°$ is not sufficient to improve flow separation at the start of the divergence section. Implementing a divergence angle of $9°$, results in a mass flow of $0.143446\ [g \cdot s^{-1}]$, contributing to a total thrust of $0.83716\ [N]$. This is slightly lower than either of the previous nozzles, indicating that there may be a thrust optimal angle between $9°$ and $15°$. However, it must be noted that the change in divergent angle did not help with the separation of the flow. It can also be noted that the location of the separation point moves closer towards the nozzle throat as the divergence angle is reduced.

To determine if the flow separation is caused by the convergent angle inducing an effect to cause the flow to separate, a simulation was done, reducing the convergent angle from $50°$ to $30°$. For this simulation, there was some difficulty in the convergence; the values only converged to $1 \cdot 10^{-3}$ for the physical parameters and to $1 \cdot 10^{-8}$ for the model residuals. However, still having a low total mass flux of $-3.259 \cdot 10^{-8}\ [kg \cdot s^{-1}]$ and a total heat transfer of $18.105\ [W]$. This results in a mass flow rate of $0.143480\ [g \cdot s^{-1}]$, resulting in a thrust of $0.862303\ [N]$. This is an increase in thrust when compared to the nozzle with a $50°$ convergence angle. However, when looking at Figure 8.31, it's clear that the flow separation is still present, in the same location as for the $50°$ convergence angle nozzle geometry.

Whilst the current design iteration with a $15°$ and $50°$ divergent and convergent angle has a thrust value of $0.851827\ [N]$, a deviation of 14.8% from the requirement. With a decrease in mass flow rate of $\sim 4\%$, it's clear that there is more contributing to the loss of thrust than a reduction in mass flow. The simulations with the altered nozzle divergent and convergent angle clearly indicate that a higher thrust value can be obtained through a more thrust-optimised nozzle geometry.

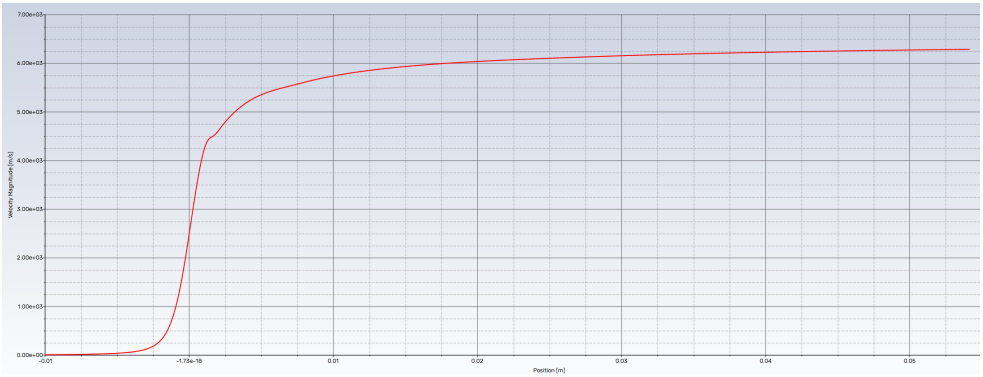

Figure 8.29: Graph showing the exhaust velocity as it travels through the convergent-divergent geometry, with a $9°$ divergent nozzle

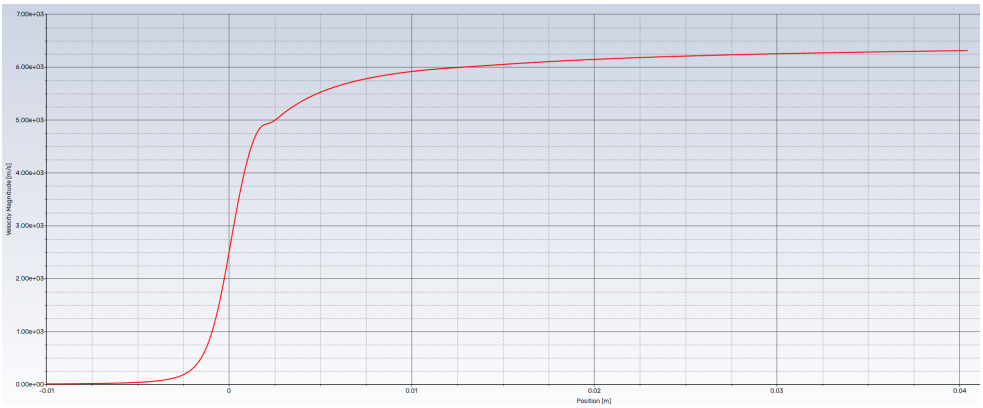

Figure 8.30: Graph showing the exhaust velocity as it travels through the convergent-divergent geometry, with a $12°$ divergent nozzle

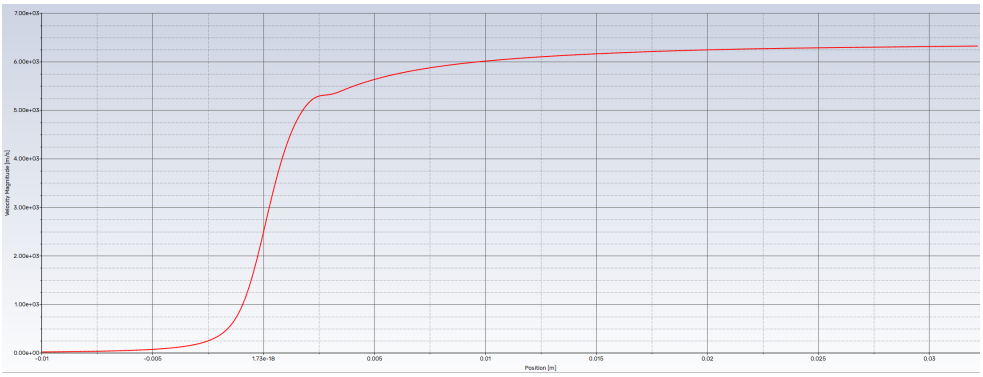

Figure 8.31: Graph showing the exhaust velocity as it travels through the convergent-divergent geometry, with a $15°$ divergent, and $30°$ convergent nozzle

To meet the requirement RCS-Sub-010, it's clear that with the current nozzle design, a change to the input variables may be needed to allow the system to reach the requirement. Thus, implementing an input pressure of $6\ [bar]$ into the 2D steady state simulation (with a $15°$ and $50°$ divergence and convergence angle). The simulation was run for 10000 iterations, reaching a convergence of $1 \cdot 10^{-11}$ to $1 \cdot 10^{-14}$, with a total mass flux of $-2.655 \cdot 10^{-11}\ [kg \cdot s^{-1}$ and a total heat transfer of $14.090\ [W]$. This results in a mass flow rate of $0.172720\ [g \cdot s^{-1}]$ and a thrust of $1.03486\ [N]$, meaning that at a chamber pressure of $6[bar]$ the model meets the requirement. Confirming that the heat-exchanger is capable of handling the increased mass flow rate, the values were implemented into the heat-exchanger sizing code, resulting in a final propellant temperature of $1482.9\ [°K]$, indicating that few changes need to be made to the heat-exchanger design to accommodate the increased chamber pressure.

8.5. Transient CFD Analysis of Nozzle

To determine the start-up of the nozzle, a transient CFD simulation is needed, thus implementing the same input and output pressure as for the steady state system, and implementing the second-order implicit time stepping method. Starting the simulation with 10 $1 \cdot 10^{-4}\ [s]$ time steps to allow the system to capture the nozzle geometry, then allowing the adaptive time stepping algorithm to step in. There was difficulty in getting the simulation to converge to the desired minimums. This was especially true at the start of the simulation, when the fluid flow was not yet well-defined, which led to each iteration using the maximum allowable number of iterations for each time step. Reducing the time step to very small values of $1 \cdot 10^{-8}\ [s]$ did allow the simulation to continue, though, with an estimated completion time of $138.8\ [hours]$ (assuming an individual time step takes $5\ [minutes]$ for a total simulation time of $1\ [ms]$). From the steady-state simulation, it was observed that once the simulation captured the throat of the nozzle, the convergence rate massively increased. After completing some higher time-stepping

simulations to evaluate the time at which the simulation captures the throat, though quite arbitrary, it was chosen to use a time of $1\ [ms]$ at which the throat is captured, splitting the initial $1\ [ms]$ of simulation time into 10, $1 \cdot 10^{-4}\ [s]$ time steps. Whilst this assumption does pin the minimum start time of the thruster to $1\ [ms]$, understanding that the throat may be captured before this time, the chosen value of $1\ [ms]$ is still 3 orders of magnitude below the requirement set by RCS-Sub-040.

Simulating a total of $10\ [ms]$, resulting in a total of 2592 individual time steps to be taken with an average step time of $3.598 \cdot 10^{-6}[s]$. The Velocity profile of the system can be seen in Figure 8.32. Nozzle flow stabilises at a time of $5.82 \cdot 10^{-3}\ [s]$. It can also be seen that again the flow is under-expanded, with the flow continuing to expand past the nozzle.

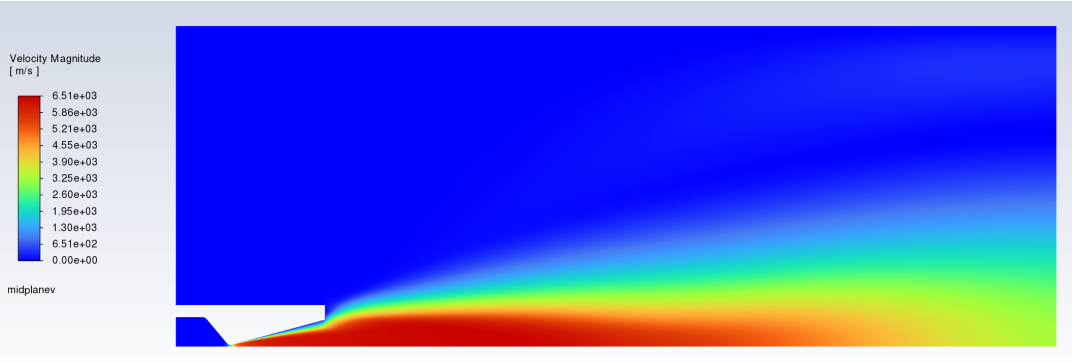

Figure 8.32: Velocity profile for the Transient Nozzle analysis, at a time of $5.82 \cdot^{-3}\ [s]$.

8.6. Validation and Verification of Simulation Results

As with any CFD simulation, it is important to evaluate the accuracy of the results generated. Therefore, the verification and validation of the numerical solutions is a vital process in obtaining accurate and trustworthy results. Thus, in this section, there will be a discussion on the validation and verification of the system in its respective subsections.

8.6.1. Validation

For both the Validation and verification of CFD results, there is still a large amount of discussion on the best protocol to follow. For validation, the current gold standard is the comparison of a real-world physical model of the system to the numerically generated data. However, this requires the creation and execution of a physical test of the system, which is not possible at this time.

One validation process that can be done is the choice of a turbulence model for the calculation of the turbulent flow in the simulation. From the Literature study, [25] provides a comparison of different turbulence models against experimental results, seen in Figure 2.17. This comparison allowed for the Validation of the turbulence models for this flow regime. With the SST k-ω and the v^2-f-2 model providing the best fitting results. The choice of either of these models would increase the trustworthiness of the results, knowing that the models have been validated for a similar flow regime.

8.6.2. Verification

For the verification of the simulation, with the use of a trusted commercial software such as those produced by Ansys, it can be acknowledged that the code has been properly verified and contains no known errors. This leaves the verification of the simulation parameters, mainly the boundary conditions and the meshing of the fluid domain. First, conducting a mesh refinement analysis, where the mesh of the system is refined to different levels to evaluate the effects on the systems thrust. Going on to a perturbation analysis for the boundary conditions, evaluating the effects on the thrust of the system.

The mesh refinement analysis allowed for the verification of the correct mesh sizing. It has already been noted that the mesh for the 3D fluid simulation of the prototype is not refined enough to fully evaluate the flow characteristics throughout the simulation. Therefore, the focus is on the mesh analysis of the 2D Nozzle flow simulation. Thus, simulating three sets of meshes, with increasing refinement, leads

to the graph seen in Figure 8.33. Whilst a more refined mesh would lead to a more accurate result, there is a computational limit, in both computing power and available time, thus a mesh is required that is refined enough to capture the required fluid flow, but still coarse enough to reduce the computing power required. Halving the mesh refinement, reducing the element number on each vertex by two, results in a small increase in thrust, a change of $\sim 0.5\%$. Increasing the mesh refinement leads to a reduction in the thrust by an even smaller amount, a change of $\sim 0.07\%$, whilst taking significantly longer to compute. Taking into account the small changes in thrust due to a change in mesh refinement, it can be verified that the mesh is of sufficient refinement to evaluate the required flow regime.

For the perturbation analysis on the boundary conditions, it is expected of the system that any small changes in the inlet or outlet pressures would result in small changes in the thrust of the system. Thus, evaluating the system for a change in pressure of $\pm 10\ [Pa]$ for both the inlet and outlet pressures, plotting the thrust of the system, seen in Figure 8.34. It can be noted that, indeed, for small changes in inlet pressure, there are in fact only small changes in the thrust of the system; the same can be said for the outlet pressure, though to a lesser extent. Though none of the perturbations cause a change in thrust larger than 0.015%. This verifies that appropriate boundary conditions have been set.

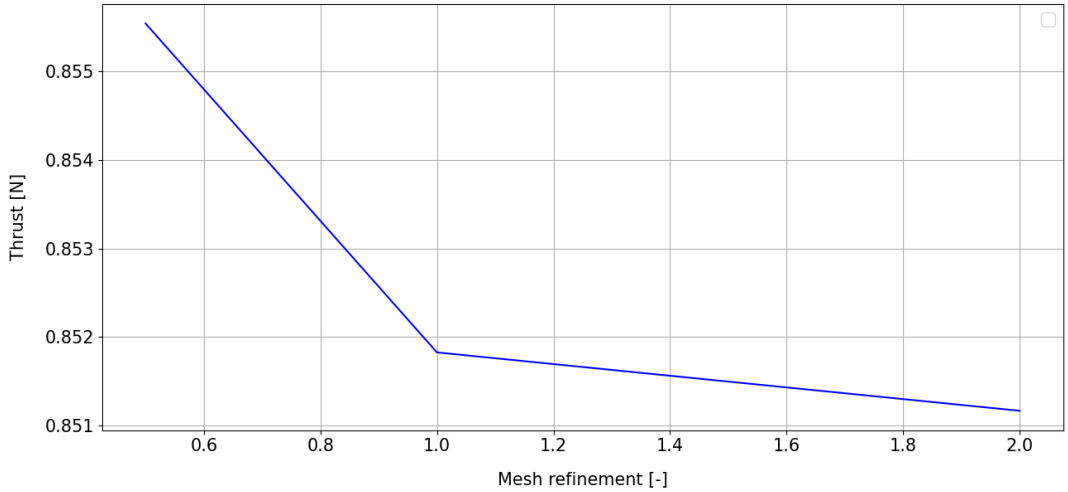

Figure 8.33: Graph showing mesh refinement sensitivity

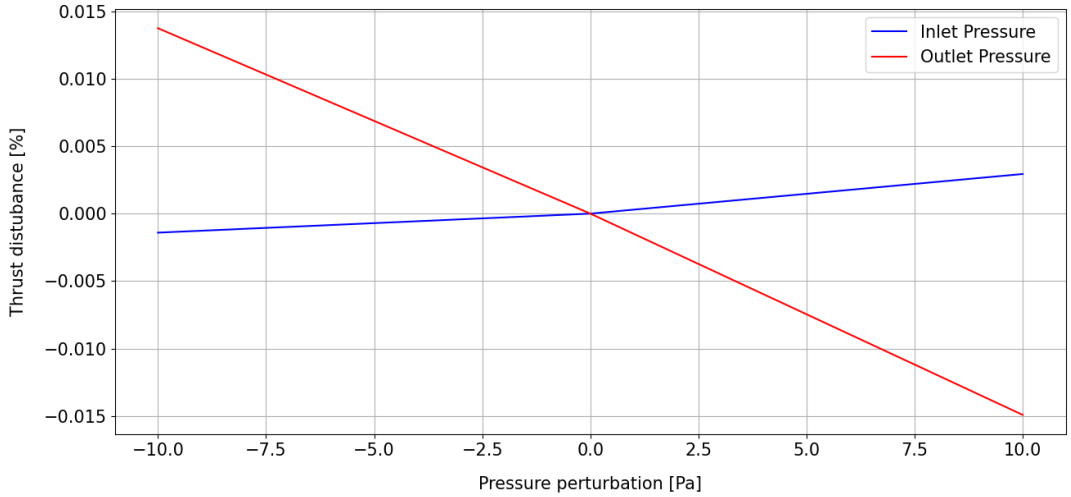

Figure 8.34: Graph showing the results of the perturbation analysis

8.7. Green SWaP Requirement Verification

Having completed the numerical simulations deemed necessary to gather the required data to properly verify the prototype against the Green SWaP requirements. Mainly, the use of a thermal simulation to determine the maximum temperatures and the initial startup time of the system, evaluating RCS-Sub-050 and RCS-Sub-090. The use of a combined thermal and fluid simulation to evaluate the operating temperature and fluid flow through the heat-exchanger, determining if the required chamber temperature and pressures are reached. Finally, completing a simplified 2D simulation of the nozzle to accurately determine the exhaust velocity and thruster characteristics, verifying RCS-Sub-010 to RCS-Sub-050. Having gathered the required data to verify the prototype design, the prototype design can be evaluated against each of the requirements. Going through how the evaluation has changed from the introduction of the numerical models, and providing a final verification of whether the prototype design meets the requirements set.

RCS-Sub-010 - Thrust Level - RCS

The RCS shall provide a vacuum thrust level of more than $1[N]$. - Having previously determined an expected thrust value with the understanding of the assumption made in ideal rocket theory, it was decided that further evaluation is needed. First, the required chamber temperature is met as seen by the steady-state fluid simulation of the system. The chamber pressure does differ from the calculated value with a value of $4.8\ [bar]$. Though the pressure drop can be accounted for by increasing the input pressure further.

To calculate a more accurate thruster performance and capture the boundary layer effects, a 2D nozzle simulation was done, producing a simulated thrust of $0.851827\ [N]$, a difference of 14.8% from the requirement. With potential to increase the thrust through an improvement to the nozzle geometry or the increase of the chamber pressure and/or temperature, as seen in Figure 5.5. Implementing an input pressure of $6\ [bar]$ into the steady state 2D simulation results in a thrust of $1.03486\ [N]$, with a mass flow of $0.172720\ [g \cdot s^{-1}]$.

RCS-Sub-020 - Specific Impulse - RCS

The RCS shall achieve a vacuum specific impulse of more than 500 seconds to ensure efficient propellant utilisation. - With the specific impulse calculated through ideal rocket theory, it indicates that the system should easily meet the requirement. With the completion of the steady state nozzle fluid simulation for the determination of the thrust, the I_{sp} can also be determined. The exhaust velocity of the nozzle being $6.323\ [km \cdot s^{-1}]$, the specific impulse can be calculated to be $644.77\ [s]$. As previously predicted, this is above both the original requirement and the revised requirement when considering the presence of water vapour in the Hydrogen.

RCS-Sub-030 - Total Propellant Throughput - RCS

The main thruster shall be able to achieve a total propellant throughput of $3\ [kg]$ [TBC]. - Having determined that the system should have a total burn time of $\sim 5.6\ [hours]$ using ideal rocket theory. This value can now be reevaluated with the simulation data. With the revised propellant mass flow calculated through the nozzle simulation, that being a mass flow of $0.14339\ [g \cdot s^{-1}]$, producing a total burn time of $5.81\ [hours]$, a slightly longer burn time than calculated through ideal rocket theory, with the result not differing enough to effect the verification of the requirement.

RCS-Sub-040 - Response Time - RCS

The thruster shall be capable of achieving full thrust within $< 5\ [s]$ [TBC] after actuation. - With it previously being evaluated that the system should meet the required response time, there was some uncertainty in this value. Having now completed a series of numerical analyses, a somewhat better prediction could be made. With the transient nozzle simulation requiring a start-up time of about $10\ [ms]$ and the calculated required time for the propellant to pass through the heat exchange of $5 \cdot 10^{-5}\ [s]$. With conservative estimations of total flow time being, $60\ [ms]$. Adding the time required for the heat-exchanger, nozzle, and the time required for the fluid to move from the inlet to the start of the heat-exchanger, estimating a length of $100\ [mm]$ with a velocity of $2\ [m \cdot s^{-1}]$. Whilst there is some uncertainty in the results, with no transient simulation being done on the whole system, the value is still two orders of magnitude lower than the requirement.

RCS-Sub-050 - Reignition Time - RCS
The RCS shall be able to reignite after a minimum of [TBD] seconds. - Having previously estimated a maximum reignition time of $29.96\ [s]$ and $33.60\ [s]$ for a material choice of Molybdenum and Rhenium, respectively. From the conducted transient thermal simulation, it can be seen that the numerically calculated reignition time for the design is $26.0\ [s]$ and $31.2\ [s]$ for Molybdenum and Rhenium, respectively. This is a slight reduction from the previous estimated values. Whilst there is no current value associated with the requirement, the reignition times calculated for this prototype are relatively low compared to other STP systems and should meet the requirement.

RCS-Sub-060 - Minimum Impulse Bit - RCS
The RCS shall be able to provide a minimum impulse bit of $100\ [mN \cdot s]$ [TBC]. - The verification of the impulse bit lies in the response time of the system, from start-up to shut-down. With the previous calculation of the thruster startup being $\sim 0.1\ [ms]$, it was stated that the system should easily meet the requirement. Having now revised the response time of the system to be $60\ [ms]$ for a conservative estimation, the verification can be revised. Whilst there is a large increase in the total response time of the system, this is a conservative estimation. The value is still below the required $100\ [ms]$ to produce a $100\ [mN \cdot s]$ impulse bit with $1\ [N]$ of thrust. Though with the reduced system thrust gained through simulation, the burn time required for a $100\ [mN \cdot s]$ impulse bit slightly increases.

RCS-Sub-070 - Thrust Accuracy – RCS
Each RCS thruster shall deliver a thrust level with a total uncertainty less than 10% (TBC) (3 sigma) with respect to the selected nominal thrust value. - Having previously evaluated that there is uncertainty in how the system's throughput is affected by external factors, with ideal rocket theory providing an idealised value. Whilst Figure 5.5, indicates the thrust sensitivity to changes in chamber pressure and temperature. With temperature swings of $\pm 500\ [^{\circ}K]$ having little effect on the thrust, and pressure inducing large changes, limiting a maximal deviation of $\pm 0.5\ [bar]$ from the nominal value.

For the thrust uncertainty, no repeated numerical nozzle simulations are being generated to evaluate the thrust at different input pressures and temperatures. Ideal rocket theory can be used to estimate the sensitivity of the thrust to changes in the chamber pressure and temperature, indicating that a change in temperature of $500\ [^{\circ}K]$ in either direction would have little change on the thrust. It is also noted that a change in chamber pressure of $0.5\ [bar]$ breaks the thrust uncertainty requirement.

RCS-Sub-080 - Power Consumption - RCS
The RCS shall not exceed [TBD] W of electrical power peak. - The system does not take into account any electronic devices that require power, meaning that no electrical power is required for this thruster to function.

RCS-Sub-090 - Propellant Compatibility - RCS
All RCS components shall be compatible with the propellants used by the system. - As stated before, the choice in materials has been confirmed to be able to withstand the expected thermal load whilst being compatible with the use of Hydrogen. The use of metals and not ceramics reduces the risk in manufacturing the parts as well as the potential for leakage with ceramics porous nature.

9

Conclusion & Future Work

Having developed a verified prototype design, a conclusion can be made on the project and a suggestion of potential future work to further evaluate the prototype design. Thus, in this chapter, the conclusion and future work will be illustrated in their respective sections.

9.1. Conclusion

With the ever-growing industrialisation of space, there is a need to increase the longevity of space missions. The total lifetime of many space missions, especially in low Earth orbit, is limited not by their components' malfunctioning but by the amount of propellant that is stored when launched. The lifetime of these spacecraft can be increased if they could produce their own propellant. To this extent, the Green Solar-to-Propellant Water Propulsion project (Green SWaP) aims to develop a system capable of converting water into propellant to be used by the system. With the mission statement being "To use solar energy to produce propellants onboard the spacecraft by converting water (H_2O) to propellants, H_2O_2 and H_2, developing innovative propulsion systems based on them." The specific aim of this report is the creation of a prototype thruster design for the reaction control system. Producing an efficient, accurate and reliable prototype that can be used for the validation of the use of a solar thermal propulsion system as a reaction control system thruster.

The paper developed a prototype thruster, generated through a concept generation and elimination process. Using a combination of analytical analysis using ideal rocket theory, fundamental thermodynamics equations, and the use of numerical simulation tools to provide the required data to properly evaluate and verify the prototype design against the requirements set by Green SWaP. Producing a potential prototype design for the Green SWaP project that has been carefully evaluated and verified against the requirements. The prototype is an efficient, accurate and reliable thruster. Having a nominal thrust of $0.851827\ [N]$, a deviation of 14.8% from the requirement, with potential to increase the thrust through an increased chamber pressure. A specific impulse value well above the requirement at $644.77\ [s]$, meeting all requirements set by Green SWaP. However, whilst this prototype does meet the requirements, it can not be called the most optimal design. With this being the first iteration of the design, some aspects could be improved and further investigated.

With this prototype, the use of a solar thermal propulsion system as a thruster for the reaction control system can be validated, furthering the mission goals of the Green SWaP project and bringing the industry one step closer to in-orbit propellant production capability.

9.2. Further Work

Throughout this report, there have been several points of interest that may warrant further investigation. Thus, in this section, suggestions will be made on how these ideas could improve the design and should be further investigated.

As alluded to in the conclusion, this concept can not be considered to be the most optimal design.

Several improvements could be made to the design, one of the most impactful is the better utilisation of the cooling channel between the system core and the outer housing. Currently being a large void, the propellant already reached $\sim 1000\ [^{\circ}K]$ before entering the heat-exchanger channels. The use of a preliminary helical channel instead of a void would increase the effectiveness of the cooling channels to cool the nozzle and improve the pre-heating effect on the propellant, allowing for an overall smaller thruster design, reducing mass and cost.

With the increased use of 3D printing and the benefits it could provide, there are two main developments of interest for an STP system. The first being the ability to print selective porous parts. This allows for the creation of a single part, where the porosity can be increased for select regions, allowing for propellant to flow, effectively increasing the convective heat transfer rate. An increased porosity could also act as insulation, reducing the thermal conductivity of the material, allowing for the isolation of the core from the nozzle or the ambient environment. The other is allowing for the creation of much more complex geometries, not possible with subtractive manufacturing. A good example of this would be the implementation of a gyroid, an infinite mathematical description of a single surface that separates a set volume into two distinct but continuous volumes. Because of these features, gyroids have long been sought after for heat-exchangers, with their separated volumes, very high surface area to volume ratio, and their impeccable strength and stiffness properties. An implementation of this geometry could increase the effective surface area of the heat-exchanger, reducing the overall size of the system.

The use of a more complex nozzle geometry, such as a bell/contour nozzle, could be done to increase the efficiency of the system further, once a known expansion ratio has been set for the design. The implementation of a multi-nozzle array could also be of great interest, especially for use in a reaction control system. With an array of nozzles theoretically providing the system with thrust vectoring capabilities through careful activation of individual thrusters in the array. Potentially allowing for a lower total number of thrusters needed for the RCS system.

Whilst this report does include an investigation into separate cavity geometries and materials for the absorption cavity, there are a lot more opportunities to investigate further. With a more in-depth investigation of the cavity, with respect to the conductive pathways to the propellant channels, and more complex geometries providing a more even luminosity gradient over the cavity length. The use of different coatings and materials to change the surface properties of the cavity should also be investigated, potentially increasing the cavity's absorption capabilities.

As mentioned before, the implementation of a better thermal battery would be a welcome addition to the system for its operational use case. The use of a phase switching material is often of interest, with a common material used for high temperatures being table salt, with a relatively high specific heat and heat of fusion. However, table salt has a melting point of around $800\ [^{\circ}C]$ far below the target temperature; therefore, it becomes difficult to find a material that has a phase transition at the required temperature, preferably from solid to liquid, that is compatible with the other elements in the design. With the highest potential being the metals such as Nickel or Titanium, which melt at $1750 - 1950\ [^{\circ}K]$ respectively.

Though the use of ceramics was not implemented in this report, they do have excellent high-temperature resistance and reduced density compared to the high-temperature metals available. For a higher temperature version of the prototype, the use of ceramics may indeed be needed. Thus, it is recommended to evaluate the use of ceramics for an STP system at this scale, focusing on the creation of single-element parts or the furthering of high-temperature bonding methodology for ceramics.

References

[1] *Brief History of Rockets*. URL: https://www.grc.nasa.gov/www/k-12/TRC/Rockets/history_of_rockets.html (visited on 02/19/2025).

[2] Stephen G. Haw. “Cathayan Arrows and Meteors: The Origins of Chinese Rocketry”. In: *Journal of Chinese Military History* 2.1 (2013), pp. 28–42. ISSN: 2212-7445, 2212-7453. DOI: 10.1163/22127453-12341243. URL: https://brill.com/view/journals/jcmh/2/1/article-p28_2.xml (visited on 02/19/2025).

[3] Jules Verne. *From the Earth to the Moon: Direct in 97 Hours 20 Minutes*. Google-Books-ID: ljK-Fxh0bLUEC. Sampson Low, Marston, Searle, & Rivington, 1876. 162 pp.

[4] K. E. Tsiolkovskiy. *Collected Works of K. E. Tsiolkovskiy*. URL: http://epizodsspace.airbase.ru/bibl/inostr-yazyki/tsiolkovskii/tsiolkovskii-nhedy-t2-1954.pdf (visited on 02/19/2025).

[5] B.T.C. Zandbergen and Delft University of Technology Faculty of Aerospace Engineering. *Thermal rocket propulsion (version 2.04): Ae4S01*. Section: .. cm. Delft: TU Delft, 2010.

[6] J. L. Turner Martin. *Rocket and Spacecraft Propulsion: Principles, Practice and New Developments*. ISBN: 9783540692034. ISBN: 978-3-540-69203-4. URL: https://www.researchgate.net/publication/321562822_Rocket_and_Spacecraft_Propulsion_Principles_Practice_and_New_Developments (visited on 02/17/2025).

[7] *RS-25*. In: *Wikipedia*. Page Version ID: 1270402974. Jan. 19, 2025. URL: https://en.wikipedia.org/w/index.php?title=RS-25&oldid=1270402974 (visited on 02/19/2025).

[8] Javier Martínez Martínez and Trevor Lafleur. “On the selection of propellants for cold/warm gas propulsion systems”. In: *Acta Astronautica* 212 (Nov. 1, 2023), pp. 54–69. ISSN: 0094-5765. DOI: 10.1016/j.actaastro.2023.07.031. URL: https://www.sciencedirect.com/science/article/pii/S0094576523003806 (visited on 02/20/2025).

[9] *Space Shuttle Main Engine (SSME) Enhancements*. FS-2002-03-60-MSFC. Marshall Space Flight Center: NASA, Mar. 2002. URL: https://www.nasa.gov/wp-content/uploads/2016/08/174534main_ssme.pdf (visited on 02/20/2025).

[10] P. Harold and Jr. Gerrish. “Solar Thermal Propulsion at MSFC”. Propulsion Systems Division Marshall Space Flight Center, Feb. 3, 2016. URL: https://ntrs.nasa.gov/api/citations/20160003173/downloads/20160003173.pdf (visited on 02/24/2025).

[11] *High temperature latent heat thermal energy storage to augment solar thermal propulsion for microsatellites - ProQuest*. URL: https://www.proquest.com/openview/0b0d53833180dabebb814f0e07e5c242/1.pdf?pq-origsite=gscholar&cbl=18750 (visited on 02/24/2025).

[12] F. G Ethridge. *Solar Rocket System Concept Analysis*. AFRPL-TR-79-79. Rockwell International, Dec. 1979.

[13] Charles R. Ford. *SOLAR THERMAL PROPULSION FOR ORBIT TRANSFER VEHICLES*. Air Force Astronautics Laboratory, Jan. 11, 1988, pp. 345–349. URL: https://www.osti.gov/servlets/purl/5580004#page=364 (visited on 02/18/2025).

[14] M. H. D. Kemp. “Solar-powered space flight”. In: *The Aeronautical Journal* 109.1102 (Dec. 2005), pp. 619–630. ISSN: 0001-9240, 2059-6464. DOI: 10.1017/S0001924000000956. URL: https://www.cambridge.org/core/product/identifier/S0001924000000956/type/journal_article (visited on 02/18/2025).

[15] F. G. Kennedy, P. Henshall, and D. Gibbon. “Preparing for Flight: The Surrey Space Centre’s Microscale Solar Thermal Propulsion Experiment”. In: 555 (Oct. 1, 2004). Conference Name: 4th International Spacecraft Propulsion Conference ADS Bibcode: 2004ESASP.555E..74K, p. 74.1. URL: https://ui.adsabs.harvard.edu/abs/2004ESASP.555E..74K (visited on 03/12/2025).

[16] Constantin Sandu et al. “On a New Type of Combined Solar–Thermal/Cold Gas Propulsion System Used for LEO Satellite’s Attitude Control”. In: *Applied Sciences* 10.20 (Jan. 2020). Number: 20 Publisher: Multidisciplinary Digital Publishing Institute, p. 7197. ISSN: 2076-3417. DOI: 10.3390/app10207197. URL: https://www.mdpi.com/2076-3417/10/20/7197 (visited on 02/17/2025).

[17] Fiona Leverone et al. “Design and characterisation of a bi-modal solar thermal propulsion and power system for small satellites”. In: *Applied Thermal Engineering* 189 (May 5, 2021), p. 116609. ISSN: 1359-4311. DOI: 10.1016/j.applthermaleng.2021.116609. URL: https://www.sciencedirect.com/science/article/pii/S135943112100065X (visited on 02/17/2025).

[18] Leonard Vance et al. “A Solar Thermal Steam Propulsion System Using Disassociated Steam for Interplanetary Exploration”. In: *Aerospace* 11.1 (Jan. 2024). Number: 1 Publisher: Multidisciplinary Digital Publishing Institute, p. 84. ISSN: 2226-4310. DOI: 10.3390/aerospace11010084. URL: https://www.mdpi.com/2226-4310/11/1/84 (visited on 02/17/2025).

[19] Shivang Khare and Ujjwal K Saha. “Rocket nozzles: 75 years of research and development”. In: *Sādhanā* 46.2 (June 2021), p. 76. ISSN: 0256-2499, 0973-7677. DOI: 10.1007/s12046-021-01584-6. URL: https://link.springer.com/10.1007/s12046-021-01584-6 (visited on 02/17/2025).

[20] G. V. R. Rao. “Recent Developments in Rocket Nozzle Configurations”. In: *ARS Journal* 31.11 (Nov. 1961), pp. 1488–1494. ISSN: 1936-9972. DOI: 10.2514/8.5837. URL: https://arc.aiaa.org/doi/10.2514/8.5837 (visited on 03/14/2025).

[21] “Engine Requirements and Preliminary Design Analyses”. In: *Modern Engineering for Design of Liquid-Propellant Rocket Engines*. Progress in Astronautics and Aeronautics. American Institute of Aeronautics and Astronautics, Jan. 1992, pp. 23–51. ISBN: 978-1-56347-013-4. DOI: 10.2514/5.9781600866197.0023.0051. URL: https://arc.aiaa.org/doi/10.2514/5.9781600866197.0023.0051 (visited on 03/26/2025).

[22] Go Guderley and E Hantsch. “Beste Formen für achsensymmetrische überschallschubdüsen”. In: *Zeitschrift für Flugwissenschaften* 3.9 (1955), pp. 305–313.

[23] Jeffrey G. Allman and Joe D. Hoffman. “Design of Maximum Thrust Nozzle Contours by Direct Optimization Methods”. In: *AIAA Journal* 19.6 (1981). Publisher: American Institute of Aeronautics and Astronautics _eprint: https://doi.org/10.2514/3.50999, pp. 750–751. ISSN: 0001-1452. DOI: 10.2514/3.50999. URL: https://doi.org/10.2514/3.50999 (visited on 03/26/2025).

[24] Manuel Frey, Konrad Makowka, and Thomas Aichner. “The TICTOP nozzle: a new nozzle contouring concept”. In: *CEAS Space Journal* 9.2 (June 1, 2017), pp. 175–181. ISSN: 1868-2510. DOI: 10.1007/s12567-016-0139-z. URL: https://doi.org/10.1007/s12567-016-0139-z (visited on 03/26/2025).

[25] A. Balabel et al. “Assessment of turbulence modeling for gas flow in two-dimensional convergent–divergent rocket nozzle”. In: *Applied Mathematical Modelling* 35.7 (July 1, 2011), pp. 3408–3422. ISSN: 0307-904X. DOI: 10.1016/j.apm.2011.01.013. URL: https://www.sciencedirect.com/science/article/pii/S0307904X11000266 (visited on 03/14/2025).

[26] Pauline M. Doran. “Chapter 7 - Fluid Flow”. In: *Bioprocess Engineering Principles (Second Edition)*. Ed. by Pauline M. Doran. London: Academic Press, Jan. 1, 2013, pp. 201–254. ISBN: 978-0-12-220851-5. DOI: 10.1016/B978-0-12-220851-5.00007-1. URL: https://www.sciencedirect.com/science/article/pii/B9780122208515000071 (visited on 03/28/2025).

[27] A. Sveningsson and L. Davidson. “Assessment of realizability constraints in v^2f turbulence models”. In: *International Journal of Heat and Fluid Flow*. Selected papers from the 4th International Symposium on Turbulence Heat and Mass Transfer 25.5 (Oct. 1, 2004), pp. 785–794. ISSN: 0142-727X. DOI: 10.1016/j.ijheatfluidflow.2004.05.014. URL: https://www.sciencedirect.com/science/article/pii/S0142727X0400092X (visited on 03/28/2025).

[28] *Reynolds stress model (RSM) – CFD-Wiki, the free CFD reference*. URL: https://www.cfd-online.com/Wiki/Reynolds_stress_model_(RSM) (visited on 03/28/2025).

[29] G. Grossman and G. Williams. “Inflatable Concentrators for Solar Propulsion and Dynamic Space Power”. In: *Journal of Solar Energy Engineering* 112.4 (Nov. 1, 1990), pp. 229–236. ISSN: 0199-6231. DOI: 10.1115/1.2929928. URL: https://doi.org/10.1115/1.2929928 (visited on 03/31/2025).

[30] Mark O’Neill et al. “Ultralight stretched Fresnel lens solar concentrator for space power applications”. In: *Proc SPIE* (Dec. 2003). DOI: 10.1117/12.505801.

[31] Mark Joseph O’Neill. “Inflatable fresnel lens solar concentrator for space power”. U.S. pat. 6111190A. Entech Inc. Aug. 29, 2000. URL: https://patents.google.com/patent/US6111190A/en (visited on 04/01/2025).

[32] Mark Joseph O’Neill. “Stretched Fresnel lens solar concentrator for space power”. U.S. pat. 6075200A. Entech Inc. June 13, 2000. URL: https://patents.google.com/patent/US6075200A/en (visited on 04/01/2025).

[33] *The Fresnel zone plate antenna : design and analysis*. Research portal Eindhoven University of Technology. URL: https://research.tue.nl/en/studentTheses/the-fresnel-zone-plate-antenna-design-and-analysis (visited on 04/01/2025).

[34] Sandip K. Chakrabarti et al. “Fresnel zone plate telescopes for X-ray imaging I: experiments with a quasi-parallel beam”. In: *Experimental Astronomy* 24.1 (May 2009), pp. 109–126. ISSN: 0922-6435, 1572-9508. DOI: 10.1007/s10686-009-9144-y. arXiv: 0910.1987[astro-ph]. URL: http://arxiv.org/abs/0910.1987 (visited on 04/01/2025).

[35] Figen S. Oktem, Farzad Kamalabadi, and Joseph M. Davila. “Analytical Fresnel imaging models for photon sieves”. In: *Optics Express* 26.24 (Nov. 26, 2018). Publisher: Optica Publishing Group, pp. 32259–32279. ISSN: 1094-4087. DOI: 10.1364/OE.26.032259. URL: https://opg.optica.org/oe/abstract.cfm?uri=oe-26-24-32259 (visited on 03/31/2025).

[36] C. C. Selph. *The Place of Solar Thermal Rockets in Space:* Fort Belvoir, VA: Defense Technical Information Center, May 1, 1981. DOI: 10.21236/ADA407602. URL: http://www.dtic.mil/docs/citations/ADA407602 (visited on 04/02/2025).

[37] Reginald Alexander and Hugh Coleman. “Thermal Characterization of a Direct Gain Solar Thermal Engine”. In: *Journal of Spacecraft and Rockets* 38 (Nov. 1, 1999). DOI: 10.2514/2.3683.

[38] F. Kennedy, P.L. Palmer, and D. Gibbon. “Design and Proto-Flight Test Strategy for a Microscale Solar Thermal Engine”. In: *Space Technology* -1 (Dec. 31, 2001), p. 815.

[39] “Pressureless consolidation of boron nitride fiber ceramics via a chemical bonding approach”. In: *Journal of the European Ceramic Society* 43.12 (Sept. 1, 2023). Publisher: Elsevier, pp. 5223–5230. ISSN: 0955-2219. DOI: 10.1016/j.jeurceramsoc.2023.05.004. URL: https://www.sciencedirect.com/science/article/pii/S0955221923003552 (visited on 04/03/2025).

[40] *What Temperature Does Steel Melt? - SteelPRO Group*. Section: Properties. Aug. 1, 2024. URL: https://steelprogroup.com/manufacturing/property-1/melting-point/ (visited on 04/03/2025).

[41] Matter Beam. *ToughSF: Liquid Rhenium Solar Thermal Rocket*. ToughSF. Oct. 23, 2017. URL: https://toughsf.blogspot.com/2017/10/liquid-rhenium-solar-thermal-rocket.html (visited on 04/03/2025).

[42] Aïmen E. Gheribi, Jesus A. Torres, and Patrice Chartrand. “Recommended values for the thermal conductivity of molten salts between the melting and boiling points”. In: *Solar Energy Materials and Solar Cells* 126 (July 1, 2014), pp. 11–25. ISSN: 0927-0248. DOI: 10.1016/j.solmat.2014.03.028. URL: https://www.sciencedirect.com/science/article/pii/S0927024814001597 (visited on 02/18/2025).

[43] H. F. Calcote et al. “Spark Ignition. Effect of Molecular Structure.” In: *Industrial & Engineering Chemistry* 44.11 (Nov. 1952), pp. 2656–2662. ISSN: 0019-7866, 1541-5724. DOI: 10.1021/ie50515a048. URL: https://pubs.acs.org/doi/abs/10.1021/ie50515a048 (visited on 04/05/2025).

[44] Eugene et al. *Safety*. Jan. 1, 2022. DOI: 10.1016/B978-0-323-90394-3.00011-4. URL: https://www.sciencedirect.com/science/article/pii/B9780323903943000114 (visited on 04/05/2025).

[45] Ju et al. “Recent research progress in hydrogen embrittlement of additively manufactured metals – A review”. In: *Current Opinion in Solid State and Materials Science* 27.5 (Oct. 1, 2023). Publisher: Elsevier, p. 101106. ISSN: 1359-0286. DOI: 10.1016/j.cossms.2023.101106. URL: https://www.sciencedirect.com/science/article/pii/S1359028623000517 (visited on 04/05/2025).

[46] H. et al. *Stress corrosion cracking (SCC) of austenitic stainless and ferritic steel weldments*. Jan. 1, 2011. DOI: 10.1533/9780857093769.3.427. URL: https://www.sciencedirect.com/science/article/pii/B9781845696733500122 (visited on 04/05/2025).

[47] *WebElements Periodic Table » Hydrogen » properties of compounds*. URL: https://www.webelements.com/hydrogen/compound_properties.html (visited on 04/05/2025).

[48] T.P Herbell et al. *(PDF) Effect of hydrogen on the strength and microstructure of selected ceramics*. ResearchGate. URL: https://www.researchgate.net/publication/236567602_Effect_of_hydrogen_on_the_strength_and_microstructure_of_selected_ceramics (visited on 04/05/2025).

[49] Alfonso Magliano et al. “A Comprehensive Literature Review on Hydrogen Tanks: Storage, Safety, and Structural Integrity”. In: *Applied Sciences* 14.20 (Jan. 2024). Number: 20 Publisher: Multidisciplinary Digital Publishing Institute, p. 9348. ISSN: 2076-3417. DOI: 10.3390/app14209348. URL: https://www.mdpi.com/2076-3417/14/20/9348 (visited on 04/16/2025).

[50] Jun Ishimoto and Satoru Shimada. “Coupled computing for reactive hydrogen leakage phenomena with crack propagation in a pressure tank”. In: *International Journal of Hydrogen Energy* 47.4 (Jan. 12, 2022), pp. 2735–2758. ISSN: 0360-3199. DOI: 10.1016/j.ijhydene.2021.10.167. URL: https://www.sciencedirect.com/science/article/pii/S0360319921042245 (visited on 04/16/2025).

[51] *2021-Nammo-Cheltenham-Spacecraft-Cold-Gas-Thruster-Valve.pdf*. URL: https://www.nammo.com/wp-content/uploads/2021/03/2021-Nammo-Cheltenham-Spacecraft-Cold-Gas-Thruster-Valve.pdf (visited on 10/24/2025).

[52] Andrew Petro et al. “A flight demonstration of plasma rocket propulsion”. In: *36th AIAA/ASME/SAE/ASEE Joint Propulsion Conference and Exhibit*. 36th AIAA/ASME/ SAE/ASEE Joint Propulsion Conference and Exhibit. Las Vegas,NV,U.S.A.: American Institute of Aeronautics and Astronautics, July 24, 2000. DOI: 10.2514/6.2000-3751. URL: https://arc.aiaa.org/doi/10.2514/6.2000-3751 (visited on 06/10/2025).

[53] *Open-source chemical kinetics, thermodynamics, and transport — Cantera*. URL: https://cantera.org/ (visited on 08/15/2025).

[54] Susana Cortés Borgmeyer, Susana Cortes-Borgmeyer, and Ariane Group. “ORBITAL PROPULSION ROBERT-KOCH-STRASSE 1 82024 TAUFKIRCHEN GERMANY”. In: ().

[55] Jon Herman and Will Usher. “SALib: An open-source Python library for Sensitivity Analysis”. In: *The Journal of Open Source Software* 2.9 (Jan. 10, 2017), p. 97. ISSN: 2475-9066. DOI: 10.21105/joss.00097. URL: http://joss.theoj.org/papers/10.21105/joss.00097 (visited on 12/11/2025).

[56] J McCarthy and H Wolf. *THE HEAT TRANSFER CHARACTERISTICS OF GASEOUS HYDROGEN AND HELIUM*. NP-10572, RR-60-12, 48427 92. Dec. 1, 1960, NP–10572, RR–60–12, 48427 92. DOI: 10.2172/4842792. URL: https://www.osti.gov/servlets/purl/4842792/ (visited on 07/28/2025).

[57] Lotfi Zeghadnia, Jean Loup Robert, and Bachir Achour. “Explicit solutions for turbulent flow friction factor: A review, assessment and approaches classification”. In: *Ain Shams Engineering Journal* 10.1 (Mar. 1, 2019), pp. 243–252. ISSN: 2090-4479. DOI: 10.1016/j.asej.2018.10.007. URL: https://www.sciencedirect.com/science/article/pii/S2090447919300176 (visited on 07/29/2025).

[58] D. Marple. “Spectral Emissivity of Rhenium”. In: *Journal of the Optical Society of America* 46 (July 1, 1956), pp. 490–494. DOI: 10.1364/JOSA.46.000490.

[59] *Speos Knowledge Base – Ansys Optics*. URL: https://optics.ansys.com/hc/en-us/categories/6336944969107-Speos-Knowledge-Base (visited on 10/15/2025).

[60] *Periodic Table – Royal Society of Chemistry*. URL: https://periodic-table.rsc.org/ (visited on 10/17/2025).

[61] *Thermal Conductivity of Metals and Alloys: Data Table & Reference Guide*. URL: https://www.engineeringtoolbox.com/thermal-conductivity-metals-d_858.html (visited on 10/17/2025).

[62] *Linear Thermal Expansion Coefficients of Materials*. URL: https://www.engineeringtoolbox.com/linear-expansion-coefficients-d_95.html (visited on 10/17/2025).

[63] *Niobium/Tantalum Price Today | Niobium/Tantalum Spot Price Chart | Historical Price of Niobium/Tantalum - Shanghai Metal Market*. URL: https://www.metal.com/en/markets/20 (visited on 12/03/2025).

[64] *Properties: Molybdenum (Mo) - Properties, Applications*. AZoM. URL: https://www.azom.com/properties.aspx?ArticleID=616 (visited on 10/17/2025).

[65] *Daily Metal Price: Ruthenium Price (USD / Kilogram) for the Last Month*. URL: https://www.dailymetalprice.com/metalprices.php (visited on 12/03/2025).

[66] *Material Science | News | Materials Engineering | News*. AZoM. URL: https://www.azom.com/ (visited on 10/17/2025).

[67] *Hafnium Price Today - Market Overview & Long-Term Outlook*. Nov. 10, 2025. URL: https://earthrarest.com/hafnium/price/ (visited on 12/03/2025).

[68] *Tungsten Powder price today | Historical Tungsten Powder Price Charts | SMM Metal Market*. URL: https://www.metal.com/Tungsten/201308090022 (visited on 12/03/2025).

[69] *Current osmium price 2025 □ in EUR, USD & CHF | Osmium chart, price, price trend & performance of the precious metal*. MetaMetals. URL: https://metametals.com/osmium-price (visited on 12/03/2025).

[70] P. Rebesan et al. “Pure molybdenum manufactured by Laser Powder Bed Fusion: Thermal and mechanical characterization at room and high temperature”. In: *Additive Manufacturing* 47 (Nov. 1, 2021), p. 102277. ISSN: 2214-8604. DOI: 10.1016/j.addma.2021.102277. URL: https://www.sciencedirect.com/science/article/pii/S2214860421004371 (visited on 10/20/2025).

[71] *Additive manufacturing of refractory metals | Plansee*. URL: https://www.plansee.com/en/expertise/manufacturing-and-technology/www.plansee.com/en/expertise/manufacturing-and-technology/additive-manufacturing.html (visited on 10/20/2025).

[72] Baizhen He et al. “Influence of roughness and temperature on the emissivity of molybdenum in RTPV system”. In: *Materials Today Communications* 40 (Aug. 1, 2024), p. 110102. ISSN: 2352-4928. DOI: 10.1016/j.mtcomm.2024.110102. URL: https://www.sciencedirect.com/science/article/pii/S235249282402083X (visited on 12/01/2025).

[73] *15.6. Setting Up the k-ω Model*. URL: https://ansyshelp.ansys.com/Views/Secured/corp/v242/en/flu_ug/flu_ug_k_omega_setup.html (visited on 12/15/2025).

[74] *15.8. Setting Up the Transition SST Model*. URL: https://ansyshelp.ansys.com/Views/Secured/corp/v242/en/flu_ug/flu_ug_sst_trans_setup.html (visited on 12/15/2025).

[75] *36.21. Convergence and Stability*. URL: https://ansyshelp.ansys.com/public//Views/Secured/corp/v242/en/flu_ug/flu_ug_sec_solve_conv_stab.html (visited on 12/16/2025).

A

Trade-Off Matrixes

For the generation of the weighting of the criteria, a decision matrix can be made to provide a less biased interpretation of the weights. Thus, for this appendix, the decision matrices will be given for the weighting of the trade-off tables produced throughout this report. Providing both the matrices themselves and a discussion on the decisions made.

Concept Evaluation Criteria Weighting

Determining the weighting of the criteria for the trade-off process of the concept evaluation. With the criteria being derived from the requirements set by Green SWaP, the weighting can be determined by evaluating the relevance of each of the criteria to the requirements. The reasoning behind the decision made is listed below. It can once again be determined that the requirement RCS-Sub-080 does not affect the weighting of the requirements. The performance and responsivity criteria are the main driving criteria for the trade-off process.

- **Reliability** - RCS-Sub-030 directly refers to the total propellant throughput of the system relating to the expected lifespan of the system. RCS-Sub-090 also refers to the compatibility of the material, with material choice heavily affecting the reliability of the design.
- **Performance** - RCS-Sub-010 and RCS-Sub-020 directly refer to the required performance for thrust and specific impulse, respectively. Whilst not a part of the Green SWaP requirements, the mass and cost also affect the performance of the system with respect to the existing commercially available RCS system.
- **Accuracy** - RCS-Sub-060 directly refers to the accuracy requirements for the thrust of the system. Where RCS-Sub-070 refers to the minimum impulse bit, where high thrust accuracy is required to achieve this value.
- **Responsivity** - RCS-Sub-040 to RCS-Sub-060, all refer to how responsive the system is, with RCS-Sub-040 directly relating to the response time of the system. RCS-Sub-050 refers to the time required for the system to be operational from a dormant state. RCS-Sub-060 requires very high responsivity to achieve the required minimum impulse bit.

Table A.1: Decision matrix, to evaluate the weighting of the criteria for the concept trade-off

	RCS-Sub-010	RCS-Sub-020	RCS-Sub-030	RCS-Sub-040	RCS-Sub-050	RCS-Sub-060	RCS-Sub-070	RCS-Sub-080	RCS-Sub-090	INT-Mass-010	INT-Cost-020	Total Wieght
Reliability			x						x			0.1818
Performance	x	x								x	x	0.3636
Accuracy						x	x					0.1818
Responsivity				x	x	x						0.2727

Material Choice Criteria Weighting

For the weighting of the criteria for the material choice for the thruster, the decision matrix can be seen in Table A.2. The matrix implements the nine requirements set by Green SWaP and two internal requirements for mass and cost reduction. Then, for each of the criteria, it is determined if the criterion is relevant to the requirement; if so, the cell is marked with an x. The total weight for each criterion is the number of markers received divided by the total number of markers placed. This approach aims to provide a less biased evaluation of the criteria weighting, with the decisions for each criterion being provided below. It can be noted that RCS-Sub-010 and RCS-Sub-080 did not have an effect on the criteria weighting. For RCS-Sub-080, this is rather obvious as the material choice does not affect the electrical power draw of the system. For RCS-Sub-010, it has been assumed that the thrust value would be held constant throughout the Ideal rocket sizing. Whilst an increase in the exhaust speed of the thruster would result in higher thrust for a constant mass flow, it is assumed that the mass flow would be reduced to bring the thrust back in line with the requirement.

- **Melting Point** - The melting point of the metal is clearly a factor when considering that the choice should be compatible with the propellant [RCS-Sub-090]. The higher the melting point, the higher the theoretical temperature of the propellant, leading to higher specific impulse, [RCS-Sub-020].
- **Density** - The density of the Thruster material in itself has little effect on the performance of the rocket, other than for its mass [INT-Mass-010].
- **Thermal Conductivity** - The higher the thermal conductivity, the smaller the temperature difference between the cavity surface and the propellant channels, leading to potentially higher propellant temperatures, [RCS-Sub-020]. Higher thermal conductivity also leads to faster heating of the thruster to operating temperatures [RCS-Sub-040, RCS-Sub-050]. Higher thermal conductivity generally also provides smoother temperature distributions, leading to potentially more accurate thrust values, [RCS-Sub-070].
- **Coefficient of Thermal Expansion** - Higher values for the coefficient of thermal expansion would lead to increased loading for each thermal cycle, potentially leading to a reduced life span, [RCS-Sub-030].
- **Specific heat Capacity** - A lower specific heat would result in a faster responding system as it reaches operating temperature at a faster rate, [RC-Sub-040, RC-Sub-050]. A higher specific heat would result in a more stable thrust value with intermittent or fluctuating input power, [RCS-Sub-070].
- **Young's Modulus** - A higher Young's modulus allows the system to be more resistant to fatigue stress and reduces the overall mass of the system, [RCS-Sub-030, INT-Mass-010]
- **Material Cost** - The material cost does not affect the properties of the material, only the final cost of the system, [INT-Cost-010].

Table A.2: Decision matrix, to evaluate the weighting of the criteria for the material choice trade-off table

	RCS-Sub-010	RCS-Sub-020	RCS-Sub-030	RCS-Sub-040	RCS-Sub-050	RCS-Sub-060	RCS-Sub-070	RCS-Sub-080	RCS-Sub-090	INT-Mass-010	INT-Cost-020	Total Wieght
Melting Point		x							x			0.143
Density										x		0.071
Thermal Conductivity		x		x	x		x					0.286
Coefficient of Thermal Expansion			x									0.071
Specific heat Capacity				x	x		x					0.214
Young's Modulus			x							x		0.143
Material Cost											x	0.071

B

Drawing Repository

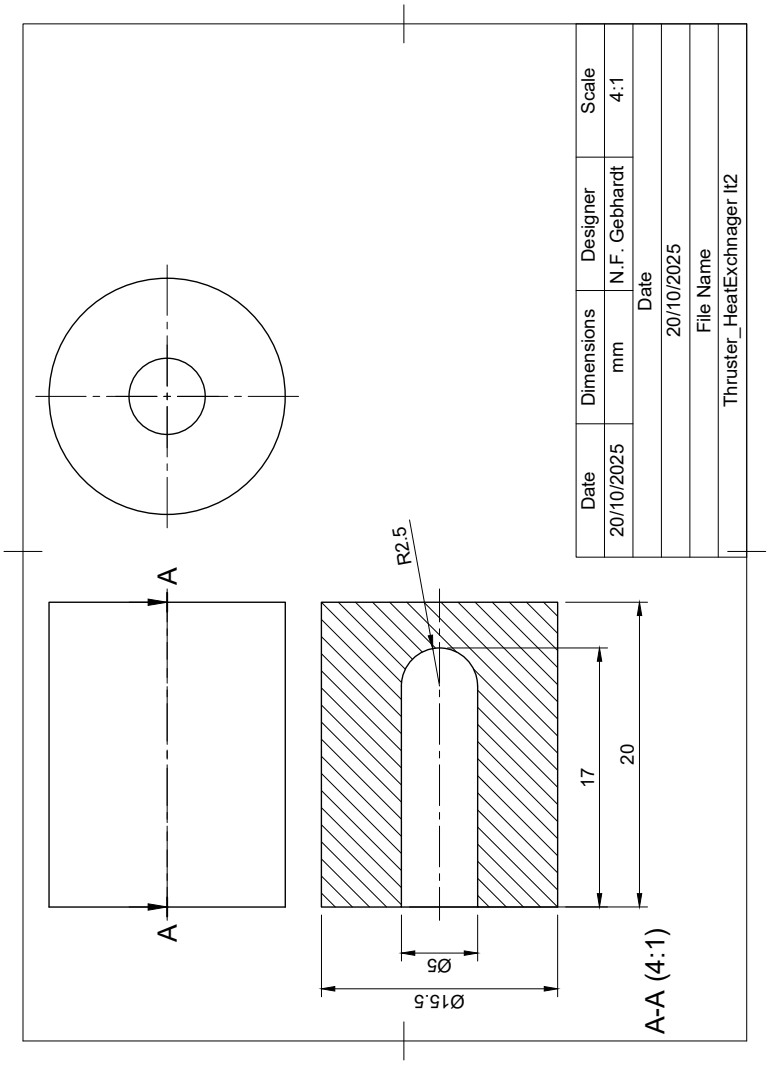

Figure B.1: Drawing of the cavity Insert

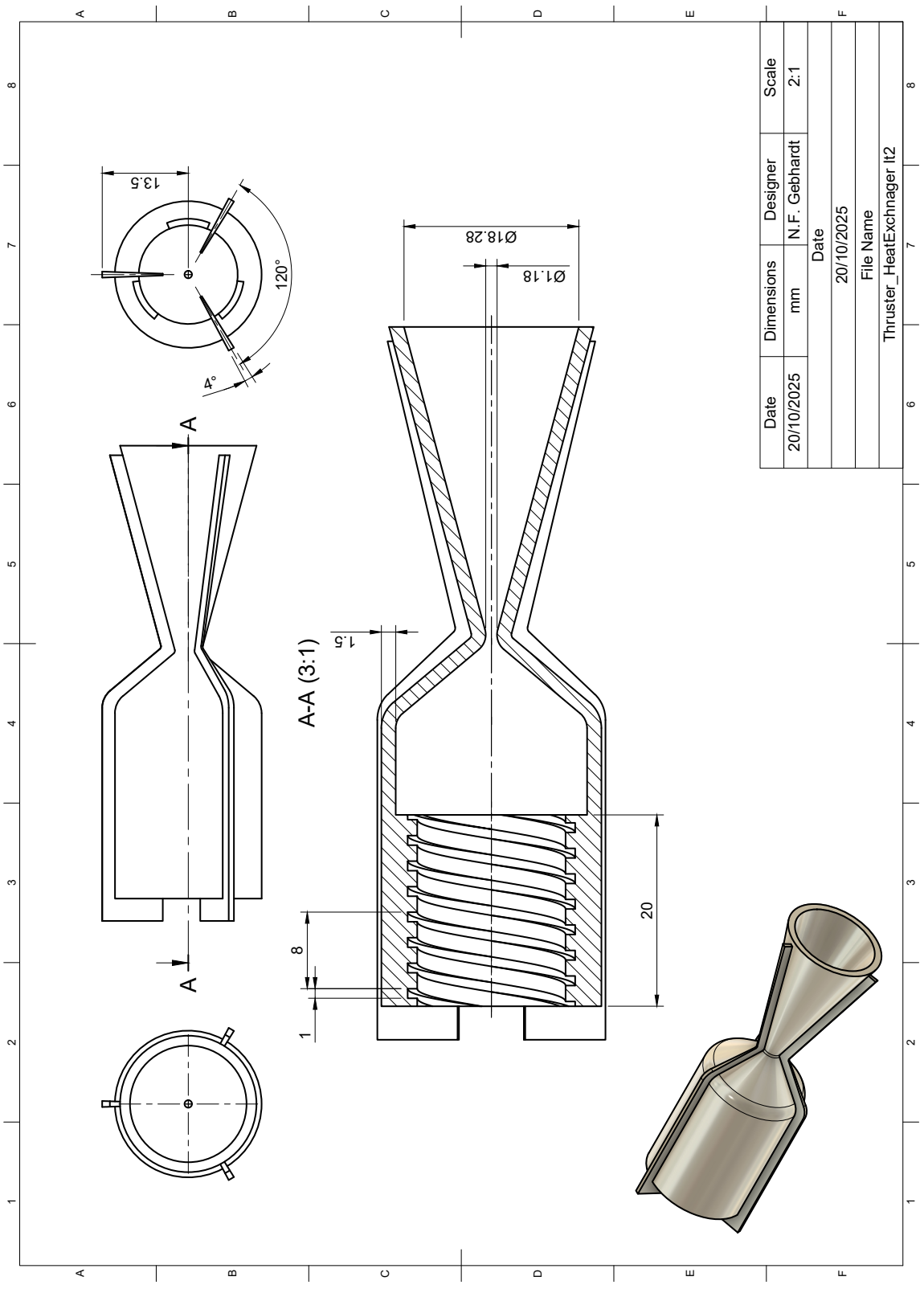

Figure B.2: Drawing of the System Core

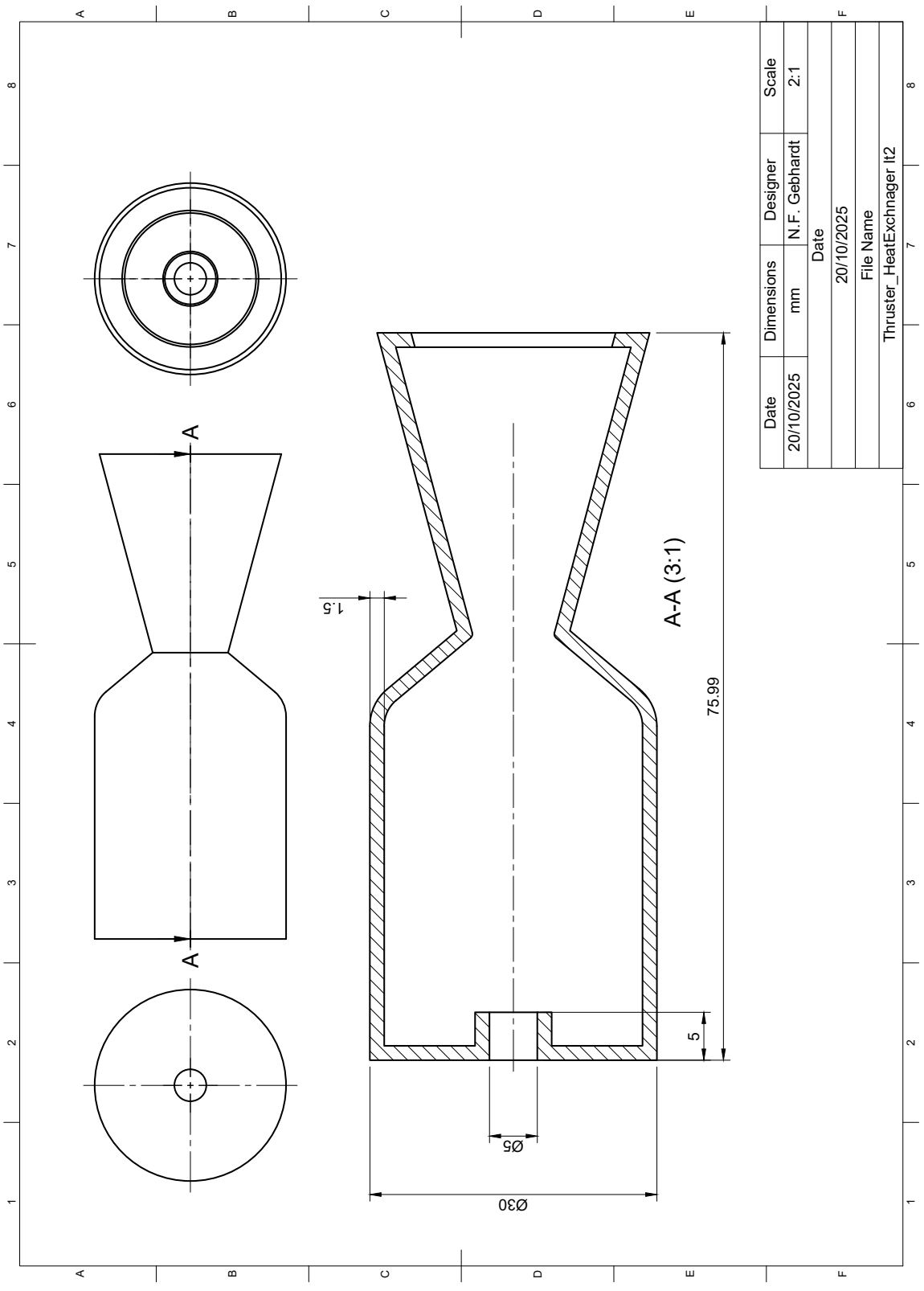

Figure B.3: Drawing of the Outer Housing

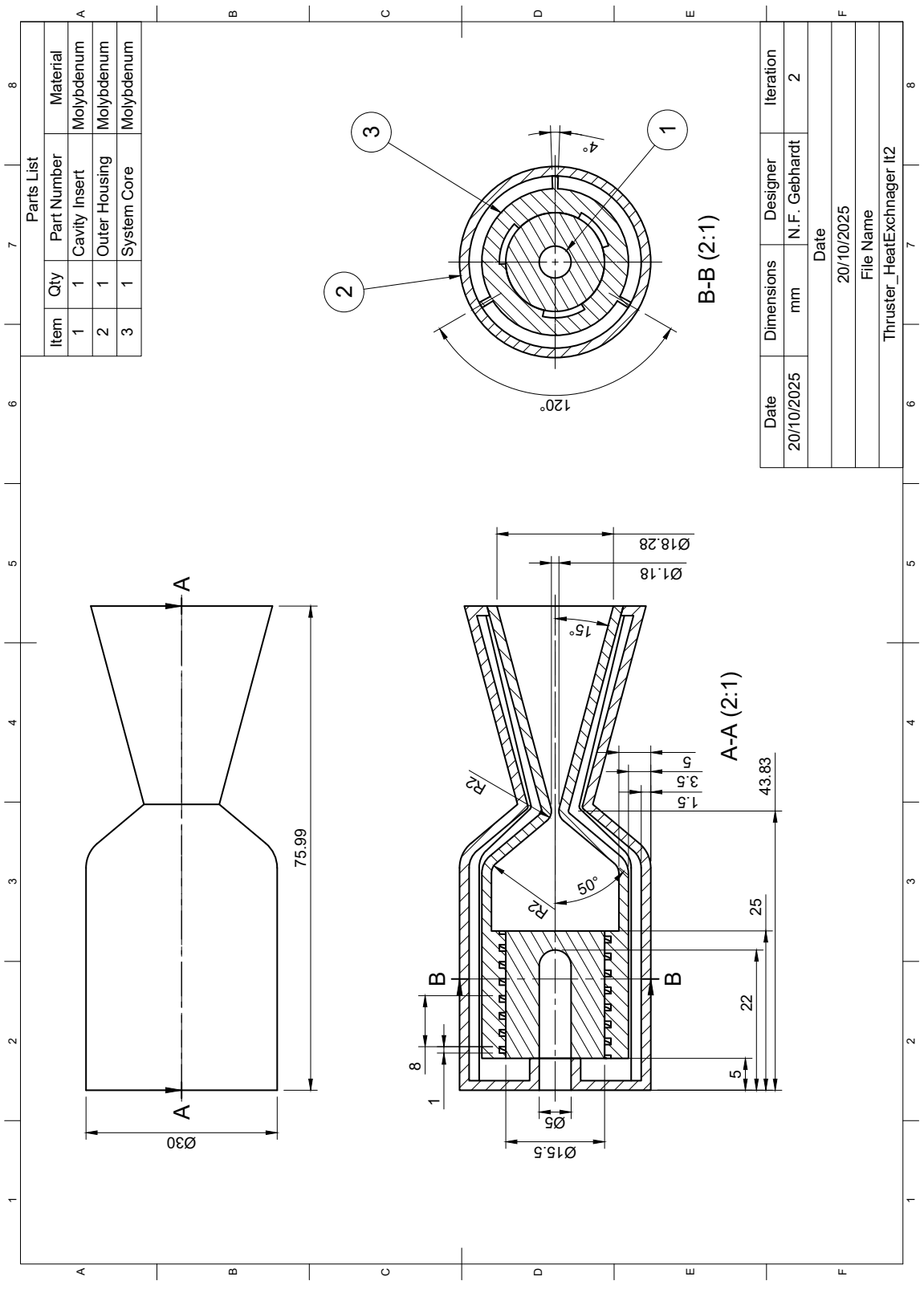

Figure B.4: Full System Drawing at a large scale

C

Graph Repository

With the aims of this report and the thesis, it is clear that some understanding of the models' response to other propellants is needed. Implementing the investigation of other propellants in the appendix to avoid confusion in the main report, with the main report focusing on the requirements which are sized for a Hydrogen-based system. Thus, for this appendix, first the results for the ideal rocket theory will be discussed for dissociated Hydrogen, Nitrogen, Argon and helium. Then the heat-exchanger sizing for dissociated Hydrogen, Nitrogen and Argon. Then going on to evaluate the raw $3\ [kW]$, and the $1\ [kW]$ ray tracing data.

C.1. Rocket Sizing

For the Ideal Rocket Theory, it's clear that the thermodynamic properties of the propellant play a large part in the overall performance of the system. Thus, for this section, each of the propellants will be evaluated, providing a quick overview of the main differences seen in the diatomic Hydrogen system as well as a quick conclusion on the use of the propellant.

Hydrogen Dissociation

The chemical Python package Cantera allowed for the calculation of the dissociation of Hydrogen for a set temperature and pressure, providing mean-averaged values for a mixture of diatomic Hydrogen and protons. Generally, at these temperatures and pressures, the dissociation of Hydrogen is very minimal, with the best possible evaluated conditions for dissociation only leading to an 8% mass fraction of protons. Because of this, there is little difference between the purely diatomic Hydrogen and the system including Hydrogen dissociation. The one main difference is that values which were independent of pressure are now influenced by a change of pressure, especially at high temperatures. Whilst theoretically, the dissociation of Hydrogen is advantageous to increase the specific impulse, with the reduction of molecular mass, at the temperature considered for this design, there is little to no dissociation. Whilst the design can be altered, and catalysts could be implemented to reduce the temperature for the dissociation of Hydrogen, the increased performance is not really needed for the Green SWaP project. For the first-order sensitivity analysis, most of the indices remain similar to diatomic Hydrogen; the mass fraction is heavily dependent on the propellant temperature and somewhat on the chamber pressure, with a large proportion attributable to higher orders.

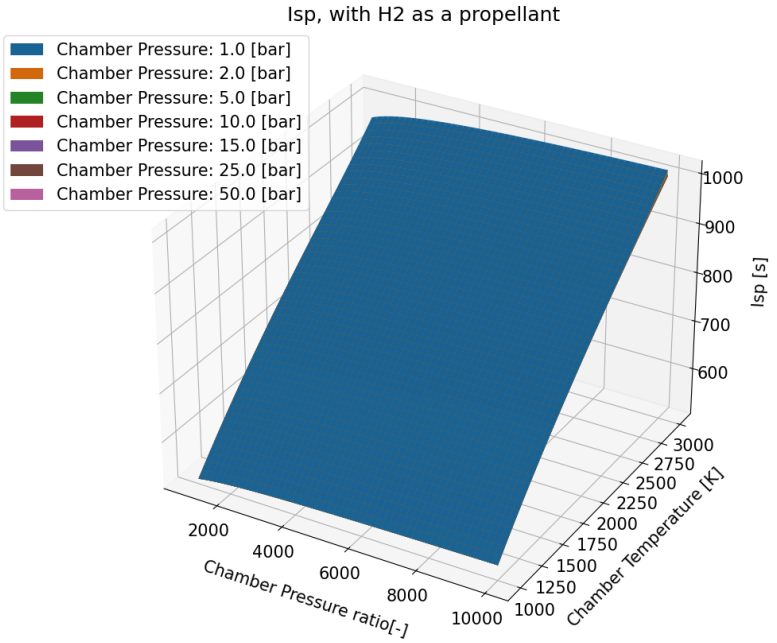

Figure C.1: H^+, H2 Isp Graph

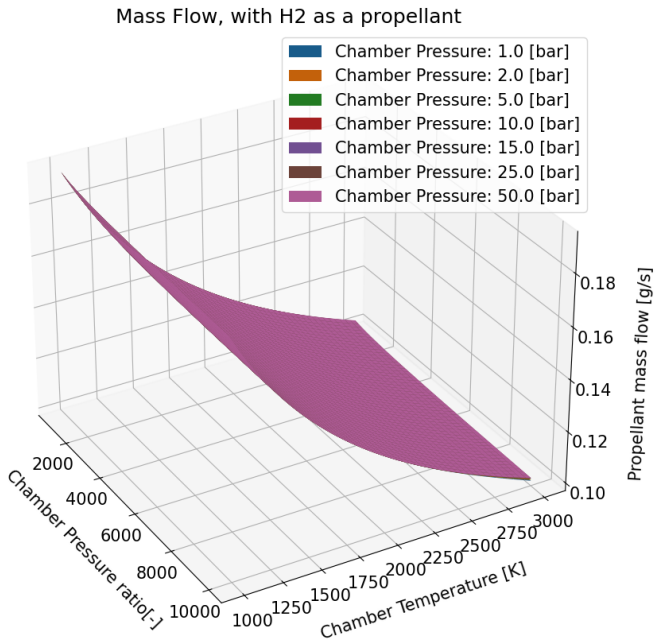

Figure C.2: H^+, H2 Mass Flow Rate Graph

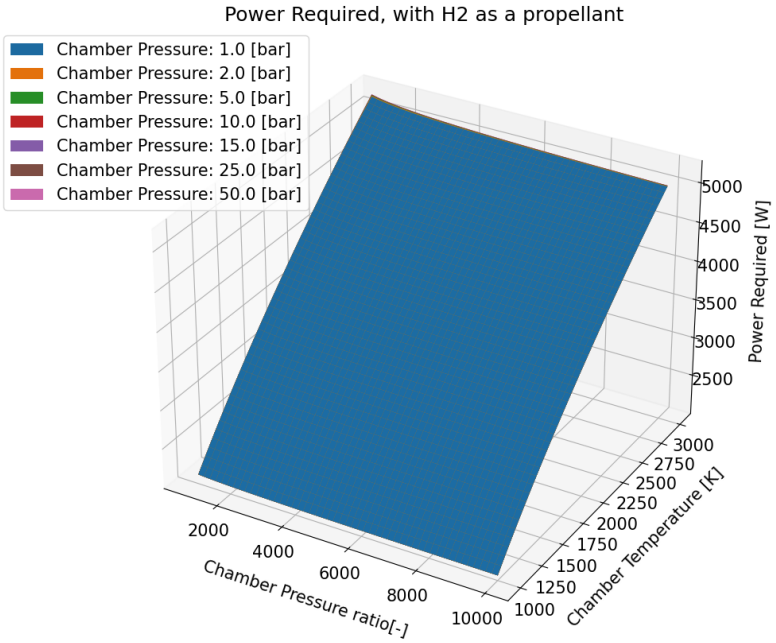

Figure C.3: H^+, H2 Power Required Graph

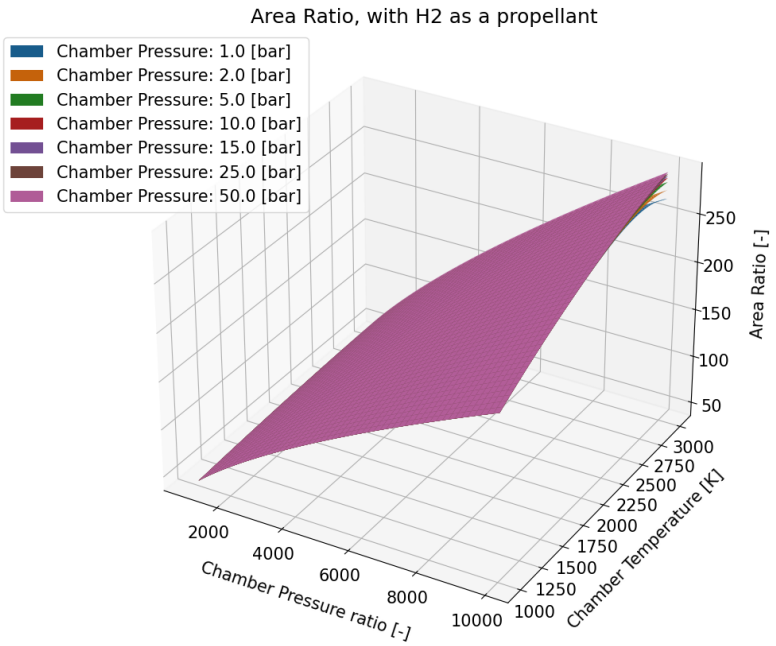

Figure C.4: H^+, H2 Area Ratio Graph

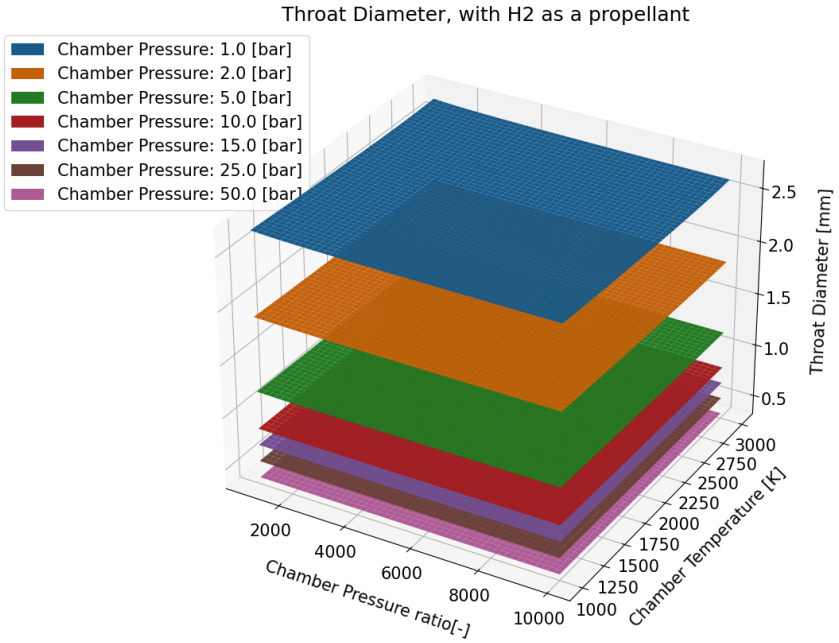

Figure C.5: H^+, H2 Throat Diameter Graph

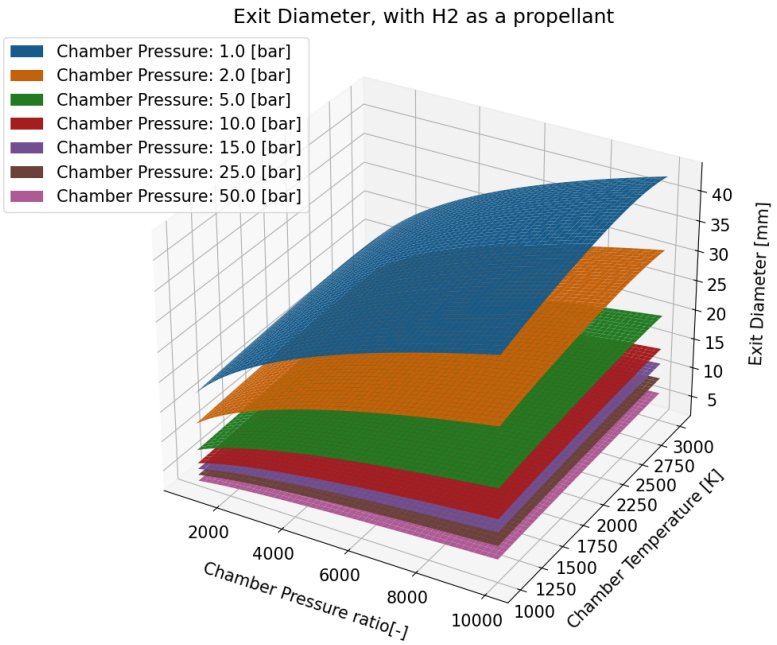

Figure C.6: H^+, H2 Exit Diameter Graph

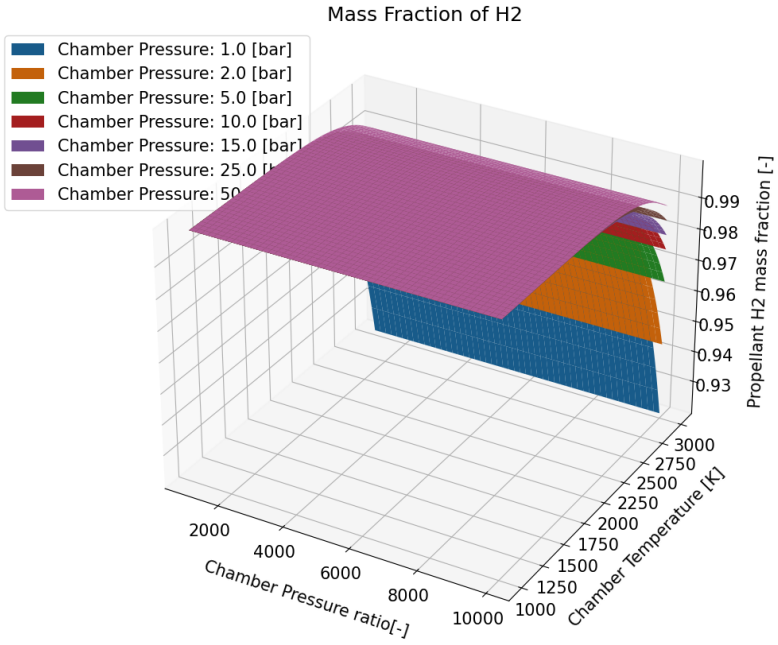

Figure C.7: H^+, H2 Mass Fraction Graph

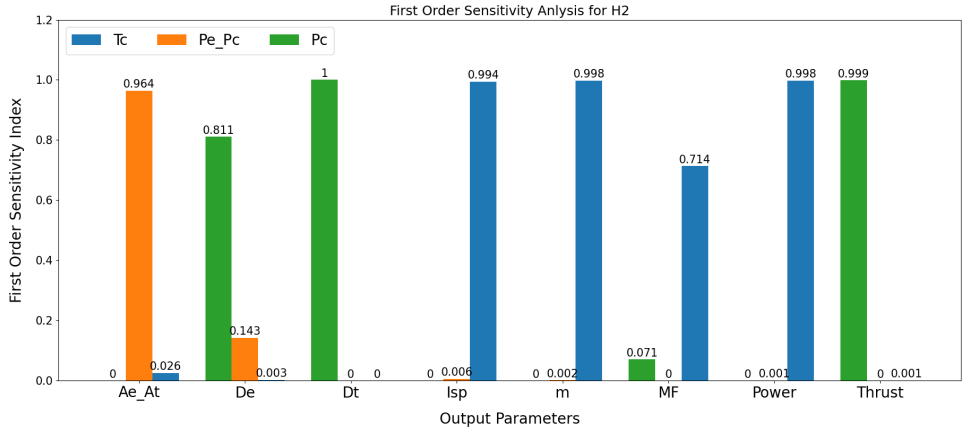

Figure C.8: H^+, H2 First Order Sensitivity analysis

Nitrogen

The largest change between the properties of nitrogen and Hydrogen is the molecular mass, with nitrogen being 14 times heavier than Hydrogen. This is clearly evident in the specific impulse of nitrogen being much lower than that of Hydrogen. Thus, to generate the required thrust of $1\ [N]$, the mass flow is increased to compensate for the reduced efficacy of the thruster. The reduced specific heat capacity of nitrogen compared to Hydrogen leads to a reduction in the power required, even when considering the increased mass flow. Since the nozzle geometry is much more dependent on the ratio of specific heat than the molecular mass, the nozzle geometry is very similar to that of Hydrogen, with the ratio of specific heat being 1.41 for Hydrogen and 1.4 for nitrogen. The use of nitrogen results in a much reduced efficacy in the thruster, but the same nozzle could be used for both Hydrogen and nitrogen, with little impact on performance.

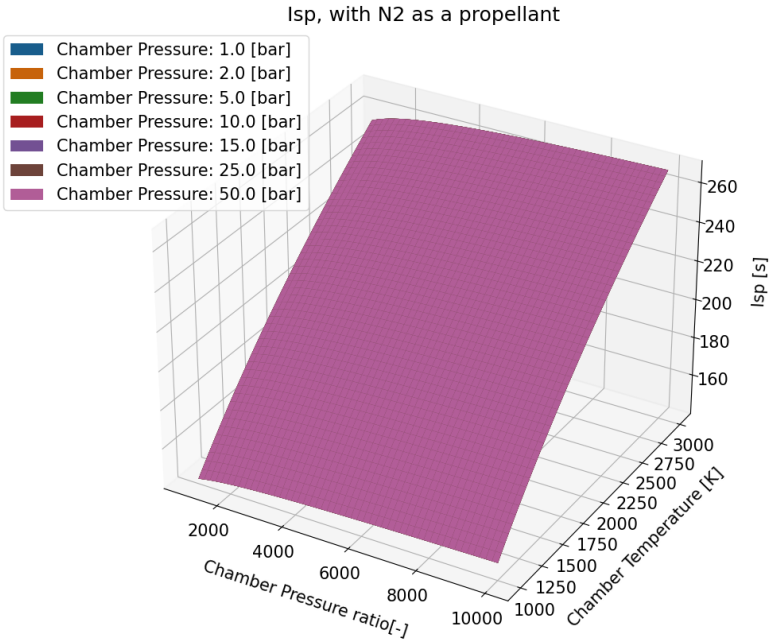

Figure C.9: Nitrogen Isp Graph

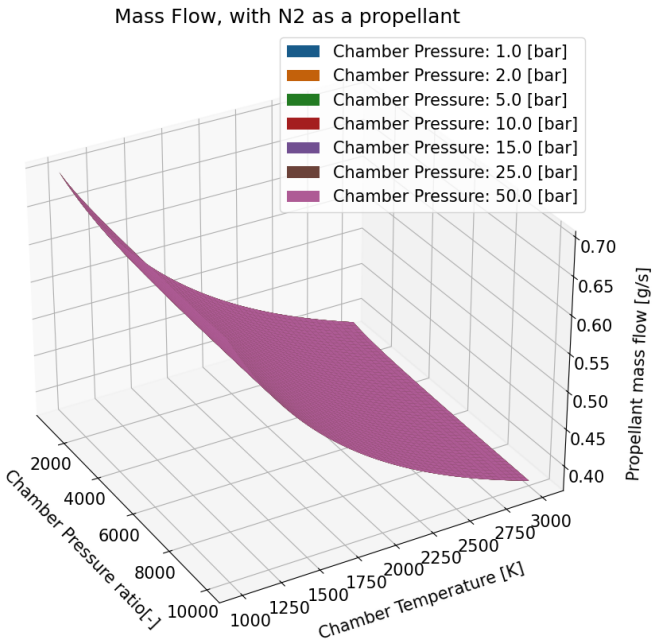

Figure C.10: Nitrogen Mass Flow rate Graph

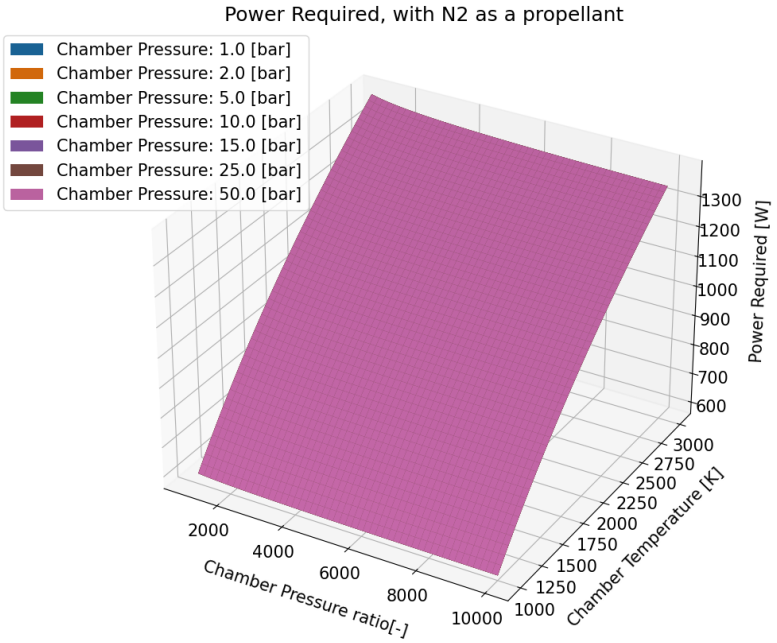

Figure C.11: Nitrogen Power Required Graph

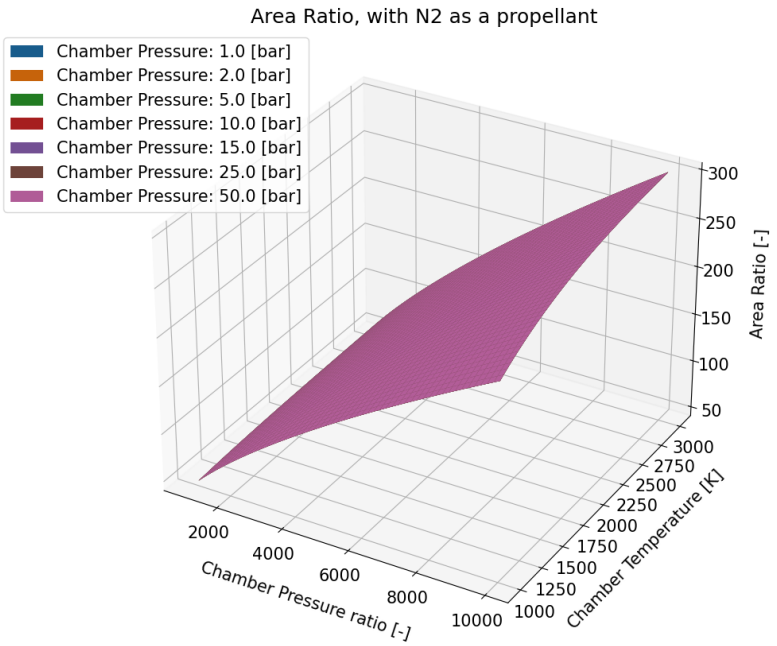

Figure C.12: Nitrogen Area Ratio Graph

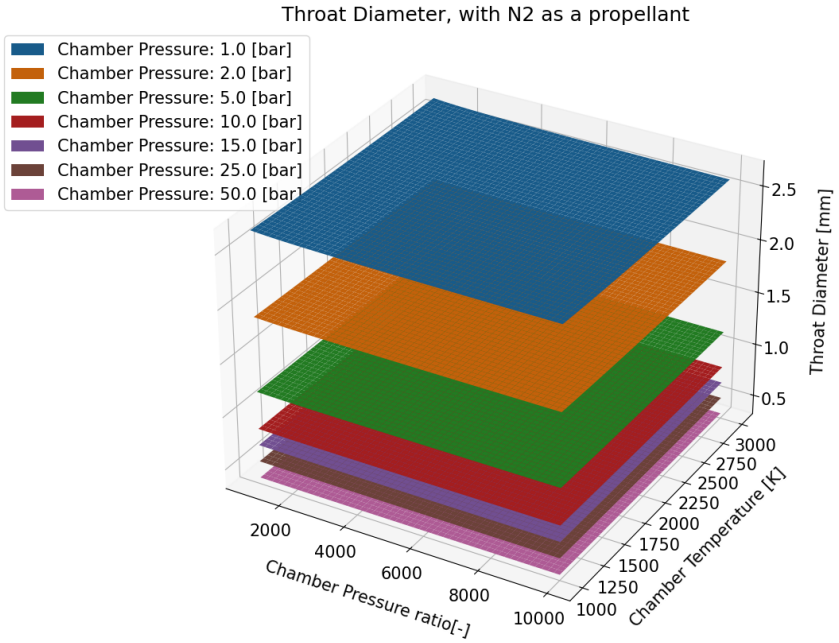

Figure C.13: Nitrogen Throat Diameter Graph

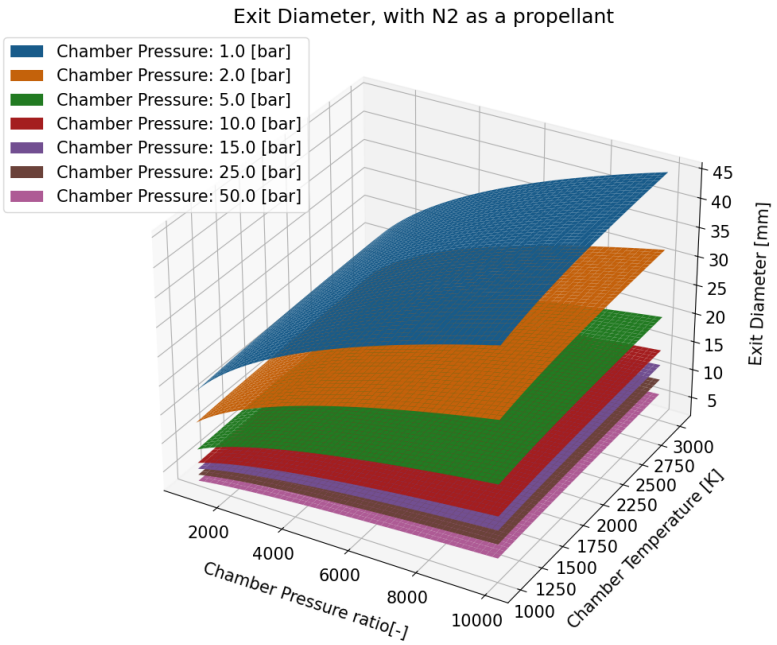

Figure C.14: Nitrogen Exit Diameter Graph

Argon

Whilst argon is a monatomic gas, it is still heavier than the diatomic nitrogen, leading to a further reduction in the specific impulse and hence an increase in mass flow rate to reach the required thrust value. Again, argon has a reduced specific heat capacity, leading to a reduction in the power required. However, argon has a higher ratio of specific heat of 1.66 when compared to Hydrogen or nitrogen, leading to larger changes in the nozzle geometry, increasing the required throat area. However, the required area ratio is much reduced, leading to a much smaller exit area for the nozzle, resulting in a smaller nozzle than what is required for Hydrogen. Argon produces the least efficient thruster but requires the least amount of power to heat the propellant, and has the shortest nozzle. Though any mass reduction in the nozzle would be overshadowed by the increased mass of the propellant required for an equivalent Δv burn.

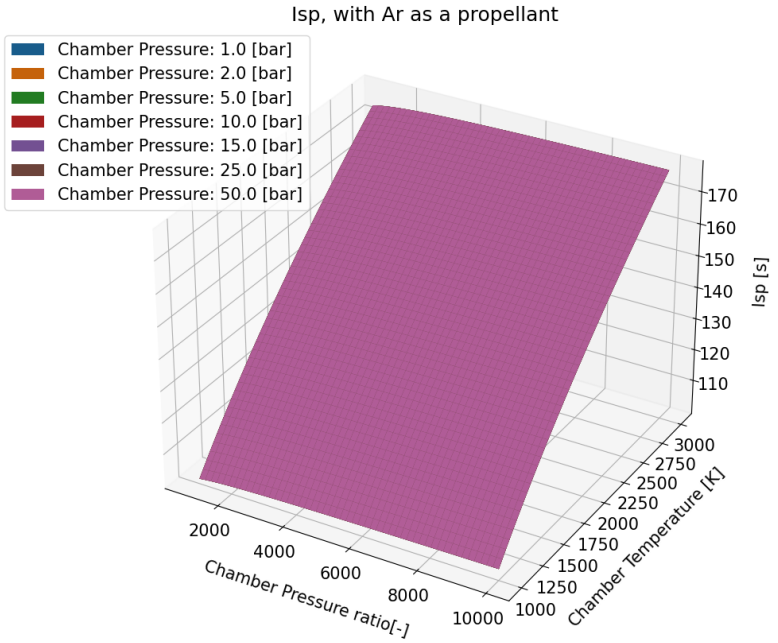

Figure C.15: Argon Isp Graph

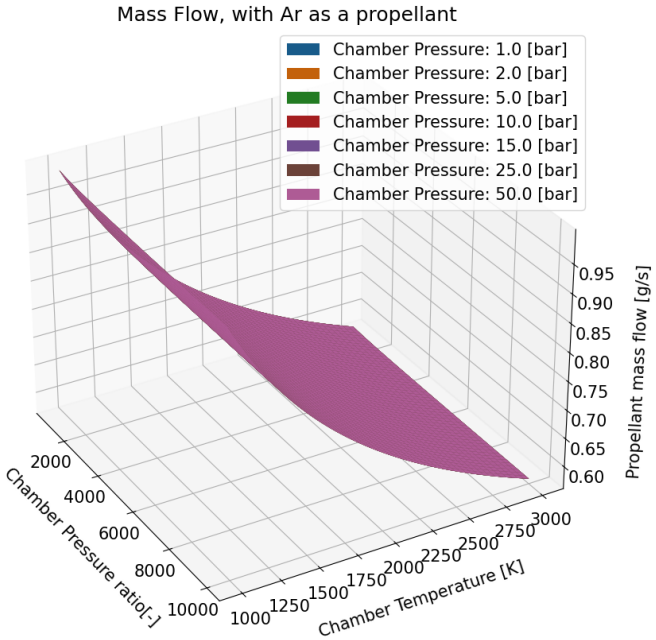

Figure C.16: Argon Mass Flow Rate Graph

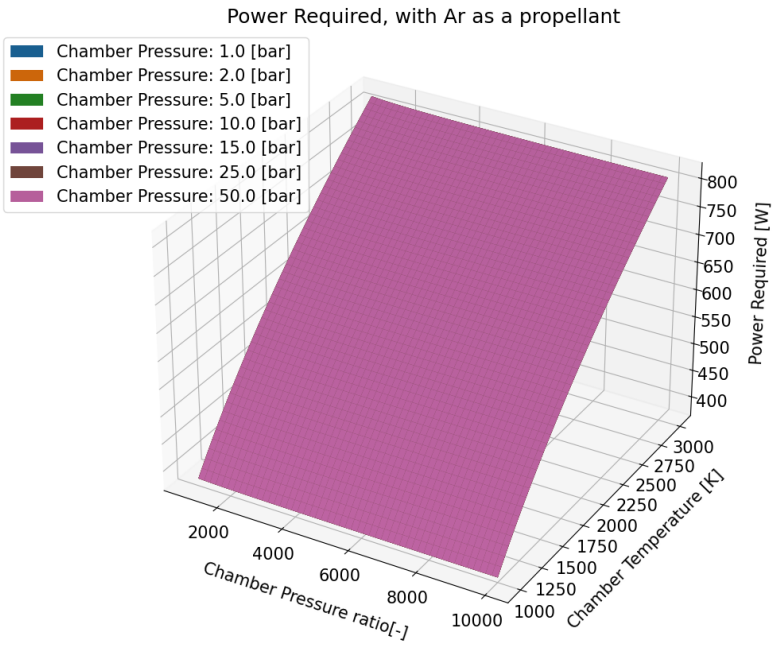

Figure C.17: Argon Power Required Graph

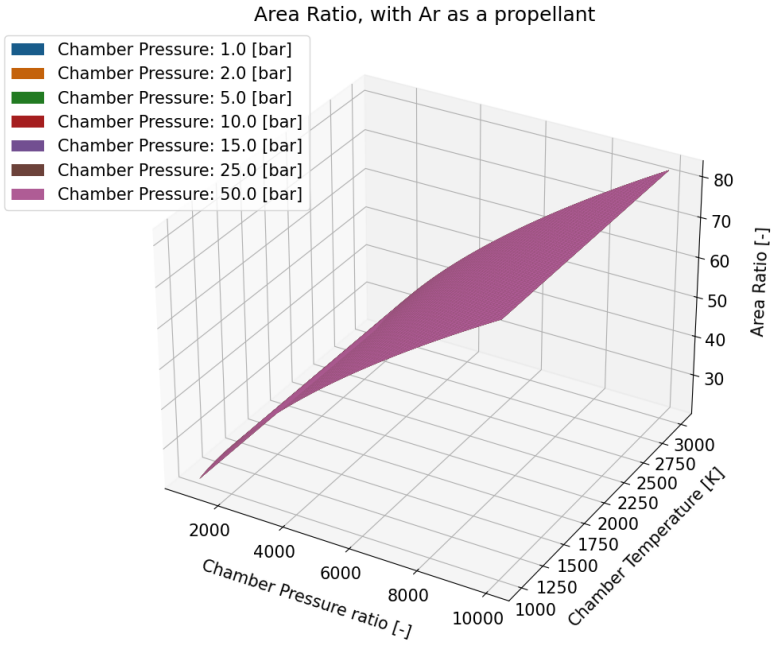

Figure C.18: Argon Area Ratio Graph

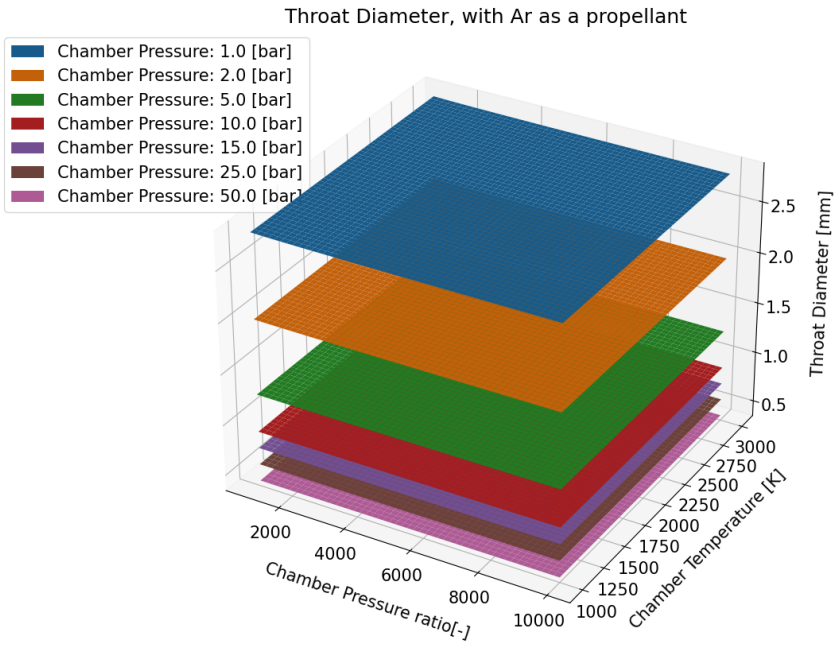

Figure C.19: Argon Throat Diameter Graph

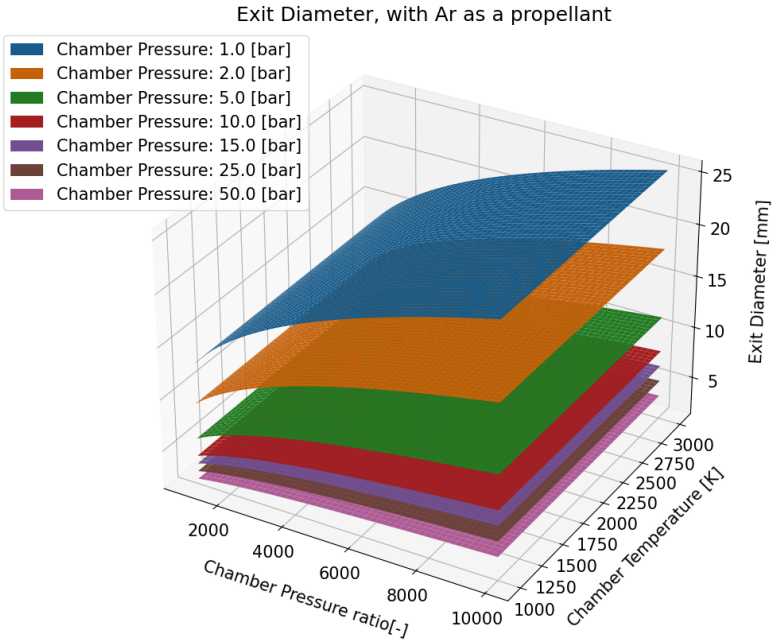

Figure C.20: Argon Exit Diameter Graph

Helium

Helium is the lightest of all the other propellants considered, leading to the smallest decrease in the specific impulse, though across the boundaries it has about halved. This results in the least increase in the mass flow rate of all the propellants, though, because of the higher specific heat capacity of helium, the power required is about halfway between Hydrogen and nitrogen. Because helium has the same ratio of specific heat as argon, the nozzle geometry follows that of argon. This results in a reduced overall length of the nozzle. Helium results in the most efficient system out of all the other propellants evaluated, whilst having a reduced overall length of the nozzle.

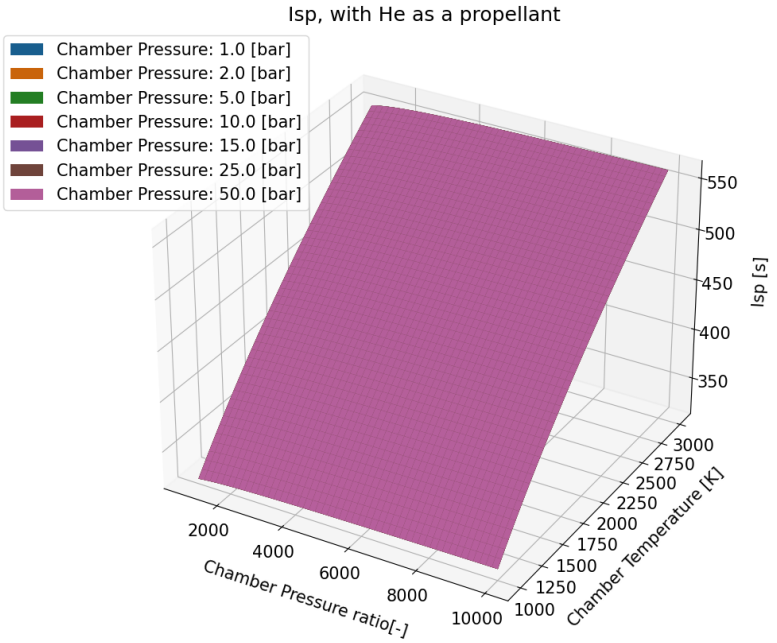

Figure C.21: Helium Isp Graph

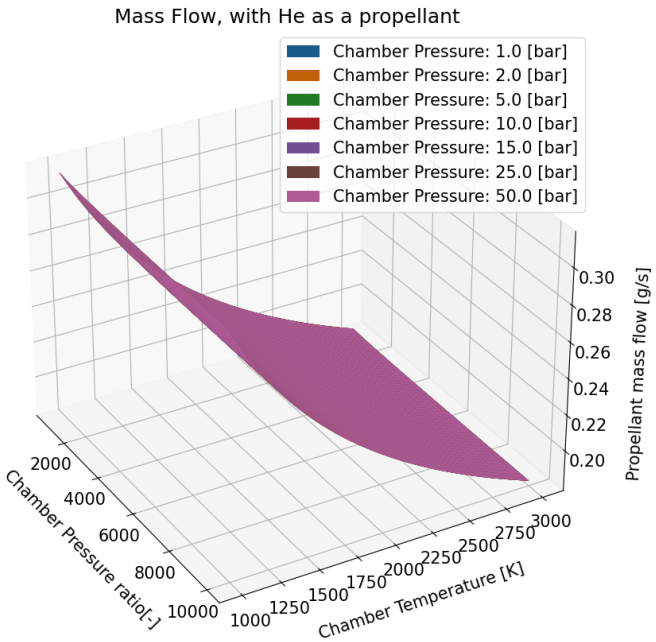

Figure C.22: Helium Mass Flow Rate Graph

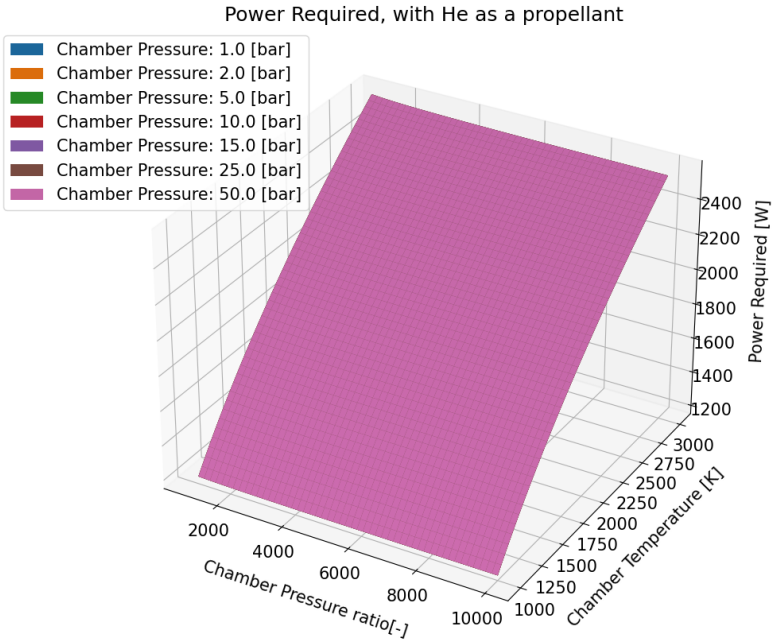

Figure C.23: Helium Power Required Graph

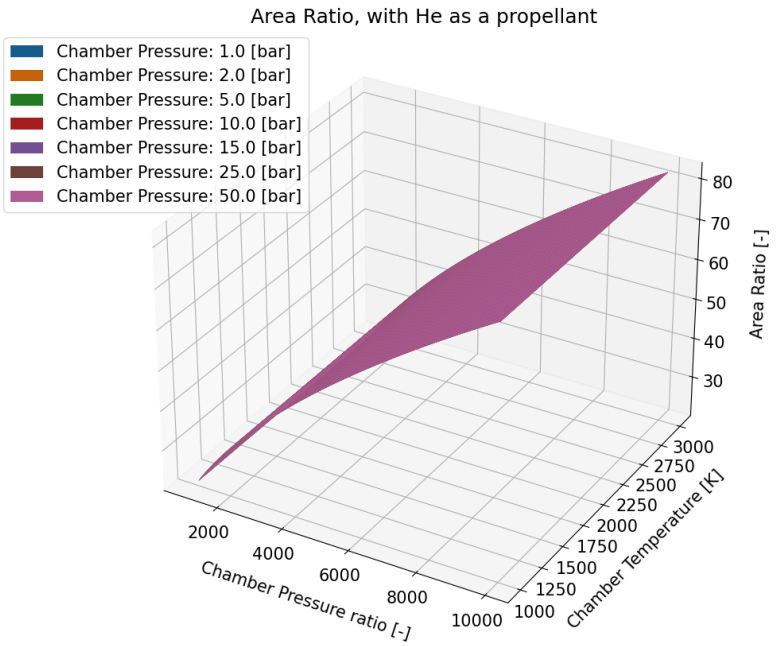

Figure C.24: Helium Area Ratio Graph

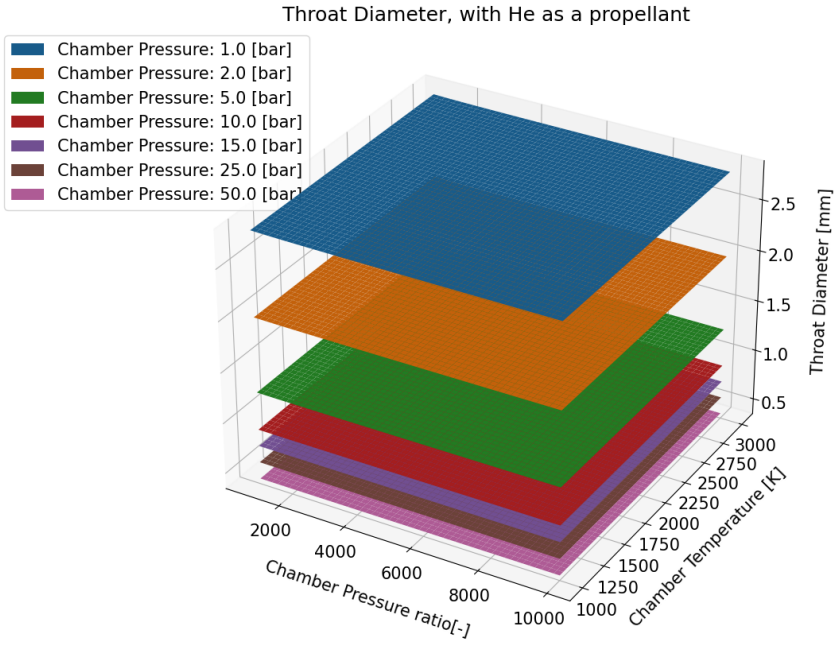

Figure C.25: Helium Throat Diameter Graph

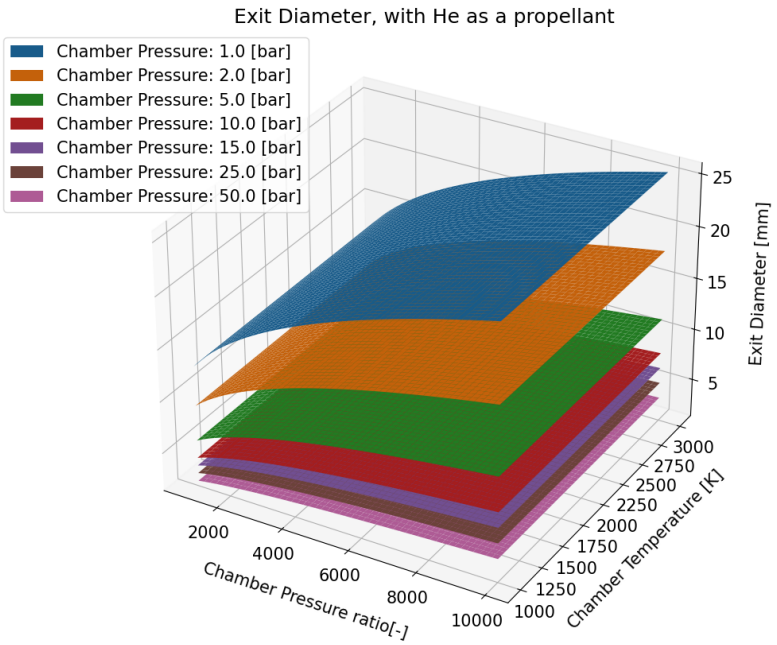

Figure C.26: Helium Exit Diameter Graph

C.2. Heat Exchanger Sizing

As for the ideal rocket theory, the heat-exchanger sizing can also be evaluated for several different propellants, these being disassociated Hydrogen, Nitrogen and Argon. Thus, going through each propellant, analysing the results and considering how this affects the system.

It has to be noted that the only variable that was changed was the propellant type, meaning that the mass flow rate, wall temperature and inlet pressure were constant for each propellant. This was done to better evaluate the effects due to a change of propellant and not due to external factors, using the chosen rocket sizing that was discussed in the report for the use of Hydrogen.

Hydrogen Dissociation

Due to the relatively low temperature of the Hydrogen, not much of the Hydrogen disassociates, leading the system to have very similar characteristics to that of pure diatomic Hydrogen. This would be very different at higher temperatures, but little change occurs at the temperature considered.

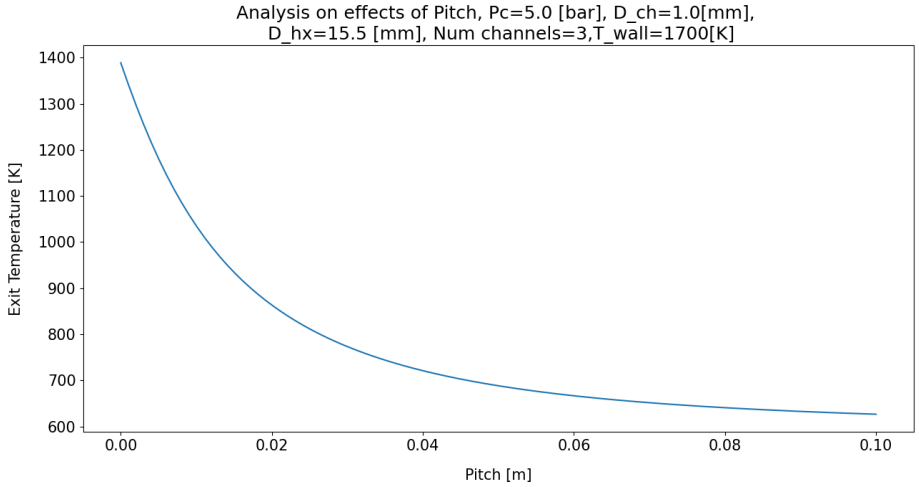

Figure C.27: H^+, H2, Pitch analysis graph

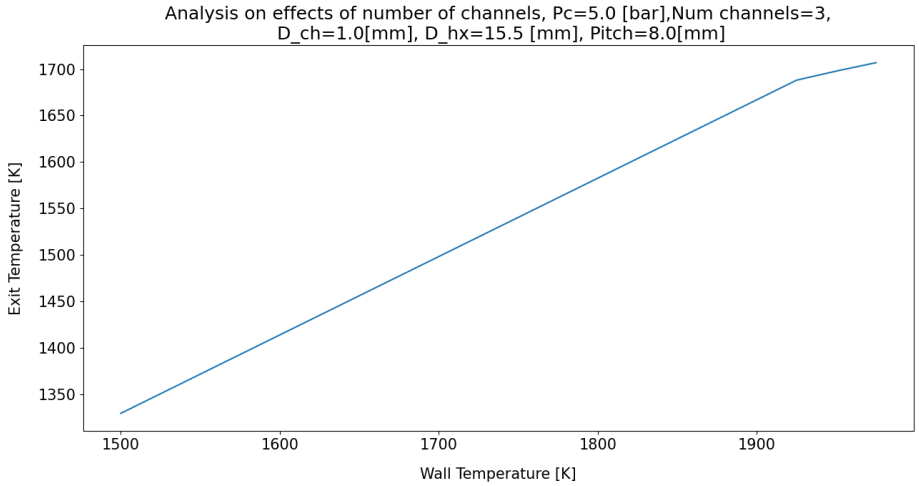

Figure C.28: H^+, H2, Wall Temperature analysis graph

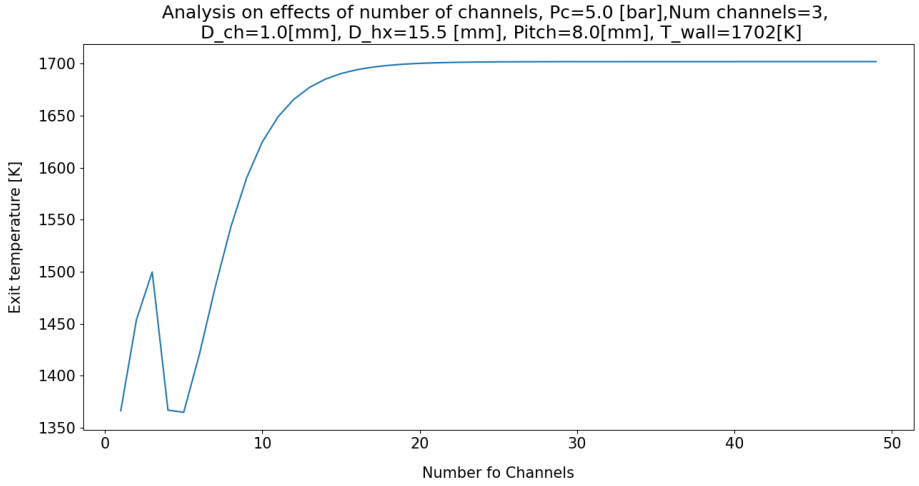

Figure C.29: H^+, H2, Number of Channels analysis graph

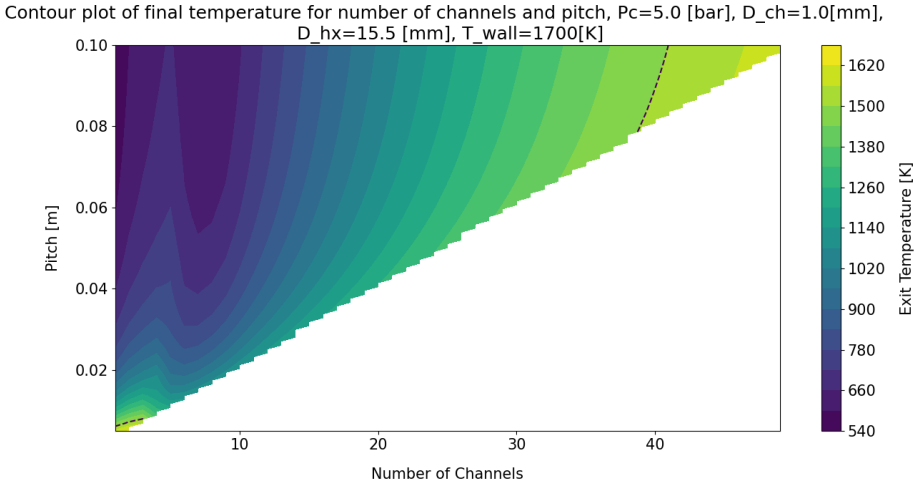

Figure C.30: H^+, H2, Pitch and Channel Number contour

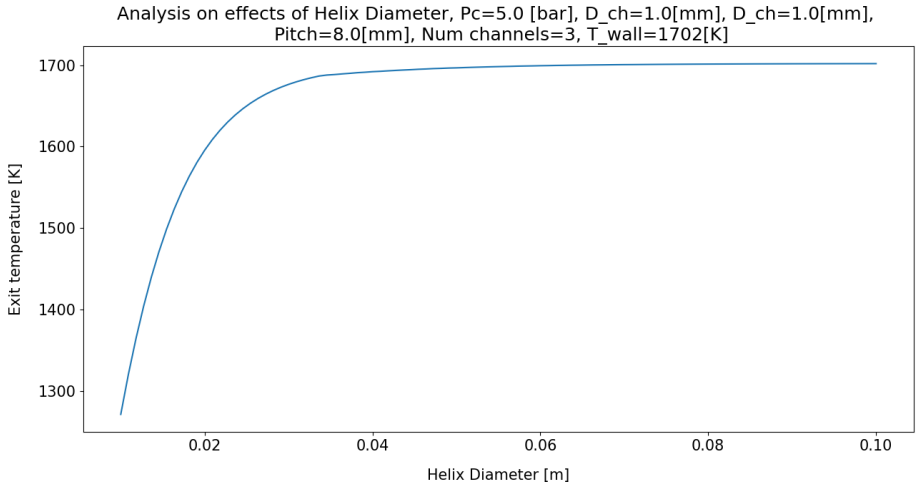

Figure C.31: H^+, H2, Helix Diameter analysis graph

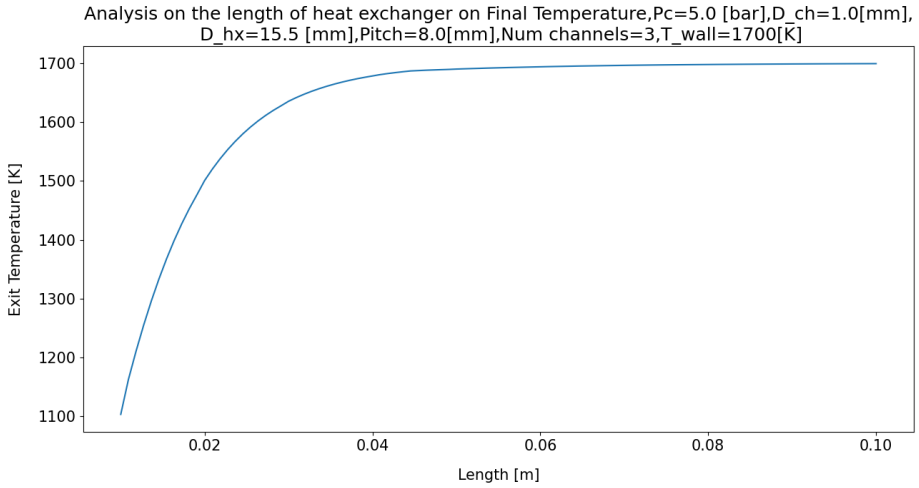

Figure C.32: H^+, H2, Helix Length analysis graph

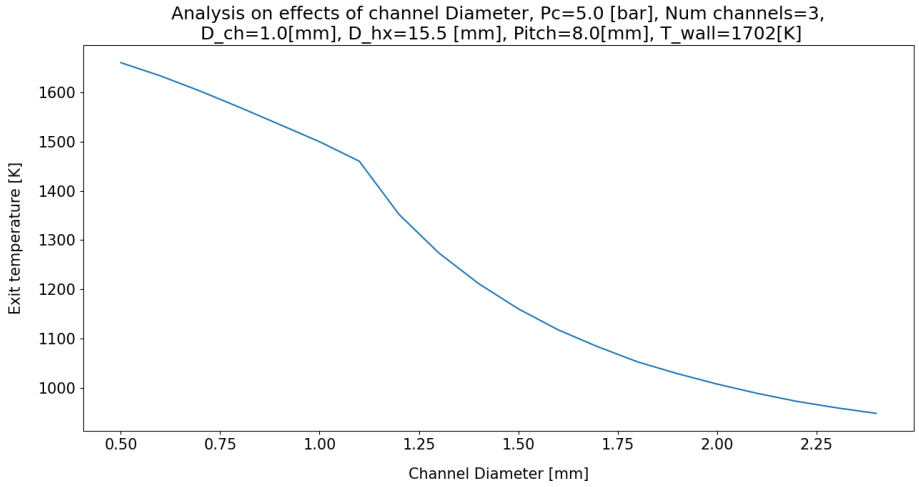

Figure C.33: H^+, H2, Channel Diameter analysis graph

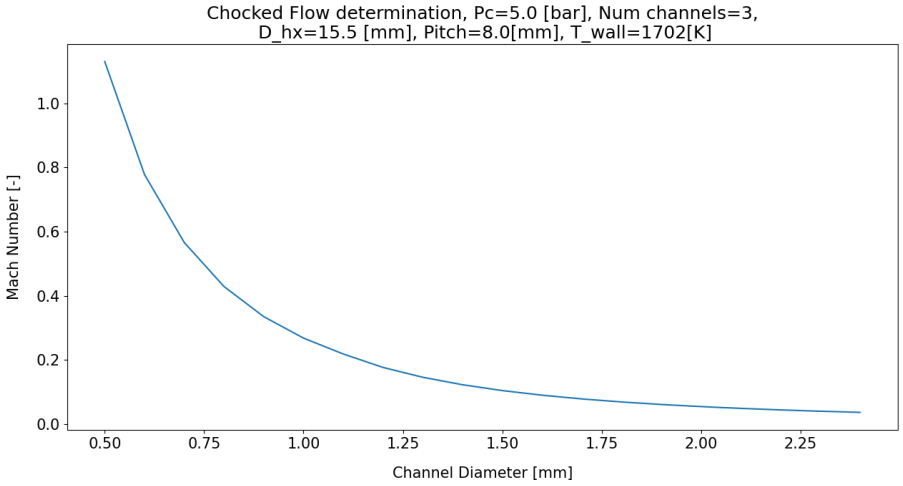

Figure C.34: H^+, H2, Choked Flow analysis graph

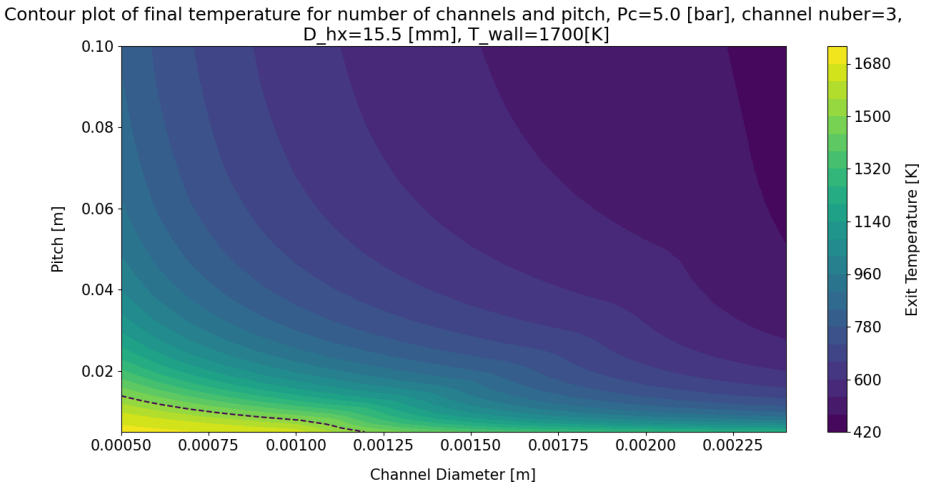

Figure C.35: H^+, H2, Pitch and Channel Diameter contour

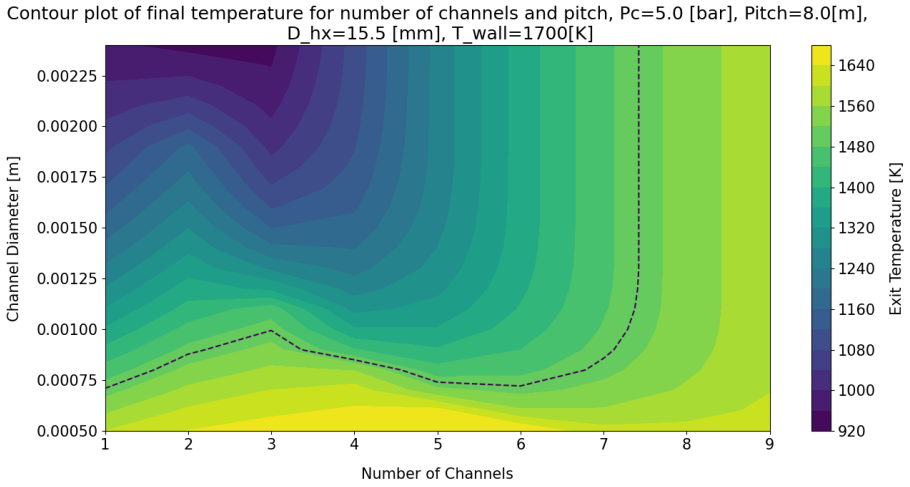

Figure C.36: H^+, H2, Channel Number and Channel Diameter contour

Nitrogen

Generally speaking, the same trend can be seen in the use of nitrogen as in the use of Hydrogen for the heat-exchanger sizing. It holds that for both Hydrogen and nitrogen, an increase in the overall length of the fluid channel will increase the exit temperature of the propellant.

The notable differences lie in the point at which the system reaches its optimal thermal transfer porosities. The turbulence point for nitrogen, the point at which the system goes from turbulent to laminar flow, occurs at only one channel, with a channel diameter of $1\ [mm]$. Where at smaller channel diameters the system may perform best with two channels.

One aspect of using the same mass flow rate for the different propellants, and considering the lower specific heat capacity of nitrogen compared to Hydrogen, the heat-exchanger should have an easier time heating the propellant. Though, of course, this is also dependent on the convective heat transfer coefficient, which is dependent on the propellant properties. Again, the use of this mass flow with nitrogen would result in a loss of thrust.

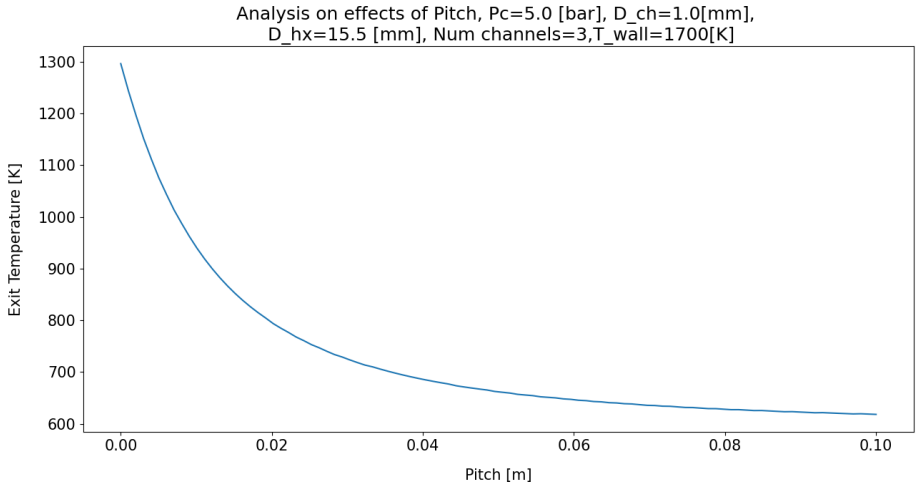

Figure C.37: Nitrogen, Pitch analysis graph

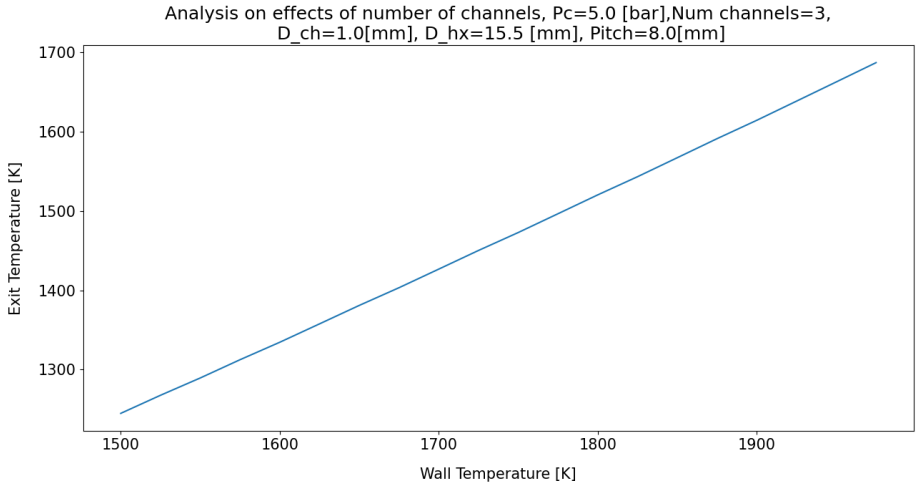

Figure C.38: Nitrogen, Wall Temperature analysis graph

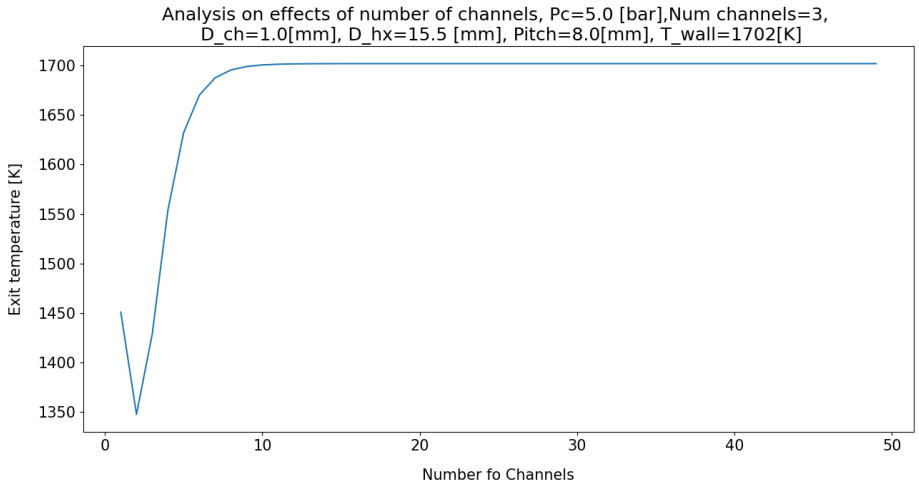

Figure C.39: Nitrogen, Number of Channels analysis graph

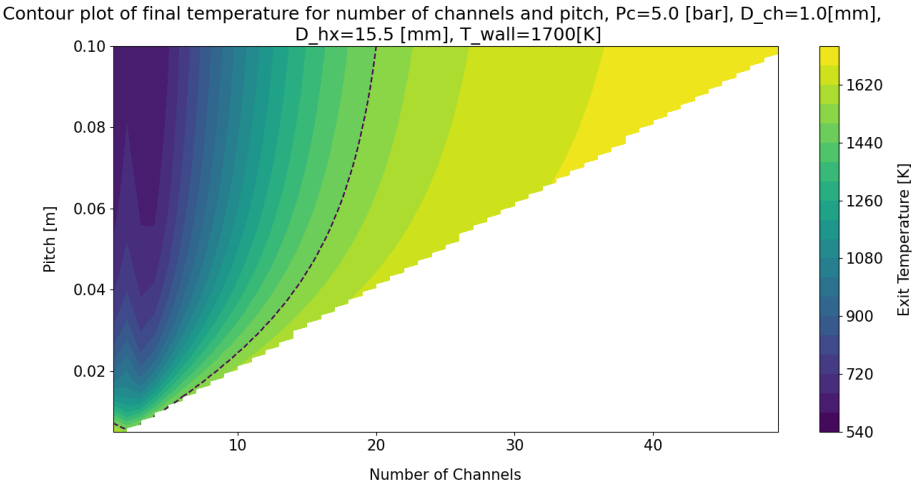

Figure C.40: Nitrogen, Pitch and Channel Number contour

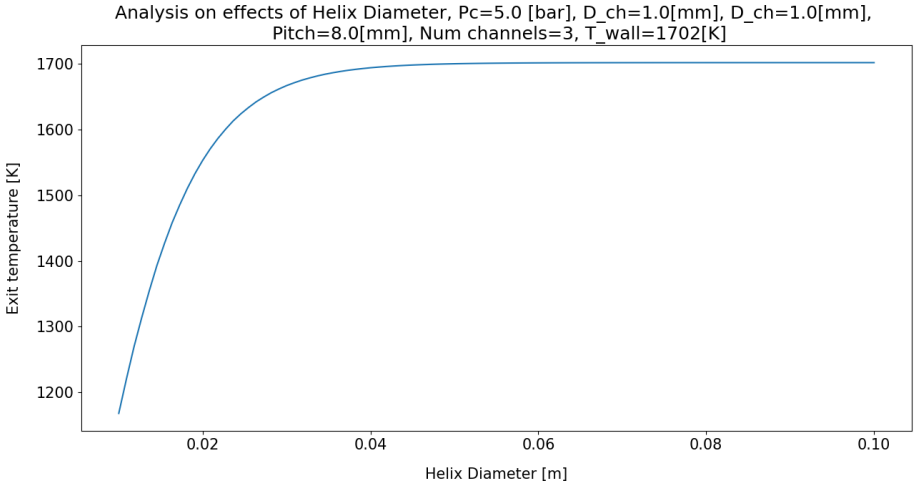

Figure C.41: Nitrogen, Helix Diameter analysis graph

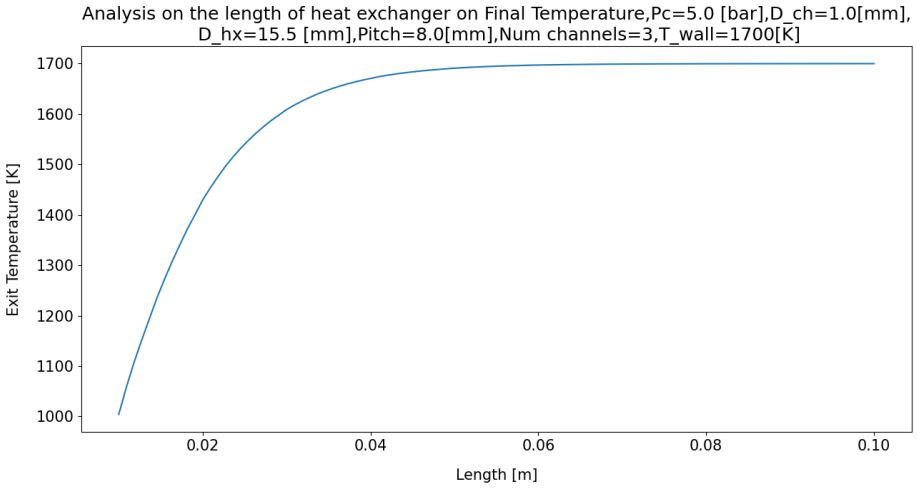

Figure C.42: Nitrogen, Helix Length analysis graph

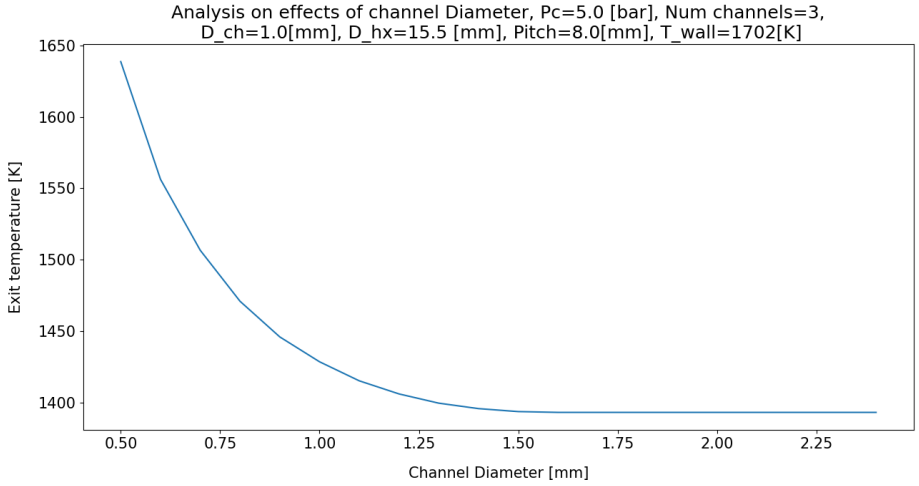

Figure C.43: Nitrogen, Channel Diameter analysis graph

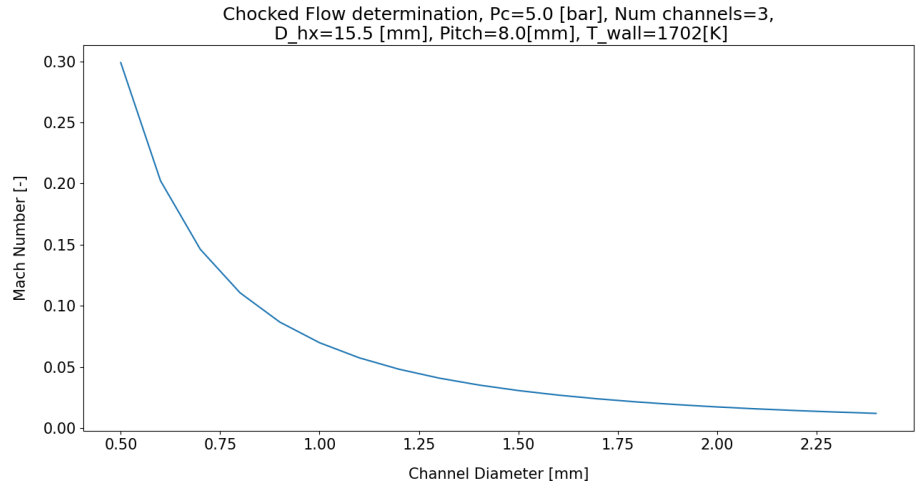

Figure C.44: Nitrogen, Choked Flow analysis graph

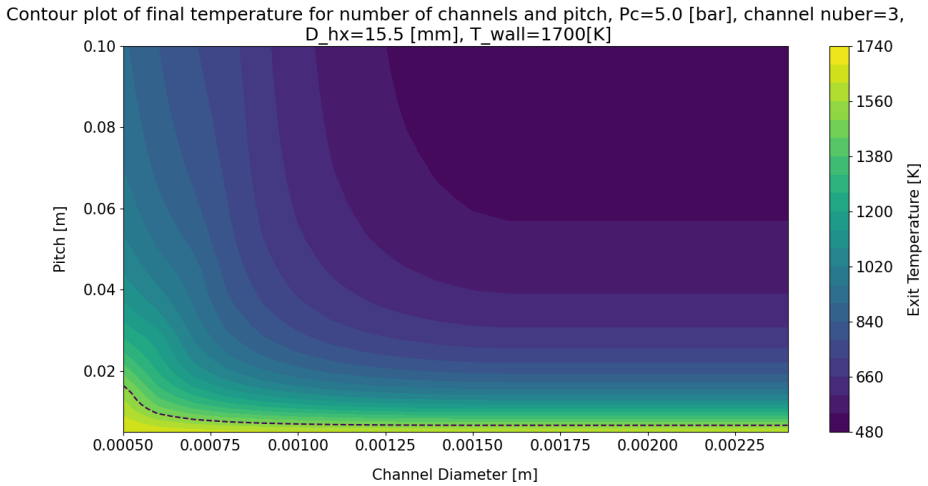

Figure C.45: Nitrogen, Pitch and Channel Diameter contour

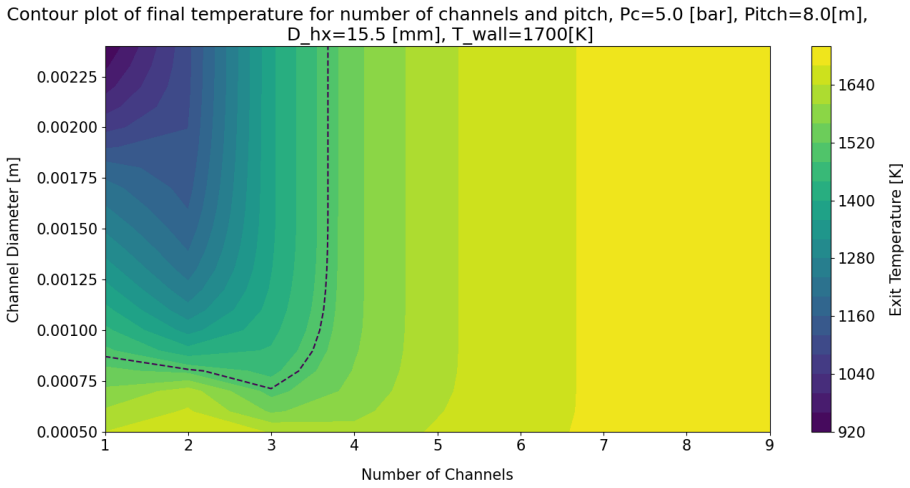

Figure C.46: Nitrogen, Channel Number and Channel Diameter contour

Argon

Argon follows the same trend as nitrogen; again, the turbulence point is at one channel number for argon. Requiring even smaller channels than that of nitrogen to move the turbulence point to higher channel numbers. Both nitrogen and argon could benefit from the use of narrower channels to better take advantage of the improved heat transfer rates that come with turbulent flow. For argon, the flow is far from being choked at a channel diameter of $0.5\ [mm]$, indicating that the channel diameter could be reduced further.

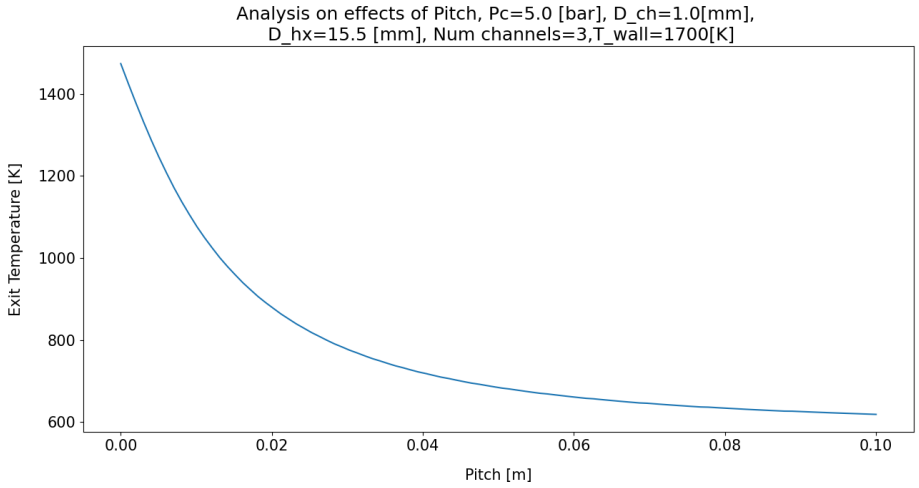

Figure C.47: Argon, Pitch analysis graph

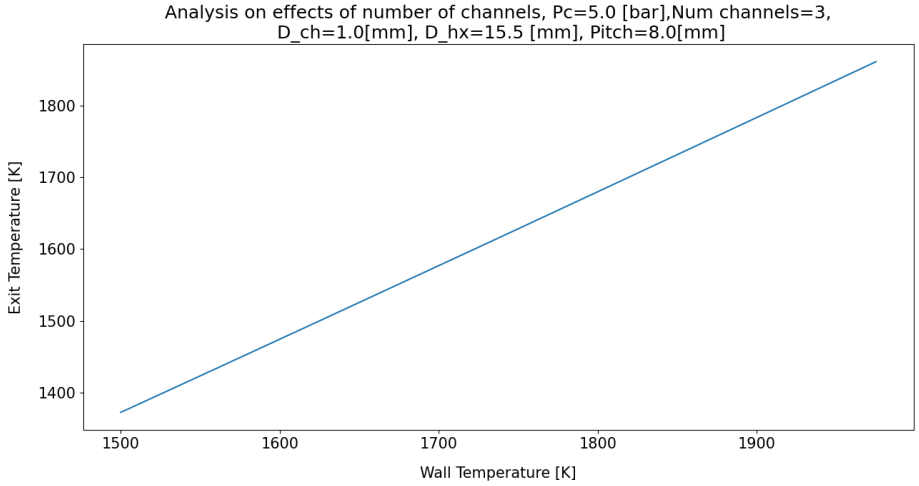

Figure C.48: Argon, Wall Temperature analysis graph

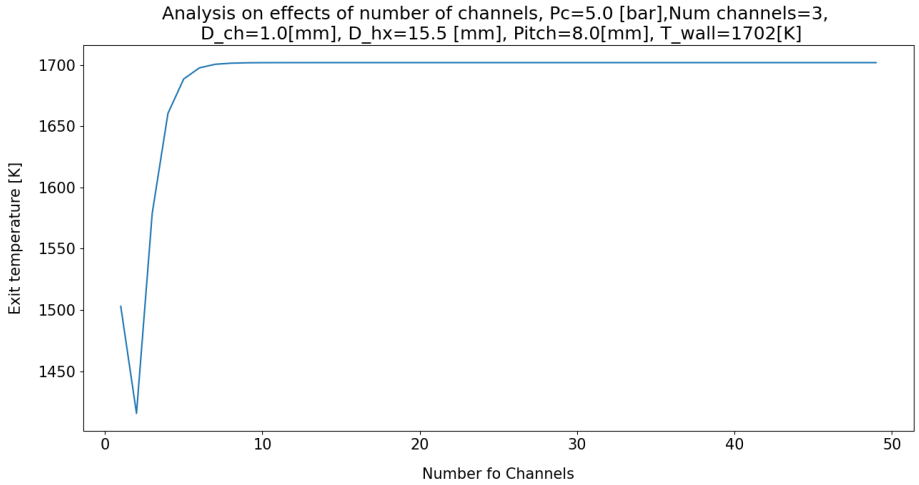

Figure C.49: Argon, Number of Channels analysis graph

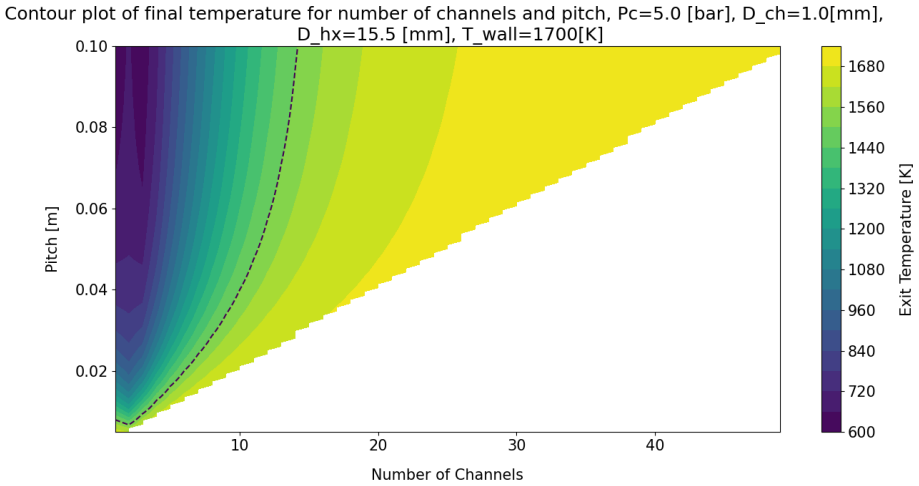

Figure C.50: Argon, Pitch and Channel Number contour

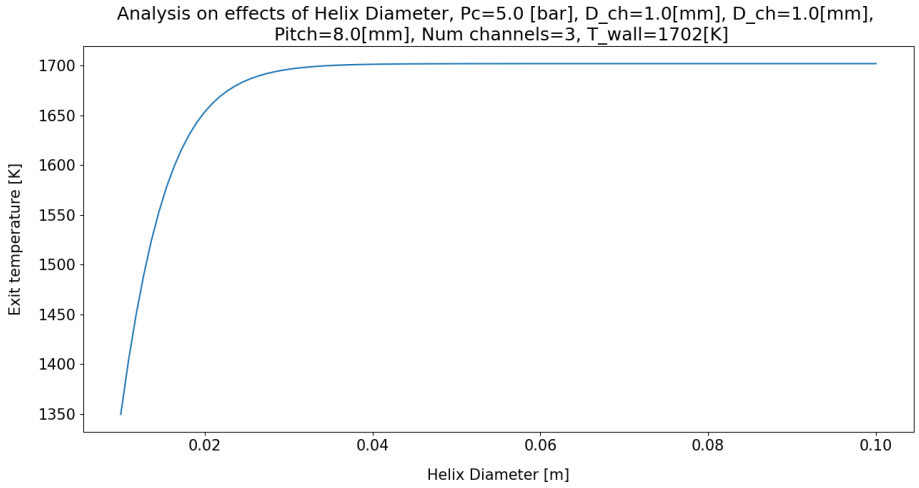

Figure C.51: Argon, Helix Diameter analysis graph

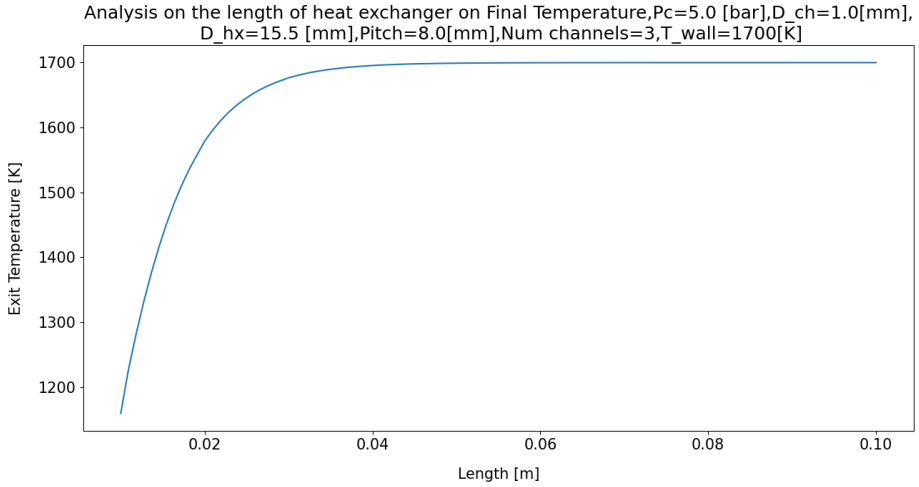

Figure C.52: Argon, Helix Length analysis graph

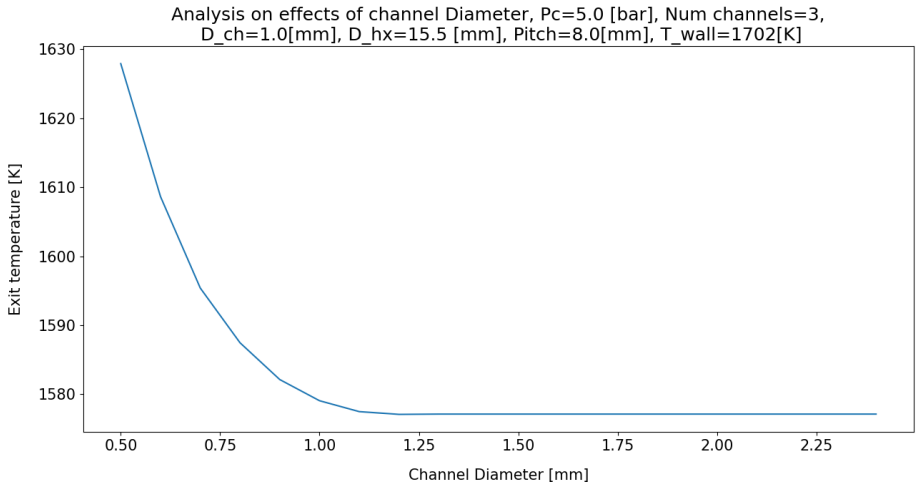

Figure C.53: Argon, Channel Diameter analysis graph

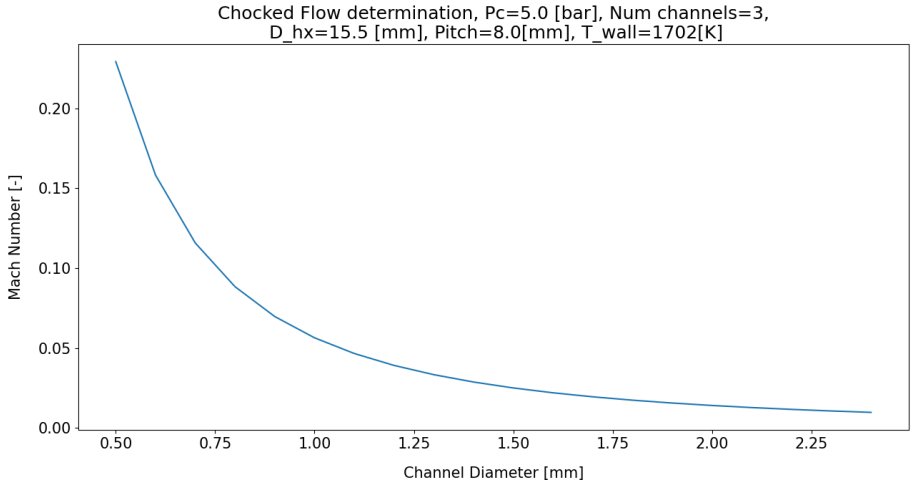

Figure C.54: Argon, Choked Flow analysis graph

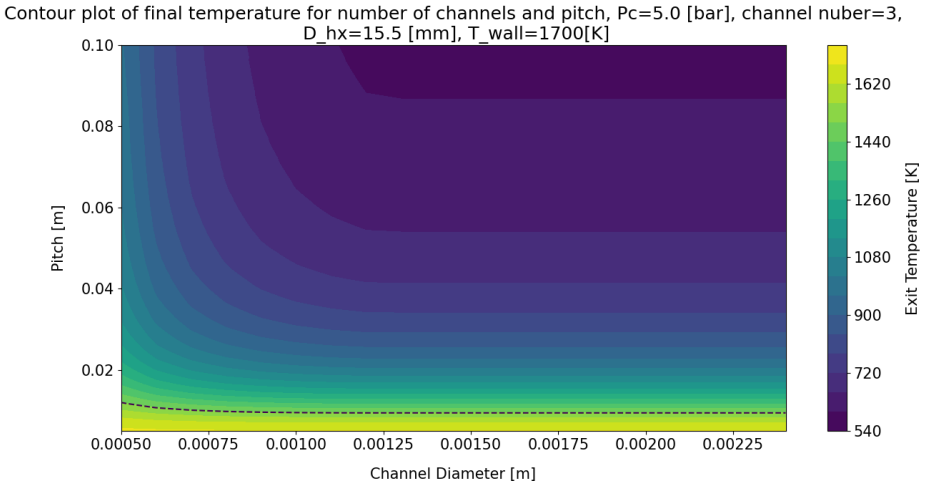

Figure C.55: Argon, Pitch and Channel Diameter contour

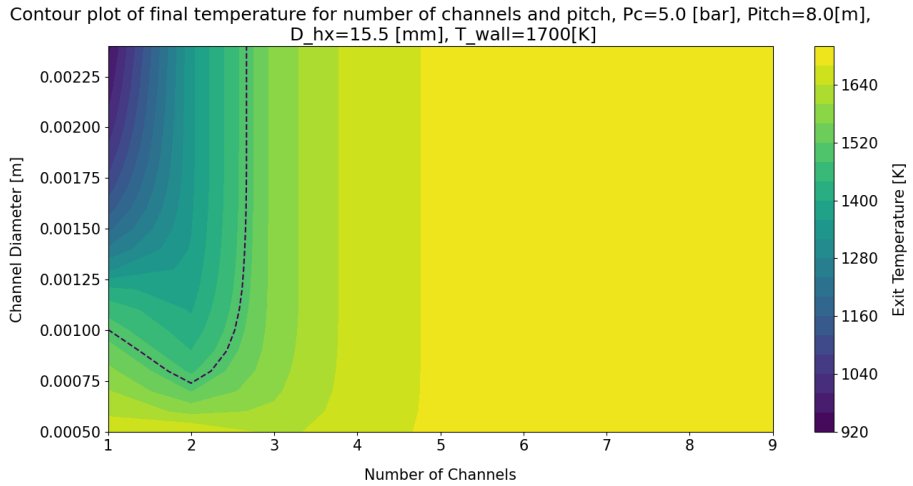

Figure C.56: Argon, Channel Number and Channel Diameter contour

C.3. Cavity Design

For transparency, the raw data for the cavity design should be made available, and the evaluation of the use of a lower power input on the luminosity distribution. Thus, in this section, the raw data will be displayed for the $3[kW]$ cavity simulation and the results for a $1[kW]$ cavity simulation.

Raw Data for 3 [kW] power input

The raw data were left out of the report due to the extremely large differences between the highest luminosity point and the rest of the cavity. Thus, it was decided to reduce the maximum displayed luminosity to a set value, providing a better illustration of the luminosity over the cavity as a whole.

As expected, for each of the different cavities, there is a hot spot directly opposite the ray source. With the limited scale, this leads to little colour resolution along the sides of the cavity.

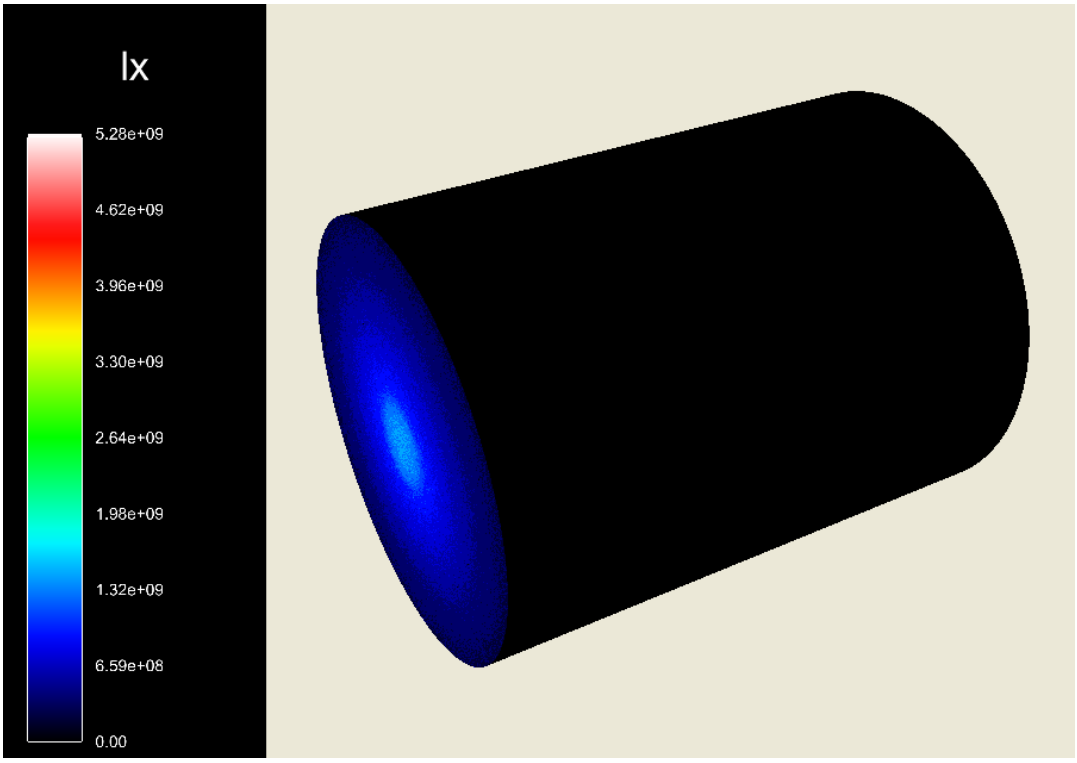

Figure C.57: Raw data for the Small Cylinder at $3\ [kW]$

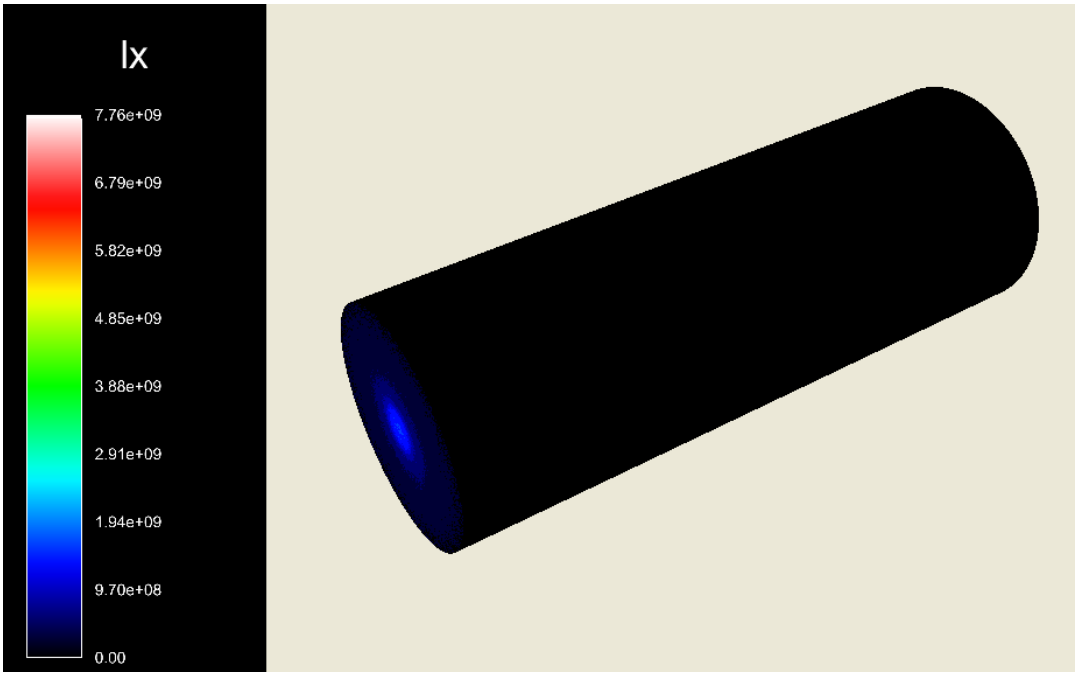

Figure C.58: Raw data for the Medium Cylinder at $3\ [kW]$

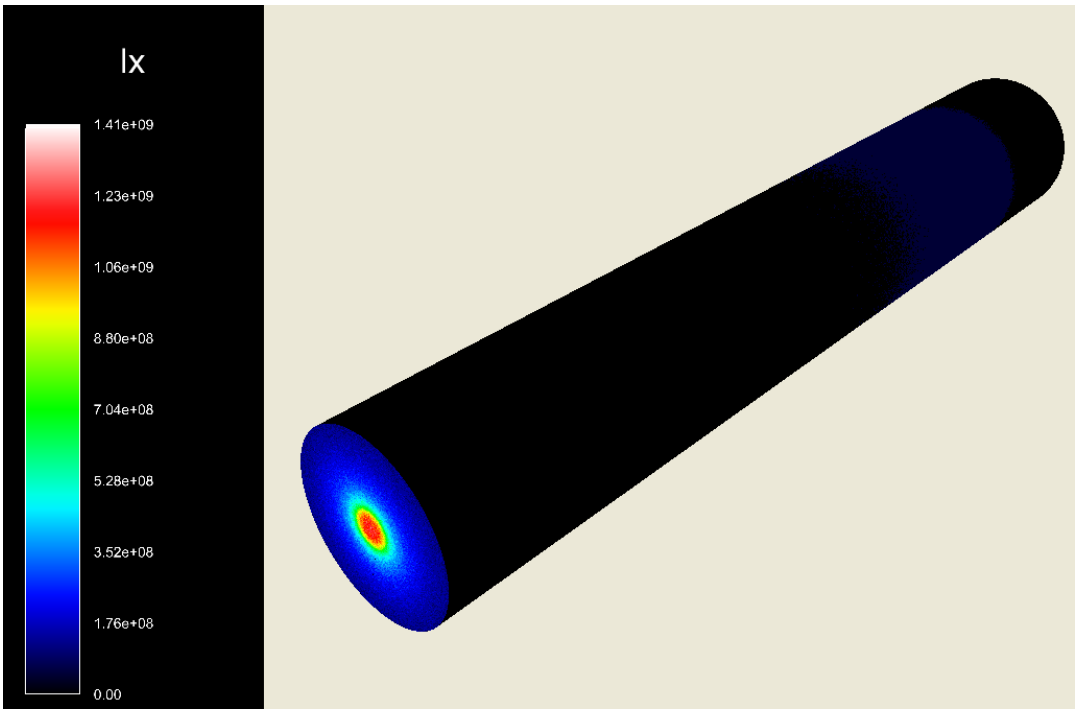

Figure C.59: Raw data for the Large Cylinder at $3\ [kW]$

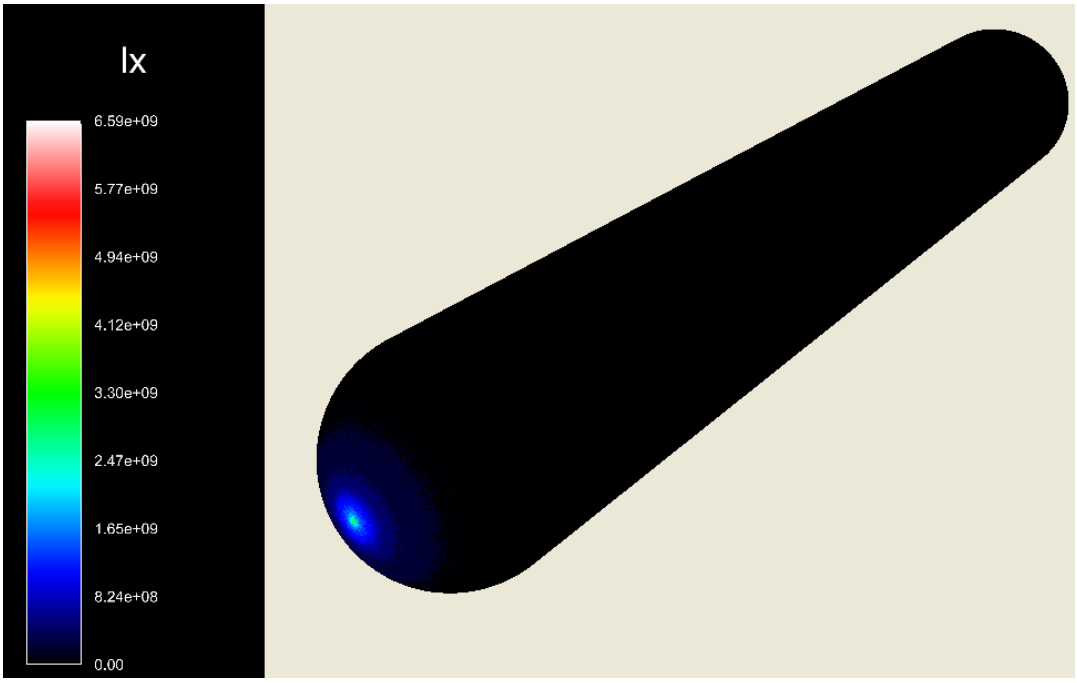

Figure C.60: Raw data for the Spherical Capped Cylinder at $3\ [kW]$

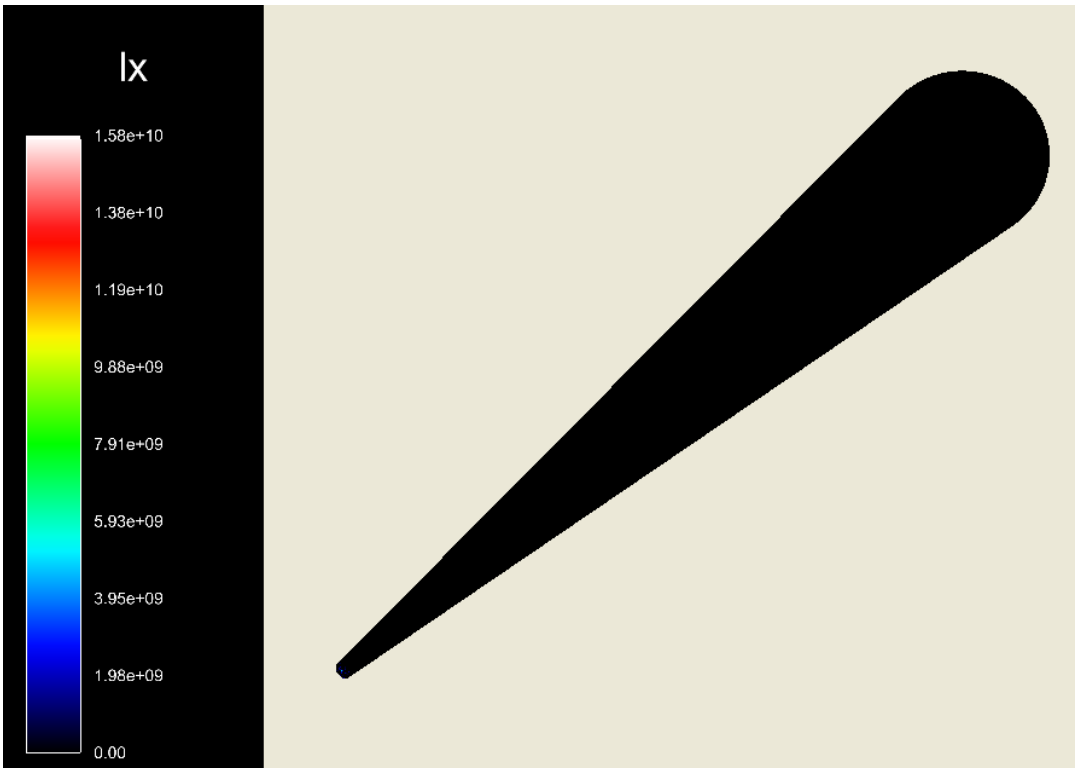

Figure C.61: Raw data for the Cone at $3\ [kW]$

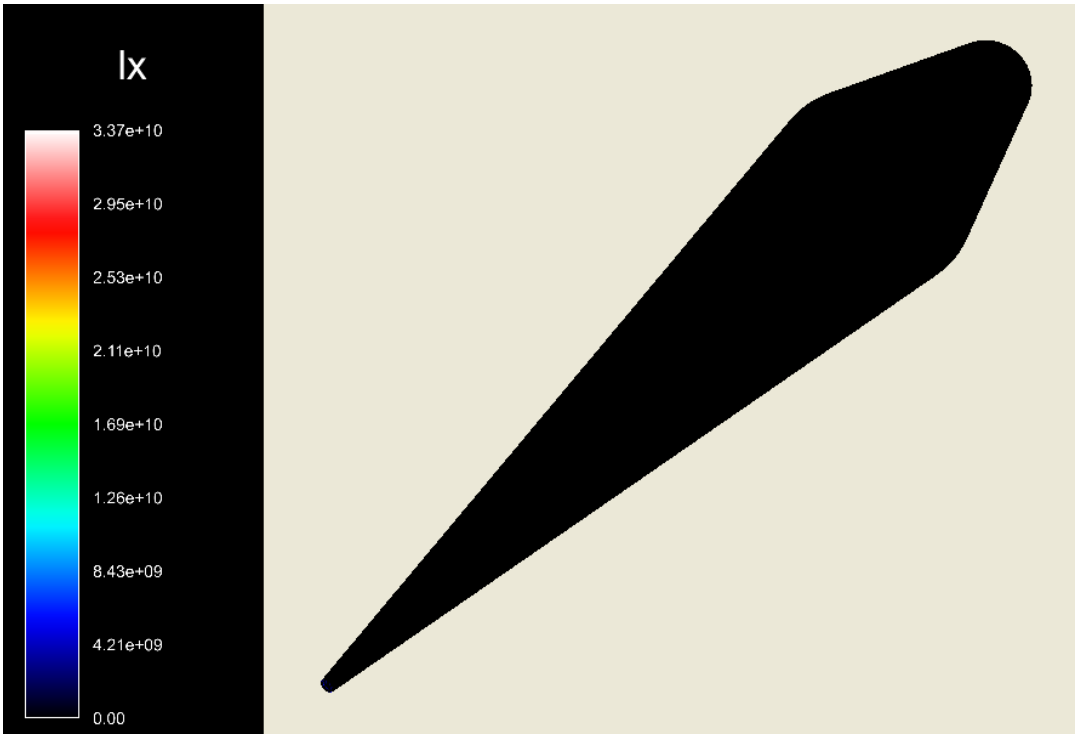

Figure C.62: Raw data for the Truncated Cone at $3\ [kW]$

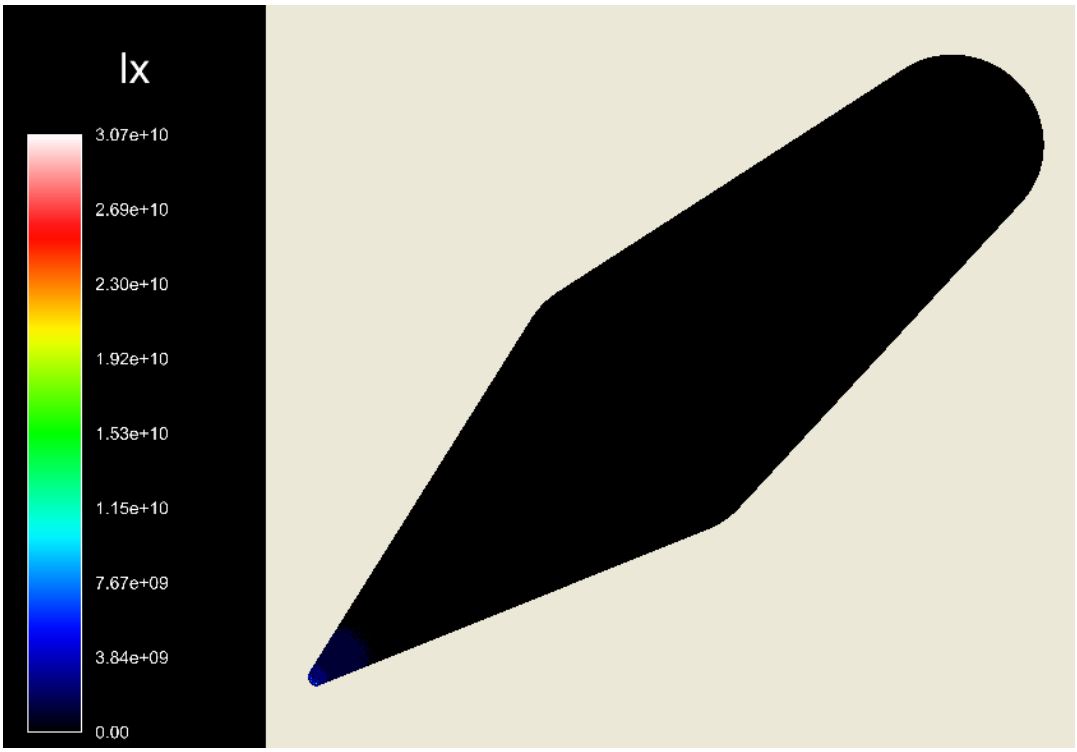

Figure C.63: Raw data for the Cone Capped Cylinder at $3\ [kW]$

Raw Data for 1 [kW] power input

As with the 3 [kW] simulation, here is the raw data for the 1 [kW] simulation. Again, there is little colour resolution along the sides of the cavity.

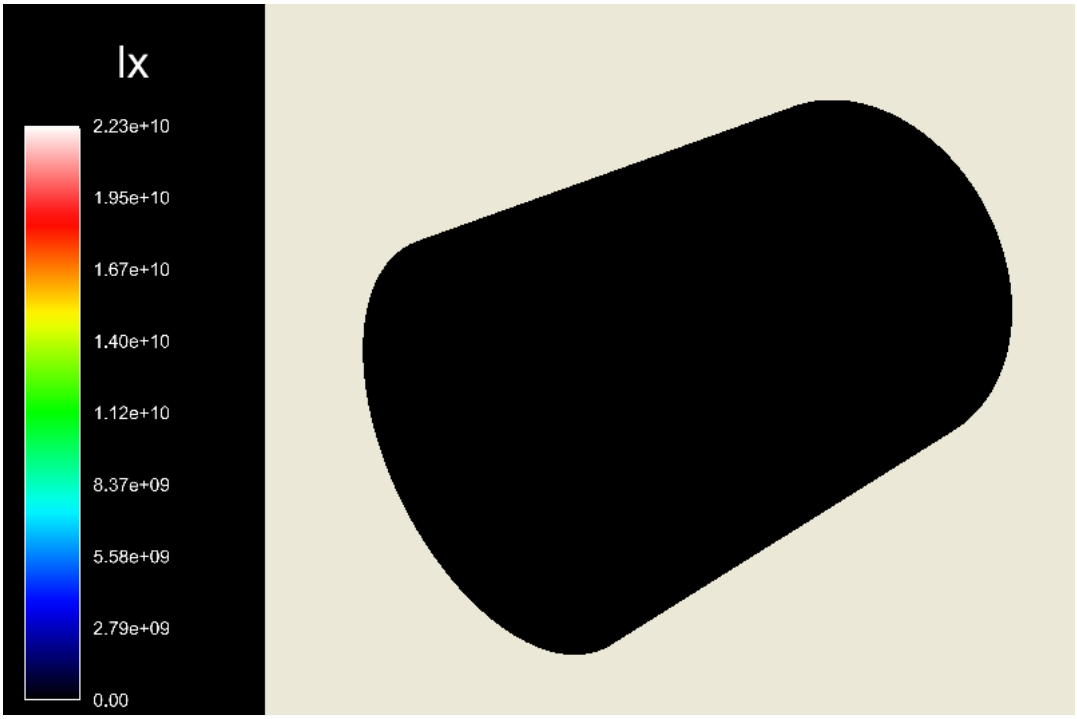

Figure C.64: Raw data for the Small Cylinder at $1\ [kW]$

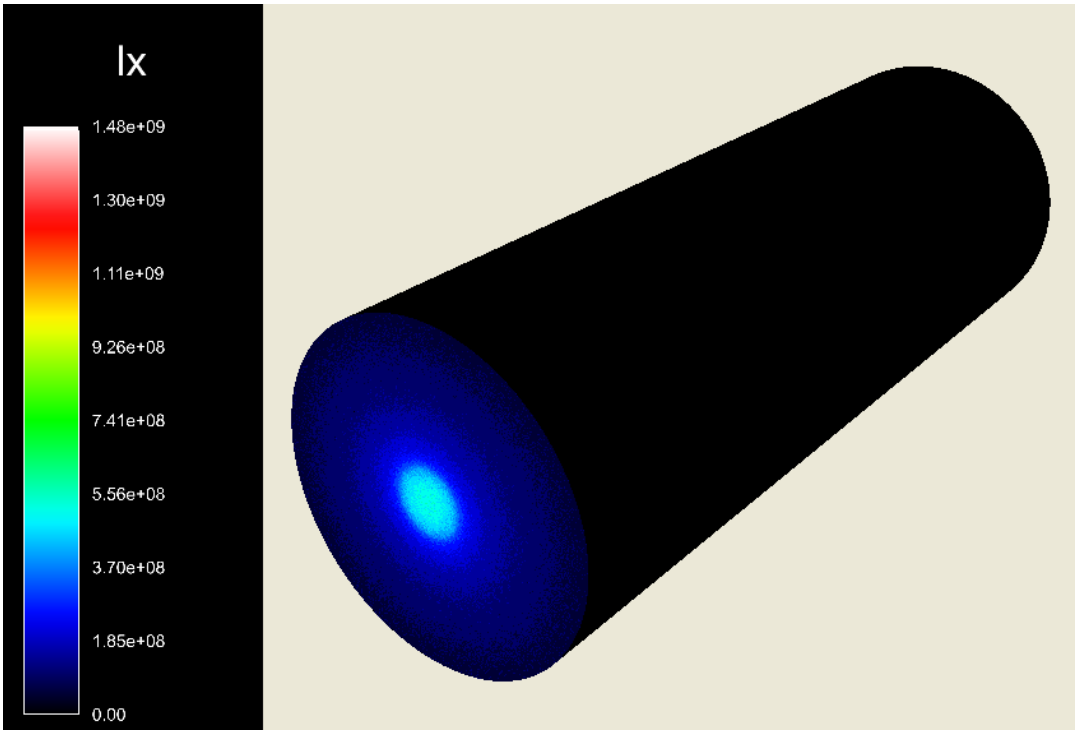

Figure C.65: Raw data for the Medium Cylinder at $1\ [kW]$

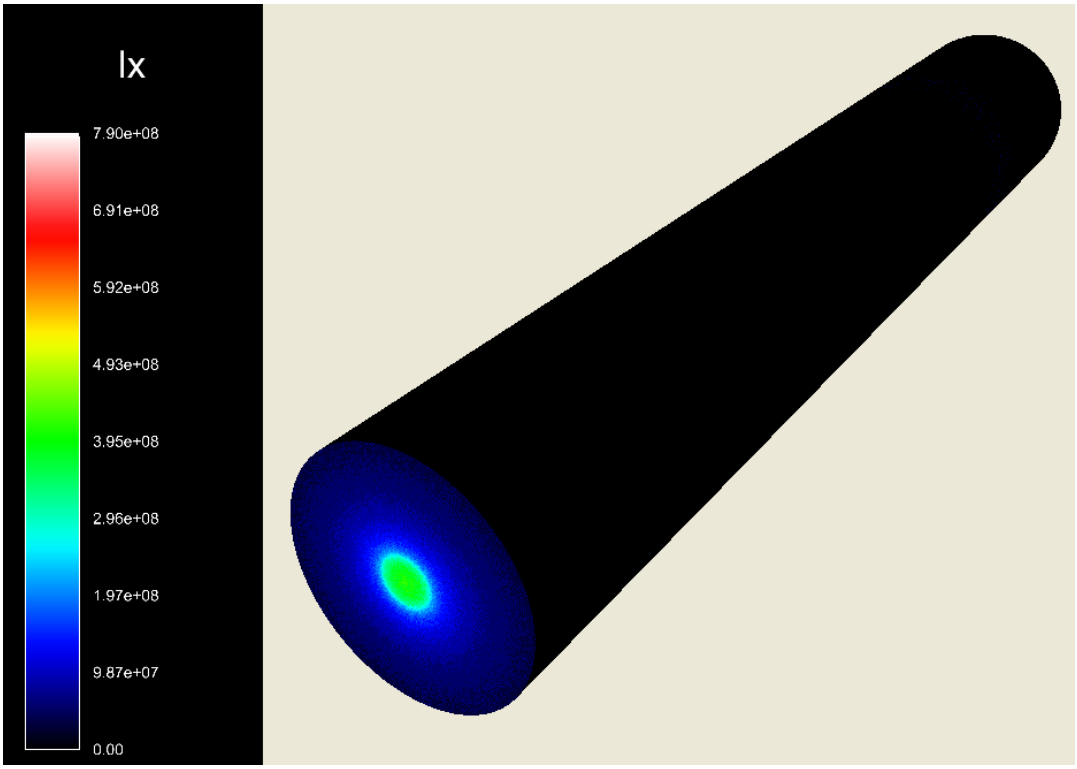

Figure C.66: Raw data for the Large Cylinder at $1\ [kW]$

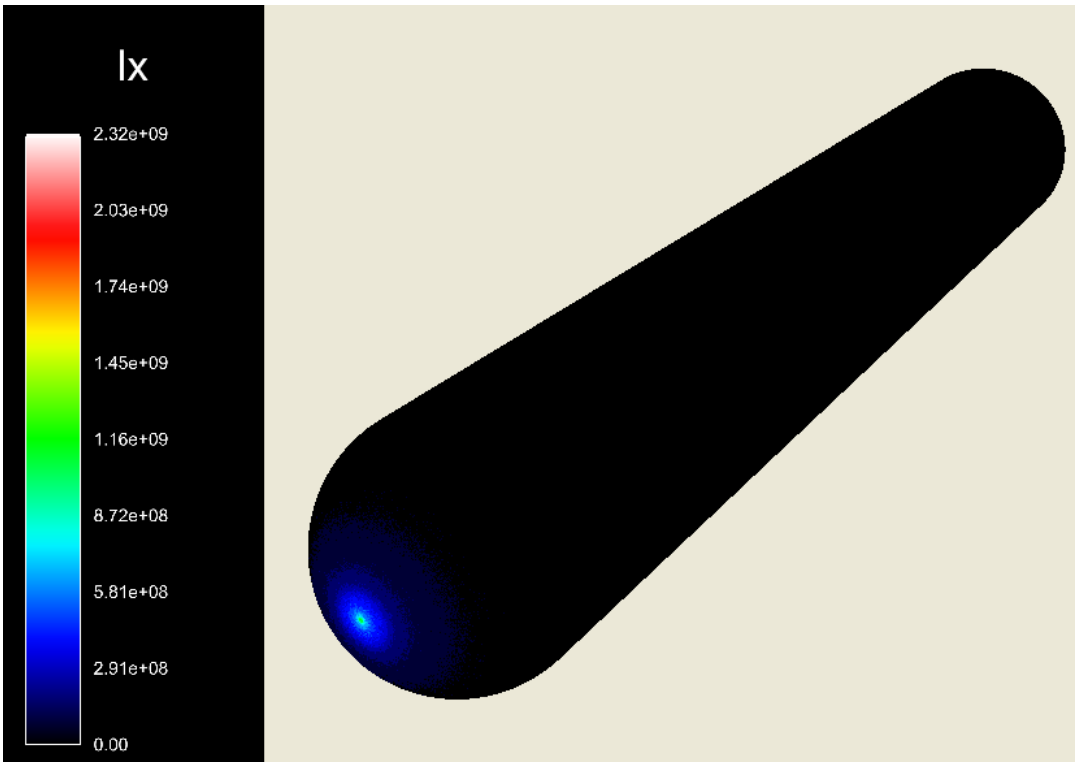

Figure C.67: Raw data for the Spherical Capped Cylinder at $1\ [kW]$

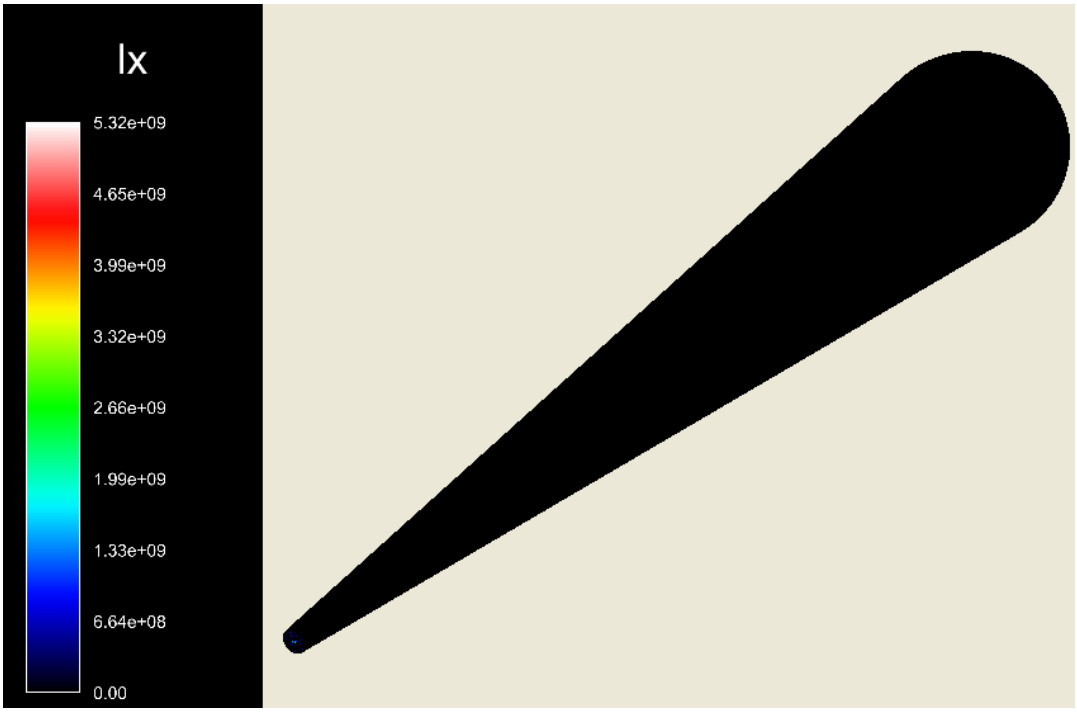

Figure C.68: Raw data for the Cone at $1\ [kW]$

Figure C.69: Raw data for the Truncated Cone at $1\ [kW]$

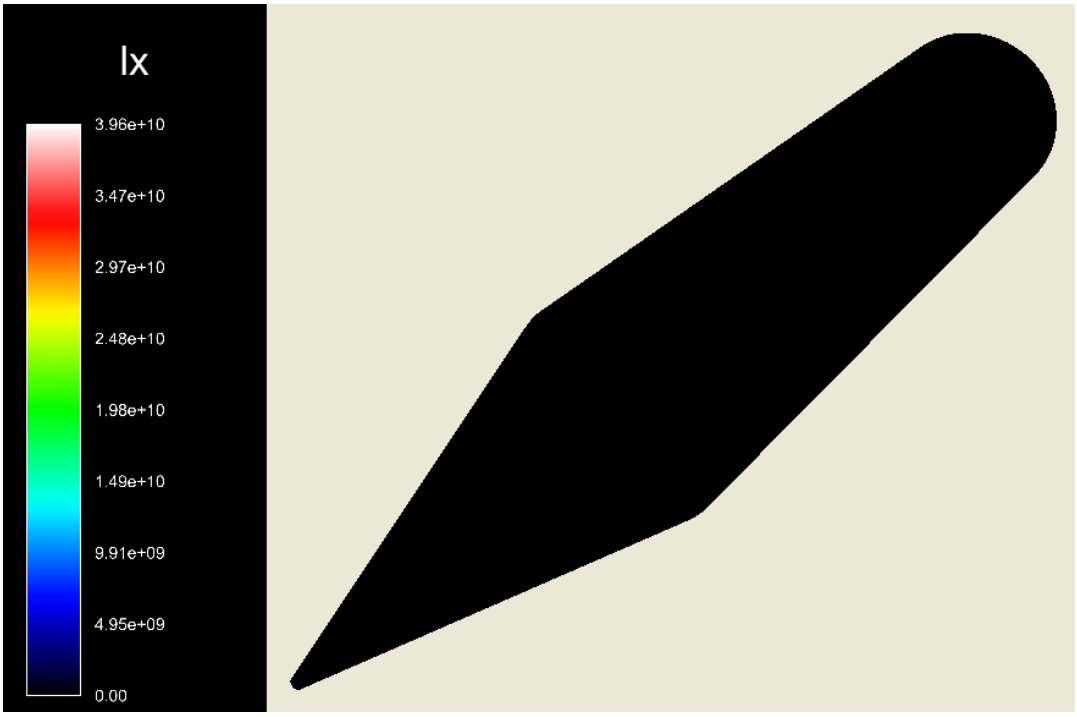

Figure C.70: Raw data for the Cone Capped Cylinder at $1\ [kW]$

Reduced Data for 1 [kW] power input

Having a look at the difference between the 1 [kW] and 3 [kW] simulations, it's clear that the same general trends are present. The location of the hotspots and the gradient in luminosity follows the same pattern. The major difference between the two, as expected, is the intensity, with the 3 [kW] simulation having higher maximum lux values than that of the 1 [kW] simulation. The gradient in the luminosity across the sides of the cavity is also much more exaggerated for the 3 [kW] simulation than that of the 1 [kW] simulation. The use of reduced power, as expected, would result in an overall reduction in luminosity as well as an apparent smoothing of the luminosity gradients across the cavity sides.

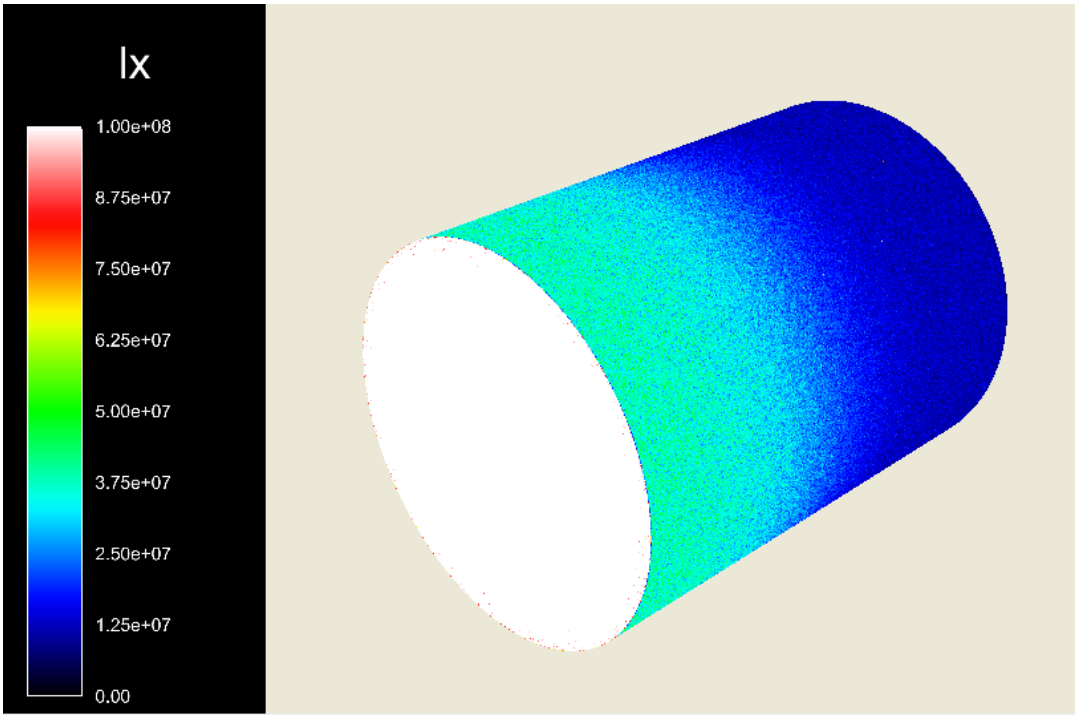

Figure C.71: Raw data for the Small Cylinder at $1\ [kW]$, max lux at $1 \cdot 10^8$

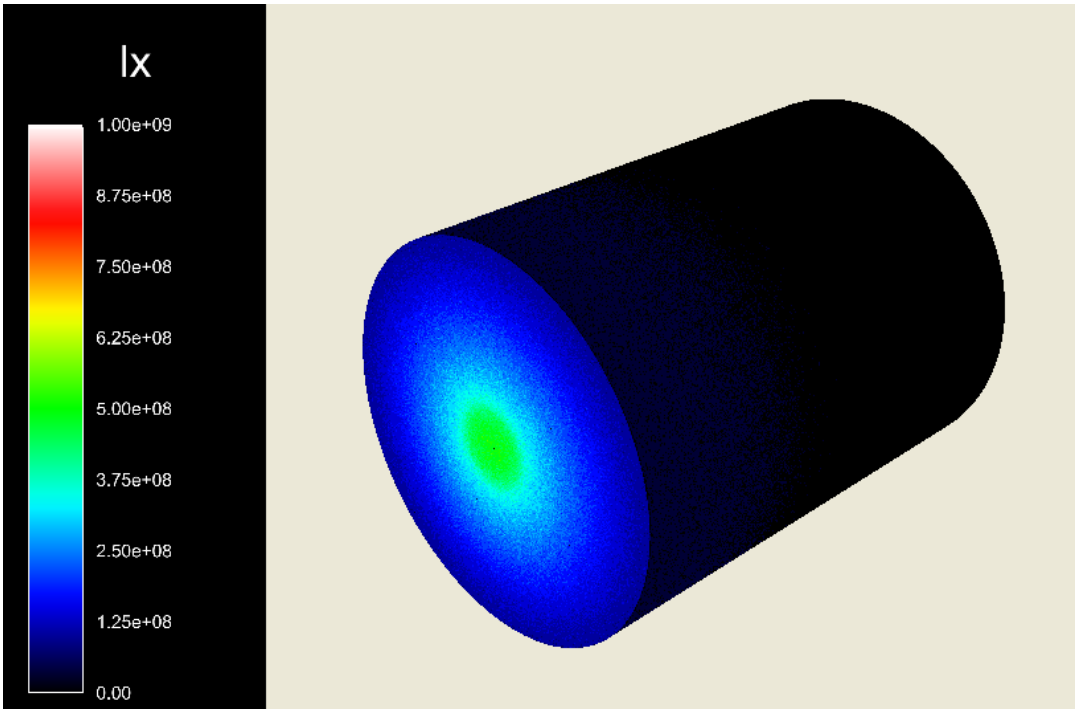

Figure C.72: Raw data for the Small Cylinder at $1\ [kW]$, max lux at $1 \cdot 10^9$

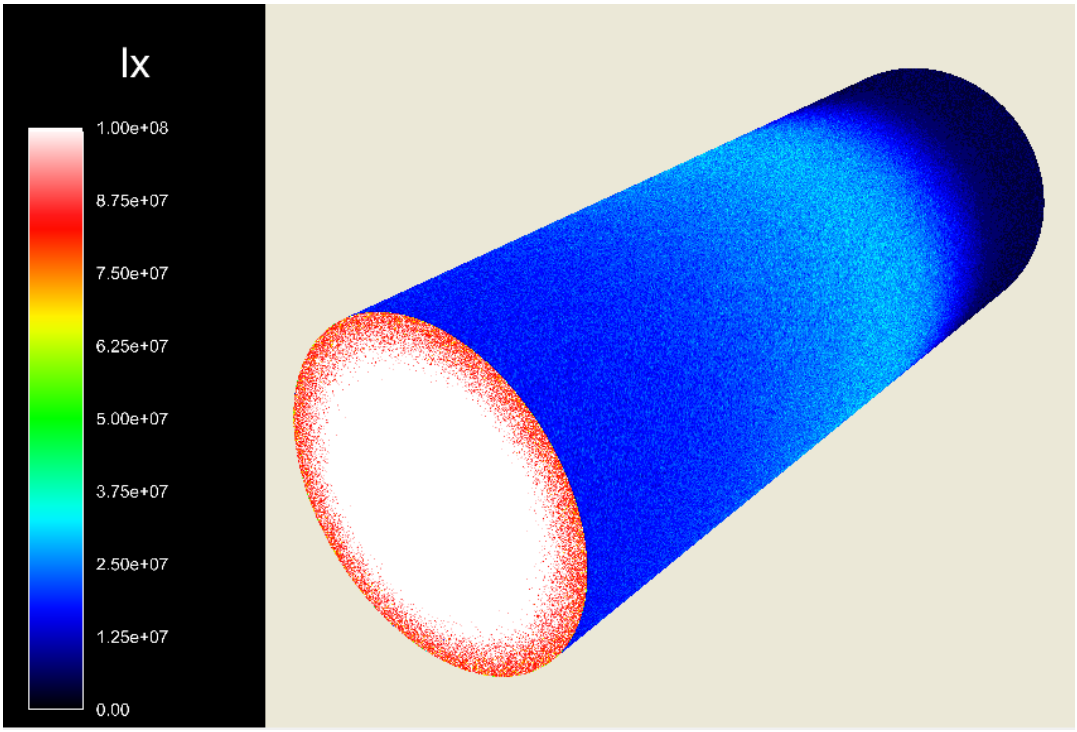

Figure C.73: Raw data for the Medium Cylinder at $1\ [kW]$, max lux at $1 \cdot 10^8$

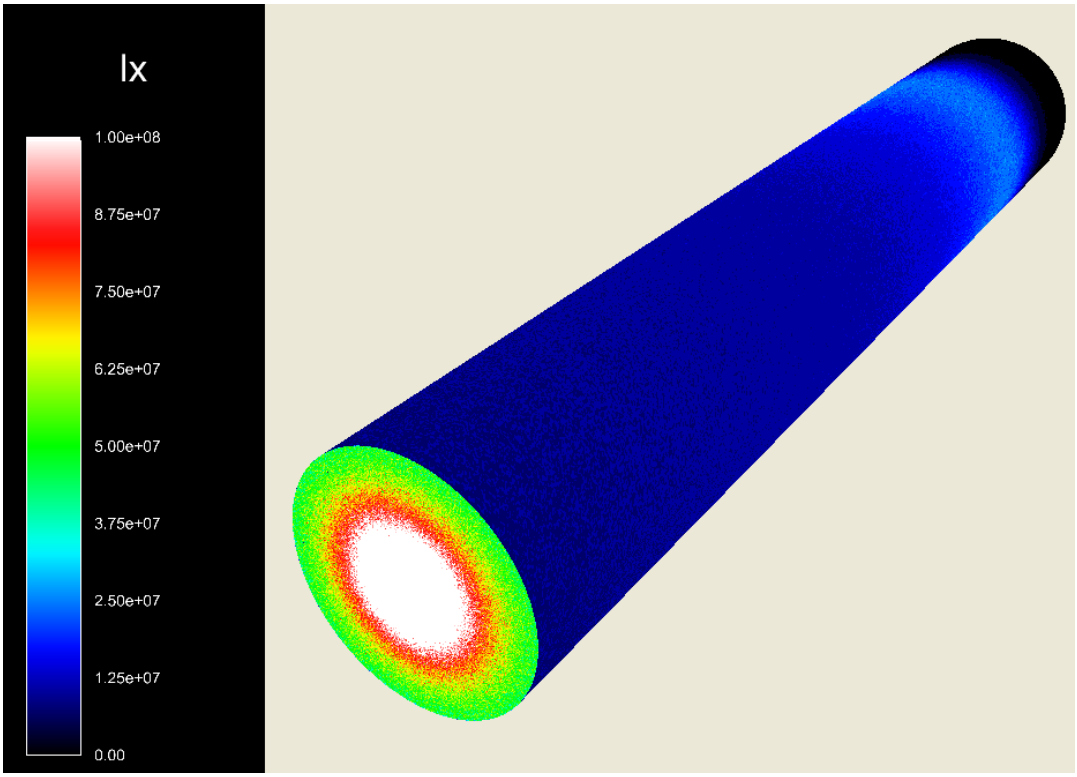

Figure C.74: Raw data for the Large Cylinder at $1\ [kW]$, max lux at $1 \cdot 10^8$

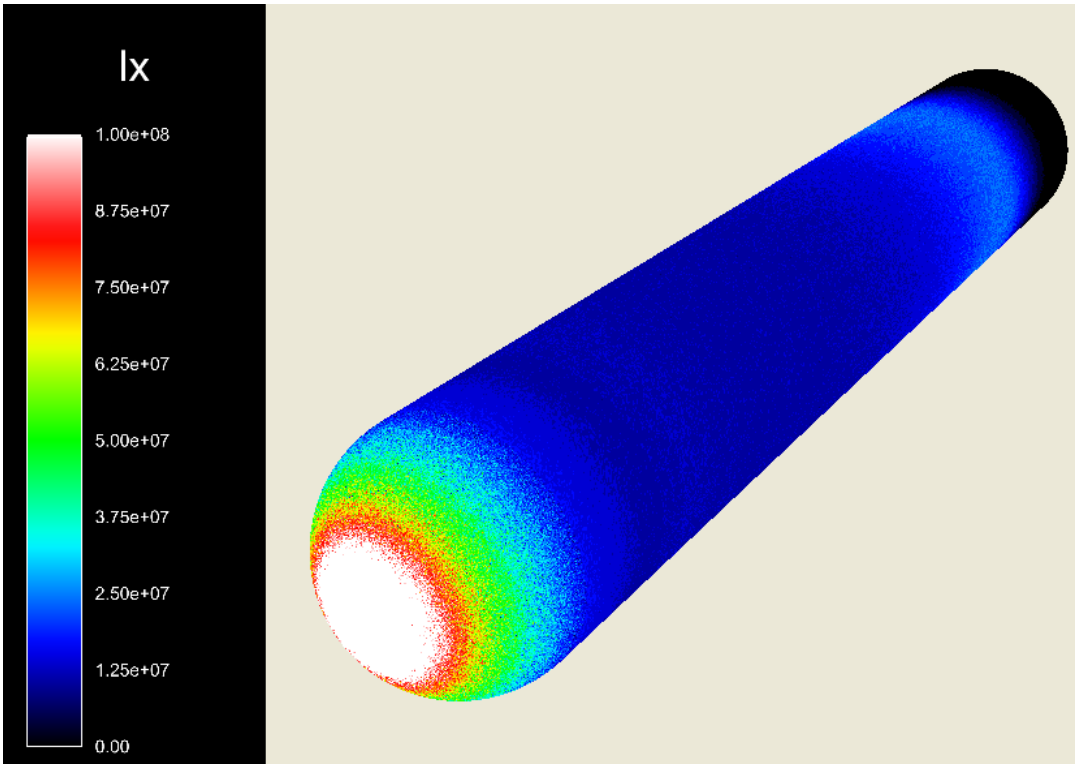

Figure C.75: Raw data for the Spherical Capped Cylinder at $1\ [kW]$, max lux at $1 \cdot 10^8$

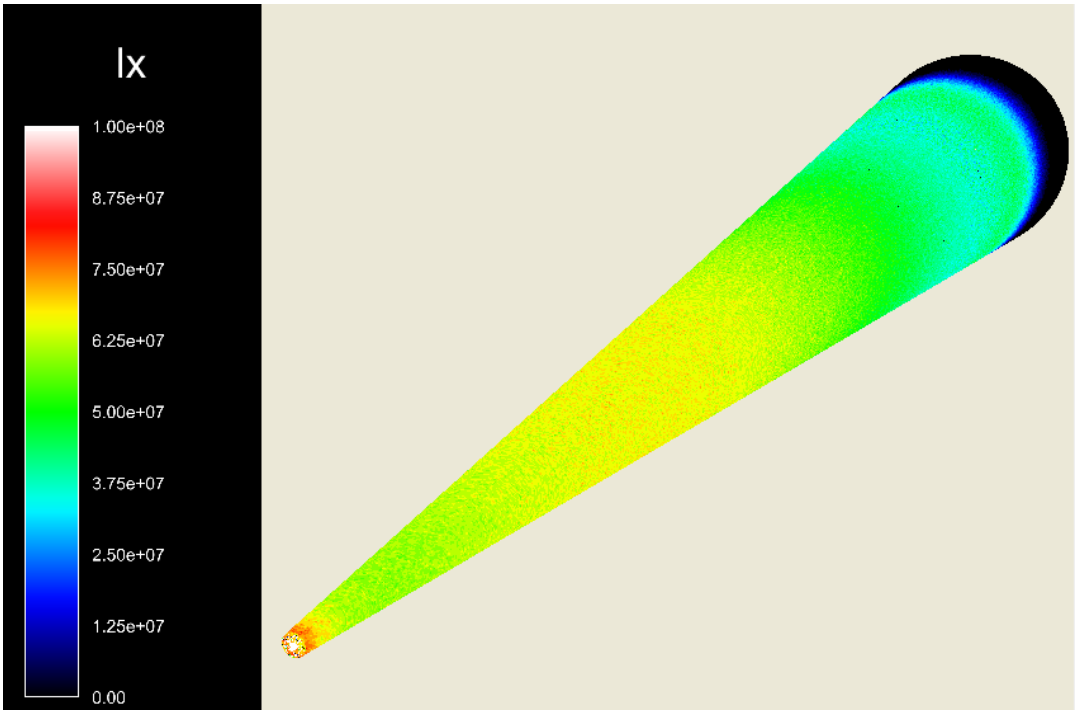

Figure C.76: Raw data for the Cone at $1\ [kW]$, max lux at $1 \cdot 10^8$

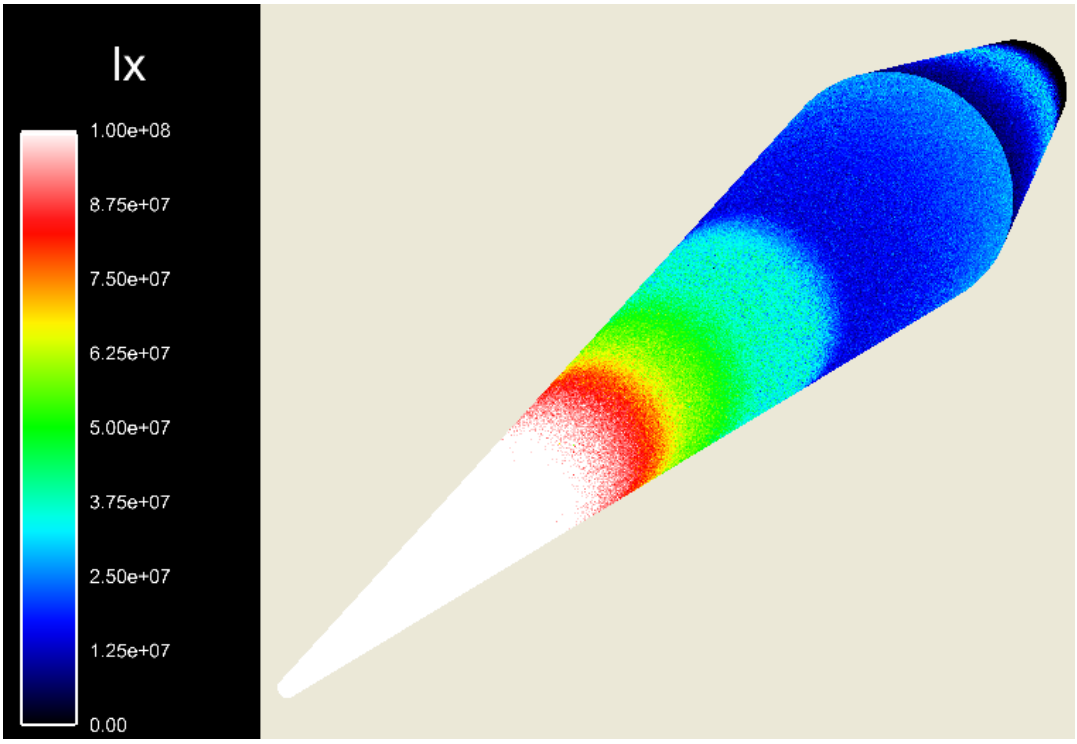

Figure C.77: Raw data for the Truncated Cone at $1\ [kW]$, max lux at $1 \cdot 10^8$

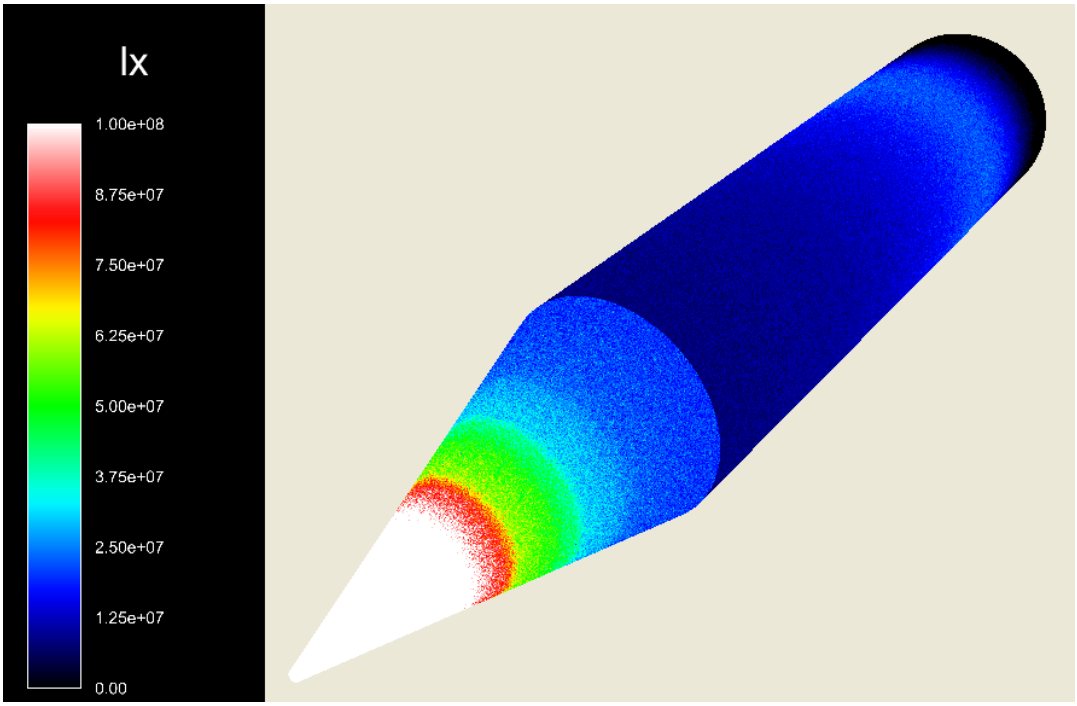

Figure C.78: Raw data for the Cone Capped Cylinder at $1\ [kW]$, max lux at $1 \cdot 10^8$

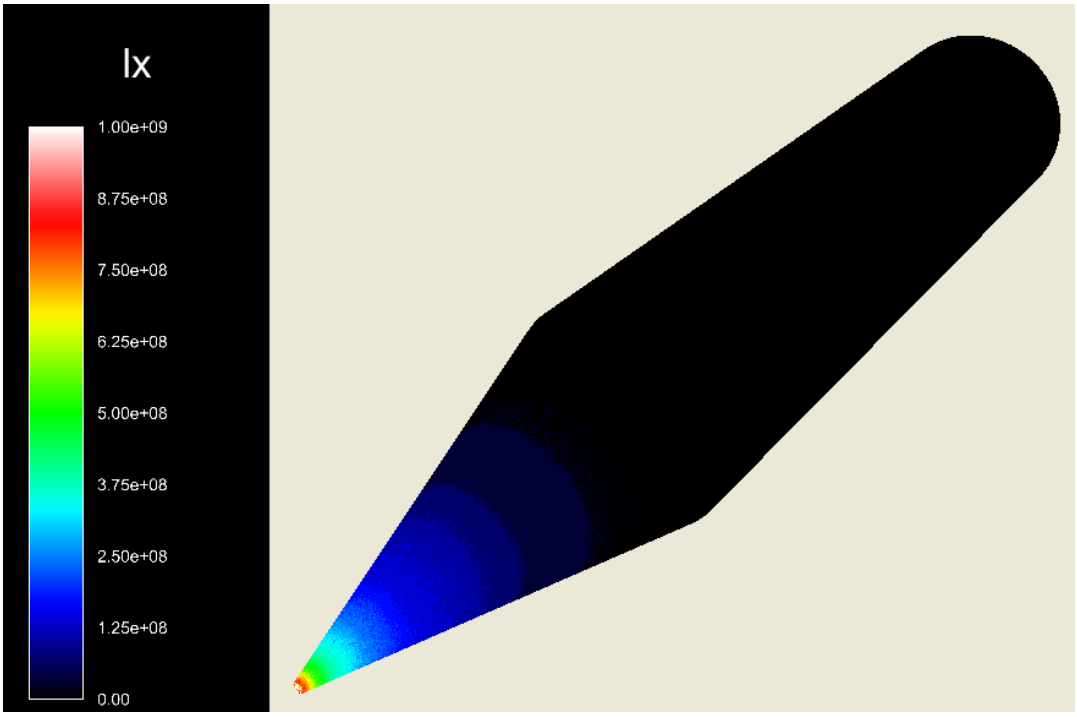

Figure C.79: Raw data for the Cone Capped Cylinder at $1\ [kW]$, max lux at $1 \cdot 10^9$

D

Code Repository

D.1. Rocket Theory Code

```
"""
Calculation of Rocket Characteristics & Sizing for a Solar Thermal Propulsion system.

Author: Niklas F Gebhardt
Data: 21/05/2025
"""
#### Libary Imports ####
import numpy as np
from SALib import ProblemSpec
import matplotlib.pyplot as plt
import cantera as ct
from matplotlib.colors import LinearSegmentedColormap
from tqdm import tqdm

#### Variables ####
Propellant = 'H2' # Propellant must be in Chemical Notation Eg H2O
Fractinal = False # Enabiling the code to calulate the dissasoiation of the propellant
Steps = 1000 #  number of steps points considered for each input varible

Tc_max = 3000 # max chamber temperature in K
Tc_min = 1000 # min chamber temperature in K

Pc_Pe_max = 10000 # Max Pressure Exit/Chamber ratio
Pc_Pe_min = 1000 # Min Pressure Exit/Chamber ratio

plt.rcParams.update({'font.size': 15}) # Set Font Size
plt.rcParams.update({'axes.labelpad': 15})
#### CONSTANTS ####
Pa = 0 # Ambient Pressure
F = 1 # Wanted Thrust Level [N]
Pc = 5E+5 # Chamber Pressure [Pa]
R = 8.31446261815324 # Gas Constant
g0 = 9.80665 # gravitational acceleration

Prop = ct.Solution(r'gri30_highT.yaml') # Importing of propellant data for, H2, Ar, N2
#Prop = ct.Solution(r'Thesis\Test.ymal') # Importing of propellant data for, He

#### MAiN CODE ####
## Functions ##

# Chem Properties Finder #
def Chem(Temp : float ,Pressure : float,Propellant : str):
    # calculation of the propellant properties, for both propellant dissasosiation or not
    if Fractinal == True:
        Prop.TPX = Temp, Pressure, f"{str(Propellant)}:0.9,{str(Propellant[0])}:0.1"
        Prop.equilibrate('TP')
        MF = Prop.mass_fraction_dict()[Propellant]
```

```
    else:
        Prop.TPX = Temp, Pressure, f"{str(Propellant)}:1.0"
        MF = 1
    gamma = Prop.cp_mass/Prop.cv_mass
    Gamma = np.sqrt(gamma * ((1 + gamma)/2)**((1 + gamma)/(1 - gamma)))
    return Prop.density, Prop.cv_mass, Prop.cp_mass, Prop.mean_molecular_weight, gamma, Gamma
        , MF

# Rocket Characteristics #
def Rocket(Tc,Pe_Pc,Pc):
    # Calcualtion of Ideal Rocket Theory
    rho, Cv, Cp, MW, gamma, Gamma, MF = Chem(Tc,Pc,Propellant) # Chemical properties input
    Ue = np.sqrt(2 * (gamma)/(gamma - 1) * R/(MW*1E-3) * Tc * (1 - Pe_Pc**((gamma-1)/gamma)))
         # Exhaust velocity
    Ae_At = Gamma/np.sqrt(((2*gamma)/(gamma-1)) * Pe_Pc**(2/gamma) * (1 - Pe_Pc**((gamma-1)/
        gamma))) # nozzle throat to exit area ratio
    Cf = Gamma * np.sqrt(((2*gamma)/(gamma-1)) * (1 - Pe_Pc**((gamma-1)/gamma))) + (Pe_Pc -
        Pa/Pc) * Ae_At # thrust coefficent
    At = F/(Cf * Pc) # nozzle throat area
    CS = 1/Gamma * (np.sqrt((Cp-Cv)*Tc)) # characteristic velocity
    Ae = At*Ae_At # nozzle exit area
    Isp = Ue/g0 # specific impulse
    m = (Gamma*Pc*At)/(np.sqrt((Cp-Cv)*Tc)) # mass flow rate
    Power = (m * Cp * (Tc - 273)) # Power required to heat propellant
    De = np.sqrt((4*Ae)/np.pi) # nozzle exit diameter
    Dt = np.sqrt((4*At)/np.pi) # nozzle throat diameter

    # Implementaion of Thrust calculation for a set Nozzle Geomitry Throat Diamiter = 1.18 mm
    Dt_fin = 1.1836260688195612e-3
    At_fin = np.pi*((Dt_fin)**2 )/ 4 # nozzle throat area
    Ae_At_fin = Gamma/np.sqrt(((2*gamma)/(gamma-1)) * Pe_Pc**(2/gamma) * (1 - Pe_Pc**((gamma
        -1)/gamma)))
    m_fin = (Gamma*Pc*At_fin)/(np.sqrt((Cp-Cv)*Tc)) # mass flow rate
    Ue_fin = np.sqrt(2 * (gamma)/(gamma - 1) * R/(MW*1E-3) * Tc * (1 - Pe_Pc**((gamma-1)/
        gamma))) # Exhaust velocity
    T_fin = m_fin*Ue_fin + (Pc*Pe_Pc)*(Ae_At_fin*At_fin)

    return list([Ae_At, De, Dt, Isp, m, MF, Power, T_fin])

def Rocket_ConG(Tc,Pc,Pe_Pc): #Calculates Thrust Sensitivity
    rho, Cv, Cp, MW, gamma, Gamma, MF = Chem(Tc,Pc,Propellant) # Chemical properties input
    Dt = 1.1836260688195612e-3
    At = np.pi*((Dt)**2 )/ 4 # nozzle throat area
    Ae_At = Gamma/np.sqrt(((2*gamma)/(gamma-1)) * Pe_Pc**(2/gamma) * (1 - Pe_Pc**((gamma-1)/
        gamma)))
    m = (Gamma*Pc*At)/(np.sqrt((Cp-Cv)*Tc)) # mass flow rate
    Ue = np.sqrt(2 * (gamma)/(gamma - 1) * R/(MW*1E-3) * Tc * (1 - Pe_Pc**((gamma-1)/gamma)))
         # Exhaust velocity
    T = m*Ue + (Pc*Pe_Pc)*(Ae_At*At)
    return T

## Plotting ##
def Plotter(Data,Tc,Pe_Pc,Pc_list):
    Tc, Pe_Pc = np.meshgrid(np.reciprocal(Pe_Pc),Tc)

    # Colour mapping #
    colors = ["red","violet","blue"]
    cmap = LinearSegmentedColormap.from_list("", colors, N=1000000)

    # Ae_At #
    fig = plt.figure(figsize=(12,10))
    ax = fig.add_subplot(111, projection='3d')
    for i in range(0,len(Pc_list),1):
        ax.plot_surface(Tc,Pe_Pc,Data[i,:,:,0],label=f'Chamber␣Pressure:␣{round(Pc_list[i]*1E
            -5,1)}␣[bar]')
    ax.set_title(f'Area␣Ratio,␣with␣{Propellant}␣as␣a␣propellant')
    ax.set_ylabel('Chamber␣Temperature␣[K]')
    ax.set_xlabel('Chamber␣Pressure␣ratio␣[-]')
    ax.set_zlabel('Area␣Ratio␣[-]')
    ax.legend(loc='upper␣left',bbox_to_anchor=(-0.2, 1))
    fig.savefig(rf'Thesis\Figures\AreaRatio_{Propellant}.png')
```

```
110
111     # Ae #
112     fig = plt.figure(figsize=(12,10))
113     ax = fig.add_subplot(111, projection='3d')
114     for i in range(0,len(Pc_list),1):
115         ax.plot_surface(Tc,Pe_Pc,Data[i,:,:,1]*1E+3,label=f'Chamber Pressure: {round(Pc_list[
                i]*1E-5,1)} [bar]')
116     ax.set_title(f'Exit Diameter, with {Propellant} as a propellant')
117     ax.set_ylabel('Chamber Temperature [K]')
118     ax.set_xlabel('Chamber Pressure ratio [-]')
119     ax.set_zlabel('Exit Diameter [mm]')
120     ax.legend(loc='upper left',bbox_to_anchor=(-0.2, 1))
121     fig.savefig(rf'Thesis\Figures\ExitDiameter_{Propellant}.png')
122
123     # At #
124     fig = plt.figure(figsize=(12,10))
125     ax = fig.add_subplot(111, projection='3d')
126     for i in range(0,len(Pc_list),1):
127         ax.plot_surface(Tc,Pe_Pc,Data[i,:,:,2]*1E+3,label=f'Chamber Pressure: {round(Pc_list[
                i]*1E-5,1)} [bar]')
128     ax.set_title(f'Throat Diameter, with {Propellant} as a propellant')
129     ax.set_ylabel('Chamber Temperature [K]')
130     ax.set_xlabel('Chamber Pressure ratio [-]')
131     ax.set_zlabel('Throat Diameter [mm]')
132     ax.legend(loc='upper left',bbox_to_anchor=(-0.3, 1))
133     fig.savefig(rf'Thesis\Figures\ThroatDiameter_{Propellant}.png')
134
135     # ISP #
136     fig = plt.figure(figsize=(12,10))
137     ax = fig.add_subplot(111, projection='3d')
138     for i in range(0,len(Pc_list),1):
139         ax.plot_surface(Tc,Pe_Pc,Data[i,:,:,3],label=f'Chamber Pressure: {round(Pc_list[i]*1E
                -5,1)} [bar]')
140     ax.set_title(f'Isp, with {Propellant} as a propellant')
141     ax.set_ylabel('Chamber Temperature [K]')
142     ax.set_xlabel('Chamber Pressure ratio [-]')
143     ax.set_zlabel('Isp [s]')
144     ax.legend(loc='upper left',bbox_to_anchor=(-0.2, 1))
145     fig.savefig(rf'Thesis\Figures\Isp_{Propellant}.png')
146
147     # Mass Flow #
148     fig = plt.figure(figsize=(12,10))
149     ax = fig.add_subplot(111, projection='3d')
150     for i in range(0,len(Pc_list),1):
151         ax.plot_surface(Tc,Pe_Pc,Data[i,:,:,4]*1E+3,label=f'Chamber Pressure: {round(Pc_list[
                i]*1E-5,1)} [bar]')
152     ax.set_title(f'Mass Flow, with {Propellant} as a propellant')
153     ax.set_ylabel('Chamber Temperature [K]')
154     ax.set_xlabel('Chamber Pressure ratio [-]')
155     ax.set_zlabel('Propellant mass flow [g/s]')
156     ax.view_init(30, -30)
157     ax.legend()
158     fig.savefig(rf'Thesis\Figures\MassFlow_{Propellant}.png')
159
160     # Mass Fraction #
161     fig = plt.figure(figsize=(12,10))
162     ax = fig.add_subplot(111, projection='3d')
163     for i in range(0,len(Pc_list),1):
164         ax.plot_surface(Tc,Pe_Pc,Data[i,:,:,5],label=f'Chamber Pressure: {round(Pc_list[i]*1E
                -5,1)} [bar]')
165     ax.set_title(f'Mass Fraction of {Propellant}')
166     ax.set_ylabel('Chamber Temperature [K]')
167     ax.set_xlabel('Chamber Pressure ratio [-]')
168     ax.set_zlabel(f'Propellant {Propellant} mass fraction [-]')
169     ax.legend(loc='upper left',bbox_to_anchor=(-0.2, 1))
170     fig.savefig(rf'Thesis\Figures\MassFraction_{Propellant}.png')
171
172     # Power Requirment #
173     fig = plt.figure(figsize=(12,10))
174     ax = fig.add_subplot(111, projection='3d')
175     for i in range(0,len(Pc_list),1):
```

```
176         ax.plot_surface(Tc,Pe_Pc,Data[i,:,:,6],label=f'Chamber Pressure: {round(Pc_list[i]*1E
                -5,1)} [bar]')
177     ax.set_title(f'Power Required, with {Propellant} as a propellant')
178     ax.set_ylabel('Chamber Temperature [K]')
179     ax.set_xlabel('Chamber Pressure ratio [-]')
180     ax.set_zlabel(f'Power Required [W]')
181     ax.legend(loc='upper left',bbox_to_anchor=(-0.2, 1))
182     fig.savefig(rf'Thesis\Figures\PowerRequired_{Propellant}.png')
183     plt.show()
184 
185     Steps = 100
186     Tc_sen_lst = np.linspace(1000,2000,Steps)
187     Pc_list = [4E+5,4.5E+5,5E+5,5.5E+5,6E+5]
188     Pe_Pc_list = np.linspace(1/5000,1/15000,Steps)
189     print(Pe_Pc_list)
190     Data_sens = np.zeros((Steps,Steps,Steps,1))
191     print(np.shape(Data_sens))
192     for i in tqdm(range(len(Tc_sen_lst))):
193         for j in tqdm(range(len(Pc_list))):
194             for k in tqdm(range(len(Pe_Pc_list))):
195                 Data_int = Rocket(Tc_sen_lst[i],Pe_Pc_list[k],Pc_list[j])
196                 Data_sens[i,j,k:] = Data_int[-1] #Rocket_ConG(Tc_sen_lst[i],Pc_list[j],
                        Pe_Pc_list[k])
197 
198     Pe_Pc_list, Tc_sen_lst = np.meshgrid(Tc_sen_lst,Pe_Pc_list)
199     fig = plt.figure(figsize=(15,10))
200     ax = fig.add_subplot(111, projection='3d')
201     for i in range(0,len(Pc_list),1):
202             ax.plot_surface(np.reciprocal(Tc_sen_lst),Pe_Pc_list,Data_sens[:,i,:,0],label=f'
                    Chamber Pressure: {round(Pc_list[i]*1E-5,1)} [bar]')
203     ax.set_title(f'Thrust Sensitivity Analysis')#,fontsize=50)
204     ax.set_ylabel('Chamber Temperature [K]')#,fontsize=50)
205     ax.set_xlabel('Chamber/Exit pressure ratio [bar]')#,fontsize=50)
206     ax.set_zlabel('Thrust [N]')#,fontsize=50)
207     ax.legend(loc='upper left',bbox_to_anchor=(-0.2, 1))
208     plt.show()
209     fig.savefig(rf'Thesis\Figures\TrustSensitivity_{Propellant}.png')
210 
211     return
212 
213 ## Main Loop ##
214 Ae_At, De, Dt, Isp, m, MF, Power, T = Rocket(1500,1/10000,5E+5) # evaluation of final design
        varible
215 print('Ae_At=',Ae_At,'De=', De*1E+3,'Dt=', Dt*1E+3,'Isp=', Isp,'m=', m*1E+3,'MF=', MF,'Power=
        ', Power)
216 Tc_list = np.linspace(Tc_min,Tc_max,Steps)
217 Pe_Pc_list = np.reciprocal(np.linspace(Pc_Pe_min,Pc_Pe_max,Steps))
218 Pc_list = [1E+5,2E+5,5E+5,10E+5,15E+5,25E+5,50E+5] # list of pressure values to be
        investigated
219 Data = np.zeros((len(Pc_list),Steps,Steps,8))
220 
221 # Main calulation loop over the three varibles Chamber pressure and temperature and exit/
        chamber pressure ratio
222 for i in tqdm(range(len(Pc_list))):
223     for j in tqdm(range(len(Tc_list))):
224         for k in range(len(Pe_Pc_list)):
225             Data[i,j,k:] = Rocket(Tc_list[j],Pe_Pc_list[k],Pc_list[i])
226 
227 #with open(r'Thesis\RocketData.txt','wb') as f:
228     #pickle.dump(Data,f)
229 
230 #with open(r'Thesis\RocketData.txt','rb') as f:
231     #Data_new = pickle.load(f)
232 
233 # Main ploting function to visualisa data
234 Plotter(Data,Tc_list,Pe_Pc_list,Pc_list)
235 
236 #Setting Up Problem Space
237 sp = ProblemSpec({
238     'names' : ['Tc','Pe/Pc','Pc'],
239     'bounds' : [
```

```
        [1000,3000],
        [1/Pc_Pe_max,1/Pc_Pe_min],
        [1E+5,50E+5]
    ],
    'outputs': ['Ae_At', 'De', 'Dt', 'Isp', 'm', 'MF', 'Power', 'Thrust']
})

#Creating a wrapping loop to to have the Rocket Function output an array
def wrapped_Rocket(X: np.ndarray, func=Rocket) -> np.ndarray:
    N, D = X.shape
    results = np.empty((N,8))
    for i in range(N):
        Tc,Pe_Pc,Pc = X[i, :]
        results[i] = func(Tc,Pe_Pc,Pc)

    return results

#Calculates the Statistical Analysis of the model
(
    sp.sample_sobol(2**16)#2**16
    .evaluate(wrapped_Rocket)
    .analyze_sobol()
)

# gathers The Total, First and Second order sensitivity indexes
S1s = np.array([sp.analysis[_y]['S1'] for _y in sp['outputs']])
S2s = np.array([sp.analysis[_y]['S2'] for _y in sp['outputs']])
STs = np.array([sp.analysis[_y]['ST'] for _y in sp['outputs']])
print(sp)
x = np.arange(len(sp['outputs']))
width = 0.25  # the width of the bars
multiplier = 0
offset = width * multiplier
# Plots the Total sensitivity indices
fig, ax = plt.subplots(layout='constrained',figsize=[18,8])

Tc_reacts = ax.bar(x+width, np.round(STs[:,0],3), width, label='Tc')
Pe_Pc_reacts = ax.bar(x, np.round(STs[:,1],3),width,label='Pe_Pc')
Pc_reacts = ax.bar(x-width, np.round(STs[:,2],3),width,label='Pc')

ax.set_title(f'Total Sensitivity Anlysis for {Propellant}')
ax.set_ylabel('Total Sensitivity Index',fontsize=20)
ax.set_xlabel('Output Parameters',fontsize=20)
ax.bar_label(Tc_reacts, padding=1)
ax.bar_label(Pe_Pc_reacts, padding=1)
ax.bar_label(Pc_reacts, padding=1)
ax.set_xticks(x, sp['outputs'], fontsize=20)
ax.legend(loc='upper left', ncols=3, fontsize=20)
ax.set_ylim(0, 1.2)
fig.savefig(rf'Thesis\Figures\Total_Sens_Analsys{Propellant}.png')
# Plots the Total sensitivity indices
fig, ax = plt.subplots(layout='constrained',figsize=[18,8])

Tc_reacts = ax.bar(x+width, np.round(S1s[:,0],3), width, label='Tc')
Pe_Pc_reacts = ax.bar(x, np.round(S1s[:,1],3),width,label='Pe_Pc')
Pc_reacts = ax.bar(x-width, np.round(S1s[:,2],3),width,label='Pc')

ax.set_title(f'First Order Sensitivity Anlysis for {Propellant}')
ax.set_ylabel('First Order Sensitivity Index',fontsize=20)
ax.set_xlabel('Output Parameters',fontsize=20)
ax.bar_label(Tc_reacts, padding=1)
ax.bar_label(Pe_Pc_reacts, padding=1)
ax.bar_label(Pc_reacts, padding=1)
ax.set_xticks(x, sp['outputs'],fontsize=20)
ax.legend(loc='upper left', ncols=3, fontsize=20)
ax.set_ylim(0, 1.2)
fig.savefig(rf'Thesis\Figures\First_Order_Sens_Analsys{Propellant}.png')

# Plots the Total sensitivity indices
fig, ax = plt.subplots(layout='constrained',figsize=[18,8])

```

```
Tc_reacts = ax.bar(x+width, np.round(S2s[:,0,1],3), width, label='(Tc, Pe/Pc)')
Pe_Pc_reacts = ax.bar(x, np.round(S2s[:,0,2],3),width,label='(Tc, Pc)')
Pc_reacts = ax.bar(x-width, np.round(S2s[:,1,2],3),width,label='(Pe/Pc, Pc)')

ax.set_title(f'Second Order Sensitivity Anlysis for {Propellant}')
ax.set_ylabel('Second Order Sensitivity Index',fontsize=20)
ax.set_xlabel('Output Parameters',fontsize=20)
ax.bar_label(Tc_reacts, padding=1)
ax.bar_label(Pe_Pc_reacts, padding=1)
ax.bar_label(Pc_reacts, padding=1)
ax.set_xticks(x, sp['outputs'],fontsize=20)
ax.legend(loc='upper left', ncols=3, fontsize=20)
ax.set_ylim(0, np.nanmax(S2s) + 0.2)
fig.savefig(rf'Thesis\Figures\Secon_Order_Sens_Analsys{Propellant}.png')

plt.show()
```

D.2. Heat-Exchanger Code

```
"""
Calculate the Channel Temperature of a heat exchanger.

Auther: Niklas Gebhardt
"""
import numpy as np
import matplotlib.pyplot as plt
import cantera as ct
from matplotlib import colormaps
import matplotlib as mpl
import matplotlib.cm as cm
import scipy.interpolate as spi
from tqdm import tqdm

# Constants #
Prop = ct.Solution(r'gri30_highT.yaml')
m = 0.1494E-3 # mass flow rate
P = 5E+5 # pressure of fluid
eps = 10E-10 # Surface roughness height of channel wall
T_w = 1702 # Temperature of the wall
dx_a = 0.0001 # Vertical dx
T_int = 293 # Starting Tempearture
L_max = 0.02 # max length of heat exchanger

# Varibles #
Propellant = 'N2' # Preopellant used
D = 1E-3 # Diameter of flow channel
length_lst = np.arange(0,L_max,dx_a)
Num_channels = 3 # number of channels
Pitch_Global = 0.008e+3 # global channel pitch
Helix_Diameter_Global = 0.0155e+3 # global helix diameter
Fractinal = False # Enabiling the code to calulate the dissasoiation of the propellant
plt.rcParams.update({'font.size': 15}) # Set Font Size
plt.rcParams.update({'axes.labelpad': 15}) # Set Axes gap

### Main Code ###
## Functions ##

def Gemoitry_Helix(Diameter: float, pitch: float):
    #Calculates the geometry of the helix
    Geomitry = np.zeros((len(length_lst),4))
    i = 0
    for z in np.arange(0,L_max,L_max/len(length_lst)):
        x = Diameter/2 * np.cos(z*(2 * np.pi)*1/pitch)
        y = Diameter/2 * np.sin(z*(2 * np.pi)*1/pitch)
        z = z
        Geomitry[i][:] = [x,y,z,0]

        i = i + 1
    return Geomitry

```

```
def Gemoitry_Strait(x: float, y: float):
    #Calculates geometry of straight
    Geomitry = np.zeros((len(length_lst),4))
    i = 0
    for z in np.arange(0,L_max,L_max/len(length_lst)):
        x = x
        y = y
        z = z
        Geomitry[i][:] = [x,y,z,0]

        i = i + 1
    return Geomitry

def Chem_gen(Temp : float, Pressure : float, Propellant : str):
    #Calculates the chem properties of propellant
    if Fractinal == True:
        Prop.TPX = Temp, Pressure, f"{str(Propellant)}:0.9,{str(Propellant[0])}:0.1"
        Prop.equilibrate('TP')
    else:
        Prop.TPX = Temp, Pressure, f"{str(Propellant)}:1.0"
    return Prop.thermal_conductivity, Prop.density, Prop.viscosity, Prop.cp_mass

def Rotate_z(data,angle_rad):
    # calculates the roation of the data set for visual representation.
    x, y, z, t = data[:,0], data[:,1], data[:,2], data[:,3]
    x_new = x * np.cos(angle_rad) - y * np.sin(angle_rad)
    y_new = x * np.sin(angle_rad) + y * np.cos(angle_rad)
    rotated = np.column_stack((x_new, y_new, z, t))
    return rotated
# Main Loop

def Main_loop(Helix: bool,T_int: float, P_int: float, Helix_Diameter: float, Pitch: float,
    Num_chanels: int, dx_a: float):
    # Import Gemoetry
    if Helix == True:
        Gemoitry = Gemoitry_Helix(Helix_Diameter, Pitch)
        a = np.arctan(Pitch/(Helix_Diameter*np.pi))
        l = (L_max/Pitch) * np.sqrt((np.pi * Helix_Diameter)**2 + Pitch**2)
    else:
        Gemoitry = Gemoitry_Strait(0,0)
        a = np.pi/2
        l = L_max

    # calculate initial Values
    k_f, rho_f, u_f, Cp_f = Chem_gen(T_int,P_int,Propellant) # import chemical properties
    m_int = m/Num_chanels # divide mass flow over number of channels
    v_int = (4 * m_int)/(np.pi * D**2 * rho_f) # calculate initial flow velocity
    v_in = v_int # set input velocity
    T_in = T_int # set input Temperature
    P_in = P_int # set input Pressure
    Time = 0 # initiate time
    for i in np.arange(0,L_max/dx_a,1):
        # Calculate input values and dimensinless numbers
        k_f, rho_f, u_f, Cp_f = Chem_gen(T_in,P_in,Propellant) # Calates new chamical
            properties
        v_int = (4 * m_int)/(np.pi * D**2 * rho_f)
        Re, Pr = (rho_f * v_in * D)/u_f, (Cp_f * u_f)/k_f # caculates Reynolds and Prandtl
            numbers

        # Cacluates the Nusselt number for laminar and turbulant flow
        if Re < 2300:
            Nu = 3.66
        else:
            Nu = 0.045 * Re ** 0.8 * Pr ** 0.4 * (l/D) ** -0.15 * (T_w/T_in) ** -0.55

        # Calculate change to fluid tempearture
        h = (k_f * Nu)/D # calcualtes convective heat flux

        dT = (h * np.pi * D * dx_a * (T_w - T_in))/(m_int * Cp_f * np.sin(a)) # calculates
            change in tempearture over discretisation
        T_out = T_in + dT # updates next iteration's temperature
```

```
        # Calculate pressure loss due to friction for laminar and turbulant flow
        if Re < 2300:
            f_d = 64/Re
        else:
            delta = 6.0173/(Re * (0.07*(eps/D) + Re**-0.885)**0.109) + (eps/D)/3.71
            f_d = ((2.51/Re + 1.1213*delta)/(delta - (eps/D)/3.71 - 2.3026*delta*np.log(delta
                )))**2 # Vatankhah 2014 friction function

        dP = f_d * dx_a/(np.sin(a) * D) * (v_in**2 * rho_f)/2 # -DarcyWeisbach equation
        P_out = P_in - dP
        P_out = P

        # Caculate velocity change due to density changes
        _, rho_f_new, _, _ = Chem_gen(T_out,P_out,Propellant) # calcualtes new density value
        v_out = v_in * (rho_f/rho_f_new) # calculates next velocity
        Time = dx_a/v_out + Time # calculates time required for discretisation step
        Gemoitry[int(i),3] = T_out # implements thermal data into geometry

        v_in = v_out # initiating next discretisation step for Velocity
        P_in = P_out # initiating next discretisation step for Pressure
        T_in = T_out # initiating next discretisation step for Temperature
        #print(Time)
    return Gemoitry, v_in

# Visual representation of fluid channels
dx_a = 0.000001
length_lst = np.arange(0,L_max,dx_a)
results, _ = Main_loop(True,293,P,0.0155,0.008,3,dx_a)
results_120 = Rotate_z(results,2/3*np.pi)
results_240 = Rotate_z(results,4/3*np.pi)

fig = plt.figure()
ax = fig.add_subplot(projection='3d')
p = ax.scatter(results[:,0]*1e+3,results[:,1]*1e+3,results[:,2]*1e+3,c=results[:,3],cmap=mpl.
    colormaps['magma'])
p = ax.scatter(results_120[:,0]*1e+3,results_120[:,1]*1e+3, results_120[:,2]*1e+3,c=
    results_120[:,3],cmap=mpl.colormaps['magma'])
p = ax.scatter(results_240[:,0]*1e+3,results_240[:,1]*1e+3, results_240[:,2]*1e+3,c=
    results_240[:,3],cmap=mpl.colormaps['magma'])
ax.set_title(f'Channel␣Visualisation,␣with␣temperature␣gradient␣in␣K,␣Pc={P*1E-5}␣[bar],␣D_ch
    ={D*1e+3}[mm],\n␣D_hx={Helix_Diameter_Global}␣[mm],␣Pitch={Pitch_Global}[mm],␣Num␣
    channels={Num_channels},␣T_wall={T_w}[K]')
fig.colorbar(p, ax=ax,label='Flow␣Temperature␣[K]')
ax.set_xlabel('Width␣[mm]')
ax.set_ylabel('Depth␣[mm]')
ax.set_zlabel('Length␣[mm]')
fig.set_figheight(12)
fig.set_figwidth(12)
fig.savefig(rf'Thesis\Figures\Heat_Exchanger\3D_Visulisation_{Propellant}.png')
#print(results[-1,-1])

dx_a = 0.0001
length_lst = np.arange(0,L_max,dx_a)

# Channel Diameter Sensitivity
sen_lst = []
Chan_Diam_lst = np.arange(0.5e-3,2.5e-3,0.1e-3)
for Chan_Diam in Chan_Diam_lst:
    D = Chan_Diam
    results, _ = Main_loop(True,293,P,0.0155,0.008,3,dx_a)
    sen_lst.append(results[-1,3])

D = 1e-3
fig = plt.figure()
ax = fig.add_subplot()
ax.plot(np.arange(0.5e-3,2.5e-3,0.1e-3)*1e+3,sen_lst)
ax.set_xlabel('Channel␣Diameter␣[mm]')
ax.set_ylabel('Exit␣temperature␣[K]')
ax.set_title(f'Analysis␣on␣effects␣of␣channel␣Diameter,␣Pc={P*1E-5}␣[bar],␣Num␣channels={
    Num_channels},\n␣D_hx={Helix_Diameter_Global}␣[mm],␣Pitch={Pitch_Global}[mm],␣T_wall={T_w
    }[K]')
```

```
fig.set_figheight(7)
fig.set_figwidth(15)
fig.savefig(rf'Thesis\Figures\Heat_Exchanger\ChanDiamSens_{Propellant}_dis.png')

# Chocked Flow Sensitivity
sen_lst = []
Chan_Diam_lst = np.arange(0.5e-3,2.5e-3,0.1e-3)
for Chan_Diam in Chan_Diam_lst:
    D = Chan_Diam
    results, v_exit = Main_loop(True,293,P,0.0155,0.008,3,dx_a)
    speed_sound = np.sqrt(1.4 * 4124.2 * results[-1,3])
    results_mach = v_exit/speed_sound
    sen_lst.append(results_mach)

D = 1e-3
fig = plt.figure()
ax = fig.add_subplot()
ax.plot(np.arange(0.5e-3,2.5e-3,0.1e-3)*1e+3,sen_lst)
ax.set_xlabel('Channel Diameter [mm]')
ax.set_ylabel('Mach Number [-]')
ax.set_title(f'Chocked Flow determination, Pc={P*1E-5} [bar], Num channels={Num_channels},\n D_hx={Helix_Diameter_Global} [mm], Pitch={Pitch_Global}[mm], T_wall={T_w}[K]')
fig.set_figheight(7)
fig.set_figwidth(15)
fig.savefig(rf'Thesis\Figures\Heat_Exchanger\ChokedFlowSens_{Propellant}_dis.png')

# Helix Diameter sensitivity
sen_lst = []
Dim_len_lst = np.linspace(0.01,0.1,100)
for Dim_len in Dim_len_lst:
    results, _ = Main_loop(True,293,P,Dim_len,0.008,3,dx_a)
    sen_lst.append(results[-1,3])

fig = plt.figure()
ax = fig.add_subplot()
ax.plot(np.linspace(0.01,0.1,100),sen_lst)
ax.set_xlabel('Helix Diameter [m]')
ax.set_ylabel('Exit temperature [K]')
ax.set_title(f'Analysis on effects of Helix Diameter, Pc={P*1E-5} [bar], D_ch={D*1e+3}[mm], D_ch={D*1e+3}[mm], \n Pitch={Pitch_Global}[mm], Num channels={Num_channels}, T_wall={T_w}[K]')
fig.set_figheight(7)
fig.set_figwidth(15)
fig.savefig(rf'Thesis\Figures\Heat_Exchanger\HelixDiamSens_{Propellant}.png')

# Channel Number sensitivity
sen_lst = []
Num_len_lst = np.arange(1,50,1)
for Num_Chan in Num_len_lst:
    results, _ = Main_loop(True,293,P,0.0155,0.008,Num_Chan,dx_a)
    sen_lst.append(results[-1,3])

fig = plt.figure()
ax = fig.add_subplot()
ax.plot(np.arange(1,50,1),sen_lst)
ax.set_xlabel('Number fo Channels')
ax.set_ylabel('Exit temperature [K]')
ax.set_title(f'Analysis on effects of number of channels, Pc={P*1E-5} [bar], Num channels={Num_channels}, \n D_ch={D*1e+3}[mm], D_hx={Helix_Diameter_Global} [mm], Pitch={Pitch_Global}[mm], T_wall={T_w}[K]')
fig.set_figheight(7)
fig.set_figwidth(15)
fig.savefig(rf'Thesis\Figures\Heat_Exchanger\ChanNumbSens_{Propellant}.png')

# Wall Temperature sensitivity
sen_lst = []
Wall_temp_lst = np.arange(1500,2000,25)
for Wall_temp in Wall_temp_lst:
    T_w = Wall_temp
    results, _ = Main_loop(True,293,P,0.0155,0.008,3,dx_a)
    sen_lst.append(results[-1,3])
```

```
248
249 T_w = 1700
250 fig = plt.figure()
251 ax = fig.add_subplot()
252 ax.plot(np.arange(1500,2000,25),sen_lst)
253 ax.set_xlabel('Wall␣Temperature␣[K]')
254 ax.set_ylabel('Exit␣Temperature␣[K]')
255 ax.set_title(f'Analysis␣on␣effects␣of␣number␣of␣channels,␣Pc={P*1E-5}␣[bar],Num␣channels={
    Num_channels},\n␣D_ch={D*1e+3}[mm],␣D_hx={Helix_Diameter_Global}␣[mm],␣Pitch={
    Pitch_Global}[mm]')
256 fig.set_figheight(7)
257 fig.set_figwidth(15)
258 fig.savefig(rf'Thesis\Figures\Heat_Exchanger\WallTempSens_{Propellant}.png')
259
260 #Pitch Sensitivity
261 sen_lst = []
262 Pitch_lst = np.linspace(0.01,0.1,100)
263 for Pitch in Pitch_lst:
264     results, _ = Main_loop(True,293,P,0.0155,Pitch,3,dx_a)
265     sen_lst.append(results[-1,3])
266
267 fig = plt.figure()
268 ax = fig.add_subplot()
269 ax.plot(np.linspace(0,0.1,100),sen_lst)
270 ax.set_xlabel('Pitch␣[m]')
271 ax.set_ylabel('Exit␣Temperature␣[K]')
272 ax.set_title(f'Analysis␣on␣effects␣of␣Pitch,␣Pc={P*1E-5}␣[bar],␣D_ch={D*1e+3}[mm],␣\n␣D_hx={
    Helix_Diameter_Global}␣[mm],␣Num␣channels={Num_channels},T_wall={T_w}[K]')
273 fig.set_figheight(7)
274 fig.set_figwidth(15)
275 fig.savefig(rf'Thesis\Figures\Heat_Exchanger\Pitch_{Propellant}.png')
276
277 #Length analysis
278 sen_lst = []
279 L_max_lst = np.linspace(0.01,0.1,100)
280 for L_max_int in L_max_lst:
281     L_max = L_max_int
282     length_lst = np.arange(0,L_max_int,dx_a)
283     results, _ = Main_loop(True,293,P,0.0155,0.008,3,dx_a)
284     sen_lst.append(results[-1,3])
285
286 L_max = 0.02
287 length_lst = np.arange(0,L_max,dx_a)
288 fig = plt.figure()
289 ax = fig.add_subplot()
290 ax.plot(np.linspace(0.01,0.1,100),sen_lst)
291 ax.set_xlabel('Length␣[m]')
292 ax.set_ylabel('Exit␣Temperature␣[K]')
293 ax.set_title(f'Analysis␣on␣the␣length␣of␣heat␣exchanger␣on␣Final␣Temperature,Pc={P*1E-5}␣[bar
    ],D_ch={D*1e+3}[mm],\n␣D_hx={Helix_Diameter_Global}␣[mm],Pitch={Pitch_Global}[mm],Num␣
    channels={Num_channels},T_wall={T_w}[K]')
294 fig.set_figheight(7)
295 fig.set_figwidth(15)
296 fig.savefig(rf'Thesis\Figures\Heat_Exchanger\Length_{Propellant}.png')
297
298 #Pressure analysis
299 sen_lst = []
300 P_lst = np.linspace(1E+5,50E+6,100)
301 for P_int in P_lst:
302     results, _ = Main_loop(True,293,P_int,0.0155,0.008,3,dx_a)
303     sen_lst.append(results[-1,3])
304
305 fig = plt.figure()
306 ax = fig.add_subplot()
307 ax.plot(np.linspace(1E+5,50E+6,100),sen_lst)
308 ax.set_xlabel('Pressure␣[Pa]')
309 ax.set_ylabel('Exit␣Temperature␣[K]')
310 ax.set_title(f'Analysis␣on␣the␣length␣of␣heat␣exchanger␣on␣Final␣Temperature,␣Pc={P*1E-5}␣[
    bar],D_ch={D*1e+3}[mm],\n␣D_hx={Helix_Diameter_Global}␣[mm],Pitch={Pitch_Global}[mm],Num␣
    channels={Num_channels},T_wall={T_w}[K]')
311 fig.set_figheight(7)
```

```
fig.set_figwidth(15)
fig.savefig(rf'Thesis\Figures\Heat_Exchanger\Pressure_{Propellant}.png')

#Pitch channel number Contour
Pitch_lst = np.linspace(0.005,0.1,100)
Num_len_lst = np.arange(1,50,1)
results_lst = np.zeros((49,100))
for j in tqdm(range(len(Num_len_lst))):
    for i in tqdm(range(len(Pitch_lst))):
        if Pitch_lst[i]/Num_len_lst[j] > (D + 0.001):
            results, _ = Main_loop(True,293,P,0.0155,Pitch_lst[i],Num_len_lst[j],dx_a)
            results_lst[j][i] = results[-1,3]
        else:
            results_lst[j][i] = None

Pitch_lst, Num_len_lst = np.meshgrid(Pitch_lst, Num_len_lst)
fig, ax = plt.subplots()
c = ax.contourf(Num_len_lst, Pitch_lst, results_lst,20)
ax.contour(Num_len_lst, Pitch_lst, results_lst,[1500],linestyles='dashed')
plt.colorbar(c, ax=ax, label='Exit Temperature [K]')
ax.set_xlabel('Number of Channels')
ax.set_ylabel('Pitch [m]')
ax.set_title(f'Contour plot of final temperature for number of channels and pitch, Pc={P*1E
    -5} [bar], D_ch={D*1e+3}[mm], \n D_hx={Helix_Diameter_Global} [mm], T_wall={T_w}[K]')
fig.set_figheight(7)
fig.set_figwidth(15)
fig.savefig(rf'Thesis\Figures\Heat_Exchanger\Pitch_ChanNum_Contour_{Propellant}.png')

#channel Diameter, Pitch
Pitch_lst = np.linspace(0.005,0.1,100)
Chan_Diam_lst = np.arange(0.5e-3,2.5e-3,0.1e-3)
results_lst = np.zeros((20,100))
for j in tqdm(range(len(Chan_Diam_lst))):
    for i in tqdm(range(len(Pitch_lst))):
        D = Chan_Diam_lst[j]
        results, _ = Main_loop(True,293,P,0.0155,Pitch_lst[i],3,dx_a)
        results_lst[j][i] = results[-1,3]

Pitch_lst, Chan_Diam_lst = np.meshgrid(Pitch_lst, Chan_Diam_lst)
fig, ax = plt.subplots()
c = ax.contourf(Chan_Diam_lst, Pitch_lst, results_lst,20)
ax.contour(Chan_Diam_lst, Pitch_lst, results_lst,[1500],linestyles='dashed')
plt.colorbar(c, ax=ax, label='Exit Temperature [K]')
ax.set_xlabel('Channel Diameter [m]')
ax.set_ylabel('Pitch [m]')
ax.set_title(f'Contour plot of final temperature for number of channels and pitch, Pc={P*1E
    -5} [bar], channel nuber={Num_channels}, \n D_hx={Helix_Diameter_Global} [mm], T_wall={T_w
    }[K]')
fig.set_figheight(7)
fig.set_figwidth(15)
fig.savefig(rf'Thesis\Figures\Heat_Exchanger\Pitch_ChanDiam_Contour_{Propellant}.png')

#channel Diameter, channel number
Chan_Diam_lst = np.arange(0.5e-3,2.5e-3,0.1e-3)
Num_len_lst = np.arange(1,10,1)
results_lst = np.zeros((9,20))
for j in tqdm(range(len(Num_len_lst))):
    for i in tqdm(range(len(Chan_Diam_lst))):
        D = Chan_Diam_lst[i]

        results, _ = Main_loop(True,293,P,0.0155,0.008,Num_len_lst[j],dx_a)
        results_lst[j][i] = results[-1,3]

Chan_Diam_lst, Num_len_lst = np.meshgrid(Chan_Diam_lst, Num_len_lst)
fig, ax = plt.subplots()
c = ax.contourf(Num_len_lst, Chan_Diam_lst, results_lst,20)
ax.contour(Num_len_lst, Chan_Diam_lst, results_lst,[1500],linestyles='dashed')

plt.colorbar(c, ax=ax, label='Exit Temperature [K]')
ax.set_xlabel('Number of Channels')
ax.set_ylabel('Channel Diameter [m]')
```

```
ax.set_title(f'Contour␣plot␣of␣final␣temperature␣for␣number␣of␣channels␣and␣pitch,␣Pc={P*1E-5}␣[bar],␣Pitch={Pitch_Global}[mm],\n␣D_hx={Helix_Diameter_Global}␣[mm],␣T_wall={T_w}[K]')
fig.set_figheight(7)
fig.set_figwidth(15)
fig.savefig(rf'Thesis\Figures\Heat_Exchanger\ChanNumb_ChanDiam_Contour_{Propellant}.png')

#Sensitivity analsys
sen_lst = []
for dx_a_int in [1,1e-1,1e-2,1e-3,1e-4,1e-5,1e-6,1e-7]:
    print(dx_a_int)
    D = 1E-3
    length_lst = np.arange(0,L_max,dx_a_int)
    results, _ = Main_loop(True,293,P,0.01,0.01,10,dx_a_int)
    sen_lst.append(results[-1,3])
fig = plt.figure()
ax = fig.add_subplot()
#sen_lst = [26991.896905106485, 2962.8896905106485, 1482.3488985570327, 1466.2342590088715,
#1464.3557677957965, 1464.2078667175936, 1464.194343062647, 1464.19171289134,
    1464.1914266760302] raw data
ax.plot([1,1e-1,1e-2,1e-3,1e-4,1e-5,1e-6,1e-7],sen_lst)
ax.set_xscale('log')
ax.set_yscale('log')
ax.set_xlabel('Step␣Size␣[m]')
ax.set_ylabel('Exit␣temperature␣[K]')
ax.set_title(f'Analysis␣on␣effects␣of␣step␣size␣on␣simulation␣results,Pc={P*1E-5}␣[bar],D_ch={np.round(D)*1e+3}[mm],\n␣D_hx={0.01E+3}␣[mm],Pitch={0.01E+3}[mm],Num␣channels={10},T_wall={T_w}[K]')
fig.set_figheight(7)
fig.set_figwidth(15)
fig.savefig(rf'Thesis\Figures\Heat_Exchanger\DiscritiasationSens_{Propellant}.png')
plt.show()

## Cavity Plotting ##
#Sampled Data from Cavity Simulaion
lx_Small = [1.23212e+1,
    7.02588,7.11272,7.20755,7.30237,7.39719,7.4921,7.58825,7.68617,7.78606,7.88814,7.99274]#,6.25912e+1]
lx_Mid = [8.57378,
    4.49285,4.84697,5.22463,5.60229,5.97995,6.36418,6.4885,6.63541,6.78232,6.92923,7.06258]#,4.850522e+1]
lx_large = [5.92336,
    4.6215,4.52738,4.43083,4.33316,4.23374,4.12203,3.91698,3.71469,3.51616,3.32366,3.17734]#,2.80277e+1]
lx_SphLarge = [3.94696,
    4.60495,4.62951,4.65243,4.67242,4.68721,4.63985,4.54005,4.4407,4.34205,5.46893]#,1.4585E+2] # 1.0833E+2
lx_Cone = [6.06707, 7.82051,8.93178,9.9777,1.09903e+1,1.20598e+1,1.31515e+1,1.43424e+1,1.55142E+1,1.67381e+1,1.80243e+1]#,4.538E+1]
lx_TCone = [4.10794, 4.2122,5.16676,5.13455,4.07532,9.76821,1.19025E+1,1.39469e+1,1.73373e+1,3.18246E+1,2.62434E+1]#,1.43064e+2]
lx_TSCone = [8.31699E-1,4.31746,4.17285,4.0517,3.90577,3.65152,3.38566,1.0556e+1,1.96921e+1,3.67721e+1]#,3.79749e+2]

Data = [lx_Small,lx_Mid,lx_large,lx_SphLarge,lx_Cone,lx_TCone,lx_TSCone]
Names = ["Small", "Medium", "Large", "Spherical␣Capped", "Cone", "Diverging-Converging␣Cone", "Cone␣Capped"]
fig, ax01 = plt.subplots(figsize=(10,8))

fig, ax02 = plt.subplots(figsize=(10,8))


j = 0
# Genration of spline and gradient
for data in tqdm(Data):
    y = np.linspace(0,1,len(data))
    fsmooth = spi.UnivariateSpline(y, data)
    Y_sample = np.linspace(0,1,10000)
    gradient = np.gradient(fsmooth(Y_sample),Y_sample)
    i = 0
    ax01.plot(Y_sample,fsmooth(Y_sample)*1e+7,label=Names[j])
```

```
434     ax02.plot(Y_sample,gradient,label=Names[j])
435     j = j + 1
436 #plotting of graphs
437 ax01.set_xlabel("Cavity␣Length␣[L/L_max]")
438 ax01.set_ylabel("Luminocity␣[lux]")
439 ax01.legend()
440 ax01.grid()
441 ax02.set_xlabel("Cavity␣Length␣[L/L_max]")
442 ax02.set_ylabel("Luminocity␣gradient␣[-]")
443 ax02.legend()
444 ax02.grid()
445 plt.show()
```